

Arctic low-level mixed-phase clouds and their complex interactions with aerosol and radiation

Remote sensing of the Arctic troposphere with the shipborne supersite OCEANET-Atmosphere

Der Fakultät für Physik und Geowissenschaften
der Universität Leipzig
genehmigte

D I S S E R T A T I O N

zur Erlangung des akademischen Grades

DOCTOR RERUM NATURALIUM
Dr. rer. nat.

vorgelegt

von Hannes Jascha Griesche M.Sc. Meteorologie
geboren am 13. Juni 1988 in Mettingen, Deutschland

Gutachter:

Prof. Dr. Andreas Macke
Prof. Dr. Ian Brooks

Tag der Verleihung: Leipzig, den 21. März 2022

Bibliographische Beschreibung:

Griesche, Hannes Jascha

Arctic low-level mixed-phase clouds and their complex interactions with aerosol and radiation

— *Remote sensing of the Arctic troposphere with the shipborne supersite OCEANET-Atmosphere*

Universität Leipzig, Dissertation

139 S., 284 Lit., 45 Abb., 1 Tabellen, 1 Anlage

Referat:

Im Rahmen dieser Arbeit wurden niedrige arktische Mischphasenwolken und ihre Wechselwirkung mit Aerosolen und Strahlung untersucht. Dazu wurden Messungen mit der schiffsgestützten Fernerkundungs-Supersite OCEANET-Atmosphere während der PS106-Expedition im arktischen Sommer 2017 durchgeführt. OCEANET-Atmosphere vereint, u.a., ein Multiwellenlängen-Polarisations-Lidar Polly^{XT} und ein Mikrowellen-Radiometer HATPRO. Für PS106 wurde OCEANET-Atmosphere erstmalig um ein stabilisiertes, vertikal ausgerichtetes Doppler-Wolkenradar Mira-35 erweitert. Die Doppler-Geschwindigkeit wurde in Bezug auf die Vertikalbewegung des Schiffes korrigiert. Dank Stabilisierung und Korrektur war, z.B., die Ableitung von Wirbeldissipationsraten aus den Doppler-Geschwindigkeiten möglich.

Unter Anwendung des synergetischen Cloudnet-Algorithmus wurde aus den kombinierten Wolkenradar, Lidar und Mikrowellenradiometer Messungen ein Datensatz der mikro- und makrophysikalischen Wolkeneigenschaften für PS106 erstellt. Im Rahmen dieser Arbeit wurde Cloudnet verbessert, um der komplexen Struktur der arktischen Wolken Rechnung zu tragen. Ein neuer Ansatz zur Erkennung der häufig beobachteten niedrigen Stratuswolken wurde entwickelt, basierend auf dem Lidar-Signal-zu-Rausch-Verhältnis. Diese Wolken, die unterhalb des untersten Höhenlevels des Wolkenradars auftraten, wurden während 50 % der Beobachtungszeit identifiziert. Ein neuer Ansatz für die kontinuierliche Bestimmung des effektiven Radius der Eiskristalle wurde eingeführt. Dank dieser neuen Methode eignet sich der erstellte Datensatz für die Durchführung von Strahlungstransfersimulationen.

Zum ersten Mal wurde eine Temperaturbeziehung für heterogene Eisbildung in arktischen Mischphasenwolken in Abhängigkeit ihres Oberflächen-Kopplungsstatus abgeleitet. Bei Temperaturen über -15°C war die relative Häufigkeit von Eis beinhaltenden Wolken doppelt so hoch und die Anzahl fünf Mal höher wenn sie mit der Oberfläche gekoppelt waren, als bei entkoppelte Wolken. Mögliche Ursachen für den beobachteten Effekt wurden anhand von Sensitivitätsstudien und einer Literaturanalyse diskutiert. Instrumentelle und methodische Effekte sowie früher veröffentlichte ähnliche Beobachtungen konnten als mögliche Erklärung ausgeschlossen werden. Die wahrscheinlichste Ursache für den beobachteten Effekt wurde auf ein größeres Reservoir an biogenen Eiskristallisationskeimen in der oberflächengekoppelten marinen Grenzschicht zurückgeführt. Dieses größere Reservoir hat zu einer höheren Gefriereffizienz in Wolken geführt, die zumindest ihre Basis in dieser Schicht hatten.

Die Bedeutung der detaillierten Klassifizierung von tiefliegenden Wolken auf Strahlungstransfersimulationen wurde hervorgehoben. Der simulierte Effekt der Wolken auf den Strahlungshaushalt unterschied sich bis zu 100 W m^{-2} , unter Berücksichtigung dieser Wolken.

Bibliographic Description:

Griesche, Hannes Jascha

Arctic low-level mixed-phase clouds and their complex interactions with aerosol and radiation

— *Remote sensing of the Arctic troposphere with the shipborne supersite OCEANET-Atmosphere*

University of Leipzig, Dissertation

139 p., 284 ref., 45 fig., 1 tab., 1 appendix

Abstract:

In the course of this thesis, Arctic low-level mixed-phase clouds and their interaction with aerosol and radiation have been investigated. To do so, measurements with the shipborne remote sensing supersite OCEANET-Atmosphere were conducted during the PS106 expedition in the Arctic summer 2017. OCEANET-Atmosphere comprises among other instruments a multiwavelength polarization lidar Polly^{XT} and a microwave radiometer HATPRO. For PS106 the OCEANET-Atmosphere facility was complemented for the first time with a motion-stabilized vertically pointing Doppler cloud radar Mira-35. The cloud radar Doppler velocity was corrected for the ship's vertical movement. The stabilization and the correction enabled, e.g., the derivation of eddy dissipation rates from the Doppler velocities.

A data set of cloud microphysical and macrophysical properties was derived by applying the synergistic Cloudnet algorithm to the combined measurements of cloud radar, lidar, and microwave radiometer. Within this thesis, the set of the Cloudnet retrievals was improved to account for the complex structure of the Arctic cloud system. A new detection approach for the frequently observed low-level stratus clouds was developed based on the lidar signal-to-noise ratio. These clouds, which were below the lowest range gate of the cloud radar were observed during 50 % of the observational time. A new approach for the continuous determination of the ice crystal effective radius was introduced. This new retrieval made the data set suitable to perform high-resolved radiative transfer simulations.

The retrieved data set was utilized to derive the first temperature relationship for heterogeneous ice formation in Arctic mixed-phase clouds. A strong dependence of the surface-coupling state for high subzero ice-formation temperatures was found. For an ice-formation temperature above -15°C , surface-coupled ice-containing clouds occur more frequently by a factor of 5 in numbers of observed clouds and by a factor of 2 in frequency of occurrence. Possible causes of the observed effect were discussed by sensitivity studies and a literature survey. Instrumental and methodological effects, and previously published similar observations of an increased ice occurrence at such high subzero temperatures have been ruled out as a possible explanation. The most likely cause of the observed effect was attributed to a larger reservoir of biogenic ice-nucleating particles in the surface-coupled marine boundary layer. This larger reservoir led to a higher freezing efficiency in these clouds which had at least their base in that layer.

Finally, the importance of the detailed classification of the low-level clouds was highlighted by the evaluation of radiative transfer simulations. A difference in the cloud radiative effect of up to 100 W m^{-2} was calculated when these clouds were considered.

Table of Contents

1	Introduction	1
2	Arctic — Amplified climate change	7
2.1	The Arctic climate system	7
2.2	Cloud radiation budget	9
2.3	Arctic mixed-phase clouds	12
2.4	Heterogeneous ice formation in Arctic mixed-phase clouds — constraints and previous findings	13
2.5	Motivating research questions	17
3	Data set — Applied instrumentation, processing, and retrievals	19
3.1	Introduction to ground-based active remote sensing of aerosol and clouds . .	19
3.1.1	Lidar principle	20
3.1.2	Radio Detection and Ranging — Radar	24
3.2	The Arctic expedition PS106	27
3.3	Instrumentation	28
3.3.1	The OCEANET-Atmosphere observatory	28
3.3.2	Other instruments used in this study	32
3.4	Data processing and synergistic retrievals	33
3.4.1	Correction of vertical-stare cloud radar observations for ship motion .	33
3.4.2	Retrieval of eddy dissipation rate from Doppler radar spectra	37
3.4.3	Cloud macro- and microphysical properties from instrument-synergies	41
3.5	Summary of the data processing for PS106	46
4	Cloud and aerosol observations during PS106	49
4.1	Meteorological conditions during PS106	49
4.2	Case studies	51
4.3	Cloud and aerosol statistics during PS106	64
4.4	Discussion of the observational data sets	66
5	Contrasting surface-coupling effects on heterogeneous ice formation	73
5.1	Methodology	74

5.1.1	Ice-containing cloud analysis	74
5.1.2	Surface-coupling state	77
5.2	Results: influence of surface coupling on heterogeneous ice formation temperature	78
5.3	Discussion of the observed surface-coupling effects	80
5.3.1	Methodological and instrumental effects	80
5.3.2	Possible causes for increased ice occurrence in surface-coupled clouds .	84
6	Application of the data set in collaborative studies and radiative transfer simulations within (AC)³	91
6.1	Radiative transfer simulations and cloud radiative effect	92
6.2	LLS treatment for improved radiative transfer simulations	93
6.3	Discussion	102
7	Summary and outlook	106
	Appendices	110
A	Determination of a volume depolarization threshold for lidar-based ice detection	110
	Bibliography	113
	List of abbreviations and acronyms	137

Chapter 1

Introduction

Already more than a century ago, Arrhenius [1897] predicted that an increase in the atmospheric carbon dioxide (CO_2) concentration will cause a global temperature rise, which will be especially pronounced in the Arctic. Today, global warming is one of the greatest threats to society [IPCC, 2014]. The mean global surface temperature of the period of 2011 to 2020 was increased by more than 1°C compared to the period of 1850 to 1900, caused almost exclusively by human activities [IPCC, 2013]. Heavy precipitation events, floods, and hot extremes have become more frequent, while at the same time the risk of droughts increased over many regions of the world [IPCC, 2019], just to name a few impacts. Also, the hypothesis that the Arctic will be a hotspot of global climate change has proven to be true. This fact is observable in the change of several parameters such as the drastic decline of the Arctic sea ice during all seasons, but especially in summer, in both extent and thickness [Meier et al., 2014]. In the past 30 years, the mean Arctic near-surface air-temperature anomaly increased at least by a factor of two faster compared to the global mean [Serreze and Barry, 2011]. For example, the surface temperature anomaly of 2013 with respect to the mean of 1970 – 1999 was $2 - 3\text{ K}$ above the one of the mid-latitudes [Francis and Skific, 2015]. Moreover, the impacts of the changes in the Arctic climate system are not restricted to the high northern latitudes. The differential heating will likely have consequences for the mid-latitudinal circulation, leading to reduced zonal winds, and consequently more-steady weather periods with the accompanied larger regional risk of severe droughts or wet periods [Francis and Skific, 2015].

The changes in the Arctic are summarized by the term Arctic amplification and are assumed to be driven by several feedback mechanisms [Wendisch et al., 2017]. A major feedback, for example, is associated with the ice and snow loss, and the respective decrease in surface albedo [Flanner et al., 2011]. Yet, the understanding of the causes and impacts of climate change, whether globally or Arctic-wide, is still a challenge in atmospheric science [IPCC, 2013]. The largest uncertainty is associated with aerosol particles and their interactions with clouds and radiation. These interactions are assumed to be among the few forcing agents that can have a negative impact on the radiation budget [IPCC, 2013]. The

68 % confidence interval for the present-day total aerosol forcing based on model comparisons and satellite observations was reported to spread between -1.6 W m^{-2} and -0.6 W m^{-2} [Bellouin et al., 2020]. Reasons for the uncertainties are on the one hand related to aerosol particles which directly change the atmospheric radiation fluxes by scattering and absorbing incoming and outgoing radiation [e.g., Anderson et al., 2005; Satheesh and Krishna Moorthy, 2005], which is called aerosol-radiation-interaction (ARI). When the particles sediment to snow and ice surfaces, they can decrease the surface albedo and hence increase the absorbed radiation [Hansen and Nazarenko, 2004] with the consequence of accelerated melting. On the other hand, aerosol particles have numerous indirect effects on the Earth’s climate, e.g., by influencing the geochemical cycle, the cryosphere, and, most prominent in terms of radiative impact, the cloud microphysical and radiative properties via aerosol-cloud-interaction (ACI) mechanisms [IPCC, 2013]. Given the possible widespread consequences of Arctic amplification, it is essential to understand the physical processes leading to this rapid change. There is still a lack of understanding in the interplay of these feedback mechanisms, their seasonality, as well as in quantifying their relative importance and magnitude [Goosse et al., 2018; Pithan and Mauritsen, 2014; Serreze and Barry, 2011].

An increase in the abundance of atmospheric aerosol particles that can activate droplet formation, so-called cloud condensation nuclei (CCN), will lead to the formation of numerous but smaller droplets which increases, in turn, the cloud albedo [Twomey, 1974, 1977]. This Twomey effect can be observed for example in the case of stratiform cloud decks, which were influenced by exhaust particles along ship tracks [Radke et al., 1989]. Also, smaller droplets are less likely to form precipitation and thus increase the cloud lifetime [Albrecht, 1989]. These effects on liquid-water clouds might even play a larger role in the Arctic, where cloud regimes have been observed in which droplet formation was rather limited by CCN availability than by liquid-water abundance [Mauritsen et al., 2011]. At the same time, another population of aerosol can initiate ice crystal formation, the ice-nucleating particles (INPs). Different processes involving INPs are known to trigger ice formation. These mechanisms are summarized by the term heterogeneous ice formation which takes place in the temperature regime between approximately -38°C to 0°C [Hoose and Möhler, 2012; Pruppacher and Klett, 1997]. In this temperature range, clouds may be composed of either pure ice, liquid, or both. The coexistence of liquid and ice inside a single cloud is referred to as mixed-phase. The Wegener-Bergeron-Findeisen process [Bergeron, 1935; Findeisen, 1938; Wegener, 1912], describes the growth of ice crystals at the expense of liquid-water droplets if both phases are present. Thus, mixed-phase clouds without significant vertical air motions or a moisture source from above or below the cloud are assumed to glaciate completely [Fan et al., 2011; Korolev and Field, 2008; Solomon et al., 2011]. Below approximately -38°C , ice formation can also happen via homogeneous freezing processes for which no INPs are necessary [Pruppacher and Klett, 1997].

Besides the evident role of sea ice loss in the warming process, a key role in Arctic

amplification is attributed to the radiative effects of clouds [Vavrus, 2004]. Kay and L’Ecuyer [2013] obtained a climatology of Arctic clouds and radiation conditions for the first decade of the 21st century. They highlight the importance of clouds in the Arctic climate system but they also note that both conditions — presence as well as the absence of clouds — can contribute to Arctic amplification, depending on season and sea-ice conditions. Moreover, Goosse et al. [2018] showed that the impact of clouds on the Earth’s energy budget can be both, positive or negative, depending on the clouds macrophysical and microphysical properties. They reported that a higher fraction of low clouds, e.g., caused by decreased sea-ice extent increases the downwelling longwave radiation during polar night, which is a positive feedback. During polar day, in contrast, a higher fraction of liquid water in mixed-phase clouds was found to increase the cloud albedo which, in turn, enhances the reflection of incoming shortwave radiation at the top of the atmosphere (TOA) [Goosse et al., 2018], and thus produces a negative feedback. Yet, the underlying processes controlling Arctic cloud phase and occurrence, and hence the connected feedback mechanisms driving Arctic amplification are not completely understood [Goosse et al., 2018; Kalesse et al., 2016a; Pithan and Mauritsen, 2014; Serreze and Barry, 2011; Shupe et al., 2013; Stuecker et al., 2018].

Detailed observations of Arctic clouds are key requirements to study the Arctic energy budget but they are still rare. Measurements from ground-based stations, such as the observatories of the International Arctic Systems for Observing the Atmosphere (IASOA) [Uttal et al., 2016] are of great value, e.g., due to their long-term data sets. However, they are limited to one location of observation, influenced by their surrounding orography [e.g., Gierens et al., 2020], and local anthropogenic contamination, such as traffic and industry [Creamean et al., 2018b; Herenz et al., 2018]. A new development are drifting buoys, which can enter any place in the Arctic ice and provide valuable observations in this harsh environment. Their equipment is steadily optimized and becomes increasingly sophisticated. The latest developments are buoys equipped with autonomous lidar systems [Mariage et al., 2017], allowing measuring vertical profiles of clouds and aerosol. But, their movement depends on the ice drift and they are limited in their payload and cannot yet replace intricate measurements from observatories or campaigns. Observations of spaceborne cloud radar and lidar, as done aboard CloudSat [Stephens et al., 2008] and CALIPSO (Cloud-Aerosol Lidar and Infrared Pathfinder Satellite Observation) [Winker et al., 2010] provide, in addition, a large-scale overview of the Arctic cloud coverage [Liu et al., 2012]. However, the respective data sets lack information on the lowest cloud levels as well as the highest latitudes. To study Arctic clouds, different aircraft campaigns have been conducted in recent years [e.g., Curry et al., 2000; Jacob et al., 2010; McFarquhar et al., 2011; Wendisch et al., 2019]. While airborne measurements yield a unique, accurate description of the observed cloud, they cannot measure continuously the entire tropospheric column over a long period, a feature active remote sensing can offer. Given their capability, ground-based remote-sensing methods are suitable to investigate the spatiotemporal distribution of clouds [Bühl et al., 2013], their phase partitioning [de Boer et al., 2009; Kalesse et al., 2016a; Zhang et al., 2014], and their

interaction with aerosol particles [Ansmann, 2019; Engelmann et al., 2021; Radenz et al., 2021; Seifert et al., 2010; Zhang et al., 2018]. The wide range of variability in the processes involved in ACI and cloud formation require detailed observations from small particles to large hydrometeors. However, a single instrument only measures a specific parameter. Therefore, instrument synergy will result in insights that are more accurate. The presence and characterization of ice crystals, vertical motions inside clouds, and multilayer situations are best observed using a cloud radar. A lidar, in turn, is highly sensitive to aerosol particles and liquid-water cloud droplets, and can, depolarization capabilities provided, be used for cloud-phase partitioning. Synergistic processing of lidar and radar measurements, such as within Cloudnet as proposed by Illingworth et al. [2007] and ARSCL (Active Remote Sensing of Clouds) [Shupe, 2007], can deliver data sets of cloud macro- and microphysical properties. These data sets serve, e.g., as a basis for model evaluation [Illingworth et al., 2007; Neggers et al., 2019] and radiative transfer calculations [Barrientos Velasco et al., 2020; Ebell et al., 2019]. Hence, in addition to the airborne campaigns, several shipborne campaigns equipped with remote-sensing instrumentation have been conducted in the past few years in the Arctic [e.g., Achtert et al., 2015; Granskog et al., 2018; Sotiropoulou et al., 2016; Tjernström et al., 2014, 2004; Uttal et al., 2002; Vüllers et al., 2021; Wendisch et al., 2019].

To study the feedback mechanisms causing Arctic amplification, the collaborative research centre (AC)³ (Arctic Amplification: Climate Relevant Atmospheric and Surface Processes and Feedback Mechanisms) conducted two complementary field campaigns in the Arctic summer of 2017: ACLOUD (Arctic Cloud Observations Using Airborne Measurements during Polar Day), an airborne campaign performed with the research aircraft Polar 5 and Polar 6, and the PASCAL (Physical Feedbacks of Arctic Boundary Layer, Sea Ice, Cloud and Aerosol) expedition deployed on and around the research icebreaker Polarstern [Macke and Flores, 2018; Wendisch et al., 2019]. These campaigns took place in May and June 2017 in the regions north and northeast of Svalbard with the aim to combine remote-sensing and in-situ observations. During PASCAL, a 2-week ice floe camp was performed in the vicinity of Polarstern and a large number of measurements were conducted on the ice. PASCAL took place from 25 May until 21 June 2017 and was the first part of the split Polarstern cruise PS106. The second leg of PS106 was the Survival of Polar Cod in the Arctic Ocean (SiPCA) campaign, which ended on 20 July 2017. During the full period of PS106, continuous remote sensing of aerosol and clouds was performed with the OCEANET-Atmosphere platform from the Leibniz Institute for Tropospheric Research (TROPOS), Leipzig, Germany, aboard Polarstern. Measurements with the multiwavelength polarization lidar Polly^{XT}_OCEANET, a 35-GHz cloud radar Mira-35, and a microwave radiometer (MWR) HATPRO (Humidity And Temperature Profiler) were conducted. Within (AC)³ the OCEANET-Atmosphere observations have the essential role to describe the temporal evolution of the vertical structure of aerosol and clouds in the central Arctic. They constitute the prerequisite for further studies of aerosol-cloud interaction, model evaluation, or radiative transfer modeling, which are partly covered by other projects of (AC)³.

The following thesis evolved around the OCEANET-Atmosphere data from the PASCAL/PS106 campaign. Chapter 2 provides an overview of the processes driving Arctic amplification and the role of clouds therein, which leads to the formulation of motivating research questions for this work. Chapter 3 introduces the measurements performed during PS106 and presents the data set obtained. A brief introduction to active remote-sensing techniques used in this study is given. Afterward, the applied processing steps and retrieval algorithms are presented. A crucial part of this work was to overcome the challenges of conducting continuous remote sensing on an icebreaker in the High Arctic. A method was developed for the correction of the influence of the ship's movement on the cloud radar Doppler velocity, which is explained and extensively evaluated. An approach to derive a measure of turbulence in terms of eddy dissipation rate from the vertical Doppler velocity is given. Additionally, retrievals of microphysical and macrophysical cloud properties are explained. This Section covers, besides existing retrievals, the introduction of newly developed retrievals for 1) quantifying the frequent occurring low-level cloud decks and 2) the derivation of the effective radius of ice crystals from cloud radar observations. Chapter 4 shows the application of the prepared synergistic data set. Three case studies and a statistical overview of the cloud situation during the cruise are presented and show the capabilities of the observations and retrieved products. The focus of Chapter 5 are the frequently observed low-level clouds and heterogeneous ice formation events therein. Links between thermodynamic surface-coupling of low-level Arctic clouds and cloud ice occurrence are presented. For the first time it has been shown, that surface-coupled clouds in the Arctic show a higher fraction of ice-containing clouds at temperatures above -15°C than decoupled clouds. Possible explanations of the observed different ice-formation temperature for surface-coupled and free-tropospheric clouds are discussed. The focus of Chapter 6 are radiative transfer simulations and how a more detailed characterization of the low-level clouds can improve their results. Radiative closure for a multilayer cloud situation was found by implementing the novel low-level cloud detection into the radiative transfer simulations. A conclusion and summary are given in Chapter 7. Parts of this thesis are based on work published in Griesche et al. [2020a] and Griesche et al. [2021].

Chapter 2

Arctic — Amplified climate change

The role of the Arctic system and the complex interactions between aerosol particles, clouds, and radiation but also surface properties in the context of global climate change were emphasized in the introduction chapter. Here, an introduction to the Arctic climate system is given, the construct of feedback mechanisms is exemplified, and factors that can vary the radiation budget in the Arctic are summarized. Subsequently, the role of mixed-phase clouds in Arctic amplification with a focus on heterogeneous ice formation is presented.

2.1 The Arctic climate system

An above global average Arctic warming can be observed since about 1990 from long-term observations and model reanalysis data as shown in Figure 2.1. The reason for the enhanced warming in the Arctic (called Arctic amplification) is assumed to be related to several feedback mechanisms [e.g., Goosse et al., 2018]. The principle of such a feedback is based on an initial radiative forcing, which leads to a change in the global mean near-surface air-temperature. This temperature change in turn can trigger a transformation in other components of the Earth’s system causing further temperature variations. The magnitude of this temperature change, which is needed to establish an energy balance following the forcing or in response to a feedback is called climate sensitivity [IPCC, 2013].

One example of such a forcing is the increase in greenhouse gas concentration in the atmosphere, which leads to an increase in the global energy budget and eventually the global mean temperature [Donohoe et al., 2014]. A vertical homogeneous rise of the atmospheric temperature profile increases the Earth’s black body emission and counteracts the temperature rise, an effect that is called the Planck feedback [Goosse et al., 2018].

A vertical inhomogeneous alternation of the temperature profile, by a global warming trend, leads to changes in the downward directed longwave radiation, the so-called lapse rate feedback [Mauritsen et al., 2013]. Due to the convective nature of the tropical troposphere

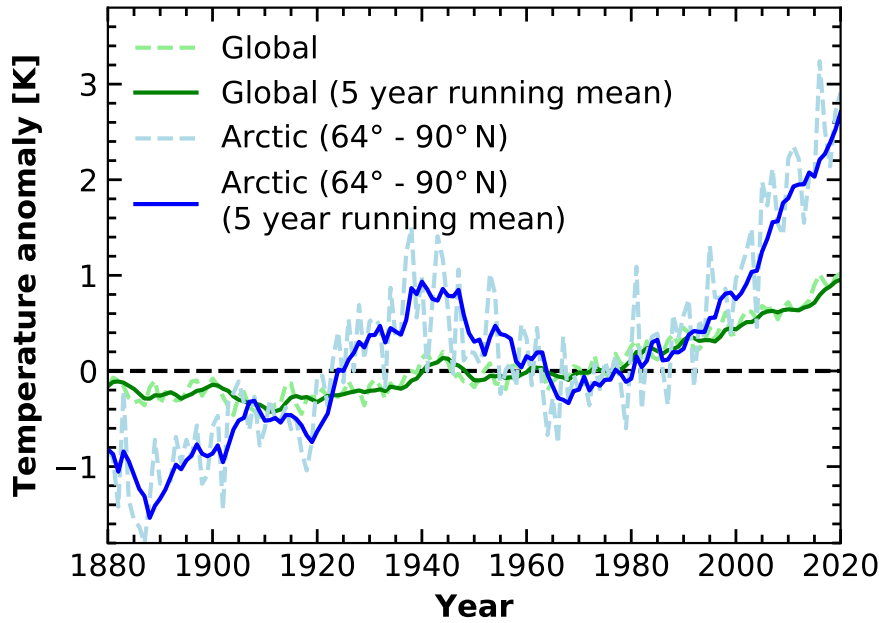


Figure 2.1: Annual mean near-surface air-temperature anomaly globally (green) and only for the Arctic region ($>64^\circ\text{N}$, blue) relative to the 1951 – 1980 mean. Data from the Goddard Institute for Space Studies Surface Temperature Analysis version 4 [GISTEMP-Team, 2021; Lenssen et al., 2019].

and the stable nature of the Arctic troposphere, the lapse rate feedback has a different sign at high latitudes compared to lower ones. Deep convection in the Tropics leads to enhanced warming in higher altitudes, which increases the outgoing longwave radiation [Manabe and Wetherald, 1975]. Accordingly, the lapse rate feedback is negative close to the equator [e.g., Pithan and Mauritsen, 2014]. In contrast, the stable stratification of the lower Arctic troposphere causes warming, which is bottom-heavy, i.e., the warming close to the surface is higher than at the TOA. The energy flux leaving the Earth system is smaller for this case when compared to a theoretical radiation perturbation with vertically uniform warming. Hence, the lapse rate feedback is positive at high latitudes. The Planck feedback and the lapse rate feedback together are called the temperature feedback.

Higher temperatures in the Arctic will lead to a decrease in sea-ice and snow concentration, exposing darker surfaces, and decreasing the surface albedo. More incoming radiation will be absorbed and the warming will be amplified. This so-called ice-albedo feedback [Curry et al., 1995] is a positive feedback in the Arctic. Also, a warmer atmosphere can contain more water vapor, which itself is a potent greenhouse gas [e.g., Manabe and Wetherald, 1967; Schneider et al., 1999]. Furthermore, the climate sensitivity due to clouds is still rather uncertain [Block et al., 2020] and is discussed in Section 2.2. Further important feedbacks are connected to a change in the meridional atmospheric and oceanic mass and energy transport

pattern and aerosol occurrence [Pithan and Mauritsen, 2014].

Quantification of the single feedbacks in the Arctic is challenging as these processes most likely do not occur independently [Feldl et al., 2017, 2020; Graversen et al., 2014]. Mauritsen et al. [2013] showed for example that both the surface albedo and the lapse rate feedback are strongly dependent on the cloud and water-vapor occurrence. Interactions of different feedbacks can introduce synergy effects such that the sum of two feedbacks can be larger (or smaller) than the individual impact. Also, Chung et al. [2021] suggest that a major contribution to Arctic amplification is the seasonal linkage between the summertime ocean heat uptake and wintertime heat release. In addition, some of these feedbacks follow a seasonality. While for example, the ice-albedo feedback requires sunlight conditions, the warming in the Arctic, and thus the vertical temperature structure that induces the lapse-rate feedback is most pronounced in wintertime [Pithan and Mauritsen, 2014; Stuecker et al., 2018]. Additionally, the feedbacks show significant intermodel differences [Block et al., 2020], which reveals that the physical processes behind Arctic amplification are still not well understood and represented in models.

Seven Arctic ship campaigns, which were conducted between 1997 – 2020 to study Arctic atmospheric processes and ocean-ice-atmosphere interactions, are depicted in Figure 2.2: Surface Heat Budget of the Arctic (SHEBA) [1997 – 1998, Uttal et al., 2002], Arctic Ocean Experiment (AOE) [2001, Tjernström et al., 2004], Arctic Summer Cloud Ocean Study (ASCOS) [2008, Tjernström et al., 2014], Arctic Clouds in Summer (ACSE) [2014, Sotiropoulou et al., 2016], Arctic Ocean 2018 (AO2018) [2018, Vüllers et al., 2021], Multidisciplinary Drifting Observatory for the Study of Arctic Climate (MOSAiC) [2019 – 2020, Shupe et al., 2018], and PS106 (2017, PASCAL + SiPCA). To the knowledge of the author, these are the only campaigns performed in the Arctic Ocean that have been equipped with a cloud radar and a collocated lidar. Moreover, there have been even fewer studies in the Arctic with sea-motion-stabilized cloud radars, whose availability is a requirement to also determine cloud vertical dynamics accurately from a shipborne platform. From the seven campaigns introduced, only two were equipped with a stabilized cloud radar: ACSE with a 94-GHz cloud radar and PS106 a 35-GHz cloud radar. The few comparable observations available in the Arctic highlight the importance of the PS106 cruise. The background color of Figure 2.2 shows the near-surface air-temperature anomaly for the year 2017, which indicates that the area where PS106 was performed is one of the hot spots of Arctic amplification.

2.2 Cloud radiation budget

The radiation budget at the surface, or respectively at the TOA, is defined as the sum of the incoming and outgoing short- and longwave radiation. Two variable components, which can strongly modulate these fluxes are the surface albedo and clouds. The ice-albedo

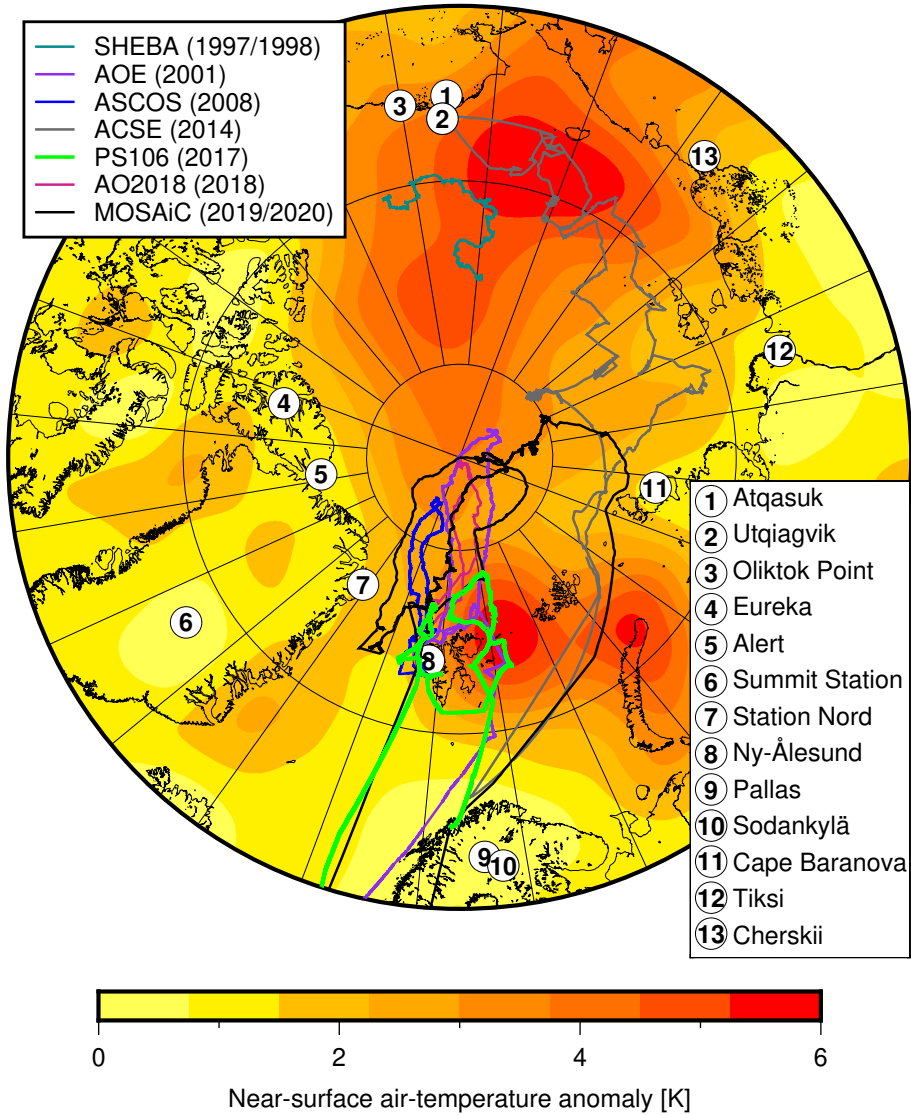


Figure 2.2: Near-surface air-temperature anomaly in the Arctic (north of 75° N) for the year 2017 relative to the climatological mean of 1981 – 2010. Colored lines represent the tracks of Arctic ship campaigns, which were equipped with a cloud radar and lidar since 1997. The numbers represent different permanent Arctic research stations (1: Atqasuk, 2: Utqiagvik (formally known as Barrow), 3: Oliktok Point, 4: Eureka, 5: Alert, 6: Summit Station, 7: Station Nord, 8: Ny-Ålesund, 9: Pallas, 10: Sodankylä, 11: Tiksi, 12: Cherskii, 13: Cape Baranova). Map created with the generic mapping tool [GMT, Wessel et al., 2019].

feedback was introduced at the beginning of this chapter. A major source of uncertainty when quantifying Arctic amplification [Goosse et al., 2018; Tan and Storelvmo, 2019] is the climate sensitivity of clouds due to their high variability and their complex and non-linear interactions with other feedbacks. Even the sign of the cloud climate sensitivity is still unclear [Block et al., 2020]. A brief discussion of the cloud radiative effects will be given

below because they are a relevant topic for this thesis.

Clouds can directly influence the radiation budget in two ways. They can cool the surface by shading incoming shortwave radiation (cloud-albedo-effect), and they can warm the surface by hindering the emission of longwave radiation (cloud-greenhouse effect). The net of the cloud-greenhouse effect and the cloud-albedo effect is called the cloud radiative effect or cloud-feedback. These two competitive processes, which work against another, cause the cloud-feedback to be the origin of the largest uncertainties and intermodel spread [Block et al., 2020].

Shortwave cooling at the surface is only effective during summertime when sunlight is available. The longwave heating however, is active during the entire year. Hence, except for the summer months, the net effect caused by the presence of clouds will be a warming factor [e.g., Curry et al., 1996; Intrieri et al., 2002; Schweiger and Key, 1994]. The role of clouds on the surface radiation budget is a function of their vertical extent, their shape, and their microphysics. Further critical parameters, which impinge on the cloud radiative effect are the surface albedo and the solar zenith angle. Highly reflective surfaces below clouds can introduce multiple reflections between the cloud and the surface and thus increase the incoming solar radiation on the ground [e.g., Rouse, 1987; Shine, 1984].

The cloud phase is a key parameter in assessing the cloud radiative impact [e.g., Sun and Shine, 1995]. Especially the liquid-to-ice ratio in mixed-phase clouds has, besides the absolute amount of ice and liquid water, a large influence on the cloud radiative effect [Choi et al., 2014; Komurcu et al., 2014; Yoshida and Asano, 2005]. Additionally, the vertical distribution of liquid water and ice influences the cloud radiative properties. Yoshida and Asano [2005] found a change of the near-infrared cloud reflectance and absorptance of up to 10 % by varying the vertical distribution of liquid and ice-water occurrence even when the column-integrated amount of liquid water and ice was kept constant in their model. Also, the strong dependence of the cloud radiative effect on cloud microphysics is a major challenge for models to accurately determine the effect of clouds [Hashino et al., 2016]. The larger the amount of liquid water in mixed-phase clouds, relative to ice (but also in total), the more the cloud reflects incoming solar radiation [e.g., Goosse et al., 2018]. Yet, when it comes to simulating the supercooled liquid-water fraction of Arctic mixed-phase clouds, global climate models exhibit great biases towards lower values [e.g., Morrison et al., 2019; Tan and Storelvmo, 2019] and thus introduce an underestimation of the cloud radiative effect [e.g., Cesana et al., 2012]. Tan et al. [2016] showed that when the supercooled liquid-water fraction in the National Center for Atmospheric Research’s Community Atmosphere Model version 5.1 (CAM5.1) [Neale et al., 2012] is constrained by satellite observations (i.e., increased) the cloud-induced warming increases globally stronger compared to the Arctic. Furthermore, the increase of liquid water at the expense of ice decreases the precipitation, as liquid-water droplets tend to be smaller than ice crystals and hence are less likely to precipitate [Pruppacher and Klett, 1997]. This effect increases the warming of the Arctic by

increasing the cloud fraction and thus the downwelling longwave radiation at the surface [Tan and Storelvmo, 2019]. Intrieri et al. [2002] analyzed the annual circle of the cloud radiative effect during the SHEBA campaign and found a net warming effect at the surface. The cloud-greenhouse effect of these clouds was most sensitive to the liquid-water path (LWP) for $\text{LWP} < 30 \text{ gm}^{-2}$, while the cloud-albedo effect increased with increasing LWP even for higher values [Shupe and Intrieri, 2004]. Also, decreasing surface albedo and increasing solar elevation angle increased the shortwave cloud forcing [Shupe and Intrieri, 2004]. Mauritsen et al. [2011] showed by alternating the CCN concentration in radiative transfer simulations that under the unique atmospheric composition in the Arctic droplet formation and hence cloud forcing can be limited by the CCN availability. They found a lower threshold (depending on the choice of parameters, in their case 10 CCN cm^{-3}), below which an increase of CCN caused a net warming effect. In this low-CCN regime, the longwave warming was dominating over the shortwave cooling. Above this threshold, the observed effect was a cooling one, as the longwave forcing was constant with CCN alternations while the shortwave effect was still increasing.

To summarize, there are numerous ways how clouds can change the radiative budget in the Arctic, which are not yet completely understood. Detailed observations of the cloud phase, but also in-cloud motions and vertical and temporal occurrence is inevitable to study the Arctic cloud radiative effects.

2.3 Arctic mixed-phase clouds

The main feature of Arctic clouds is associated with the frequent occurrence of multi-layer temperature and humidity inversions, which lead to the formation of temporally stable multi-level mixed-phase cloud decks [Morrison et al., 2012; Shupe et al., 2011; Verlinde et al., 2013]. These cloud layers are of complex macro- and microphysical structure and frequently occur at heights close to the ground, which are not easily trackable. Liu et al. [2017] pointed out that space-borne remote-sensing techniques fail to detect 25 to 40 % of the clouds below 500 m height and underestimate the fraction of mixed-phase and ice clouds between the surface and 1000 m height. In turn, ground-based profiling studies from the Arctic, which rely on lidar and radar observations, usually provide reasonable data only at heights above 100 – 150 m above ground. This is for example the case for the 35-GHz Ka-band ARM zenith radar (KAZR) of the US Department of Energy (DOE) Atmospheric Radiation Measurement (ARM) program at the NSA (North Slope of Alaska) site in Utqiagvik, USA. Cloud processes that take place at lower heights can thus not thoroughly be characterized with common remote-sensing techniques.

Shupe and Intrieri [2004] found for the SHEBA campaign that the amount of liquid water in mixed-phase clouds mostly controls the cloud effect on both the shortwave and longwave radiation. Using observational and reanalysis data from the SHEBA campaign,

Engström et al. [2014] showed that an accurate representation of cloud microphysical properties in atmospheric models is important to understand and accurately simulate the Arctic climate. Especially the longevity of these clouds puts high demands on the research community. Big efforts were needed to establish model frameworks that are capable of simulating such cloud systems [e.g., Diedenhoven et al., 2009; Fridlind et al., 2007; Klein et al., 2009; Morrison et al., 2011; Neggers et al., 2019], even in the case of single-layer clouds of low complexity. The different processes involved in forming and sustaining supercooled liquid-water or mixed-phase clouds were thoroughly discussed by Morrison et al. [2012]. Large-scale advection of water vapor is considered to be the prerequisite for formation and persistence of Arctic stratus decks, especially over closed ice surfaces.

Shupe et al. [2011] provided a comparison of the macrophysical cloud properties using ground-based remote-sensing measurements from different periods for six of the observatories and field campaigns presented in Figure 2.2 (Atkasuk, Utqiaġvik, Eureka, Ny-Ålesund, Summit Station, and SHEBA). The observed annual cloud fraction ranged from 58 % (Summit Station) to 83 % (Utiqiaġvik). At most sites, the annual cycle showed a maximum during the late summer to fall month (August – October) and a minimum during the late winter month (December – March). In a companion paper, Shupe [2011] analyzed the microphysical properties of the observed clouds at three of these sites, which were equipped with a cloud radar, a lidar, and a microwave radiometer: Utqiaġvik, Eureka, and SHEBA. Distinct differences in the occurrence of pure liquid-water, mixed-phase, and pure-ice clouds have been found. Pure ice clouds were observed at least 40 % and on average during 60 – 70 % of the time during any month at any site. The liquid-water cloud occurrence was lowest during winter with 10 – 20 %. The highest occurrence of pure liquid-water clouds was observed at Barrow in the summer with 40 – 50 % of the time. Pure liquid water was confined to the lowest 3 km height at temperatures and down to -24°C . At SHEBA the mixed-phase fraction was highest and mixed-phase clouds have been found up to 7 – 8 km height and down to -40°C . The highest cloud top followed the annual cycle of the tropopause and reached up to 11 km height.

2.4 Heterogeneous ice formation in Arctic mixed-phase clouds — constraints and previous findings

In the Arctic, the marginal sea ice zone (transition zone between closed ice surface and open sea) plays a crucial role due to its complex ocean-ice-atmosphere interactions. But the role of surface sources of heat and moisture in promoting cloud processes relative to in-cloud or advective sources is still uncertain [Harrington and Olsson, 2001; Shupe et al., 2013]. The microphysical evolution of the Arctic stratiform cloud decks is subject to the availability of CCN and INP [Fridlind et al., 2007; Kalesse et al., 2016a; Stephens, 2005]. Numerous studies provide evidence that the occurrence and efficiency of heterogeneous

ice formation at ambient conditions depends strongly on both temperature [Shupe, 2011; Zhang et al., 2017] and the type and quantity of the aerosol burden present at cloud level [Ansmann, 2019; Kanitz et al., 2011; Sassen, 2005; Seifert et al., 2010; Zhang et al., 2018]. Recently, the first remote-sensing-based closure study of aerosol effects on Arctic cloud microphysical properties was presented by Engelmann et al. [2021] based on MOSAiC observations. The INPs for heterogeneous ice formation of different origins start to be ice active at different temperatures. Mineral dust, e.g., triggers heterogeneous ice formation below a temperature of about -15°C [Hoose and Möhler, 2012] while sea spray aerosol INPs have been found to be already ice active at -5°C [DeMott et al., 2016]. INPs from biological origin are assumed to be one of the most ice active ones at low to moderate supercooling [Hartmann et al., 2021; Murray et al., 2012; O’Sullivan et al., 2018; Schnell and Vali, 1976; Szyrmer and Zawadzki, 1997; Zeppenfeld et al., 2019].

Many studies report that respective INP reservoirs for Arctic clouds are mainly provided from long-range transport from lower latitudes [Morrison et al., 2012]. An increasing number of studies, however, suggest that also local aerosol sources can provide significant numbers of CCN and INPs that stem from marine processes [Bigg, 1996; DeMott et al., 2016; Hartmann et al., 2020] or even from ship emissions or industry [Creamean et al., 2018a; Thomson et al., 2018]. These findings suggest that also Arctic clouds are subject to anthropogenic emissions [Lohmann, 2017]. Wex et al. [2019] found an annual cycle in INP number concentration (INPC) at four different land-based stations in the Arctic, with the largest INPC in summer. Hartmann et al. [2020] analyzed filter measurements from the Arctic airborne campaign PAMARCMiP 2018 (Polar Airborne Measurements and Arctic Regional Climate Model Simulation Project 2018), performed in late winter in the vicinity of the Villum Research Station, Greenland (81°N , 16°W) above the Arctic Ocean and Fram Strait. They found the highest INPC during low-level flights above open leads and polynyas. Heat sensitivity of the sampled INPs as well as high-temperature freezing onset hints towards biogenic origin. Low flight altitudes, a large number of open leads in the vicinity of the aircraft flight track, and detected sea salt in the aerosol samples suggest that these INPs originate from local marine sources rather than from long-range transport. The occurrence of mixed-phase clouds is constrained to the presence of layers of supercooled liquid water, which is the case for the majority of cloud layers with top temperatures above -25°C [Ansmann et al., 2008; de Boer et al., 2011; Westbrook and Illingworth, 2011]. Changing aerosol conditions in the Arctic thus have the potential to modify the general occurrence of heterogeneous ice formation. This question sets a definite requirement to advance the understanding of the current state of how heterogeneous ice formation can be described in the Arctic.

One way of evaluating the relationship between temperature, aerosol conditions, and the efficiency of heterogeneous ice formation is the utilization of remote sensing. From combined cloud radar, lidar, and microwave-radiometer observations, the vertical structure and microphysical composition of clouds and precipitation over a specific site can be

obtained [Illingworth et al., 2007; Shupe, 2007]. For optically thin cloud layers also the application of single systems such as polarization lidar can be used to obtain the required information [Ansmann et al., 2009; Sassen, 2005]. Thermodynamic properties of the atmosphere are provided by radio soundings or model data. Studies suggest that aerosol particles potentially influence the structure and microphysics of Arctic clouds. Norgren et al. [2018] show that aerosol might be responsible for the reduction in the cloud ice content in low-level Arctic mixed-phase clouds. They analyzed a 9-year data set of ground-based aerosol, clouds, and atmospheric-state observations from Utqiagvik and found that mixed-phase clouds that were present in a clean aerosol state have a higher ice-water content (IWC) at cloud base compared to similar clouds in cases with higher aerosol loading. In the case of the clean aerosol state, the IWC was increased by a factor of 1.22 to 1.63, for which they suggested more efficient ice mass growth processes throughout the cloud layer. Furthermore, Jouan et al. [2014] hypothesized that emissions of sulfur dioxide (SO_2) may reduce the ice-nucleating properties of INPs through acidification, resulting in a smaller concentration of larger ice crystals that lead to an increase in precipitation.

A unique characteristic of low-level Arctic mixed-phase stratocumulus clouds is their ability to persist for several days [Morrison et al., 2012], a feature that still is not completely understood. A key question to understand the longevity of these clouds is, besides the source of water vapor, attributed to the (limited) supply of INPs, which are necessary to maintain the cloud for such a long period [Westbrook and Illingworth, 2013]. Steady ice precipitation observed below these clouds would otherwise lead to a depletion of INP in the cloud. The two different aerosol regimes identified in the Arctic, which may supply INP, are long-range transport or locally produced aerosol. The INP differ in their origin but also in their vertical distribution and seasonal abundance [e.g., Creamean et al., 2021; Shaw, 1995; Willis et al., 2018]. During winter and spring, Arctic haze (aged pollution aerosol from mid-latitude sources with relatively high mass concentrations) can be found in the entire tropospheric column, while the summertime planetary boundary layer is characterized by locally produced particles. During fall, the aerosol concentration usually reaches its minimum when local biogenic sources become less active and the long-range transport from lower latitudes is limited. Additionally, the process of INP recycling (INPs from precipitated and sublimated ice crystals, which are mixed back into the cloud) is assumed to play a role in heterogeneous ice formation in Arctic clouds [Solomon et al., 2015]. Also, cloud top cooling may cause a continuous activation of INPs [Fu and Xue, 2017]. The strong stratification of the Arctic lower troposphere limits the vertical mixing of INPs from local sources into the free troposphere and vice versa. Only in the case of surface-coupling, when the layer between the surface and cloud base is vertically well mixed, an exchange of cloud-active particles between surface sources and the cloud is likely [e.g., Brooks et al., 2017; Shupe et al., 2013].

Even though indications are given that local aerosol sources may play a role in heterogeneous ice formation, none of the studies available so far investigated any potential

effects of the surface-coupling state of Arctic clouds on the frequency and efficiency of ice formation. Investigations of potential effects of the surface-coupling were so far restricted to bulk properties such as ice-water path or liquid-water path, without clearly referencing any relations between ice formation and temperature, or even aerosol conditions.

Shupe et al. [2013] found only moderate differences in surface-coupled versus decoupled clouds. They report that clouds, which are thermodynamically linked with the surface, tend to show colder temperature profiles within the cloud and slightly weaker in-cloud turbulence. These clouds often have a higher LWP and ice-water path (IWP), for which the authors suggest as a reason the additional moisture supply from below. Qiu et al. [2015] studied the occurrence of Arctic mixed-phase clouds in relation to the presence and strength of humidity and temperature inversions but they did not provide any information about the overall frequency of ice formation in the different coupling states. Similar to Qiu et al. [2015], Qiu et al. [2018] used the opportunity to study the influence of both surface conditions and different air masses on thermodynamic variables and on the properties of Arctic mixed-phase clouds. At the coastal location of the Utqiagvik site in northern Alaska, where the data set for their study was obtained, marine air masses are transported by northerly winds, while more continental air masses are transported by southerly winds. The authors reported stronger precipitation processes during advection from the north. They attributed this finding to the less polluted air masses in this case. The authors suggested also that increased stability in the lower atmosphere might cause a lower occurrence of Arctic mixed-phase clouds during southerly wind conditions. However, this study investigated mixed-phase cloud properties only. The efficiency of ice formation was not investigated. Sotiropoulou et al. [2014] provide a detailed study of the properties of coupled and decoupled Arctic clouds utilizing ground-based remote-sensing and in-situ measurements and radiosonde profiles. The authors found for the thermodynamic-phase partitioning, that the LWP and IWP as well as their ratio of coupled and decoupled clouds are similar. Gierens et al. [2020] studied surface-coupling effects on mixed-phase clouds based on a 2-year data set from ground-based remote sensing in Ny-Ålesund, Svalbard. They found a seasonal cycle of the coupling state, with most surface-coupled clouds observed during summer. The LWP in coupled clouds was roughly 40 % higher compared to decoupled clouds, but only minor differences have been found in the IWP. Their findings are affected by the surrounding orography of the measurement site. Glacier outflows tend to be decoupled, while for clouds transported from the open sea towards Ny-Ålesund coupling was most common. The open sea west of Svalbard also might act as a local humidity and heat source.

Furthermore, models have difficulties accurately reproducing heterogeneous ice formation in clouds. Nomokonova et al. [2019] reported in agreement with Sandvik et al. [2007] that single-layer mixed-phase clouds tend to be underestimated in models compared to results from the synergy of different ground-based instruments. Without considering any surface-coupling effects in their study, they found in a temperature regime

between -20°C and -5°C a lower occurrence of mixed-phase clouds in favor of pure-ice clouds.

2.5 Motivating research questions

From the literature debate on the role of clouds and aerosol in Arctic amplification above different topics arise, which are addressed in this thesis.

1. The height limitation of remote-sensing instruments is crucial for Arctic mixed-phase clouds. How is an improved quantification of such low-level clouds possible?
2. Aerosol particles play a dominating role in the heterogeneous ice formation process and Arctic clouds are frequently occurring either coupled or decoupled to the surface and to corresponding local aerosol sources. Are differences in the characteristics of heterogeneous ice formation processes observable between surface-coupled and surface-decoupled clouds?
3. How can advanced remote-sensing methods of aerosol and clouds improve current radiative transfer simulations?

The answers to these questions require sophisticated measurements of high quality. Given the rough environment of the Arctic and the challenges conducting remote sensing on a moving platform, not only a careful preparation of the instrumentation was necessary, but also an in-depth processing of the data and the correction of the ship movement was inevitable. The scope of this thesis was thus also to apply the new instrumentation and data-analysis methods, to produce the OCEANET-Atmosphere based cloud and aerosol data sets for the cruise PS106. Thanks to the polarization lidar operated during PS106, in this study a temperature relationship of the frequency of ice occurrence in Arctic clouds and their surface-coupling state is presented for the first time.

Chapter 3

Data set — Applied instrumentation, processing, and retrievals

As stated in the introduction, sophisticated measurements of clouds and aerosol are still scarce in the High Arctic. Two complimentary field campaigns were conducted in the Arctic summer 2017 by the initiative (AC)³ in order to fill parts of this data gap: the airborne ACLOUD campaign and the ship-borne PASCAL cruise. PASCAL was the first of two legs of the PS106 expedition during which the remote-sensing OCEANET-Atmosphere platform of TROPOS was operated. In this chapter, the instrumentation and data analysis methods that were used to produce the Cloudnet-based cloud and aerosol data sets for the cruise PS106 are introduced. The majority of the material presented in this chapter was published in Griesche et al. [2020a].

3.1 Introduction to ground-based active remote sensing of aerosol and clouds

Active remote sensing is based on the transmission of an electromagnetic radiation pulse and the detection of a backscattered signal. When applying active remote-sensing methods to atmospheric research, the respective scatterers are usually molecules, particles, or hydrometeors. The pulse emitted by the instrument is scattered at different distances from the instrument. Using the time t_s between the emission and the detection of the signal and knowing the speed of light c_L , the distance z to the scatterer can be determined:

$$z = \frac{c_L \cdot t_s}{2} \quad (3.1)$$

Two common active remote-sensing instruments are radar (radio detection and ranging) and lidar (light detection and ranging). The received signal sensitivity differs strongly for a lidar and a radar due to the large difference in the applied wavelengths: The lidar used in this thesis, a Polly^{XT}, emits light at 355, 532, and 1064 nm, while the specific type of radar used in this thesis, a cloud radar Mira-35, operates at 35 GHz or with a wavelength of 8.6 mm, respectively. The lidar signal from a liquid-water droplet with a diameter of D is proportional to D^2 while for the cloud radar the signal is proportional to D^6 [O'Connor et al., 2005]. In the following, introductions to atmospheric remote sensing by lidar and cloud radar are given in Sec. 3.1.1 and in Sec. 3.1.2, respectively.

3.1.1 Lidar principle

A lidar emits light at or close to the visible spectrum and makes use of elastic backscattering and in the case of a Raman lidar also of inelastic Raman backscattering. Following Weitkamp [2005] the received lidar signal power $P(z, \lambda)$ can be expressed by the lidar equation

$$P(z, \lambda) = P_0(\lambda) \frac{\tau c_L}{2} A \eta(\lambda) \frac{O(z)}{z^2} \beta(z, \lambda) \exp \left[-2 \int_0^z \alpha(z', \lambda) dz' \right], \quad (3.2)$$

with

λ	—	wavelength of the laser beam,
$P_0(\lambda)$	—	average power of a single laser pulse at wavelength λ ,
τ	—	temporal laser pulse length,
A	—	area of the receiver telescope,
$\eta(\lambda)$	—	wavelength-dependent receiver efficiency,
$O(z)$	—	overlap function of the lidar system,
$\beta(z, \lambda)$	—	wavelength-dependent backscatter coefficient at distance z ,
$\alpha(z, \lambda)$	—	wavelength-dependent extinction coefficient at distance z .

The overlap function $O(z)$ limits the lowest detection height of the lidar and hence is particular crucial for the study of low-level Arctic clouds. The optical lidar geometrical determines that at short distances to the lidar, the emitted laser beam can only be partially imaged onto the receiver. This part is described by $O(z)$, which is zero at the lidar and becomes unity when the complete laser beam can be imaged on the detector. Below the height where $O(z)$ reaches a value of 1, an overlap correction can be applied, yet, not to arbitrary low heights. The strong increase of the lidar signal strength close to the emitter also limits the detector's dynamic range at high altitudes. This is a reason why the height of the complete overlap is intentionally designed to be at a certain distance from the lidar. To overcome this compromise, lidar systems are sometimes equipped with different receiver telescopes to cover multiple altitude ranges, as the Polly^{XT} [e.g., Engelmann et al., 2016], which is used in this thesis.

The lidar equation is in general composed of system-dependent and atmospheric parameters. When Eq. (3.2) is transformed in such a way that all known system-dependent parameters are resolved, the attenuated backscatter coefficient β_{att} is obtained:

$$\beta_{\text{att}}(z, \lambda) = \beta(z, \lambda) \exp \left[-2 \int_0^z \alpha(z', \lambda) dz' \right] = 2P(z, \lambda) \frac{z^2}{\tau c_L P_0(\lambda) A \eta(\lambda) O(z)}. \quad (3.3)$$

The backscatter coefficient β and the extinction coefficient α are the two optical parameters of interest in the scattering air volume. The remaining parameters of Eq. (3.2) are instrument characteristics and can be considered as constant during the measurement. β and α can be decomposed as the sum of the respective molecular (mol) and particle (par) contribution

$$\beta(\lambda) = \beta^{\text{mol}}(\lambda) + \beta^{\text{par}}(\lambda), \quad (3.4)$$

and

$$\alpha(\lambda) = \alpha^{\text{mol}}(\lambda) + \alpha^{\text{par}}(\lambda). \quad (3.5)$$

The molecule backscattering and extinction coefficients can be calculated, e.g., from radiosonde data because the scattering cross-section of air is well known. To derive the particle contribution of Eq. (3.4) and (3.5), two methods are common: the Raman and the Klett-Fernald-Sasano methods. Both are described in detail in Weitkamp [2005] and will only be summarized here.

Klett-Fernald-Sasano method

The Klett-Fernald-Sasano method [Fernald, 1984; Klett, 1985; Sasano et al., 1985], often simply called Klett-method, only uses the elastic-backscatter signal. It makes use of an assumed particle lidar ratio S^{par} , which is the extinction-to-backscatter ratio

$$S^{\text{par}}(z) = \frac{\alpha^{\text{par}}(z)}{\beta^{\text{par}}(z)}. \quad (3.6)$$

The lidar ratio is a characteristic quantity for specific aerosol types. For example, marine sea-salt aerosol has a typical lidar ratio of 20 sr, mineral dust of 40 – 60 sr, and highly absorbing smoke particles can reach values of up to 70 – 100 sr [e.g., Müller et al., 2007].

Analog to S^{par} the molecule extinction to backscatter ratio S^{mol} is defined and has a constant value of

$$S^{\text{mol}}(z) = \frac{\alpha^{\text{mol}}(z)}{\beta^{\text{mol}}(z)} = \frac{8}{3}\pi. \quad (3.7)$$

The profile of the particle backscatter coefficient for a specific wavelength can be obtained by assuming a reference value $\beta(z_{\text{ref}})$ at a reference height z_{ref} . By solving Eq. (3.2) $\beta(z_{\text{ref}})$ can be derived as

$$\beta^{\text{par}}(z) = -\beta^{\text{mol}}(z) + \frac{\zeta_1(z, z_{\text{ref}})}{\zeta_2(z_{\text{ref}}) + 2 \int_z^{z_{\text{ref}}} S^{\text{par}}(z') \zeta_1(z', z_{\text{ref}}) dz'} \quad (3.8)$$

with

$$\zeta_1(x, z_{\text{ref}}) = P(x)x^2 \exp \left\{ 2 \int_x^{z_{\text{ref}}} [S^{\text{par}}(x') - S^{\text{mol}}] \beta^{\text{mol}}(x') dx' \right\} \quad (3.9)$$

where x represents either z or z' and

$$\zeta_2(z_{\text{ref}}) = \frac{P(z_{\text{ref}})z_{\text{ref}}^2}{\beta^{\text{par}}(z_{\text{ref}}) + \beta^{\text{mol}}(z_{\text{ref}})}. \quad (3.10)$$

The reference height is usually chosen at an altitude that is assumed to be aerosol-free and the backscatter coefficient can be obtained by applying the estimate $\beta^{\text{par}}(z_{\text{ref}}) \ll \beta^{\text{mol}}(z_{\text{ref}})$. However, any region with a known particle backscatter coefficient also satisfies the requirements of this method.

Raman method

The Raman method makes use of the inelastic backscatter signal at the Raman-shifted wavelength λ_{Ra} . The intensity of the returned signal at λ_{Ra} is much smaller compared to the elastic signal. Therefore, longer averaging times and low background noise (e.g., during measurements without sunlight) are required. In doing so, the backscatter and extinction coefficients can be obtained independently from each other, i.e. the lidar ratio S^{par} can be directly derived. Thus, a particle-type classification is possible. The measured power of the inelastic scattered return signal P_{Ra} can be expressed as [Ansmann et al., 1990]

$$P_{\text{Ra}}(z, \lambda_{\text{Ra}}) = N_{\text{Ra}}(z) \frac{d\sigma(\pi, \lambda)}{d\Omega} P_0 \frac{c_L \tau}{2} A\eta(\lambda_{\text{Ra}}) \frac{O(z)}{z^2} \cdot \exp \left\{ - \int_0^z [\alpha(r, \lambda) + \alpha(r, \lambda_{\text{Ra}})] dr \right\}. \quad (3.11)$$

Here, N_{Ra} is the number density of the desired Raman scattering molecule (usually nitrogen or oxygen), $\frac{d\sigma(\pi, \lambda)}{d\Omega}$ the corresponding molecular backscattering cross-section.

From Eq. (3.11) the particle extinction coefficient can be derived after Ansmann et al. [1990] as

$$\alpha^{\text{par}}(z, \lambda) = \frac{\frac{d}{dz} \ln \left[\frac{N_{\text{Ra}}(z)O(z)}{z^2 P_{\text{Ra}}(z, \lambda_{\text{Ra}})} \right] - \alpha^{\text{mol}}(z, \lambda) - \alpha^{\text{mol}}(z, \lambda_{\text{Ra}})}{1 + \left(\frac{\lambda}{\lambda_{\text{Ra}}} \right)^{\tilde{A}}}, \quad (3.12)$$

where

$$\mathring{A} = \frac{\ln [\alpha^{\text{par}}(\lambda)/\alpha^{\text{par}}(\lambda_{\text{Ra}})]}{\ln(\lambda_{\text{Ra}}/\lambda)} \quad (3.13)$$

describes the wavelength dependence of the particle extinction coefficient, also known as particle-extinction-related Ångström exponent.

Similar to the Klett-method, to obtain the particle backscatter coefficient a reference value $\beta(z_{\text{ref}})$ at distance z_{ref} needs to be defined, where ideally the absence of scattering particles can be assumed. The solution for particle backscatter coefficient β^{par} is [Ansmann et al., 1992a]

$$\begin{aligned} \beta^{\text{par}}(z, \lambda) = & -\beta^{\text{mol}}(z, \lambda) + [\beta^{\text{par}}(z_{\text{ref}}, \lambda) + \beta^{\text{mol}}(z_{\text{ref}}, \lambda)] \\ & \cdot \frac{P(z_{\text{ref}}, \lambda_{\text{Ra}}) P(z, \lambda) N_{\text{Ra}}(z)}{P(z_{\text{ref}}, \lambda) P(z, \lambda_{\text{Ra}}) N_{\text{Ra}}(z_{\text{ref}})} \\ & \cdot \frac{\exp\{-\int_{z_{\text{ref}}}^z [\alpha^{\text{par}}(r, \lambda_{\text{Ra}}) + \alpha^{\text{mol}}(r, \lambda_{\text{Ra}})]dr\}}{\exp\{-\int_{z_{\text{ref}}}^z [\alpha^{\text{par}}(r, \lambda) + \alpha^{\text{mol}}(r, \lambda)]dr\}}. \end{aligned} \quad (3.14)$$

Polarization lidar

Modern lidar systems can determine the ratio at which the emitted radiation is depolarized by in the scattering volume. The volume linear depolarization ratio δ^{vol} is defined as [Schotland et al., 1971]

$$\delta(z, \lambda)^{\text{vol}} = \frac{\beta_{\perp}(z, \lambda)^{\text{mol}} + \beta_{\perp}(z, \lambda)^{\text{par}}}{\beta_{\parallel}(z, \lambda)^{\text{mol}} + \beta_{\parallel}(z, \lambda)^{\text{par}}}. \quad (3.15)$$

The parallel polarization plane of the detected light with respect to the laser-polarized plane is denoted with the subscript \parallel and the perpendicular plane with \perp . In the case of the Polly^{XT} system, the volume depolarization ratio δ^{vol} is determined using the ratio of the cross-polarized (\perp) and total backscattered light [no subscript, Engelmann et al., 2016]

$$\delta^{\text{vol}}(z, \lambda) = \frac{C_{\delta}(\lambda) - \frac{P_{\perp}(z, \lambda)}{P(z, \lambda)}}{\chi(\lambda) \frac{P_{\perp}(z, \lambda)}{P(z, \lambda)} - \chi_{\perp}(\lambda) C_{\delta}(\lambda)}, \quad (3.16)$$

where $C_{\delta}(\lambda)$ denotes the calibration constant, which is determined using the $\Delta 90^\circ$ calibration method following Freudenthaler et al. [2009]. In order to correct the polarization cross-talk between the real lidar detection channels, the transmission ratios $\chi(\lambda)$ and $\chi_{\perp}(\lambda)$ (which have been measured under laboratory conditions) have to be considered [Engelmann et al., 2016].

From δ^{vol} the particle linear depolarization ratio $\delta^{\text{par}} = \frac{\beta_{\perp}(z, \lambda)^{\text{par}}}{\beta_{\parallel}(z, \lambda)^{\text{par}}}$ can be determined. The particle linear depolarization ratio is characteristic for particles shapes. δ^{par} close to 0 is typical for spherical particles. Mineral dust produces a particle linear depolarization ratio up to 0.35 and ice crystals show values of δ^{par} of up to 0.5 [e.g., Freudenthaler et al., 2009; Mishchenko and Sassen, 1998]. Hence, δ^{par} is suitable for aerosol typing and cloud phase determination.

3.1.2 Radio Detection and Ranging — Radar

The emitted electromagnetic radiation of a cloud radar (also called millimeter-wave radar) is usually in the GHz frequency range. The cloud radar utilized in this thesis, a Mira-35, operates at 35 GHz [Görsdorf et al., 2015]. Due to the relatively large wavelength of 8.6 mm, compared for example to a lidar, the attenuation by clouds is less pronounced and hence cloud radars can provide valuable information of the cloud structure and microphysical properties even in the case of multilayer and optically thick clouds.

According to Görsdorf et al. [2015] the calibrated power P_R at the antenna feed of Mira-35 is calculated by

$$P_R = R_{\text{SN}} \cdot k_B T_0 B F_N, \quad (3.17)$$

where R_{SN} denotes the signal-to-noise-ratio and is defined as

$$R_{\text{SN}} = \frac{P_R^*}{P_N} = \frac{\sum_{v_k=v_1}^{v_2} [S(v_k) - S_N]}{\sum_{v_k=v_1}^{v_2} S_{\text{RN}}(v_k)} \quad (3.18)$$

with

- k_B — Boltzmann constant,
- T_0 — system temperature,
- B — receiver bandwidth,
- F_N — noise of the receiver,
- P_R^* — uncalibrated signal power,
- S_N — noise level determined by the Hildebrand-Sekhon algorithm (may vary due to atmospheric condition or wet antenna),
- P_N — noise power,
- S_{RN} — noise level measured at the receiver,
- $v_{1,2}$ — Doppler velocity integration limits.

The cloud radar determines the Doppler spectrum from the received signal $S(v_k)$ from which the probed volume can be characterized. $S(v_k)$ usually is expressed as a function of velocity $v_k = f_k(c_L f_P)/(2N_F)$. With f_k denoting the Doppler frequency, c_L the speed of light, f_P the pulse repetition frequency, and N_F the number of Fast Fourier Transformation (FFT) points.

A cloud radar with polarization capabilities determines the reflectivity in the co- and cross-channels, which are perpendicular to one another. An example Doppler spectrum for the co- (\parallel , green) and cross-channel (\perp , red) is given in Figure 3.1, with positive Doppler velocity denoting upward motion. The Gaussian shape of both spectra indicates that the measured signal is dominated by one hydrometeor species. The presence of different hydrometeor species would skew the spectrum to either side or produce a secondary peak if those species fall with different velocities. The mean Doppler velocity of the peak of roughly -0.7 m s^{-1} points towards smaller cloud particles and the strong signal in the cross-channel indicate ice particles rather than liquid-water droplets. Larger hydrometeors like rain or snow would shift the spectrum towards more negative (fast falling) velocities and in-cloud turbulence would cause a broadening of the spectrum. Also, downward or upward air-motion (with the cloud particles therein) can shift the spectrum towards more negative or positive Doppler velocities, respectively. A spectrum is calculated for each cloud-radar range gate and is used to derive the radar moments, like radar reflectivity factor Z , mean Doppler velocity v , and linear depolarization ratio (LDR).

The radar reflectivity factor Z is dependent on the droplet size distribution of the sample volume $N_V(D)$ and can be expressed in a general form as

$$Z = \int_0^\infty D^6 N_V(D) dD, \quad (3.19)$$

where D is the equivalent droplet spherical diameter [e.g Battan, 1973]. Z is the integral of the Doppler spectrum, after noise- and range-correction and the multiplication with the

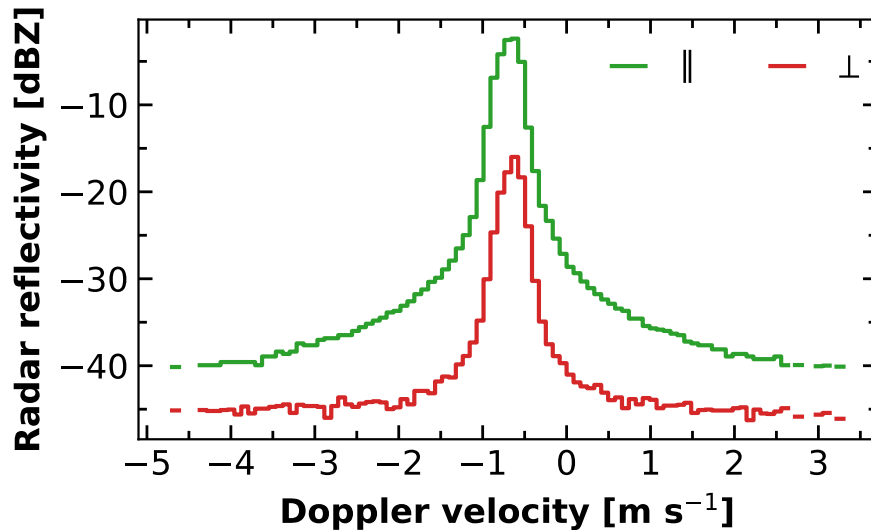


Figure 3.1: Example Doppler spectrum, measured with Mira-35 on 8 June 2017 20:24 UTC at 935 m height. The spectra of the co- (green) and cross-channels (red) are shown. Negative velocities indicate falling particles.

system constant of the radar. Since the droplet size distribution of the probed volume usually is unknown, the equivalent reflectivity Z_e , the reflectivity uniformly distributed cloud droplets would return, is used instead of the actual reflectivity. Z_e can be expressed as [Görsdorf et al., 2015]

$$Z_e = \frac{2^7 \lambda^2 l_t l_r l_{MF} z^2 k_B T_0 B F_N R_{SN}}{\pi^2 P_t G^2 c_L \tau |K_w|^2 I} \quad (3.20)$$

with

- λ — wavelength,
- $l_{t/r}$ — losses due to the transmitting (t) and receiving (r) waveguides,
- l_{MF} — matched filter loss,
- P_t — transmitted power,
- G — antenna gain
- c_L — speed of light
- τ — pulse width,
- K_w — constant depending on the complex refractivity index of water,
- I — integral of the antenna radiation pattern.

Z_e can span over several orders of magnitude and is commonly expressed in terms of decibel

$$dBZ_e = 10 \log_{10}(Z_e). \quad (3.21)$$

The Doppler velocity v is the mean weighted velocity between the integration limits of the Doppler spectrum and calculated by

$$v = \frac{1}{P_R^*} \sum_{v_k=v_1}^{v_2} v_k [S(v_k) - S_N] \quad (3.22)$$

also called the second moment of the spectrum.

Comparable to a depolarization lidar, a polarimetric cloud radar can determine the depolarization ability of the scatterers by emitting linearly polarized radiation and measuring the co- (\parallel) and cross-component (\perp) of the received signal and thus determining the LDR. The LDR is the ratio of the calibrated signals received in the channel parallel and the channel perpendicular to the emitted linear polarized signal

$$R_{LD} = \frac{P_{R,\perp}}{P_{R,\parallel}} \quad (3.23)$$

with R_{LD} denoting the linear depolarization ratio.

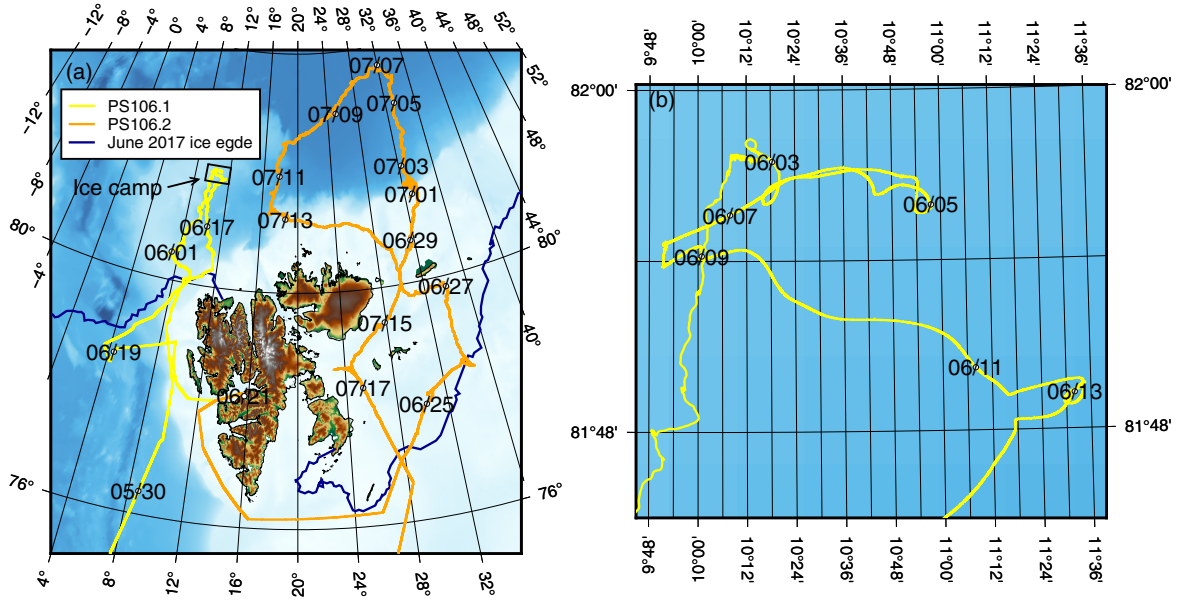


Figure 3.2: (a) Track of RV Polarstern during PS106. PASCAL (PS106.1, yellow) was the first part of PS106, comprising a 2-week drift [black box in (a)] during which the ice-floe camp was maintained. SiPCA (PS106.2, orange) was the second leg of PS106. In (b) the track of the ice drift is shown. The dark blue line marks the average ice edge for June 2017. The map was created with GMT [Wessel et al., 2019].

During the emission of the pulse, no detection is possible and the radar, therefore, has a minimum detection limit. In the case of the Mira-35, the minimum range gate is located 155 m above the instrument [Görsdorf et al., 2015].

3.2 The Arctic expedition PS106

The measurements that are subject of the presented thesis have been conducted during the 8-week cruise PS106 of the research icebreaker Polarstern. The PS106 expedition was split into two legs. The first leg was the PASCAL campaign conducted in the framework of (AC)³ and the second leg was called SiPCA. PS106 was performed in the marginal ice zone between Greenland and Svalbard in May – July 2017. The campaign started on 24 May 2017 in Bremerhaven. Polarstern crossed 60°N on 26 May, and the ice edge was reached on 31 May. A central part of PASCAL was an ice-floe camp, which was installed on the ice around Polarstern. The corresponding ice floe was reached on 3 June and measurements on the ice were performed until 16 June. Between 21 and 23 June a crew exchange was performed in Longyearbyen, Svalbard, and subsequently Polarstern went back into the Arctic ice north and northeast of Svalbard for the second leg of PS106. On 18 July 2017, the expedition ended in Tromsø. The cruise track is shown in Figure. 3.2.

During the complete cruise PS106, a comprehensive number of remote-sensing instruments was deployed aboard the research vessel (RV) Polarstern to conduct continuous observations of clouds and aerosol. To a large extent, these instruments comprised the OCEANET-Atmosphere observatory [Kanitz et al., 2013a]. The OCEANET-Atmosphere platform has been complemented for PS106 for the first time with a vertical-looking cloud radar Mira-35. To obtain mass and number concentration as well as optical properties and filter samples of the aerosol at the surface, a container from TROPOS equipped with instrumentation for aerosol in-situ measurements was installed on the deck of Polarstern and measured continuously during the whole 2-month cruise [Kecorius et al., 2019]. A network of 15 pyranometer stations for measurements of the spatiotemporal variability of solar radiation was installed on the ice flow [Barrientos Velasco et al., 2020]. Furthermore, turbulence and radiation observations inside the Arctic boundary layer were performed using a tethered balloon during the ice floe camp [Egerer et al., 2019].

3.3 Instrumentation

The locations of the OCEANET-Atmosphere equipment and other atmospheric key instruments as deployed during PS106 are depicted in Figure 3.3. In Figure 3.4 more detailed impressions of the instruments are given. Table 3.1 summarizes the technical details of the equipment applied in the synergistic Cloudnet processing that is further described in Section 3.4.3. In the following, the different instruments are briefly introduced.

3.3.1 The OCEANET-Atmosphere observatory

The OCEANET-Atmosphere observatory was already frequently operated aboard Polarstern [Bohlmann et al., 2018; Kanitz et al., 2013b; Yin et al., 2019]. Yet, before this study only for transects from the Northern Hemisphere to the Southern Hemisphere (or vice versa) but never in the Polar Regions. The OCEANET-Atmosphere is based on a container that is by default equipped with the multiwavelength polarization Raman lidar Polly^{XT}_OCEANET (hereafter referred to as Polly^{XT}), to provide continuous profiles of cloud and aerosol properties [Engelmann et al., 2016]. The Polly^{XT} is part of Raman and polarization lidar network Polly^{NET}, comprising more than 20 measurement sites around the globe [Baars et al., 2016].

The Polly^{XT} system measures profiles of particle backscatter coefficient at three wavelengths (355, 532, and 1064 nm), and profiles of extinction coefficient as well as of the linear depolarization ratio at two wavelengths (355 and 532 nm), respectively. For details, see Baars et al. [2016]. Four near-field channels for detection of elastically and Raman-scattered light from nitrogen molecules are implemented at 355, 387, 532, and 607 nm to enable observations already at low heights starting at about 50 m above the instrument. An additional channel for detection of Raman-scattered light from water vapor

Table 3.1: Overview of the instruments deployed during PS106 that have been used for processing and evaluating the OCEANET-Atmosphere observations.

<u>Instrument</u>	Reference	Measured Quantities	ν : Frequency λ : Wavelength R: Range of Measurement P: Precision	Time Resolution
<u>Raman Lidar</u>				
Polly ^{XT} (OCEANET)	Engelmann et al. [2016]	Particle backscatter coefficient	λ : 355, 532, 1064 nm R: 0.1 – 15 km, 0 – 1 km ⁻¹ sr ⁻¹ P: 7.5 m; 10 ⁻⁵ km ⁻¹ sr ⁻¹	10 min – 1 hour
		Particle extinction coefficient	λ : 355, 532 nm R: 0.3 – 5 km, 0 – 10 km ⁻¹ P: 300 m; 10 ⁻² km ⁻¹	
		Particle linear depolarization ratio	λ : 355, 532 nm R: 0.1 – 15 km, 0 – 0.5; P: 7.5 m; 0.02	
<u>Microwave Radiometer</u>				
RPG-HATPRO-G2 first generation dual profiler (OCEANET)	Rose et al. [2005]	Integrated water vapor (IWV)	ν : 22.24 – 31.4 GHz R: 0 – 35 kg m ⁻² P = 0.2 kg m ⁻²	1 s
		Liquid-water path (LWP)	ν : 22.24 – 31.4 GHz R: 0 – 1 kg m ⁻² P = 0.02 kg m ⁻²	
		Temperature profile	ν : 51.0 – 58.0 GHz R: 0 – 330 K P: 0.2 – 1 K	
<u>Doppler Cloud Radar</u>				
Metek Mira-35 (OCEANET)	Görsdorf et al. [2015]	Radar reflectivity factor	ν = 35.5 GHz R: 150 – 13000 m; –55 – 20 dBZ P: 3 m; 2 dBZ	0.25 s / 3 s (raw data / after averaging)
		Linear depolarization ratio	R: 150 – 13000 m; –55 – 20 dB P: 30 m; 1 dB	
		Hydrometeor vertical velocity	R: 150 – 13000 m; –11 – 11 m s ⁻¹ P: 30 m; 0.08 m s ⁻¹	
<u>Pyranometer / Pyrgeometer</u>				
Pyranometer CMP21 (OCEANET)	Kipp and Zonen [2021b]	Solar irradiance	R: 0.285 – 2.8 μ m	5 s (response time)
Pyrgeometer CGR4 (OCEANET)	Kipp and Zonen [2021a]	Near-infrared irradiance	R: 4.5 – 42 μ m	18 s (response time)
15 Pyranometer EKO Instruments ML-020VM	Barrientos Velasco et al. [2020]	Solar irradiance	R: 0.3 – 1.1 μ m	10 ms (response time)
<u>Optical Disdrometer</u>				
Eigenbrodt ODM470	Klepp et al. [2018]	Particle size distribution	λ = 880 nm R: 0.04 – 22 mm P: 0.03 – 0.5 mm	1 min
<u>Tethered balloon</u>				
Ultrasonic anemometer	Egerer et al. [2019]	3-D wind vector;	R: 0 – 20 m s ⁻¹	50 Hz
Metek uSonic-3 Class A (BELUGA)		sonic (virtual) temperature	R: –35 – 55 °C	50 Hz
<u>Sun photometer</u>				
Solar Light 540 Microtops II	Porter et al. [2001]	Aerosol optical thickness	λ : 340, 380, 440, 500, 675, 870, 936, 1020 nm	On demand
<u>Polarstern Meteorology</u>				
RS92-SGP Radiosonde	Jensen et al. [2016]	Profiles of atmospheric pressure, temperature, humidity, wind vector	P: 1 hPa (pressure), 5 % (relative humidity), 0.5 °C (Temperature), 2° (wind direction), 0.15 m s ⁻¹ (wind speed)	1 s (= 5 m at 5 m s ⁻¹ ascend speed) launch every 6 hours

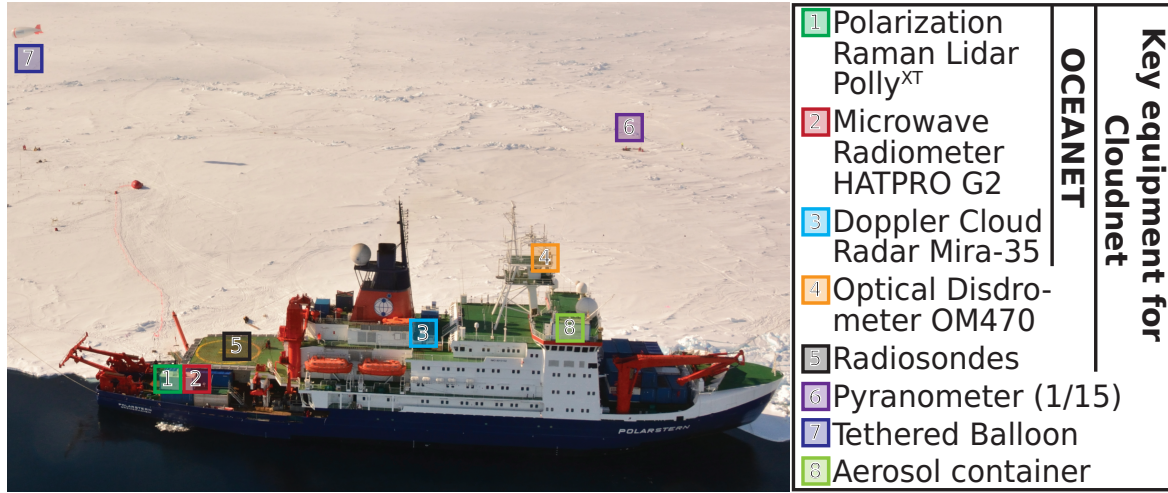


Figure 3.3: Polarstern at the ice floe camp during PASCAL. The locations of selected instruments for atmospheric measurements are annotated. The labels (1) – (5) indicate the positions of the key instruments used for Cloudnet processing: Polly^{XT}, HATPRO, Mira-35, a disdrometer, and a radiosonde station. Label (6) denotes one of the 15 pyranometers comprising pyranometer network; label (7) is the tethered balloon launching site and at (8) aerosol in-situ measurements were conducted. Equipment items (1 – 3) are a permanent part of OCEANET-Atmosphere. (Picture: N. Fuchs).

at 407 nm allows the retrieval of the water vapor mixing ratio [Dai et al., 2018] during low-sunlight conditions. From the Polly^{XT} backscatter and extinction measurements, aerosol classification by their optical properties [Baars et al., 2017; Müller et al., 2007] up to the retrieval of particle size distribution and number concentration [Baars et al., 2012; Müller et al., 1999] can potentially be derived. The polarization-sensitive detection channels allow distinguishing between spherical and nonspherical aerosol and cloud particles [Kanitz et al., 2013a] and, for instance, to separate dust and non-dust particles in mixed aerosol layers [Baars et al., 2011]. Heterogeneous ice formation in mixed-phase clouds can be studied by applying the shape-detection capabilities of the polarization channels for the discrimination of spherical liquid-water droplets from nonspherical ice particles [Seifert et al., 2015]. Another application of depolarization observations in mixed-phase cloud studies is the estimation of CCN and INP concentrations [Mamouri and Ansmann, 2016]. Due to the relatively short wavelengths of the lidar, e.g., compared to the cloud radar, it follows that the lidar is sensitive to rather small particles such as aerosol or small cloud droplets. Also, attenuation especially in liquid-water clouds has to be considered. The lidar beam of Polly^{XT} is tilted off-zenith by 5° to avoid the misinterpretation of strong backscatter signals from specular reflections caused by large, horizontally oriented plate-shaped ice crystals.

The 14-channel MWR HATPRO [Rose et al., 2005] provides estimates of the LWP, integrated water vapor (IWV), as well as atmospheric humidity and temperature profiles with a temporal resolution of 1 Hz. The MWR measures the emission of radiation

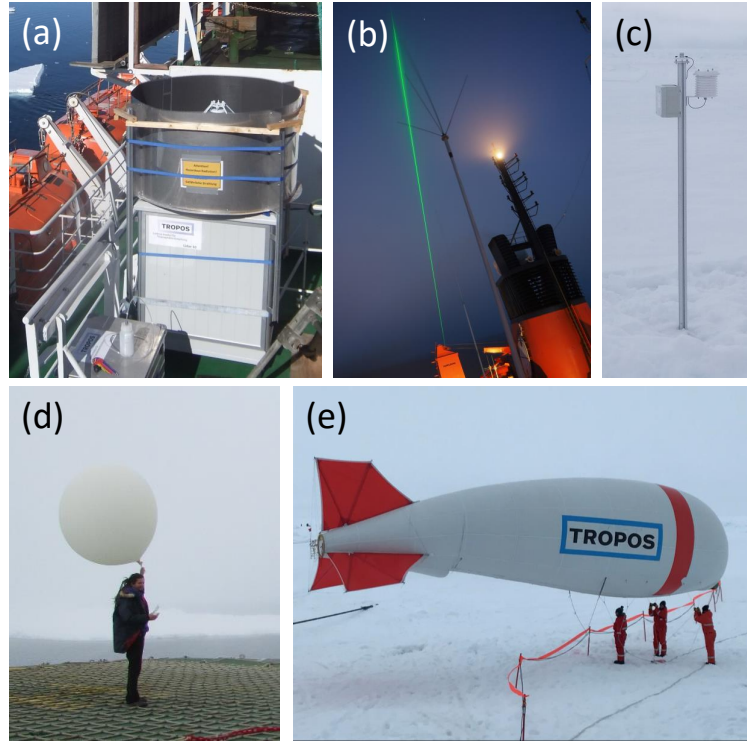


Figure 3.4: Impressions of the instruments applied in this study. Panel (a) shows the cloud radar Mira-35. In (b) the laser beam of the lidar Polly^{XT} is visible. This picture was taken while Polarstern was still south enough to experience darkness during the night. Panel (c) shows one of the 15 pyranometers of the pyranometer network. In (d) a launch of a radiosonde performed by Hannes Griesche during PS106 is shown and in (e) the tethered balloon is depicted. (Pictures: H. Griesche, M. Hartmann, M. Gottschalk).

from the atmosphere in two frequency bands ranging from 22.24 to 31.4 GHz and from 51.0 to 58.0 GHz with 7 channels each. The MWR data sets shown in this study are based on a retrieval that was created from a long-term radiosonde data set at Ny-Ålesund, Svalbard, Norway (78.9° N, 11.8° E, 11 m height above sea level, WMO Code 6260) according to Löhnert and Crewell [2003]. Additionally, for measurements of the global solar downward directed irradiance (SW_{\downarrow}) and global terrestrial downward directed irradiance (LW_{\downarrow}) a pyranometer and a pyrgeometer were installed on the roof of the container.

For the first time, the OCEANET-Atmosphere observatory was complemented by a vertically pointing motion-stabilized 35-GHz polarimetric Doppler Ka-band Doppler radar of type Mira-35 [Görsdorf et al., 2015] for continuous vertically resolved measurements of Doppler spectra produced by vertical cloud motions during PS106 [Griesche et al., 2020a]. Mira-35 was set up to emit pulses with a width of 208 ns at a pulse repetition frequency of 5000 Hz. This setting corresponds to a vertical resolution of 31.18 m. The upper limit of the measurement range was set to 15 km. The Doppler spectrum was derived from the

backscattered signals of 256 consecutive pulses.

The installation and operation of the instruments and the motion correction of the cloud radar data after the cruise were a significant part of this thesis. The motion correction was necessary as a vertical movement of the cloud radar superimposes with the Doppler velocity. That means if the cloud radar moves upward, the measured Doppler velocity would be reduced compared to the actual hydrometeor movement and vice versa. Hence, based on the ship's movement, the vertical velocity of the cloud radar itself was calculated and subtracted from the measured Doppler velocity. The whole cloud radar Doppler spectrum (including noise) has been stored with a temporal resolution of 0.25 s and with Doppler spectral resolution of 0.08 ms^{-1} , to enable the correction of the cloud radar data for the vessel movement. This correction is explained and evaluated in detail in Section 3.4.1. The different moments such as radar reflectivity, Doppler velocity, and Doppler spectral width were determined from the profiles of the Doppler spectra as described in Görsdorf et al. [2015]. The LDR was obtained from the ratio of the radar reflectivity factor observed in the co- and cross-channel of Mira-35 and provided information about the hydrometeor shape [Bühl et al., 2016]. The wavelength of operation of the cloud radar of 8 mm defines its sensitivity to range from cloud hydrometeors to slight precipitation. In the case of shallow stratiform clouds, which dominated the measurements during PS106, attenuation effects could be neglected. The OCEANET-Atmosphere data sets of HATPRO, Polly^{XT}, and Mira-35 were made publicly available through the Open Access library PANGAEA [Griesche et al., 2019, 2020g,i] as part of this thesis

Also aboard Polarstern, measurements of the optical thickness of the cloud-free atmosphere were performed using a hand-held Solar Light MICROTOS sun photometer. The sun photometer measurements are available through the Aerosol Robotic Network (AERONET) project.

3.3.2 Other instruments used in this study

Besides the OCEANET-Atmosphere remote sensing additional in-situ observations have been performed during PS106. During the 2-week ice floe camp in the frame of PASCAL, a tethered balloon site was set up for turbulence and radiation observations [Egerer et al., 2019]. In the context of this study, the turbulence as determined from the three-dimensional wind vector measured with a high temporal resolution of several tens of Hertz by an ultrasonic anemometer attached to the tether of the balloon was used.

An optical disdrometer, which is part of the OceanRAIN network [Klepp et al., 2018] was mounted on the crows' nest of the Polarstern. It continuously measured the precipitation rate for different hydrometeor types and size bins. Additionally, launches of Vaisala RS92-SGP radiosondes [Jensen et al., 2016] were conducted every 6 hours (shortly before 5, 11, 17 and 23 UTC to reach 100 hPa approximately at 6, 12, 18, and 24 UTC) to obtain in-situ profiles

of temperature, relative humidity, pressure, and horizontal wind speed and direction.

3.4 Data processing and synergistic retrievals

The first step of the OCEANET-Atmosphere data analysis was to provide a continuous vertically resolved view on cloud and aerosol macro- and microphysical properties. This data set is aimed to improve the understanding of the Arctic atmosphere system and to support partner projects for example with input for radiative transfer calculations and turbulence studies. To derive continuous products of cloud and aerosol properties, the shipborne OCEANET-Atmosphere remote-sensing data set were processed using the synergistic retrieval algorithm Cloudnet [Illingworth et al., 2007]. In this Section, the extension of the standard Cloudnet algorithms by additional operationally applicable products providing estimates of cloud droplet and ice crystal effective radius and the cloud-turbulence parameter eddy dissipation rate (EDR) are described. The developed procedure for removing the influence of the ship’s motion on the measurement of vertical velocities with Mira-35, which are required for the EDR retrieval, is also explained below.

3.4.1 Correction of vertical-stare cloud radar observations for ship motion

A structural requirement to derive valid vertical Doppler velocities from Doppler cloud radar measurements is a permanently vertical-pointing radar. When the cloud radar is pointing off-zenith, the measured vertical-stare Doppler velocity will be biased by an additional component introduced by the horizontal wind. A correction of this bias is possible based on high resolved horizontal wind data and a known radar-beam incident-angle [Wulfmeyer and Janjić, 2005]. A different approach was chosen for PS106 to directly avoid such a bias. The cloud radar was mounted on an active stabilization platform, similar to the approach described by Achtert et al. [2015], as can be seen in the picture in Figure 3.5 (a). Figure 3.5 (b) shows the antenna, which was kept vertically oriented by the platform. This platform was a predecessor of the SOMAG AG Jena — GSM 4000 [SOMAG, 2017]. The platform actively leveled out the roll and pitch movement of the RV, ideally in a way that no correction of horizontal-wind effects was necessary. An additional bias of the true Doppler velocity occurs if the cloud radar itself moves vertically, e.g., together with the ship: the vertical velocity is superimposed on the measured Doppler velocity. The necessary heave correction was done in a postprocessing procedure.

In Figure 3.6 the vertical velocity for the cloud radar v_{c_z} is shown [calculated after Eq. (3.24) – (3.25)]. Four possible cruise sections based on the Polarstern location are marked below the time series. Transects through the North Sea, which were characterized by the strongest vertical movements of the cloud radar during PS106 with velocities up to $\pm 2 \text{ m s}^{-1}$, are highlighted in light green. During the transits through the sea ice (Ice transit, light blue),

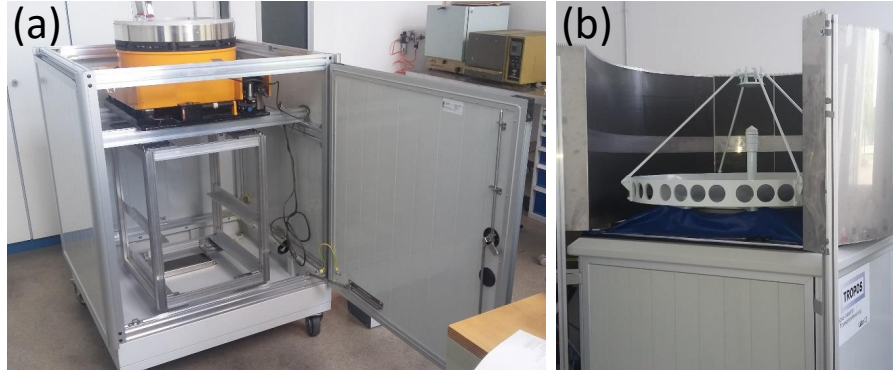


Figure 3.5: Panel (a) shows the stabilization platform mounted in the cloud radar cabinet and panel (b) the cloud radar antenna above the cabinet. (Pictures: P. Seifert).

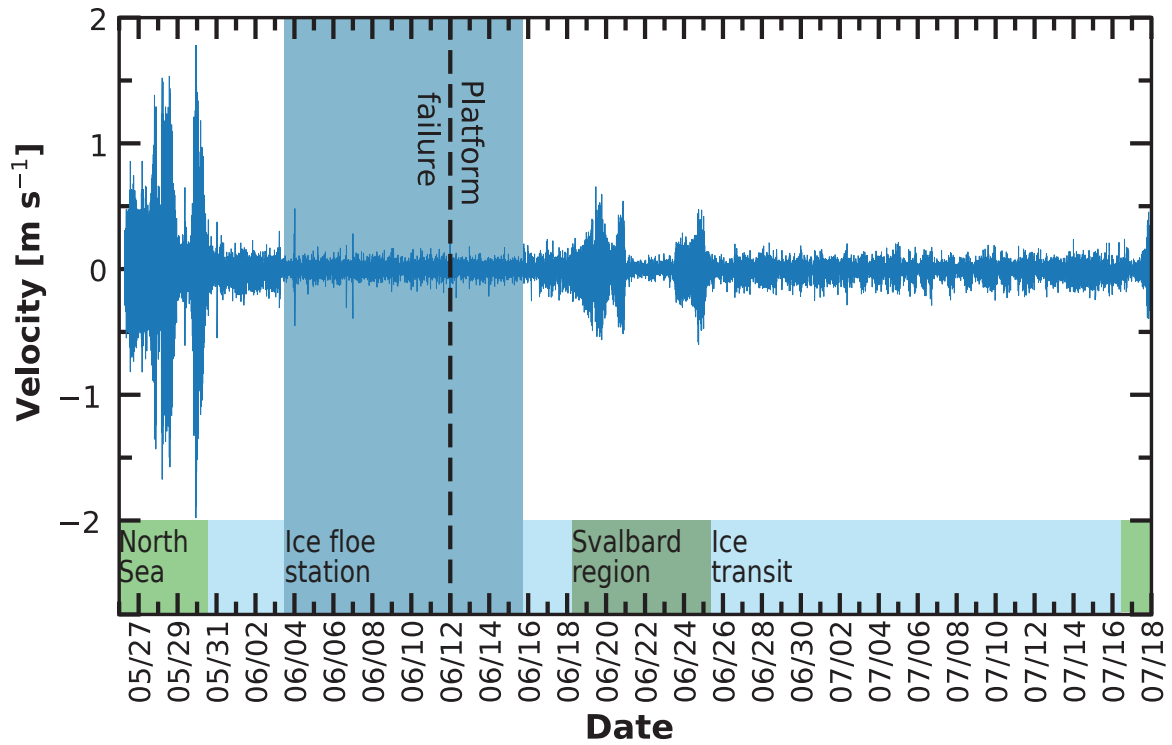


Figure 3.6: In this Figure, the time series of the cloud radar heave rate during PS106 is shown. The thick dashed vertical line indicates the moment when the stabilization platform had a malfunction. At the bottom, a rough localization of Polarstern is annotated — light green: North Sea; light blue: ice transit; dark blue: ice floe station; dark green: Svalbard region.

the vertical movement was already significantly reduced to less than $\pm 0.5 \text{ m s}^{-1}$ and while Polarstern was at the ice floe station (dark blue) the lowest vertical velocities were measured. During the period when Polarstern traveled to Ny-Ålesund (Svalbard region, dark green) for crew exchange, the vertical movements increased again to almost $\pm 1 \text{ m s}^{-1}$.

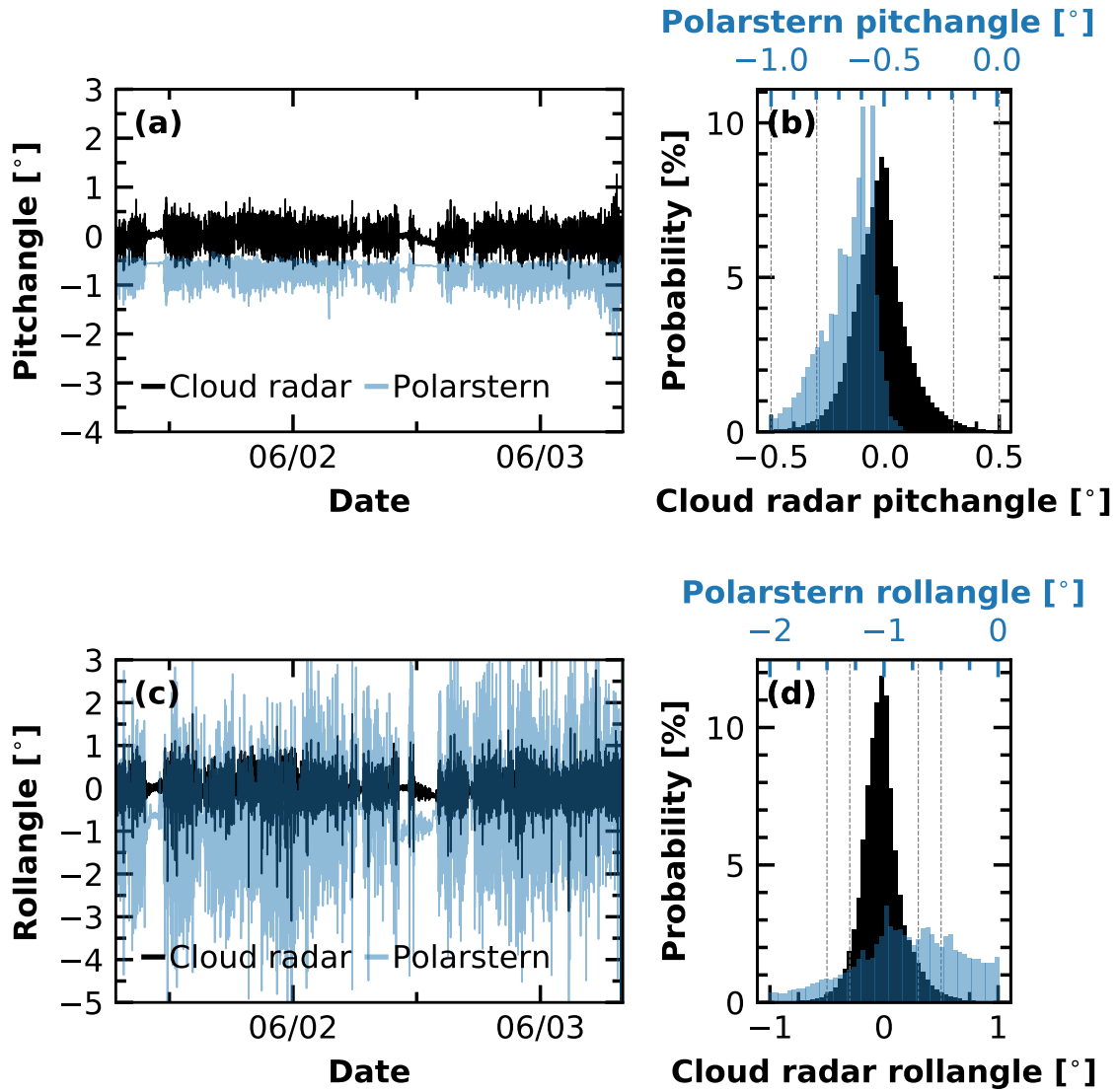


Figure 3.7: Panel (a) and (c) show times series of the pitch and roll angles, respectively, of Polarstern (blue) and the vertically stabilized cloud radar (black) during the ice transit from 1 June 2017 07:00 UTC to 3 June 2017 8:00 UTC. In (b) and (d) the respective histograms are shown [note the different axes scale of the cloud radar data (bottom axis of each histogram) and Polarstern data (top axis)]. The dashed lines indicate a rotation angle of $\pm 0.5^\circ$ and $\pm 0.3^\circ$.

Figure 3.7 shows a comparison of the pitch and roll angle time series during icebreaking conditions from 1 June 2017 07:00 UTC – 3 June 2017 8:00 UTC measured by the vessel’s inertial measurement unit (IMU) and directly at the cloud radar. For this purpose, a single-board computer (Beaglebone Blue) with integrated IMU was attached to the frame of the cloud radar, as the platform itself did not provide any position determination. The stabilization platform ensured accuracy of the leveling of $\pm 0.5^\circ$ during the ice transit and

the ice floe camp periods. The $2\text{-}\sigma$ standard deviation of the zenith-pointing during the ice transit was found to be 0.32° . Thus, 95 % of the data points show a vertical pointing of 89.68° or better. During the ice flow camp, the $2\text{-}\sigma$ standard deviation was 0.34° . During the open-sea passage of RV Polarstern, the accuracy of the stabilization was reduced to around $\pm 1^\circ$ with a 2-sigma standard deviation of 0.7° .

To perform the necessary heave correction, first, the velocity by which the cloud radar was moving vertically (heave rate of the cloud radar) had to be determined. The heave rate of the cloud radar v_{C_z} is the sum of the z-component of the Polarstern translation vector v_{T_z} and the vertical movement due to the ship's rotation v_{R_z} with respect to the ship's (high quality) IMU

$$v_{C_z} = v_{T_z} + v_{R_z}. \quad (3.24)$$

The complete cloud radar Doppler spectra for each range gate as well as the motion data (rotation and translation) of Polarstern were stored with a resolution of 4 Hz and 20 Hz, respectively, throughout the entire cruise. This ensured an accurate determination of v_{C_z} and hence enabled the heave correction. To determine the heave rate of the cloud radar, first, the cross product of the rotation velocity vector of Polarstern $\vec{\omega}_P$ (angular velocity) and the position of the radar $\vec{X} = (-5.4 \text{ m}, -2.34 \text{ m}, 16.35 \text{ m})$ relative to the IMU of Polarstern was calculated as follows

$$\vec{v}_R = \vec{\omega}_P \times \vec{X} = \begin{pmatrix} \omega_\psi \\ \omega_\phi \\ \omega_\theta \end{pmatrix} \times \begin{pmatrix} X_x \\ X_y \\ X_z \end{pmatrix} = \begin{pmatrix} v'_{R_x} \\ v'_{R_y} \\ v'_{R_z} \end{pmatrix}, \quad (3.25)$$

with ω_ψ , ω_ϕ , and ω_θ the rotational velocity in pitch (ψ), roll (ϕ), and yaw (θ) direction. v'_R is the velocity of the cloud radar caused by the ship's rotation within the ship's coordinate system. Thus, \vec{v}'_R had to be transformed into the Earth's coordinate system using the rotation matrices. For the z-component (vertical velocity) this transformation results in

$$v_{R_z} = \vec{v}'_R \circ \begin{pmatrix} -\sin(\psi) \\ \cos(\psi) \sin(\theta) \\ \cos(\psi) \cos(\theta) \end{pmatrix} \quad (3.26)$$

where ψ and ϕ represent the rotation angles of the ship (pitch and roll angle) with respect to the Earth system and \circ denotes the dot product. v_{T_z} and $\vec{\omega}_P$ were provided by the ship's IMU and recorded during the cruise.

The heave-rate correction is explained next. In an initial step, the cross-correlation between the timestamps of the two data sets, the cloud radar Doppler spectrum and the cloud radar heave-rate was calculated to check for a possible time shift between both data sets. This time shift was found to be 0.25 s. Subsequently, the values of v_{C_z} were linearly

interpolated onto the respective time grid of the Doppler spectrum. The number of bins the respective spectrum needed to be shifted was calculated from the Doppler resolution ($\Delta v_k = 0.08 \text{ m s}^{-1}$) and the interpolated heave rate. Finally, the spectra were shifted accordingly. After this correction, the corrected spectra were incoherently averaged to 3 s and the Doppler moments were determined.

The improvement of the data set after the heave correction is shown in Figure 3.8 for a case study from 30 May 2017 between 00:00 and 01:00 UTC when a nimbostratus cloud with precipitating ice particles was present above Polarstern. The measured uncorrected Doppler velocity and the respective histogram of the velocities are presented in Figure 3.8 (a) and (b). The radar’s vertical movement on the ship is visible, in both, in the time-height cross-section of the Doppler velocity as stripes of enhanced or reduced velocity throughout the whole column as well as in the broadening of the histogram. The corrected Doppler velocity and the respective histogram are presented in Figure 3.8 (c) and (d).

The Fourier spectrum of the corrected and uncorrected Doppler velocity was calculated to evaluate the effect of the heave correction [Figure 3.8 (e) and (f)]. Continuous time-series of 1 hour of Doppler velocity in the upper 3 km of the cloud presented here were analyzed. The Fourier spectra of the Polarstern pitch- and roll-movement are shown in blue in Figure 3.8 (e) and (f). In each plot additionally, the spectra of the corrected (black) and uncorrected (purple) Doppler velocity are depicted. The velocity contribution caused by the pitch and roll motions of the ship is obvious in the Doppler velocity spectra. Especially in the pitch but also in roll spectrum a strong peak at a wavenumber of 1.5 m^{-1} is visible. This peak is also obvious in the uncorrected Doppler velocity spectrum and was reduced after the correction. The integral of the frequency range which was most affected by the ship’s movement ($0.02 - 0.3 \text{ m}^{-1}$) was calculated both, for the corrected and the uncorrected data. The heave correction reduced the fraction of the ship’s movement in the power spectral density of the Doppler velocity (or its variance) by a factor of 15.

3.4.2 Retrieval of eddy dissipation rate from Doppler radar spectra

A measure of atmospheric turbulence is the turbulence kinetic energy (TKE). The TKE is the mean kinetic energy per mass unit and is defined as

$$E_{\text{TK}} = \frac{1}{2} \left[\overline{(u'_x)^2} + \overline{(u'_y)^2} + \overline{(u'_z)^2} \right] \quad (3.27)$$

with $\overline{(u'_i)^2}$ the variance of the velocity components of the turbulent flow. The rate at which the TKE is transferred from larger eddies into smaller ones and eventually dissolves into thermal energy is the EDR. Hence, the EDR can be used as a quantitative proxy of atmospheric turbulence.

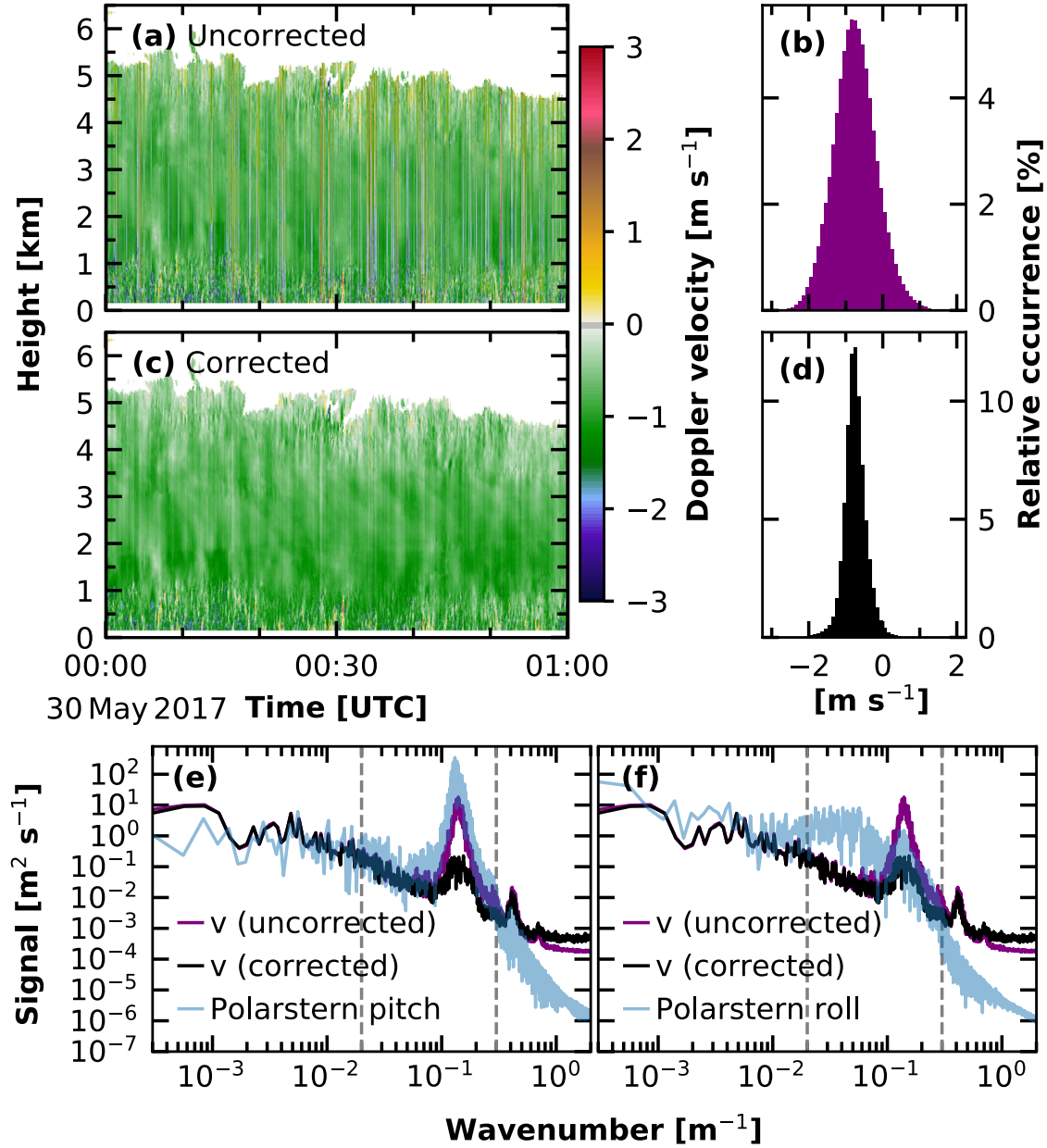


Figure 3.8: (a) Uncorrected and (c) corrected Doppler velocity during PASCAL on 30 May 2017 between 00:00 and 01:00 UTC measured with the cloud radar. Panels (b) and (d) represent the respective histogram of the presented Doppler velocities. Negative values denote downward motion. In (e) and (f) the mean Fourier spectrum of the uppermost, continuous time series of the Doppler velocity during the same period is shown. In (e) in addition the spectrum of the Polarstern pitch movement during this period is depicted. In (f) the respective spectrum of the roll movement is shown. The velocity spectra are identical in (e) and (f). The dashed lines in (e) and (f) indicate the frequency range, in which the heave correction significantly changed the spectra.

Several approaches to retrieve the EDR are available. Methods exist for in-situ measurements from aircraft- [Meischner et al., 2001; Nicholls, 1978; Nucciarone and Young, 1991], helicopter- [Siebert et al., 2006a], and balloon-borne instruments [Brooks et al., 2017; Caughey et al., 1979; Siebert et al., 2006b], and for meteorological tower instruments [Caughey et al., 1979; Kaimal et al., 1976; Zhou et al., 1985]. Additional retrievals for remote sensing have been developed [Borque et al., 2016; Sathe and Mann, 2013]. These methods are based on the Doppler velocity structure function derived from vertically pointed Doppler lidar [Frehlich and Cornman, 2002] or Doppler radar [Lothon et al., 2005] or a combination of the width of the Doppler spectrum and the Doppler velocity measurements [Meischner et al., 2001]. Other retrievals use time-series analyses of vertical velocities from vertical-stare Doppler radar [Kalesse and Kollias, 2013; Shupe et al., 2012] or Doppler lidar observations [O'Connor et al., 2010].

Typical values for EDR in clouds spread between $10^{-1} \text{ m}^2 \text{ s}^{-3}$ and $10^{-8} \text{ m}^2 \text{ s}^{-3}$. Borque et al. [2016] reported EDR of maritime and continental stratiform clouds on the order of $10^{-4} - 10^{-2} \text{ m}^2 \text{ s}^{-3}$ and $10^{-7} - 10^{-2} \text{ m}^2 \text{ s}^{-3}$, respectively. In cumulus clouds with weak updrafts, EDR have been found in a range between $5 \cdot 10^{-5} \text{ m}^2 \text{ s}^{-3}$ and $10^{-2} \text{ m}^2 \text{ s}^{-3}$, whereas values up to $10^{-1} \text{ m}^2 \text{ s}^{-3}$ were found for cumulus clouds with strong updrafts [Siebert et al., 2006a]. In cumulonimbus clouds, Meischner et al. [2001] found values for EDR between $10^{-6} - 5 \cdot 10^{-2} \text{ m}^2 \text{ s}^{-3}$. For low clouds or fog at Chilbolton, UK, O'Connor et al. [2010] estimated the EDR to be on the order of $10^{-4} - 5 \cdot 10^{-2} \text{ m}^2 \text{ s}^{-3}$. Shupe et al. [2012] analyzed mixed-phase Arctic stratocumulus clouds and retrieved EDR from cloud radar observations in the range of $10^{-6} - 10^{-3} \text{ m}^2 \text{ s}^{-3}$.

The reported range of EDR for different cloud conditions leads to the assumption that Arctic clouds might show characteristic differences for varying atmospheric conditions. The vertical alignment of the cloud radar during PS106 allowed the determination of the EDR from the vertical air motions observed in cloud layers. Thus, the retrieval technique for EDR that can be applied to the OCEANET-Atmosphere data set is presented in the following.

Following Borque et al. [2016] and references therein, the spectrum of the TKE as a function of wavenumber k , $S(k)$, can be describes within its inertial subrange as

$$S(k) = \kappa \varepsilon^{2/3} k^{-5/3}, \quad (3.28)$$

assuming the turbulent energy dissipation is a homogeneous and isotropic process. Here $\kappa = 0.5$ is the Kolmogorov constant for a 1-D wind spectra [Sreenivasan, 1995]. k is related to a length scale L ($k = 2\pi/L$) and to frequency f with $k = f/v_h$. v_h is the horizontal wind speed, and assuming a linear wind field.

If the spectrum plotted against wavenumbers follows in a log-log plot within the inertial

subrange a $-5/3$ slope, ε can be estimated by

$$\varepsilon = \left(\frac{10^{k_{\text{lin}}}}{\kappa} \right)^{3/2} \quad (3.29)$$

where k_{lin} represents the corresponding intercept with the x-axis of the linearized fit.

For this study, power spectra of the Doppler velocity with a sampling frequency of 4 Hz from continuous time series covering 5 minutes were calculated. For the best estimation of the inertial subrange 34 arbitrary chosen idealized spectra were defined. These spectra, defined by the given wavenumber intervals Δk_i , are depicted in Figure 3.9 by the gray lines. The linearized fit was determined by calculating a linear least-squares regression of the spectrum within each interval. Additionally, the spectrum of the vertical velocity observed on 7 June 2017, from 10:28 to 10:43 UTC is shown from cloud radar Doppler velocities in blue and from balloon measurements in red.

According to Borque et al. [2016], a good fit was defined with a slope from the linear regression of $-5/3 \pm 20\%$ ($-5/3 \pm 1/3$). If within more than one wavenumber interval a $-5/3$ was observed the mean of all ε_i for the corresponding spectrum was calculated and taken as the EDR. In order to evaluate the EDR estimated by cloud radar measurements, it was compared to EDR derived from the tethered balloon [Egerer et al., 2019]. The periods used for deriving EDR from the tethered balloon were 15 min, during which it was located at a constant height above the ground. As a measure to quantify the uncertainties of the two retrievals the standard deviation of all good fits was calculated.

Three comparisons were done for situations where the tethered balloon was at a constant height in a cloud. The first one was done for measurements taken on 7 June 2017. On this day between 10:28 and 10:43 UTC the balloon was located at 380 m height. Figure 3.9 shows the intercomparison of the power spectrum derived by the tethered balloon measurements (red) with the spectrum derived from the cloud radar Doppler velocity (blue) according to the techniques described above is shown for this period. Due to the higher sampling frequency of the balloon-borne turbulence sensor, eddies with a higher wavenumber can be resolved in the the spectrum from the balloon measurements. The derived EDR for the cloud radar measurements was $(6.84 \pm 7.61) \cdot 10^{-4} \text{ m}^2 \text{ s}^{-3}$ and for the tethered balloon $(2.65 \pm 3.59) \cdot 10^{-5} \text{ m}^2 \text{ s}^{-3}$. The other two comparisons were done on 5 June 2017 13:50 – 14:05 UTC at 330 m height and on 9 June 2017 09:00 – 09:15 UTC at 500 m height. The EDR values for these cases from the tethered balloon measurements were $(8.90 \pm 1.07) \cdot 10^{-5} \text{ m}^2 \text{ s}^{-3}$ and $(6.39 \pm 5.48) \cdot 10^{-6} \text{ m}^2 \text{ s}^{-3}$ while the cloud radar measurements gave $(5.98 \pm 3.53) \cdot 10^{-5} \text{ m}^2 \text{ s}^{-3}$ and $(2.26 \pm 1.64) \cdot 10^{-5} \text{ m}^2 \text{ s}^{-3}$, respectively.

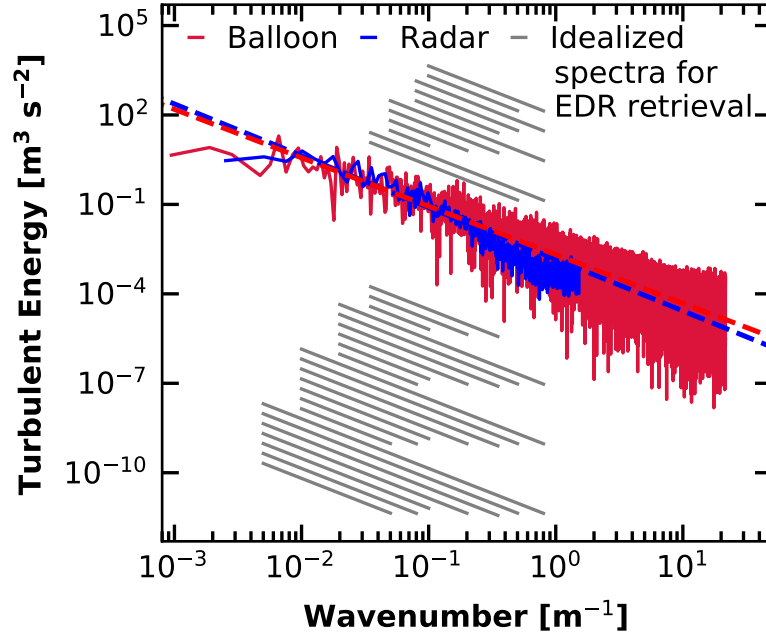


Figure 3.9: In blue the Fourier spectrum derived from cloud radar Doppler velocities and in red from tethered balloon turbulence measurements on 7 June 2017 between 10:27 and 10:43 UTC at 380 m height are shown. The dashed lines depict the respective averaged linearized fit. Gray lines: illustration of the idealized spectra in given wavenumber intervals which had been used to check for a $-5/3$ slope of the Fourier spectrum.

3.4.3 Cloud macro- and microphysical properties from instrument-synergies

The instrument synergistic approach Cloudnet [Illingworth et al., 2007] was applied to acquire a data set suitable for the statistical evaluation of the macro- and microphysical properties of clouds observed during PS106. This data set, in addition, serves to realize model evaluations [Illingworth et al., 2007] and radiative transfer calculations, e.g. with the Rapid Radiative Transfer Model for General Circulation Models (RRTMG) [Barker et al., 2003; Clough et al., 2005; Mlawer et al., 1997]. RRTMG is currently utilized for single-column radiative transfer calculations. The model considers vertical profiles of relative humidity and temperature, standard atmospheric constituent profiles based on Anderson et al. [1986], and cloud macrophysical and microphysical properties. These requirements include vertically resolved effective radius and water content of liquid and ice hydrometeors. In the following, the approaches for achieving these data set requirements based on the PS106 remote sensing are described.

Cloudnet

The instrument synergy approach Cloudnet [Illingworth et al., 2007] combines the observations from lidar, cloud radar, microwave radiometer, disdrometer, and radiosondes. The Cloudnet algorithms were used to determine cloud physical properties during PS106. The concept of Cloudnet will now be briefly introduced.

Cloudnet is a network of ground-based remote-sensing stations with the aim to provide profiles of cloud and aerosol properties. The presented products in this thesis are processed with a Matlab-based Cloudnet version. Meanwhile, a python version (CloudnetPy) is published and freely available [Tukiainen et al., 2020]. For data processing, first, the measurements are averaged on a common grid with a vertical and temporal resolution of 31.18 m and 30 s, respectively. Radiosonde-based profiles of thermodynamic variables are interpolated on the Cloudnet data grid to estimate the temperature at the respective time-height pixel. Soundings from Ny-Ålesund [Maturilli, 2017] were applied for the periods where no radiosonde was launched from the RV but Polarstern was in the vicinity of Svalbard. As a last fall-back option, data from the Global Data Assimilation System (GDAS) with a horizontal and vertical resolution of 1° and 3 h [available at: <http://ready.arl.noaa.gov/gdas1.php>, Kanamitsu, 1989] were used as meteorological input for Cloudnet.

Based on the observations scaled on the Cloudnet data grid a categorization bit mask is derived. This bit mask assigns a series of seven distinct features about the observed targets: clear yes/no; liquid yes/no; falling yes/no; wet bulb temperature below 0 °C yes/no; melting layer yes/no; aerosol yes/no; and insects yes/no. The bitwise categorization ensures that each data point is characterized by a defined combination of these features. The detailed definition of the respective categorization bits is beyond the scope of this thesis and has already been given by Hogan and O'Connor [2004].

Based on the individual combination of the categorization bits, an atmospheric target classification is derived as follows: 'clear sky' is defined when no bit is set for the respective pixel. 'Cloud droplets only' is identified by only the droplet bit being set. The falling bit alone identifies 'drizzle or rain'. Droplet and falling bit together are interpreted as 'drizzle/rain & cloud droplets', falling and cold bit together as 'ice'. Droplet, falling, and cold bit combined give 'ice & supercooled droplets'. The melting bit being set alone identifies 'melting ice', and together with the droplet bit the pixel is defined as 'melting ice & cloud droplets'. The aerosol and insects bits are accordingly interpreted as 'aerosol', 'insects' or 'aerosol & insects'. Following previous studies [e.g., Mioche et al., 2015; Shupe, 2011], mixed-phase clouds are defined when (supercooled) liquid-water and ice particles are detected in the same data point and when an ice cloud was observed with a liquid-water or mixed-phase cloud-top layer.

Besides the phase of the cloud, the respective mass concentrations of ice and liquid-water are determined where applicable. The liquid-water content (LWC) is derived by scaling the

MWR LWP adiabatically onto the cloud pixels defined as pure-liquid or mixed phase [Frisch et al., 1998; Merk et al., 2016]. For pure-liquid data points, the approach of Frisch et al. [2002] is used to derive the cloud droplet effective radius from the observed radar reflectivity factor, LWP, and an assumed width of the lognormal cloud droplet size distribution (which was, according to Miles et al. [2000], set to 0.35 for marine stratocumulus). The IWC is calculated using an empirical formula from Hogan et al. [2006] relating cloud radar reflectivity Z_e and temperature T . This approach for IWC is only applied for clouds classified as 'ice' or 'ice & supercooled droplets'. In this step, also a correction for potential attenuation of the cloud radar signal due to the presence of liquid water is made.

Ice crystal effective radius

As discussed above, Cloudnet offers a variety of retrievals for ice microphysical parameters. Nevertheless, the continuous application of radiative transfer calculations requires a consistent availability of vertically resolved ice and liquid-water hydrometeor effective radius and water content. While Cloudnet already contains retrievals for droplet effective radius and liquid-water content, and ice water content, so far no operational retrieval for ice effective radius was available. Hence, in the course of this thesis, a new approach to calculate the ice effective radius $r_{\text{eff,ice}}$ was developed and published in Griesche et al. [2020a]. This approach is based on the combination of the definition of the effective radius as the ratio of the third to the second moment of the particle size distribution (PSD) and an empirical relationship between the visible extinction coefficient α , cloud radar reflectivity Z_e , and model temperature T . Similarly as for IWC, $r_{\text{eff,ice}}$ is only calculated for data points where Cloudnet classified 'ice' or 'ice & supercooled droplets'.

Using the ratio of the second to the third moment of the PSD, the effective radius $r_{\text{eff,ice}}$ can be related to IWC and α [Delanoë et al., 2007]. This yield for $r_{\text{eff,ice}}$

$$r_{\text{eff,ice}} = \frac{3}{2} \frac{q_i}{\rho_i \cdot \alpha} \cdot 10^6 \text{ (}\mu\text{m)}, \quad (3.30)$$

with q_i the ice water content in kg m^{-3} , α the extinction coefficient in m^{-1} , and ρ_i the density of the solid ice ($\rho_i = 917 \text{ kg m}^{-3}$). Both, IWC and α have been calculated using empirical relationships between IWC or α and the cloud radar reflectivity Z of a 35-GHz cloud radar and temperature T published by Hogan et al. [2006]. Using the IWC-Z-T and α -Z-T relationships and Eq. (3.30), finally the $r_{\text{eff,ice}}$ -Z-T relationship results to

$$r_{\text{eff,ice}} = \frac{3}{2\rho_i} 10^{C_{ZT} \cdot Z \cdot T + C_Z \cdot Z + C_T \cdot T + C_0} \cdot 10^6 \text{ (}\mu\text{m)}, \quad (3.31)$$

with $C_{ZT} = -2.05 \cdot 10^{-4}$, $C_Z = 1.6 \cdot 10^{-3}$, $C_T = -1.71 \cdot 10^{-2}$, and $C_0 = -1.52$.

To estimate the error of the identified effective radii of the ice crystals, an error propagation of Eq. (3.31) was done using an average error for IWC and α from Hogan et al. [2006] of

40 %. The error $\Delta r_{\text{eff,ice}}$ was found as

$$\Delta r_{\text{eff,ice}} = \sqrt{0.4^2 + 0.4^2} \cdot r_{\text{eff,ice}}. \quad (3.32)$$

The data set for $r_{\text{eff,ice}}$ is published in the long-term data archive Pangaea [Griesche et al., 2020b].

Detection of low-level stratus clouds

During PS106, frequent low-level stratus clouds (cloud base < 165 m) have been observed. These situations were often associated with a strong attenuation of the lidar beam within the lowest few hundred meters above Polarstern due to the high optical thickness of these clouds. The cloud radar, in turn, has its technical limitation in detecting the lowest part of the boundary layer below 155 m range (165 m above sea level). The height of the lowest Cloudnet data pixel is also at 165 m. Thus, on the one hand, the low-level clouds, which occurred during PS106 arise issues for the Cloudnet retrieval due to misinterpretation of an attenuated lidar signal as a missing signal. On the other hand, these clouds tend to be underrepresented in Arctic cloud statistics since most current statistics of Arctic clouds do not consider clouds in such a low altitude. A new Cloudnet classification category called low-level stratus (LLS) cloud was developed in the scope of this thesis to address these issues. These clouds were identified by the Polly^{XT} signal-to-noise-ratio (SNR), [Heese et al., 2010] in the lowest 165 m above sea level. The near-range channels of the Polly^{XT} system have a complete overlap already at 120 m above the instrument [Engelmann et al., 2016] and thus are suitable for the detection of clouds already well below the lowest cloud radar observation height. Even though, quantitative parameters such as (attenuated) backscatter coefficient from a single elastic backscatter signal cannot be determined below 120 m.

From a sensitivity study and visual inspection of the Cloudnet data set, LLS clouds were defined where SNR of the lidar signal exceeded the threshold value of 40. This value was obtained by evaluating signatures of attenuation in the time series of the Cloudnet attenuated backscatter coefficient, increased values of LWP, and correlation with the visibility sensor of Polarstern. An $\text{SNR} > 40$ at these low altitudes is very likely only caused by the occurrence of low-level clouds since the SNR is not range corrected. The LLS base and top have could only be derived, when the lidar signals were not fully attenuated.

Retrieval of CCN and INP number concentrations

Arctic clouds and their susceptibility to the presence of aerosol are in the focus of research [Morrison et al., 2012]. Based on the measurements of Polly^{XT}, an estimation of CCN and INP properties is possible [Mamouri and Ansmann, 2016]. To do so, profiles of the aerosol

backscatter coefficient and depolarization ratio are needed. In a second step, these profiles are converted into profiles of the particle extinction coefficient using an appropriate lidar ratio (extinction-to-backscatter ratio).

The CCN number concentration (CCNC) and INPC profiles were estimated from profiles of the lidar-derived particle extinction coefficient at 532 nm utilizing conversion parameters and published INP parameterization schemes [DeMott et al., 2010] as described by Mamouri and Ansmann [2016]. For a given supersaturation of 0.15 % the CCN number concentration can be calculated as

$$N_{\text{CCN}} = C_{\text{CCN}}(\alpha^{\text{par}})^{d_{\text{CCN}}}, \quad (3.33)$$

with N_{CCN} the CCN number concentration, α^{par} the particle extinction coefficient, and the conversion parameter set C_{CCN} and d_{CCN} .

The required conversion parameters were determined from observations of Arctic AERONET stations in the same way as outlined by Mamouri and Ansmann [2016] and published in Griesche et al. [2020a]. A multiyear (2004 – 2017) data set of sun-photometer observations of the AERONET stations Thule, PEARL (Polar Environment Atmospheric Research Laboratory), Kangerlussuaq, Ittoqqortoormiit, and Hornsund was used to obtain the set of Arctic conversion parameters. These AERONET observations were made during the summer half years.

The direct retrieval of the CCN conversion parameters from the AERONET data (level 2, version 3, inversion products) resulted in $C_{\text{CCN}_1} = 18.6 \text{ cm}^{-3}$ and for the exponent $d_{\text{CCN}_1} = 0.83$ (Albert Ansmann, personal communication, 2019) for the range of extinction coefficients from 15 to 300 Mm^{-1} (500 nm aerosol optical depths from 0.015 to 0.3 were measured). During the PS106 observations, the aerosol extinction coefficient was mostly around $1 - 10 \text{ Mm}^{-1}$ in the lower part of the troposphere. The AERONET data for this low range of extinction coefficients indicate that conversion parameters of $C_{\text{CCN}_2} = 10 \text{ cm}^{-3}$, $d_{\text{CCN}_2} = 0.9$, and $C_{\text{CCN}_3} = 3.0 \text{ cm}^{-3}$, $d_{\text{CCN}_3} = 1$ is also appropriate. The aerosol in the Arctic is fine-mode dominated and shows Ångström exponents (440 – 870 nm) typically between 0.9 and 1.8 (with an average of 1.5 to –1.6).

Following Mamouri and Ansmann [2016] a relationship for INPC was derived

$$N_{\text{INP}} = a_1(T_s - T_z)^{a_2}(a_3 \cdot \alpha^{\text{par}})^{[a_4(T_s - T_z) + a_5]} \frac{T_z \cdot p_s}{T_s \cdot p_z}, \quad (3.34)$$

with N_{INP} the INP number concentration, $a_1 = 5.94 \cdot 10^{-5}$, $a_2 = 3.33$, $a_3 = 0.22$, $a_4 = 0.0265$, $a_5 = 0.0033$, $T_s = 273.16 \text{ K}$, $p_s = 1013 \text{ hPa}$, and T_z and p_z the ambient temperature and pressure.

3.5 Summary of the data processing for PS106

A 2-month campaign of RV Polarstern, including an extensive suite of ground-based remote-sensing instruments of the OCEANET-Atmosphere platform, has been conducted north and northeast of Svalbard in the Arctic summer of 2017. This Chapter described in detail the deployed instrumentation and the applied processing schemes. A novelty of this thesis was the deployment of a motion-stabilized vertically pointing 35-GHz cloud radar during and the correction of the Doppler velocity after the cruise as specified in Section 3.4.1.

The movement of the ship had a significant effect on the measured vertical velocity of the cloud radar. The motion stabilization was evaluated utilizing a small single-board computer mounted on the cloud radar rack. The IMU of the minicomputer measured the residual of the pitch and roll movement after stabilization. A good stabilization during ice-breaking conditions with a leveling precision of $\pm 0.5^\circ$ was found. However, the observed displacement from zenith was larger and up to $\pm 1^\circ$, during rough sea. Under the strong wave conditions during these periods, it needs also to be considered that the IMU of the orientation sensor used for the cloud radar is based on so-called MEMS (micro-electro-mechanical systems). Such devices are based on spring-mounted capacitor plates and thus the measured pitch and roll angles are affected by translational motions like engine vibrations, etc. As these effects were not investigated in the frame of this thesis, it can be concluded that the actual vertical-pointing uncertainty range, especially on the open sea, was likely much lower than the one reported by the MEMS sensors, i.e., better than $\pm 1^\circ$. The theoretical accuracy should be $\pm 0.3^\circ$ according to the manufacturer.

On 12 June 2017, after roughly three weeks, a hydraulic motor of the stabilization platform had a malfunction (see Figure 3.6). After this date, the stabilization of the cloud radar was not possible anymore. However, the realization during PS106 proofed the concept. The same approach was applied while OCEANET-Atmosphere was operated during a cruise in 2021 crossing the Atlantic ocean. For this cruise, OCEANET-Atmosphere was complemented with a Doppler wind lidar which was mounted on a similar, albeit newer, stabilization platform. The same heave correction as developed for PS106 was applied.

For an automatic, seamless analysis of cloud properties from the measured remote-sensing time series, the Cloudnet algorithm was implemented. New Cloudnet products were developed and applied to the remote-sensing data set from PS106. The continuous characterization of cloud turbulence through EDR was made possible. The EDR were calculated using the corrected vertical velocities from the cloud radar and evaluated against in-cloud turbulence measurements done using a tethered balloon. The comparisons of the two retrievals showed that the values differ by a factor of 2 – 3. This difference is likely caused by the different sampling volumes and sampling frequencies of the two applied methods. However, in this thesis, it has been shown that the retrieval of EDR by cloud radar observations is possible, although with somewhat larger uncertainties compared to the tethered balloon approach.

The operation of a tethered balloon needs to be done manually and its observations are restricted in height. Based on measurements from a Doppler cloud radar continuous profiles of EDR can be derived. The presented approach will be applied, for example, to observations made during the recently conducted yearlong MOSAiC campaign [Shupe et al., 2018].

To provide a suitable data set for radiative transfer simulation the liquid and ice water content and liquid droplet effective radius were derived based on existing Cloudnet algorithms. A missing piece for the realization of the radiative transfer simulation were profiles of the ice crystal effective radius $r_{\text{eff,ice}}$. Hence, a new approach to derive $r_{\text{eff,ice}}$ continuously was developed and presented in this thesis. Accordingly to the EDR, the retrieval of $r_{\text{eff,ice}}$ will be applied for the MOSAiC data set.

Chapter 4

Cloud and aerosol observations during PS106

A detailed overview of the cloud conditions can be derived from the previously described Cloudnet algorithms and their improvements according to ice effective radius and radar correction. First, the meteorological conditions during the PS106 expedition are summarized. To introduce the OCEANET-Atmosphere data set three case studies are presented in the following. These cases were selected on the one hand to represent the capabilities of the standard Cloudnet products and Polly^{XT}. On the other hand, the selected case studies illustrate the new products introduced in this thesis. Additionally, a statistical overview of the aerosol and cloud situation during PS106 is shown. Finally, a discussion of the material presented is given. This Chapter is based on work published in Griesche et al. [2020a].

4.1 Meteorological conditions during PS106

To introduce the meteorological situation during the cruise, near-surface measurements of the downwelling short- and longwave irradiances, temperature, relative humidity, wind, and liquid-water path from sensors aboard Polarstern campaign are presented in Figure 4.1. The large-scale synoptic situation during the PASCAL and ACLOUD campaigns based on near-surface and radiosondes measurements, model data, and satellite observations was summarized by Knudsen et al. [2018]. The cruise started during what was classified by Knudsen et al. [2018] as cold period. The identified cold period lasted until 29 May 2017 and was characterized by northerly flows and dry conditions for Ny-Ålesund. From 30 May to 12 June 2017 a warm period followed with temperatures up to 8 °C at Ny-Ålesund. However, the spatial distance between the position of Polarstern and Ny-Ålesund caused distinct differences in the meteorological conditions at both sites. The cold period is hardly observable in the Polarstern data [Figure 4.1 (b)], possibly due to the still southern location of the vessel. During the warm period, the near-surface temperature at Ny-Ålesund was constantly above the freezing point and also at Polarstern 6 °C was experienced on 31 May 2017. However,

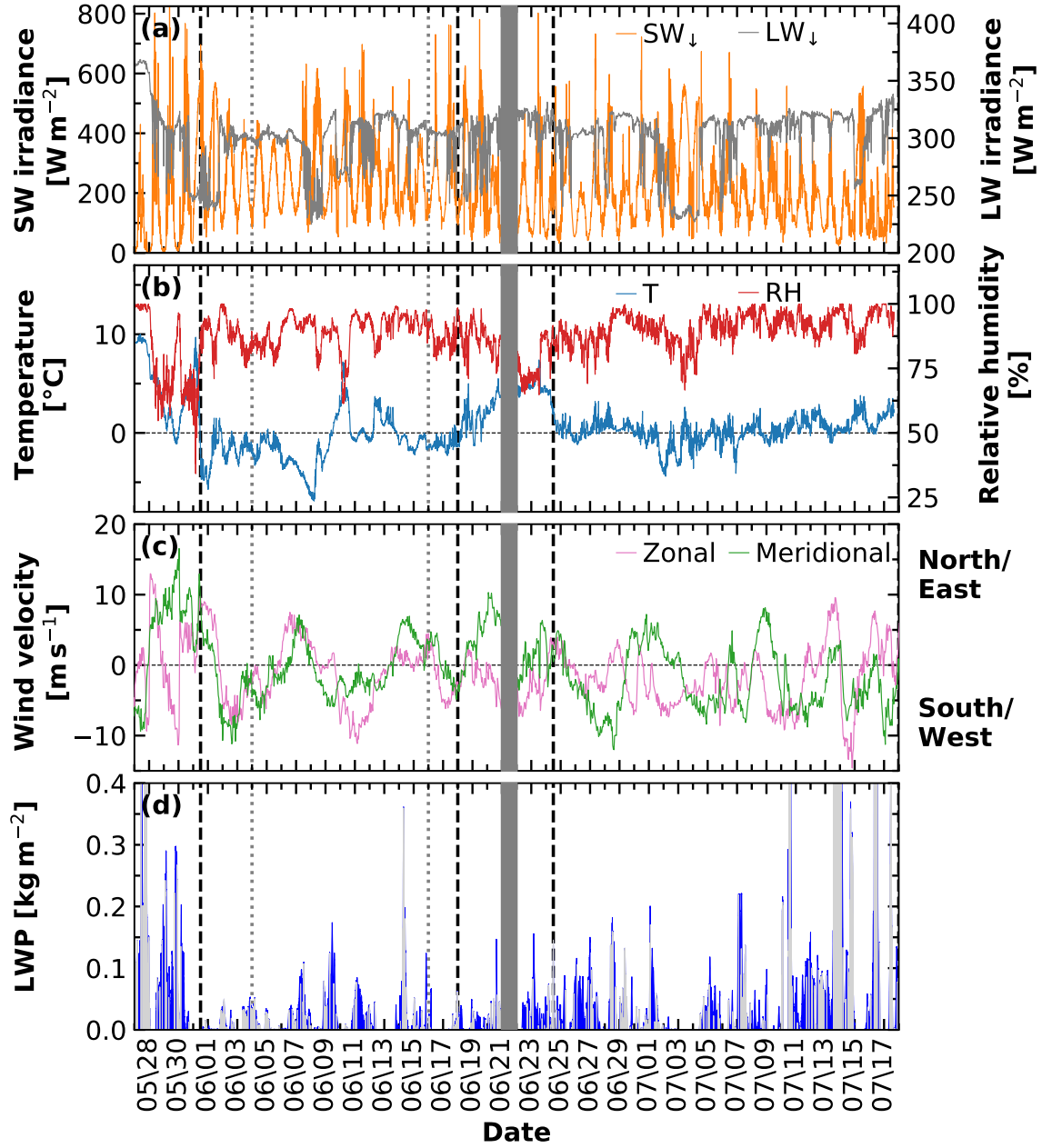


Figure 4.1: Surface observations of (a) downwelling longwave (gray) and shortwave (orange) irradiance, (b) temperature (blue) and relative humidity (red), (c) wind velocity in meridional (green) and zonal (pink) direction, and (d) LWP during the PS106 cruise (periods during precipitation conditions are shown in gray). The dashed black lines mark the ice edge crossings and the dotted gray lines mark the period of the ice floe camp. The shaded gray area is the period of crew exchange at Ny-Ålesund during which measurements were not possible.

while Polarstern was moving north and after the vessel crossed the ice edge on 31 May 2017 the temperature measured aboard the ship dropped. On 8 June 2017 the temperature reached a minimum of -7.5°C . Subsequently, the temperature increased again to 7.4°C on 10 June 2017. This rather fast temperature increase was initiated by warm air advection from the south crossing Norway and Greenland. The warm air advection reflects in the meridional surface wind component from the south with up to 5 m s^{-1} on 8 and 9 June 2017 [Figure 4.1 (c)]. On 11 June 2017, the temperature decreased again and was mostly around 0°C during the rest of the cruise. Only while Polarstern was located south of the ice edge for the crew exchange at Ny-Ålesund between 21 – 22 June 2017, the temperature also reached a value of 7.4°C . RH was mostly close to 100 %, which corresponds to the presence of a significant cloud cover during large parts of the cruise. Lower values of RH were usually associated with a temperature increase.

The observations were taken during polar day and hence constant daylight conditions (with a daily cycle) are visible in the downward directed shortwave irradiance SW_{\downarrow} [Figure 4.1 (a)]. The high northern latitude is reflected in the elevated SW_{\downarrow} minimum during nighttime. Two states can be identified in LW_{\downarrow} as known from previous publications [e.g., Morrison et al., 2012]. During cloud-free situations LW_{\downarrow} was around 250 W m^{-2} , while during cloudy conditions LW_{\downarrow} was around 320 W m^{-2} , with the exact value depending on the specific atmospheric situation. The wind direction showed many fluctuations between southerly/northerly and easterly/westerly flows in the course of the expedition. The predominant wind direction was wind from south-east. The liquid-water path shown in Figure 4.1 (d) reveals rather low values for most of the cruise, often below 0.1 kg m^{-2} . Higher amounts are largely associated with precipitation events, which are marked in gray. During precipitation, the radome of the MWR might have become wet. Under these conditions, the derived LWP values are not trustworthy. Hence, only MWR measurements which are not rain-flagged should be used in subsequent data analyses.

4.2 Case studies

Precipitating layered cloud at the ice-floe: 9 June 2017 00:00 – 18:00 UTC

An overview of the OCEANET-Atmosphere data set and the capability to analyze cloud and aerosol structures and their interactions is presented for a multilayer cloud case observed on 9 June 2017 between 00:00 and 18:00 UTC. The observations of the cloud radar, the lidar, and the MWR are depicted in Figure 4.2. The radiosonde profiles for this period are shown in Figure 4.3 up to a height of 2000 m.

The presented day reveals a rather complex situation. Starting at 00:00 UTC, Cloudnet classified a liquid-water stratocumulus layer between 600 and 900 m height as can be seen by the cloud radar and lidar observations in Figure 4.2. The cloud-top temperature derived

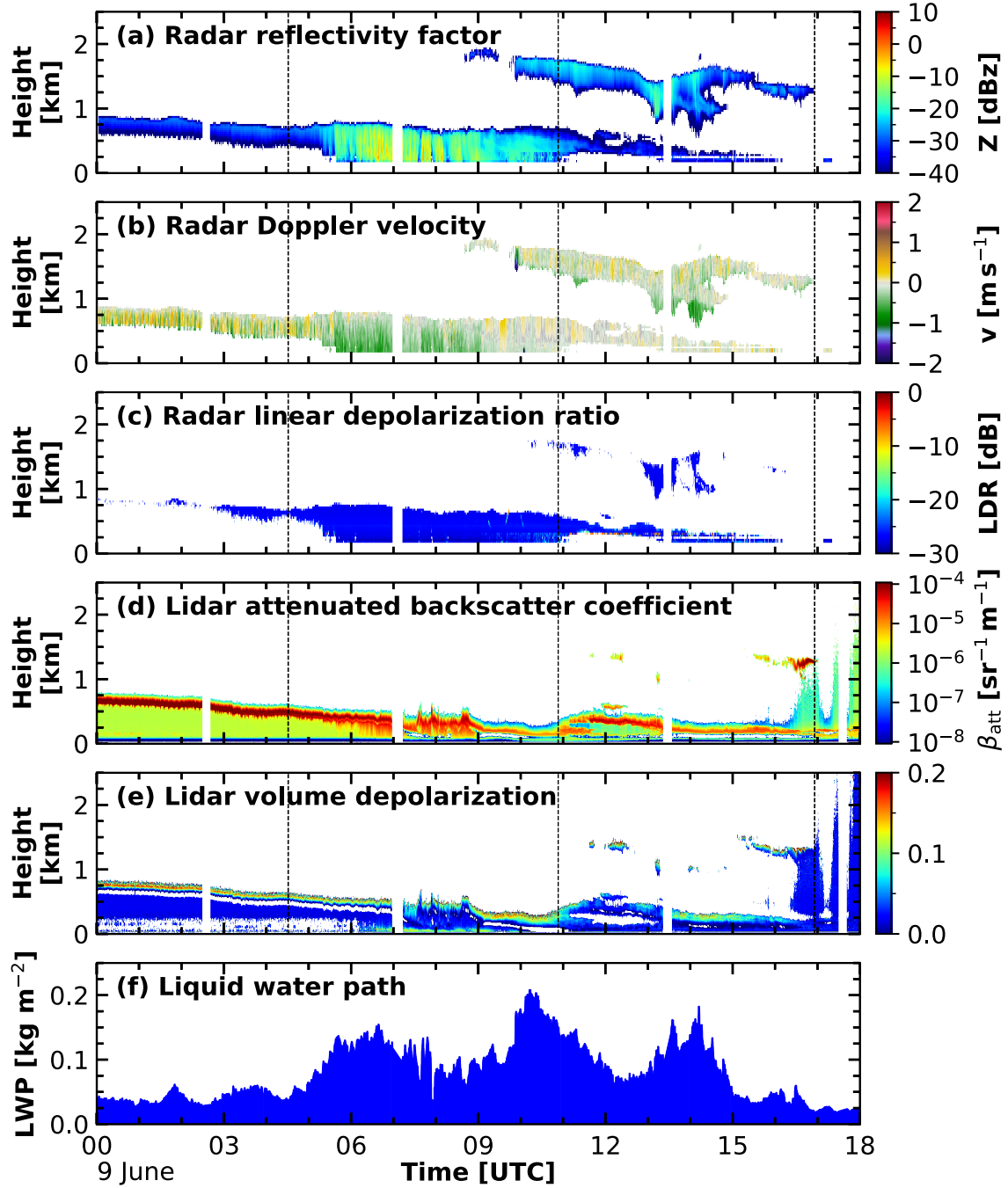


Figure 4.2: OCEANET-Atmosphere observations on 9 June 2017 between 00:00–18:00 UTC. (a), (b), and (c) show the radar reflectivity factor, Doppler velocity, and linear depolarization ratio. (d) and (e) depict the lidar attenuated backscatter coefficient at 1064 nm and volume depolarization ratio at 532 nm. In (f) the liquid-water path derived by the microwave radiometer is shown. The dashed vertical lines mark the time of the radiosonde launches on 9 June 2017 (note: the time of the first launch shown in Figure 4.3 was before the plotted profiles of the measurements start).

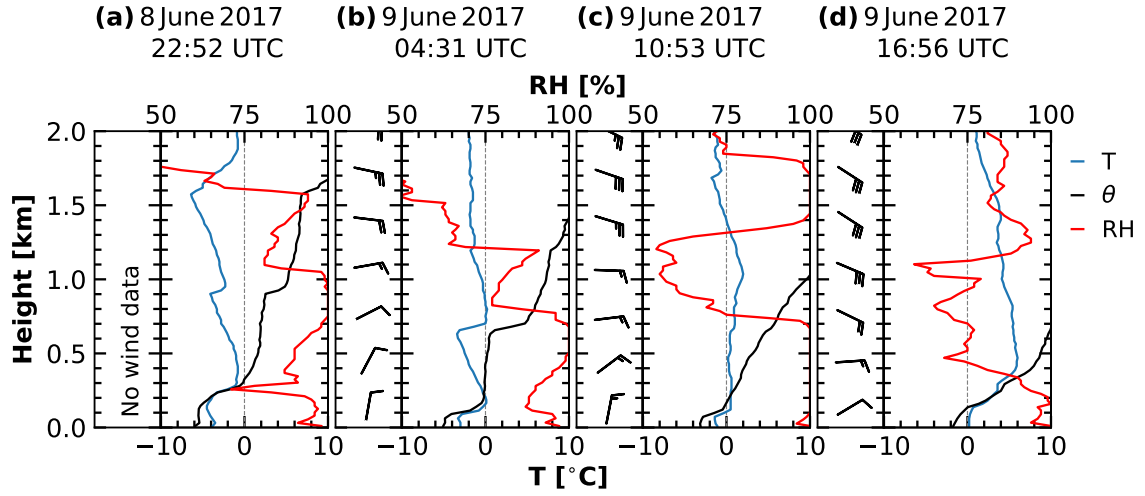


Figure 4.3: Thermodynamic profiles from radiosondes launched aboard Polarstern on (a) 8 June 2017 22:52 UTC, (b) 9 June 2017 04:31 UTC, (c) 9 June 2017 10:53 UTC, and (d) 9 June 2017 16:56 UTC up to 2000 m height. Each sounding is divided into two parts: left side the wind barbs, right side the temperature (red), potential temperature (black), and relative humidity (blue) profiles.

by the radiosonde profile from 9 June 2017 04:31 UTC [Figure 4.3 (b)] was about -4°C . This layer slowly descended, reaching a cloud base of about 400 m and cloud top of about 800 m at 05:00 UTC. The LWP during this period was rather constant with a mean value of 50 g m^{-2} with two distinct peaks: one at around 01:50 UTC and the other one around 03:45 UTC, with an LWP of up to 70 g m^{-2} , both associated with a slight increase in cloud depth. The constantly high values of EDR until roughly 05:00 UTC [$10^{-4} - 10^{-3}\text{ m}^2\text{ s}^{-3}$; Figure 4.4 (d)] indicate strong turbulent mixing of the cloud layer. Below the cloud, a shallow surface-coupled boundary layer can be identified by the potential temperature θ in Figure 4.3 (a). The increase in θ at 250 m height identifies a decoupling of the upper layer from the surface. The quasi constant values below indicate a well-mixed boundary layer below. With decreasing cloud base height, the boundary layer gets shallower [already below 100 m for the radiosonde profile shown from 9 June 2017 04:31 UTC Figure 4.3 (a)].

Around 05:30 UTC, a transformation of the cloud occurred. The LWP increased up to 160 g m^{-2} and precipitation started, almost reaching the ground (the disdrometer aboard Polarstern showed no precipitation signal, not shown here). The presence of ice was identified due to the detection of enhanced radar reflectivity and vertical velocity (falling ice particles). Thus a mixed-phase cloud was classified between 05:30 and 06:30 UTC by Cloudnet though the LDR showed no increased values. At around 06:30 UTC the wet-bulb temperature derived from the interpolated radiosonde profiles reached 0°C in the cloud top region, causing an immediate transition from a mixed-phase classification to a pure liquid-water cloud. Therefore, no IWC and no ice effective radius were determined under these conditions

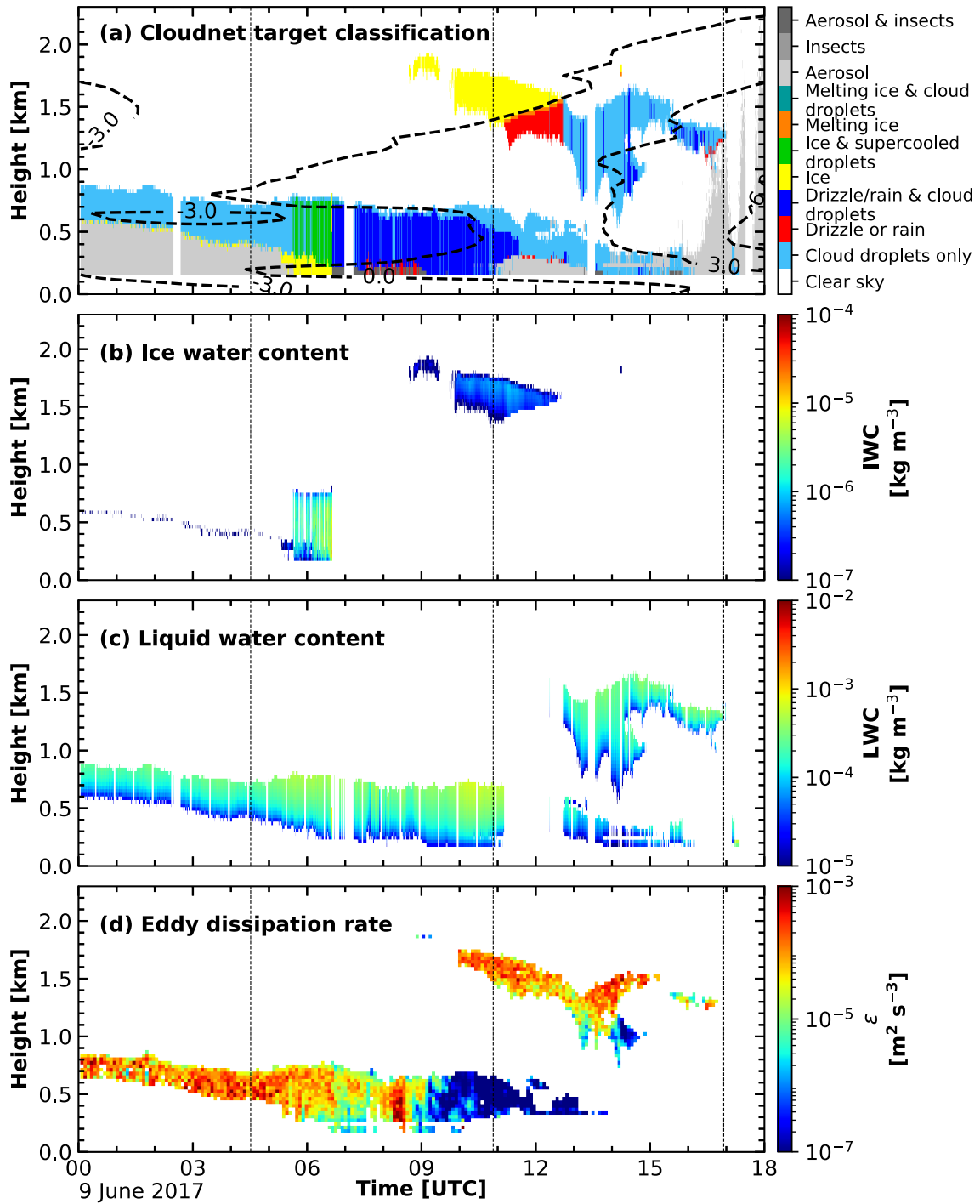


Figure 4.4: Cloudnet results for 9 June 2017 between 00:00 – 18:00 UTC. (a) target classification, (b) ice water content, (c) liquid-water content, (d) time-height profile of EDR calculated from the cloud radar Doppler velocity. In (a), additionally, the interpolated temperature from the radiosonde profiles is shown by the dashed contour lines. The dashed vertical lines mark the time of the radiosonde launches as shown in Figure 4.3.

by Cloudnet. Strong radar reflectivity and enhanced lidar volume depolarization, however, suggest that until around 11 UTC ice crystals were present inside the cloud above Polarstern. In Figure 4.4 (a) the interpolated temperature profile from the radiosondes is shown by the contour lines. The temperature follows a complex structure during this period with two inversions, one below and one above the cloud. The depicted temperature structure likely differs slightly from the actual situation above Polarstern, which may have caused the misclassification. The distance the radiosonde drifted away from Polarstern may have caused small differences, e.g., in the temperature inversion heights. Additionally, the cloud phase determination from Cloudnet is based on the wet-bulb temperature. Inside a cloud, the measured temperature and the wet-bulb temperature do not differ. In regions where the relative humidity is below 100%, however, they are different. However, the presented temperature field allows the determination of the temperature at which the observed ice was formed. The formation of the ice crystals identified by the cloud radar likely happened at a temperature of -3°C or even higher. At this temperature oblate particles like dendrites and plates are known to form [Pruppacher and Klett, 1997]. Plate-like crystals, if horizontally aligned, are also known to produce very low LDR for a vertically pointing radar [Myagkov et al., 2016], as it was observed in this case.

A second transition of the cloud situation during the presented period is associated with an altocumulus layer which was located above the stratocumulus. Around 09:00 UTC this midlevel cloud layer with a cloud-top temperature of -2°C occurred at 1900 m height over Polarstern. The upper cloud was mainly observed by the cloud radar, as shown in Figure 4.2. The altocumulus is hardly visible in the lidar measurements because the lidar signal was mostly completely attenuated in the stratocumulus. Shading effects reduced the cloud-top radiative cooling of the cloud below, as already observed in Shupe et al. [2013], as this layer increased in geometrical and optical depth. The reduced cooling capacity of the stratocumulus cloud contributed to the temperature increase in the lower cloud layer which prevented further ice formation. This situation led to a collapse of the EDR in the lower layer at around 12:00 UTC [Figure 4.4 (d)] and finally to a dissipation of the cloud. The values for the EDR ε in the altocumulus were about the same order of magnitude as for the stratocumulus, indicating that the upper cloud was able to effectively cool to space.

The altocumulus formed a two-layer structure at 1500 m and 1200 m, respectively, from about 14:00 UTC on. The lower layer of the stratocumulus lost its turbulent moment due to the shading of the upper one and the cloud dissipated shortly after. The altocumulus was classified as pure ice cloud, probably because the lidar signal was already fully attenuated in the lower layer which impedes the classification as liquid water at an ambient temperature below 0°C . However, the rather warm cloud-top temperature of this cloud of roughly -1.5°C indicates that this cloud should be mixed-phase. At around 11:00 UTC, the temperature exceeded 0°C and hence the Cloudnet classification changed from an ice cloud to a liquid-water cloud. After persisting for about 4 hours with rather low EDR,

the stratocumulus started to dissipate at around 16:00 UTC. The subsequent cloud-free period offered the lidar the opportunity to observe the aerosol structure above Polarstern [Figure 4.5 (b)].

Aerosol case: 9 June 18:00 UTC – 10 June 2017 11:00 UTC, ice floe camp

One of the rare cloud-free events of PS106 occurred between 9 June 2017 18:00 UTC and 10 June 2017 11:00 UTC and Polly^{XT} observed aerosol layers in the free troposphere [Figure 4.5 (d)]. The respective radiosonde profiles for this period are shown in Figure 4.5 (a) – (c). A southern inflow of air masses above the boundary layer is identified for this period based on a trajectory analysis of twenty-seven 10-day HYSPLIT (Hybrid Single-Particle Lagrangian Integrated Trajectory model) back trajectories [Stein et al., 2015]. The trajectories at the 2000 m height level show that the respective layers were long-range-transported aerosol layers

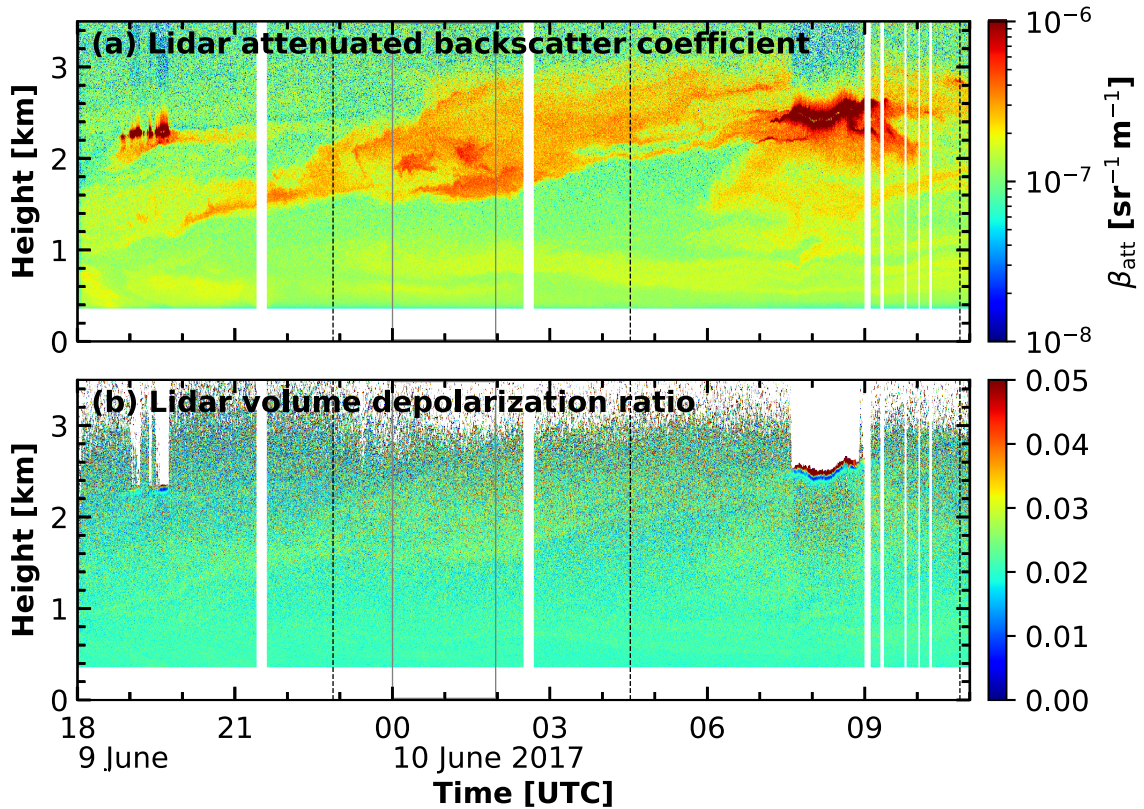


Figure 4.5: Measurements from Polly^{XT} between 9 June 2017 18:00 UTC – 10 June 2017 11:00 UTC. In (a) the 1064 nm attenuated backscatter coefficient and in (b) the 532 nm volume depolarization are shown. The black dashed vertical lines mark the time of the radiosonde launches as shown in Figure 4.6. The solid vertical gray lines indicate the period used derive the profiles shown in Figure 4.8.

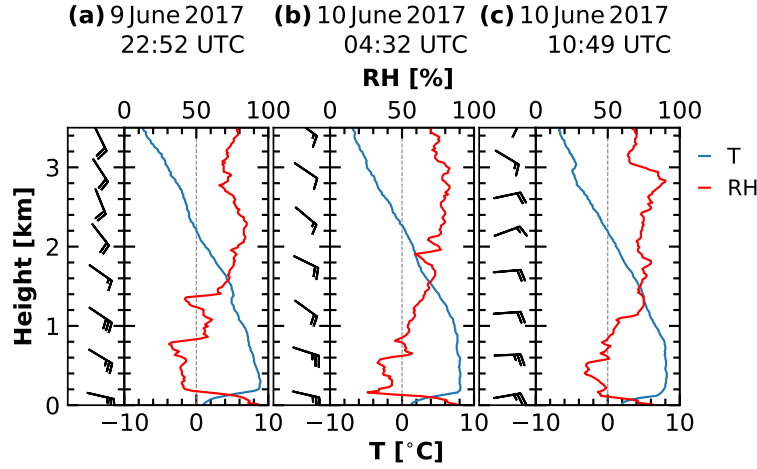


Figure 4.6: Same as Figure 4.3 but for 9 June 2017 18:00 UTC – 10 June 2017 11:00 UTC up to 3500 m height (no potential temperature is shown).

that passed over continental Europe (Figure 4.7) with a high chance of being within the planetary boundary layer at that time. Trajectories arriving below 2000 m height, indicate that pathways mainly crossed the North Sea and the Atlantic Ocean (not shown).

The 1064 nm lidar attenuated backscatter coefficient and the 532 nm volume depolarization ratio are shown in Figure 4.5 (d) and (e), respectively. These measurements reveal fuzzy layered aerosol structures. A shallow layer below 1000 m height was present almost during the entire period. Above 1000 m altitude an ascending layer structure with very low depolarization was observed by Polly^{XT}. The top of this layer reached up to 3000 m and the layer extended down by more than 1000 m at 01:00 UTC on 10 June 2017. After 06:00 UTC aerosol structures were visible in the entire column up to 3000 m height. At 07:00 UTC on 10 June 2017, a liquid-water cloud formed inside the observed aerosol structure at 2500 m height. Another aerosol layer was present between 19:00 and 21:00 UTC on 9 June 2017 above 2000 m height. Until 20:00 UTC some liquid-water cloud patches were observed at the top of this layer.

In Figure 4.8, a detailed analysis of the aerosol optical properties derived from the lidar measurements from the time period of 00:00 – 02:20 UTC is presented. During this period, two layers were detected and are visible in the profiles of the particle backscatter coefficient at all three wavelengths [Figure 4.8 (a)]. The rather strong wavelength dependence of the particle backscatter coefficient, as shown by the high Ångström exponents [Figure 4.8 (b)] in both layers, indicate the presence of small aerosol particles. The low linear particle depolarization values shown in Figure 4.8 (c) below 3% are typical for spherical parties. A back-trajectory analysis, the low values for the Ångström exponent and the linear particle depolarization indicate that air masses transporting polluted aerosol from continental Europe are most probably a source for the upper aerosol layer. The lower aerosol layer is likely a

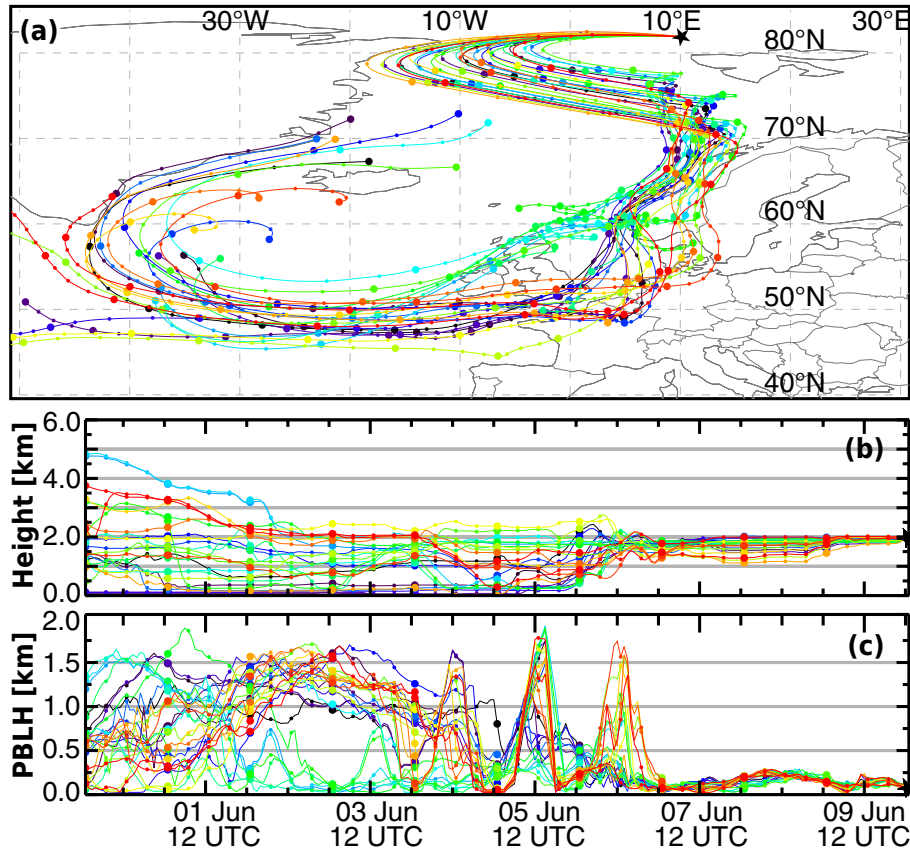


Figure 4.7: (a): Ensemble of twenty-seven 10-day back trajectories arriving at the position of Polarstern at 01 UTC on 10 June 2017 at 2000m height. (b) shows the height of the trajectory and (c) the planetary boundary layer height (PBLH) along the trajectory.

mixture of down-mixed continental and upward-mixed marine aerosol. Unfortunately, the calculation of the extinction coefficient as explained in Section 3.1.1, which would allow an even more detailed analysis of the aerosol layer and an independent retrieval of the lidar ratio, is not possible under the polar day conditions during PS106.

An estimation of the CCNC from the aerosol optical properties retrieved by Polly^{XT} was done for all three combinations of conversion factors mentioned in Section 3.4.3. The necessary extinction exponent to derive the CCNC was calculated by applying a typical lidar ratio for continental aerosol of 50 sr [Müller et al., 2007] to the particle backscatter coefficient. To illustrate the results of the retrieved CCNC and possible error margins, all three combinations of conversion parameters presented in Section 3.4.3 are shown in Figure 4.8 (d). The first combination ($C_{CCN1} = 18.6 \text{ cm}^{-3}$, $d_{CCN1} = 0.83$) is depicted by the dotted line. The second combination ($C_{CCN2} = 10 \text{ cm}^{-3}$, $d_{CCN2} = 0.9$) is presented by the solid line and the third combination ($C_{CCN3} = 3.0 \text{ cm}^{-3}$, $d_{CCN3} = 1$) is shown by the dashed line. The respective maximum values of the CCNC in the upper aerosol layer was

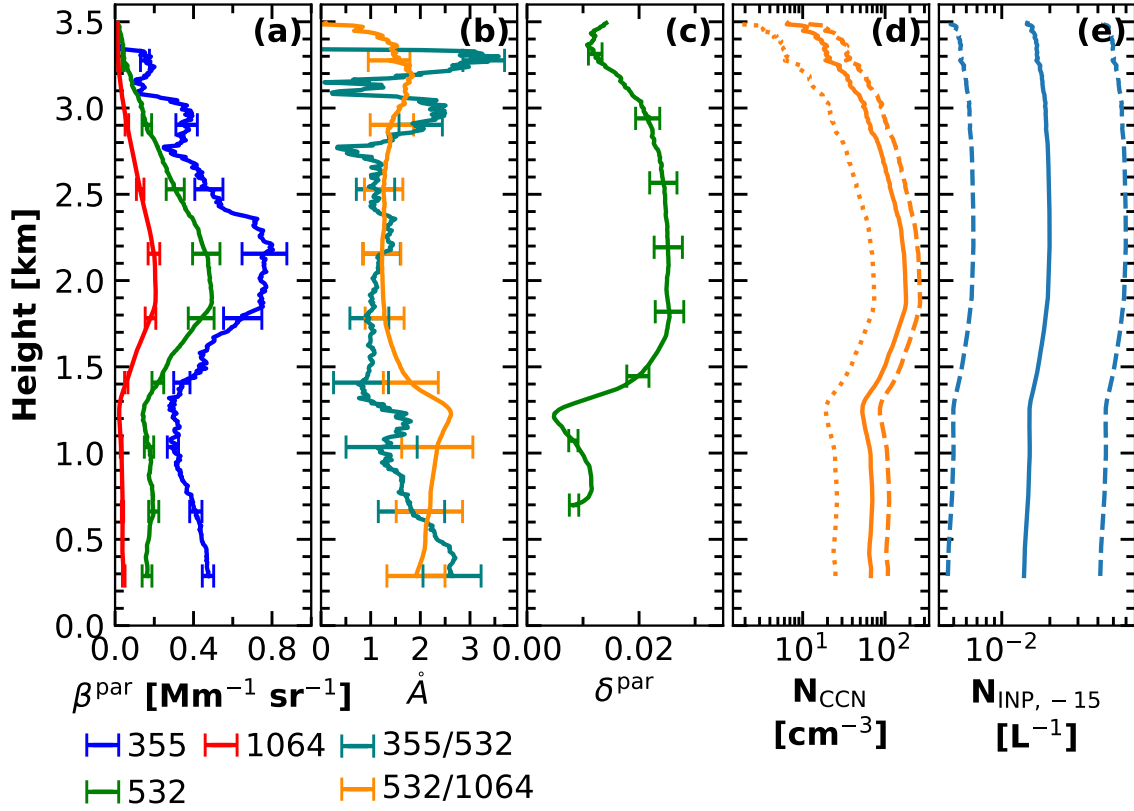


Figure 4.8: Averaged aerosol optical properties for the time period from 00:00 – 02:20 UTC on 10 June 2017 up to 3500 m height. (a) particle backscatter coefficient for three wavelengths of 355 nm (blue), 532 nm (green) and 1064 nm (red). (b) Backscatter-related Ångström exponent for 355 nm to 532 nm (cyan) and for 532 nm to 1064 nm (orange). (c) 532 nm particle depolarization ratio. In (d) the retrieved CCN number concentration for the three parameter combinations presented in Section 3.4.3 are shown. In (e) the INP number concentration for $T = -15^\circ\text{C}$ derived from the 532 nm particle backscatter coefficient profile is shown.

found as $\bar{n}_{\text{CCN},1} = 75 \text{ cm}^{-3}$ (parameter combination 1), $\bar{n}_{\text{CCN},2} = 180 \text{ cm}^{-3}$ (parameter combination 2), and $\bar{n}_{\text{CCN},3} = 265 \text{ cm}^{-3}$ (parameter combination 3). For the lower aerosol layer the maximum values were $\bar{n}_{\text{CCN},1} = 25 \text{ cm}^{-3}$, $\bar{n}_{\text{CCN},2} = 70 \text{ cm}^{-3}$, and $\bar{n}_{\text{CCN},3} = 110 \text{ cm}^{-3}$.

The cloud droplet number concentration of the observed liquid-water cloud on 10 June 2017 around 8 UTC was estimated based on the effective radius of the liquid-water droplets $r_{\text{eff,liq}}$ and the LWC from Cloudnet. Cloudnet provides $r_{\text{eff,liq}}$ and LWC based on the approach published by Frisch et al. [2002]. At the base of the liquid-water cloud $r_{\text{eff,liq}}$ was around $3.5 \mu\text{m}$ and at cloud top around $4.5 \mu\text{m}$. The respective LWC was $2 \cdot 10^{-5} \text{ kg m}^{-3}$ at cloud base and $9 \cdot 10^{-5} \text{ kg m}^{-3}$ at cloud top. To derive the liquid-water mass per m^3 from $r_{\text{eff,liq}}$ the relationship between the effective radius and the mean radius $r_{\text{eff}} = r_{\text{mean}} \cdot \exp(5/2\sigma_x^2)$

was used. Applying a lognormal size distribution (with $\sigma_x = 0.35$) for different droplet number concentrations and using the density of water, the theoretical liquid-water content was calculated. The best agreement between the calculated and the Cloudnet LWC was found for a droplet number concentration of 200 cm^{-3} .

In addition, the INPC was calculated for a fixed temperature of -15°C . The results are shown in Figure 4.8 (e). The INPC_{-15} for the lower layer was found to be around 0.6 L^{-1} for this temperature. In the upper layer, INPC_{-15} went up to values slightly above 1 L^{-1} . These calculations have an error of a factor of 3 [dashed lines in Figure 4.8 (e)] but provide a guideline about the conditions of the cloud-relevant aerosol properties.

Low-level stratus and cirrus: 7 June 2017 21:00 UTC – 8 June 09:00 UTC

In Figure 4.9, the OCEANET-Atmosphere measurements for the period from 7 June 2017 21:00 UTC – 8 June 2017 09:00 UTC are presented up to 1200 m height. This section is selected to illustrate the importance of the LLS retrieval presented in Section 3.4.3. In the radar observations in Figure 4.9 (a) no clouds are visible on 8 June 2017 between 00:00 – 01:00 UTC and after 5 UTC. However, the increased attenuated backscatter values in Figure 4.9 (d) show that almost continuously low-level clouds were present above Polarstern during the presented period. Those clouds which were completely below the lowest radar range gate at 165 m, were not considered in the standard Cloudnet classification [Griesche et al., 2020a].

The low-level cloud caused a nearly complete lidar signal attenuation until 23:30 UTC due to its high optical thickness. Backscattered lidar signals from aerosol particles above the cloud were detected only occasionally. The LWP varied between 0 g m^{-2} and 100 g m^{-2} during this period. The lower values of LWP were associated with periods when the lidar was able to detect signals from above the cloud. Higher LWP values were observed for moments when the lidar signal was attenuated already close to the cloud base. Between 7 June 2017 23:30 UTC and 8 June 2017 05:00 UTC almost no LWP was measured by HATPRO. Around 05:30 UTC the LWP increased again to values of up to 10 g m^{-2} , which in turn caused significant attenuation of the lidar signal by the low-level clouds.

Nearly during the whole period, enhanced values of the volume depolarization ratio were detected below the cloud, which exhibits the presence of ice particles. The temperature field in Figure 4.9 (a) shows that the temperature where these ice crystals formed was above -10°C . The quasi-constant potential temperature profiles below cloud base (Figure 4.10) indicates that the cloud layer is thermodynamically coupled to the surface. Above the cloud layer, a shallow humidity inversion can be observed in the radiosonde profiles (Figure 4.10). Such events have been already frequently observed in the Arctic [e.g., Egerer et al., 2021].

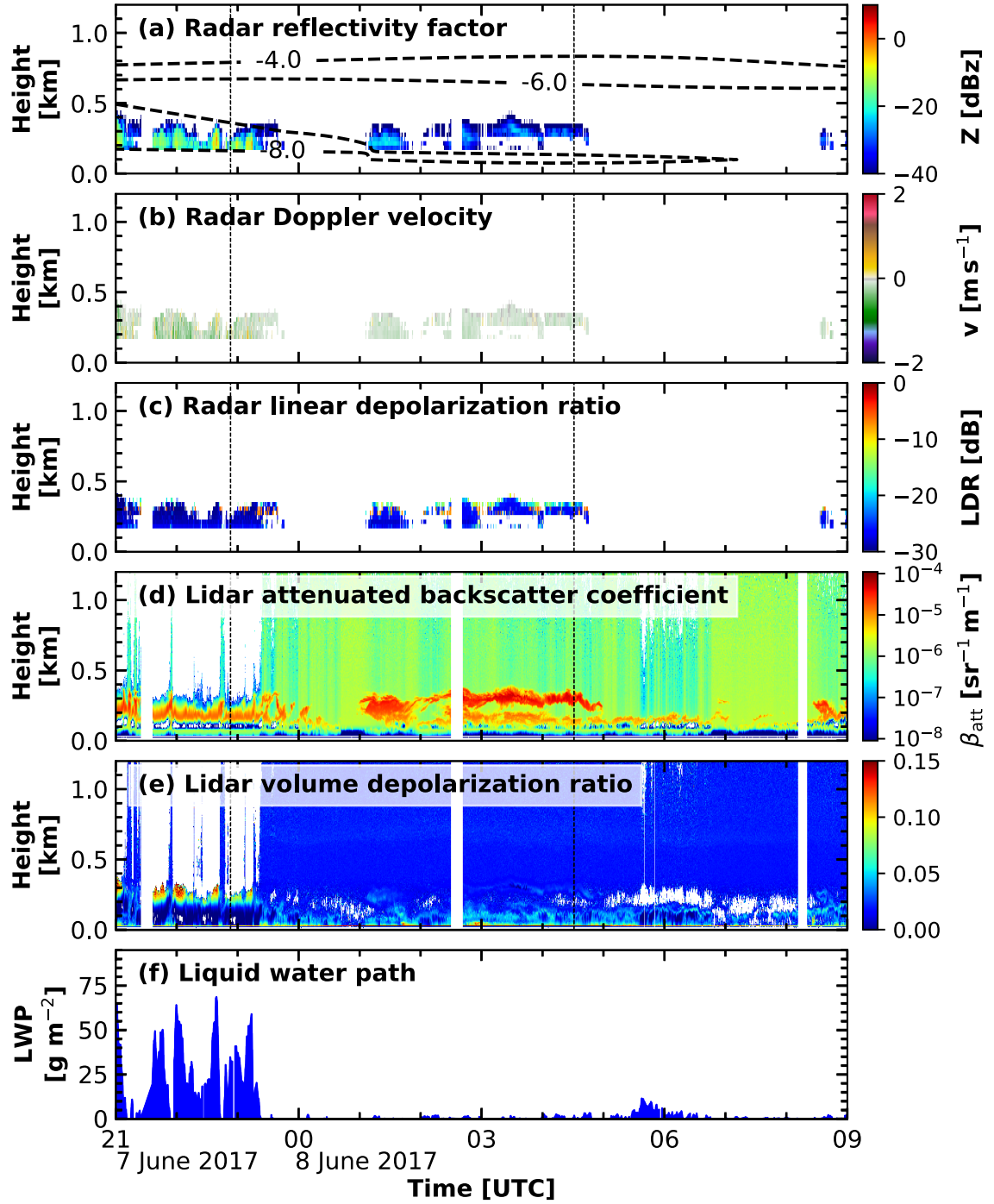


Figure 4.9: Same as Figure 4.2 but for 7 June 2017 21:00 UTC – 8 June 2017 09:00 UTC up to 1200 m height. The contour lines in panel (a) show additionally the temperature interpolated from the radiosonde profiles shown in Figure 4.10 (note: the last launch shown in Figure 4.10 was after the presented time period).

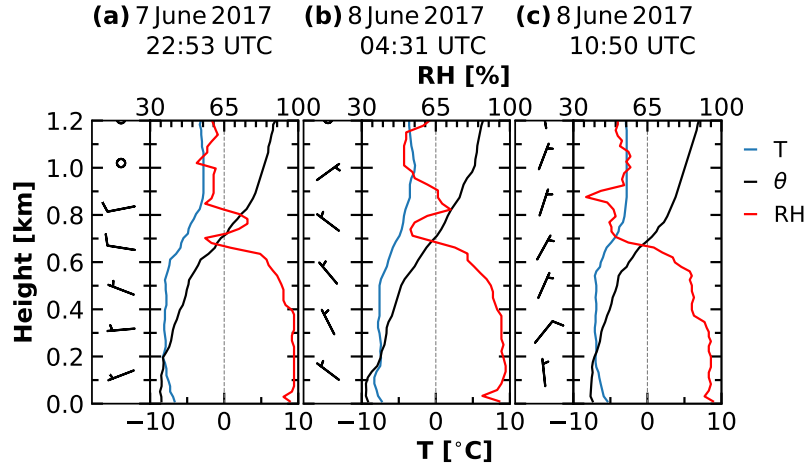


Figure 4.10: Same as Figure 4.3 but for 7 June 2017 21:00 UTC – 8 June 2017 09:00 UTC up to 1200 m height.

The derived low-level stratus classification mask combined with a simplified Cloudnet target classification mask (above 165 m height) for this period is shown in Figure 4.11. Brown areas depict detected low-level clouds. Blue and green data points indicate clear sky and aerosol, respectively. The lowest Cloudnet level is apparent by the onset of the aerosol indication at 165 m height. Below this height, cloud evidence results only from the low-level stratus classification based on the SNR of the Polly^{XT} 532 nm near-range channel.

In Figure 4.12 ice cloud related products derived by Cloudnet are shown for the same

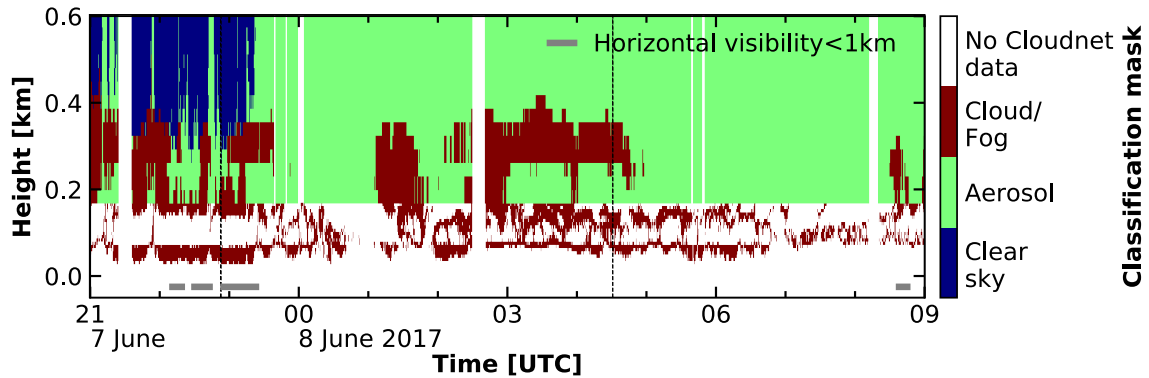


Figure 4.11: Low-level cloud mask for 7 June 2017 21:00 UTC – 8 June 2017 09:00 UTC derived from the combination of Polly^{XT} and Cloudnet data. Below 165 m height, brown colors indicate when LLS was detected. Above 165 m height, a simplified version of the Cloudnet target classification mask is shown. Each pixel classified by Cloudnet as a cloud (ice, liquid, or mixed-phase) is masked in brown. Blue depicts clear sky, and green depicts aerosol. The gray line at the bottom indicates periods when fog was detected by the horizontal visibility sensor aboard Polarstern.

period but for cirrus clouds being present well above the LLS layer. The products demonstrate the approach for the retrieval of the ice effective radius introduced in Section 3.4.3. In panel (a) the Cloudnet IWC is depicted. Panel (b) shows the ice effective radius together with the respective error in panel (c). In panel (d) the IWP is depicted. The IWP was derived by the column integral of the IWC for each profile. Cirrus clouds were observed around

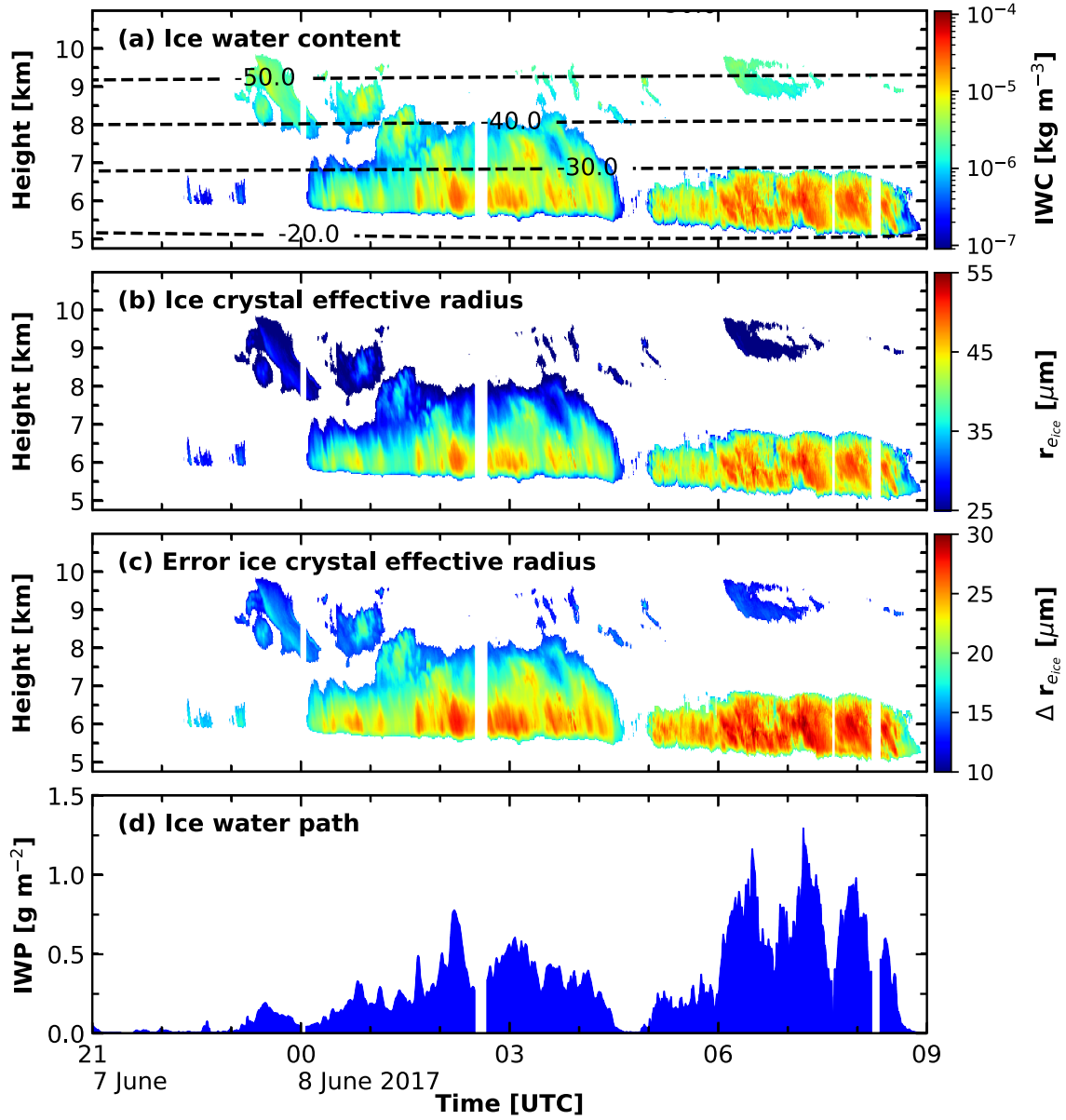


Figure 4.12: Ice cloud related Cloudnet products for 7 June 2017 21:00 UTC to 8 June 2017 09:00 UTC: (a) ice water content, (b) ice crystal effective radius, (c) uncertainty in the retrieved ice crystal effective radius as derived from error propagation, and (d) ice water path.

22:30 UTC above 6000 m height. These cirrus clouds transformed into a cirrostratus layer at 00:00 UTC, which was present between 6000 and 8000 m height. The temperature contour lines depicted in Figure 4.12 (a) show that some of the cirrus formed in the homogeneous temperature regime below -38°C while the cirrostratus formed in the heterogeneous ice formation region above -38°C . The IWC of the cirrostratus was in a range from $10^{-4} \text{ kg m}^{-3}$ to $10^{-6} \text{ kg m}^{-3}$ with lowest values at cloud top and highest values at cloud base. The clouds, which were formed in the temperature regime of homogeneous ice formation had rather low ice crystal effective radii, around $25 - 35 \mu\text{m}$. The ice crystals formed via heterogeneous ice formation had larger effective radii of up to $55 \mu\text{m}$.

4.3 Cloud and aerosol statistics during PS106

Based on the retrieved Cloudnet products from OCEANET-Atmosphere a statistical overview of the cloud and aerosol conditions during PS106 was obtained. In Figure 4.13 (a), daily statistics of the vertical distribution of low-level stratus are shown. In addition, the frequency of occurrence of this cloud type for every day is illustrated in Figure 4.13 (b). On 30 out of 51 days more than 50 % of the time LLS clouds were observed and on average during 49.35 % of the time. A statistic of the cloud type occurrence during PS106 is shown in Figure 4.13 (c). The daily frequency of occurrence as well as the total distribution for the complete campaign of low-level stratus clouds, liquid-water clouds, ice clouds, mixed-phase clouds, multi-layer clouds, and cloud-free situations are shown. In addition, an analysis of the co-occurrence of low-level stratus and other cloud types was performed and is shown in the rightmost column of Figure 4.13 (c). The rate of coexistence of the respective cloud type together with low-level stratus is indicated by a slightly varied color code.

In total, during 11 % of the time, cloud-free conditions were detected by Cloudnet during PS106. The two most prominent cloud types were multi-layer clouds and single-layer mixed-phase clouds with an occurrence frequency of 38.5 % and 36 % of the observational time, respectively. Single ice clouds were present for about 8 % and single liquid-water clouds for about 4.5 % of the time, respectively. Single events of the new Cloudnet class low-level stratus cloud were detected during 2.5 % of the time during the 2-month campaign. In addition, 27 % of the observed single liquid-water clouds and 48 % of the single ice clouds occurred simultaneously with low-level stratus (below 165 m height). Single mixed-phase clouds and multi-layer clouds were detected together with low-level stratus clouds during 24 % and 27 % of their respective observational time.

The average aerosol optical properties for the PS106 cruise derived by lidar measurements are shown in Figure 4.14 for those periods where the lidar was able to probe the free troposphere. The mean particle backscatter coefficient β^{par} is depicted in Figure 4.14 as a function of height (a) and as a function of temperature (b). A rather strong decrease in

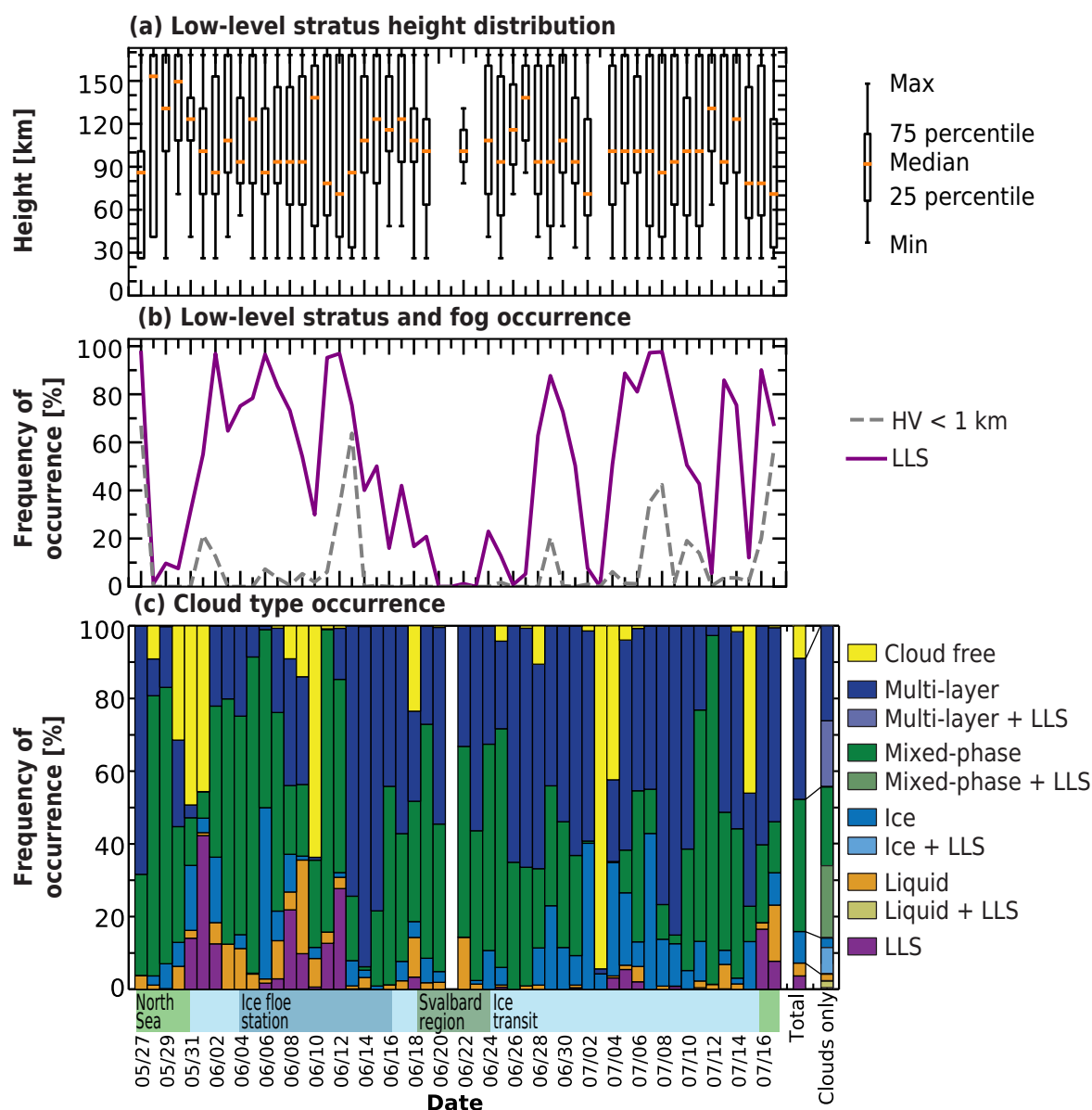


Figure 4.13: (a) Daily height distribution of the detected low-level stratus during PS106 up to 165 m. (b) daily fraction of low-level stratus occurrence derived by Polly^{XT} measurements (purple) in comparison to horizontal visibility (HV) below 1000 m distance (gray). (c) cloud type statistics including low-level stratus (LLS) clouds during PS106, determined by Cloudnet. Each column except the last two represents a day of the campaign. The second last column represents the total distribution of the different cloud types. The cloud occurrence for the complete cruise is distinguished in the last column between the respective cloud type without low-level stratus detected (same color as in the other columns) and with an additional low-level stratus detected below (slightly varied color). At the bottom, a rough localization of Polarstern is annotated — green: North Sea; light blue: ice transit; dark blue: ice floe camp; dark green: Svalbard region.

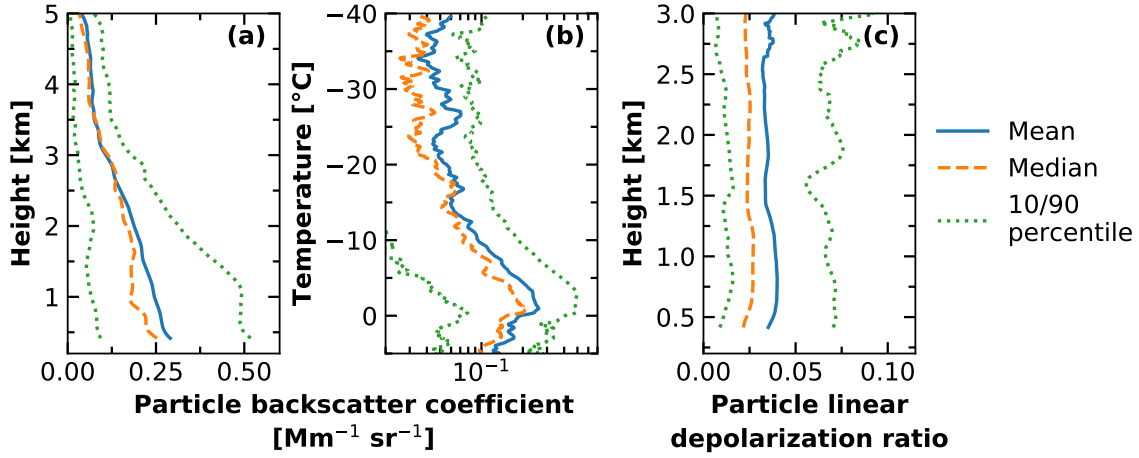


Figure 4.14: Profile of the average backscatter coefficient at 532 nm during PS106 as a function of height up to 5000 m (a) and as a function of temperature between -40°C and $+5^{\circ}\text{C}$ (b). Panel (c) shows the averaged particle linear depolarization ratio profile at 532 nm.

β^{par} can be seen above 1500 m height or -5°C , reaching a value below $0.1 \text{ Mm}^{-1} \text{sr}^{-1}$ at an altitude of 3000 m. Hence, the particle linear depolarization ratio δ^{par} in Figure 4.14 (c) is only depicted up to 3000 m. Above this altitude, the aerosol concentration was too low for a trustworthy determination of δ^{par} . The low depolarization values (mean $\delta^{\text{par}} < 0.05$) indicate that the aerosol population is dominated by spherical particles, such as aged anthropogenic aerosol from long-range transport. The presence of non-spherical aerosol, such as dust, volcanic ash or dried sea salt during PS106 can be ruled out, based on the δ^{par} observations.

In panel (a) Figure 4.15 the mean profile of the CCNC and in panel (b) the mean INPC profiles for PS106 up to 5000 m height derived as described in Section 3.4.3 are shown. The CCNC was on average around 10^2 CCN cm^{-1} below 500 m and decreased up to a height of 5000 m by a factor of 10. The average INPC is rather constant with height between the surface and 5000 m height, with around $0.7 \text{ INP}_{-15} \text{ L}^{-1}$.

4.4 Discussion of the observational data sets

An overview of the data set presented in Chapter 3.2 was demonstrated using three case studies and statistical analysis of the cloud and aerosol occurrence during the PS106 cruise. The first case study revealed limitations of the Cloudnet classification approach. The fast transition from a mixed-phase to a liquid-water cloud in the case presented in Figure 4.4 at around 6:45 UTC seems unlikely. More in agreement with the cloud radar and lidar observations would be a continuity of the mixed-phase cloud for about 4 more hours. The abrupt classified phase change was due to the temperature field used in Cloudnet, which was probably somewhat different from the actual temperature in the troposphere above

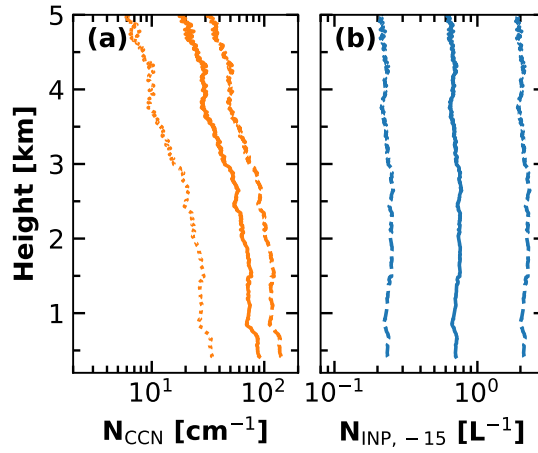


Figure 4.15: Profile of the average CCNC during PS106 up to 5000 m height (a) for all three combinations presented in Section 3.4.3 (dashed: combination 1, solid: combination 2, dotted: combination 3) for a supersaturation of 0.15 %. In (b) the average INPC profile for PS106 derived for a fixed temperature of -15°C is shown. The dashed lines in (b) show the error margins of 300 %.

Polarstern. Additionally, the missing LWC values in Figure 4.4 (c) between 11 – 13 UTC where Cloudnet had identified liquid-water [drizzle or rain in Figure 4.4 (a)], are due to the classified melting layer in the altocumulus. Under these conditions, the reliable retrieval of the LWC is not possible by Cloudnet.

The second case study showed the application of the data set towards liquid-water cloud closure studies. The cloud droplet number concentration was derived for the observed cloud, based on the theoretical relationship between effective radius and LWP. The observed combination of the cloud droplet effective radius and the LWP coincide with values reported from Shupe et al. [2005]. The calculated droplet number concentration matched well with the CCNC derived from the lidar profiles. Based on lidar observations also a direct retrieval of the cloud droplet number concentration profile would be possible [Jimenez et al., 2020]. This method uses the dual-field-of-view technique. However, the required hardware update was installed to the OCEANET-Atmosphere Polly^{XT} after the PS106 cruise.

The INPC derived for the aerosol case study is presented for a temperature of -15°C although the ambient temperature was much higher. However, the applied parameterization was developed for temperatures below -15°C [DeMott et al., 2010]. Hence, the illustrated case is only an example of the potential of the Polly^{XT} data set. A coherent retrieval of the INPC for the ambient temperature offers the opportunity for more in-depth aerosol-cloud-interaction studies. This approach in combination with a recently published lidar-radar based retrieval for ice crystal number concentrations [Bühl et al., 2019] applied, e.g., to the MOSAiC data set offers the possibility to perform cloud closure studies.

Based on published retrievals of visible extinction coefficient and ice water content, a new approach to derive the effective radius of the ice crystals was introduced in Section 3.4.3 and its application was presented in the third case study. The retrievals of the ice and liquid hydrometeor size as proposed in this thesis may be influenced by each other during this period. Both retrievals are based on the same quantity, the radar reflectivity, which is characterized by the largest peak in the Doppler spectrum. A peak separation of the Doppler spectrum as it is proposed, e.g., by Shupe et al. [2004], Kalesse et al. [2016b], or Radenz et al. [2019] would be necessary to tackle this issue. Such an approach would offer the opportunity to calculate the effective radius of the different hydrometeors species based on their particular reflectivity but is beyond the scope of this thesis. The size of the ice crystals is of significant importance to derive the surface cloud forcing [Shupe and Intrieri, 2004]. The size of the ice crystals in cirrus can even impact the sign of the radiative forcing of the cirrus clouds [Zhang et al., 1999]. While the net radiative effect of cirrus clouds usually is positive, it can change to negative for a large number ($> 10^7 \text{ m}^{-3}$) of small (mean maximum dimension $< 30 \mu\text{m}$) particles. In the Arctic, however, low-level clouds are most influential on the radiation budget at the surface [Shupe and Intrieri, 2004]. The uncertainties associated with the ice crystal effective radii, estimated by error propagation, are presented in Figure 4.12 (d). On average the uncertainty is about 50 % of the size of the radii themselves which reflects the strong influence of uncertainties in the underlying observational data on the retrieval. Previous published methods to derive the ice crystal effective radius, as the lidar-radar synergistic approach DARDAR [Cazenave et al., 2019] were not applicable due to the strong lidar attenuation in the low-level clouds. Given the challenges in deriving the effective radius of ice crystals continuously on the one hand and the necessity of having such values, e.g., for radiative transfer calculations, on the other hand, the error range is still acceptable.

In Figure 4.16, the histogram of the effective radius for all ice clouds observed during PS106 is shown. Values range from 20 to $60 \mu\text{m}$, with a peak at around $50 \mu\text{m}$. The retrieved range is consistent with previous studies of ice effective radius in Arctic clouds. Shupe et al. [2006] reported for mixed-phase clouds observed by ground-base remote sensing during the SHEBA campaign slightly higher values, with an average ice crystal diameter of $93 \mu\text{m}$ (which corresponds to an effective radius of $63 \mu\text{m}$, assuming a width of the log-normal droplet size distribution of 0.35). Also based on remote sensing Blanchard et al. [2017] retrieved for thin Arctic clouds ice crystal effective diameter between $40 - 158 \mu\text{m}$.

In addition, the third case study highlighted also the relevance of the lowest detection limit in terms of height range of remote-sensing instruments on the representativity of Arctic-cloud statistics. The standard Cloudnet algorithm is configured to have its lowest range gate at the lowest detection altitude of the cloud radar, which was 165 m above the ocean surface for PS106. Lower-level cloud layers were thus not identifiable within Cloudnet. As a contribution to Cloudnet, lower cloud structures were identified using the SNR measured

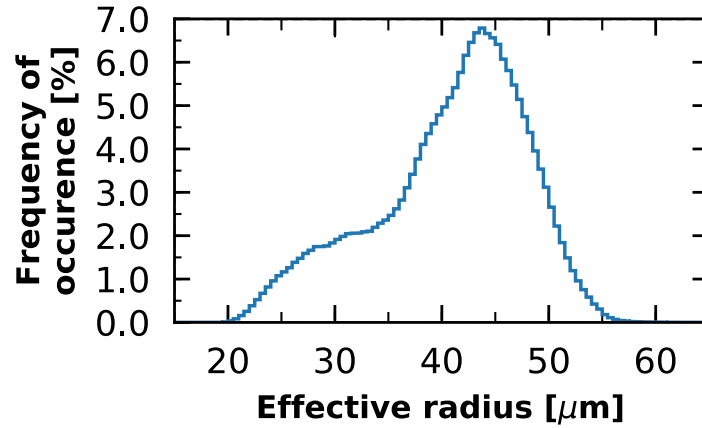


Figure 4.16: PDF of the ice particle effective radius for all ice clouds during PS106.

by the lidar Polly^{XT} for the first time [Griesche et al., 2020a]. This ability has been used to derive the occurrence of low-level stratus clouds even below the first Cloudnet range gate. Sotiropoulou et al. [2014] used a combination of cloud radar and ceilometer measurements to study stratiform Arctic clouds and found that the most stable, surface-coupled clouds have a cloud base below 200 m. Yet, so far such clouds have not been considered in many Arctic cloud climatologies derived by remote-sensing instruments. Liu et al. [2012], for example, examined the satellite-based Cloudsat data set. In this study, the authors defined clouds between 0 – 2000 m as low-level clouds. The authors reported 960 m above the ground as the height where surface contamination effects on Cloudsat become insignificant and used a vertical resolution of 240 m. Shupe [2011] summarized cloud statistics from several multiyear data sets derived from ground-based remote sensing for different sites in the Arctic. The author specified a height dependence of cloud occurrence down to 300 m by using a combination of lidar and radar. Below 300 m, however, the author provided information about cloud occurrence but without any further specification of the cloud base. Even airborne remote-sensing instruments suffer from the strong ground clutter and thus struggle to deliver information about cloud occurrence below 150 m height above the surface [Mech et al., 2019]. The autonomous buoys of the Ice Atmosphere Arctic Ocean Observing System (IAOOS) network equipped with a microlidar observed clouds in 2014 and 2015 in the Arctic with a base height below 500 m during 60 % of their observational time [Mariage et al., 2017].

The presented study shows that a higher vertical resolution and a reliable signal from very low altitudes are required to characterize the lowest-level cloud layer. These LLS occur approximately between 50 m and 165 m above ground and were observed during 50 % of the observational time of PS106. Such clouds stay undetected for ground-based in-situ sensors (because they are too high) as well as for most automatized ground-based remote sensing instruments (because they are too low). The highest frequency of occurrence of LLS was observed while Polarstern was surrounded by sea ice [see Figure 4.13 (b)]. Rather low values

occurred while Polarstern was in the vicinity of Svalbard. Sato et al. [2012] reported similar results for a comparison between measurements taken during SHEBA and research cruises performed with the Japanese RV Mirai. They found low-level clouds with a cloud base height below 500 m less often in ice-free areas, compared to ice-covered regions. To assess the presented retrieval of the low-level clouds, the frequency of occurrence of vertical visibility below 1000 m, a measure of fog, is plotted in comparison (gray, dashed line in Figure 4.13). Often fog was not detected while LLS occurred. Thus, the LLS occurred above the local surface layer and their appearance would be undetected by an in-situ sensor. So far these clouds have been not well investigated, often due to instrument limitations. Studies based on cloud radar observations often do not consider the lowest heights. This is a fact also highlighted by Vüllers et al. [2021]. The authors analyzed the AO2018 cruise performed with the Swedish icebreaker Oden in the late Arctic summer 2018. Utilizing a horizontal visibility sensor, they observed fog layers during 21 % of the time. The authors reported in their study, that 49 % of the fog occasions were too shallow to be detected by the cloud radar. In addition, the authors used the scanning capabilities of the operated cloud radar to assess the fog depth in the 500 m of the troposphere. The most frequent observed fog depth was 120 to 150 m, i.e., below the lowest cloud radar range gate. This shows, that the introduced approach in this study is well suited to detect these very shallow fog or cloud layers. The introduced bias might be less relevant for Arctic land-based observatories because the fraction of low-level clouds to total cloud cover is higher over the Arctic Ocean compared to over land [Liu et al., 2012]. The effect of LLS on radiative transfer simulation is further examined in Chapter 6.

The observed mean cloud occurrence shown in Figure 4.13 agrees with previous findings. Shupe et al. [2011], for example, found for each of the analyzed sites (Atkasuk, Eureka, Ny-Ålesund, SHEBA, Summit, and Utqiagvik) an annual cloud cover maximum during late summer. The mean cloud fraction at the sites for June and July was between 60 – 90 % in their study. The mixed-phase fraction is in agreement with the mixed-phase fraction for June and July reported by Shupe [2011] for Eureka, SHEBA and Utqiagvik. The pure ice cloud fraction is lower, as in Shupe [2011]. However, the multilayer clouds fraction identified in this thesis likely includes a considerable fraction of pure ice clouds. Nomokonova et al. [2019] provided a statistical analysis of the cloud occurrence over Ny-Ålesund, Svalbard, for the period between June 2016 and July 2017, similar to the one presented in this thesis. In contrast to their study a higher frequency of single-layer mixed-phase clouds at the expense of cloud-free and single-layer liquid-water clouds when comparing the period of PS106 was found. This may be caused by a difference in turbulence as well as a change in the cloud microphysics at locations surrounded by sea ice or open ocean [Young et al., 2016].

In addition to the cloud statistics during PS106, the average aerosol distribution was examined based on the Polly^{XT} measurements. The mean aerosol distribution derived from the average attenuated backscatter profile during PS106 followed a pattern already frequently observed in the Arctic [e.g., Rader et al., 2021; Shibata et al., 2018]. The highest

concentrations were observed in the lowest 1000 m altitude and a continuous decrease with height. It was somewhat lower than what was observed during the same time at Ny-Ålesund [Shibata et al., 2018], which is not surprising if taken into account the higher latitude of PS106 and hence greater distance to most aerosol sources. The low depolarization ratio of below 5 % on average is typical for the aerosol composition observed in previous studies in the Arctic free troposphere [e.g, Shibata et al., 2018; Willis et al., 2018] and suggests that mainly long-range transported aged anthropogenic pollution from continental areas was observed. The 90th percentile of the mean attenuated backscatter coefficient shown in Figure 4.14 (a) shows little variations with height below 1000 m height and a strong decrease above. It thus can be followed that while Polly^{XT} observed the highest aerosol loading during PS106 the lowest 1000 m were well mixed.

The retrieved mean CCNC was around 100 CCN cm^{-3} [Figure 4.15 (a)] and hence is on the upper end for typical concentration reported for the High Arctic. Mauritsen et al. [2011] reported CCNC for example for ASCOS and three other campaigns conducted in the Arctic between 1996 and 2001 measured at the surface for supersaturations between 0.1 % and 0.8 % (for the retrieval applied in this thesis a supersaturation of 0.15 % was assumed). The respective number concentrations in their study were mostly between 10 and 100 cm^{-3} and on average between $15 - 50 \text{ cm}^{-3}$. A higher number of CCN can influence the cloud droplet number concentration and hence modulate the cloud radiative effect via the Twomey effect.

This chapter has demonstrated the capabilities of the presented data set to study the spatiotemporal aerosol and cloud occurrence and their interaction. Different cases have been shown where ice formation was observed during PS106 at temperatures above -10°C . This is a temperature regime for which not many INP populations are known. Based on the OCEANET-Atmosphere observations the influence of the liquid-water layer base height and the cloud surface-coupling state on ice formation in mixed-phase clouds and the ice occurrence at these rather high temperatures can be investigated.

Chapter 5

Contrasting surface-coupling effects on heterogeneous ice formation

As specified in the introduction of this thesis, aerosol particles play a fundamental role in heterogeneous ice formation processes. Four major pathways for heterogeneous freezing mechanisms are discussed in the literature. These are namely immersion freezing (nucleation of a supercooled liquid-water droplet when reaching the activation temperature of an immersed INP), deposition freezing (water vapor deposits directly on an INP and forms the ice crystal), condensation freezing (water vapor condensates first on an INP and freezes during the condensation process), and contact freezing (a supercooled liquid-water droplet freezes due to the collision with an INP) [e.g., Hoose and Möhler, 2012]. Immersion freezing is assumed to be the most relevant process for ice formation in mixed-phase clouds.

Arctic clouds are frequently occurring either coupled to the surface or decoupled from it in the free troposphere. Thus, the corresponding aerosol particles acting as INP can be of different origins and therefore show different ice nucleating activity. Given these circumstances, it should be investigated if the characteristics of heterogeneous ice formation processes differ between surface-coupled and -decoupled clouds. The goal of this study was motivated by the need for accurate characterization of the near-surface cloud properties and the prevalent indications that the microphysical and dynamical structure of surface-coupled Arctic clouds differs from those of decoupled clouds [Qiu et al., 2015, 2018; Shupe et al., 2013]. The work is based on the introduced data set of remote-sensing instruments and atmospheric soundings from the Polarstern cruise PS106 (marginal sea ice zone between Greenland and Svalbard in May – July 2017). The data were collected in the framework of (AC)³ and the material presented in this Chapter is based on Griesche et al. [2021]. Of specific interest for the underlying study are the cloud Doppler radar Mira-35 and the multiwavelength Raman polarization lidar Polly^{XT}. Auxiliary data for the study were obtained from the regularly performed atmospheric soundings of type Vaisala RS92-SGP, which are available every sixth hour (UTC) of the day for the entire cruise. By splitting this data set into low- and high-altitude cloud layers as well as into surface-coupled and -decoupled clouds, a

separate investigation of cloud macro- and microphysical properties for the different cloud regimes was possible: free-tropospheric clouds, not depending on regional effects and local aerosol sources, and surface-coupled clouds, being linked to local phenomena and aerosol in the Arctic region.

5.1 Methodology

The set of instruments deployed for this study was used to obtain information about cloud vertical extent, atmospheric thermodynamic state, phase partitioning, and ice and liquid-water microphysical properties. The goal of this analysis was to investigate the phase partitioning of Arctic cloud systems with respect to their surface coupling state and to obtain similar statistics as presented before by, for example, Ansmann et al. [2009], Kanitz et al. [2011], and Seifert et al. [2010, 2015]. Kanitz et al. [2011] showed that the relationship of spatially and vertically distinct ice-containing cloud layers and cloud-top temperature varies strongly by region on Earth. For the presented study, however, the cloud classification procedures that were applied by Kanitz et al. [2011] or similar ones such as that of Seifert et al. [2010, 2015], were extended in such a way to account for the long-lasting nature of Arctic cloud systems. These persistent clouds frequently prevented the classification of distinct, vertically, and temporally separated cloud layers. Arctic clouds can be very persistent and occur over periods of many hours, sometimes even days. Since aerosol or temperature conditions might still change over this period the clouds were split into sections of 30 minutes intervals. The modified method for the data set of Arctic clouds is presented in the following.

5.1.1 Ice-containing cloud analysis

The applied procedure to identify and characterize individual clouds is illustrated in Figure 5.1. Initially, the data set is split into time intervals of 30 min. The subsequent analysis is based on the respective 30 min data portions of lidar-attenuated backscatter coefficient and volume depolarization ratio at 532 nm wavelength, of radar reflectivity factor Z_e and of the temporally closest radiosonde ascent.

The base of the liquid-water-dominated cloud layer (hereafter referred to as liquid-layer) was determined using the attenuated backscatter coefficient as observed with the 532 nm near-range channel of Polly^{XT}. Data from this channel were required to be able to determine the base of even the lowest clouds which can be as low as 50 m above the surface [Griesche et al., 2020a]. The minimum base height of each liquid-layer detected in a 30 min interval was identified using the attenuation approach. Each 7.5 m range gate of each 30 s lidar profile within the 30 min interval was checked for a decrease in the 532 nm attenuated backscatter coefficient by at least a factor of 10 within 250 m vertical distance. Such a signal drop could only have been caused by liquid-water-dominated clouds. The liquid-layer base of each 30 s lidar profile was then determined as the height

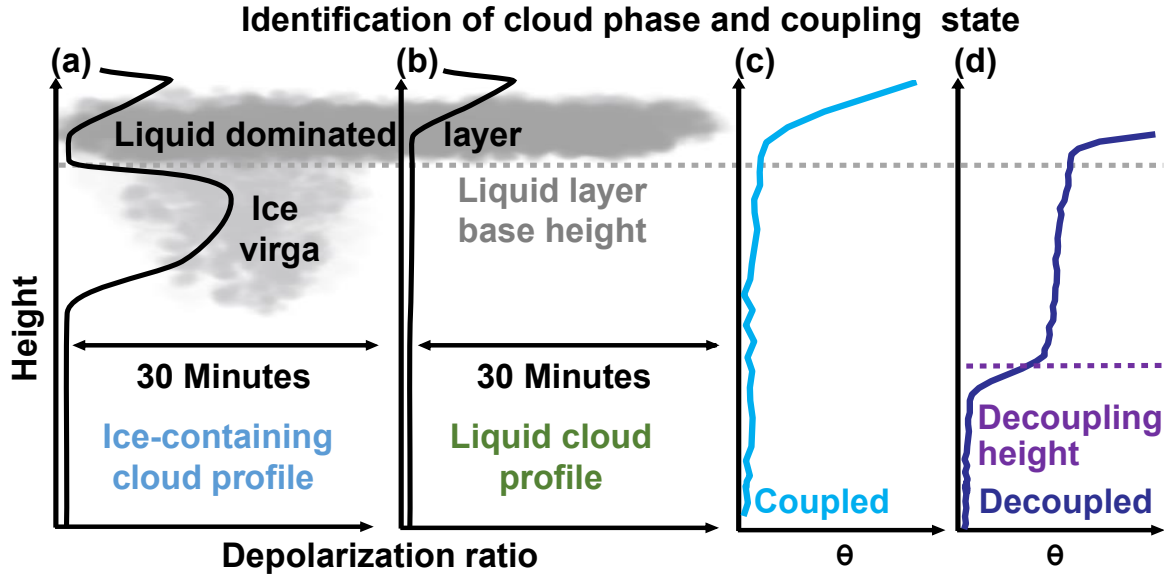


Figure 5.1: Sketch of the applied method to identify the cloud phase and coupling state: panel (a) and (b) show two example profiles of the lidar volume depolarization ratio. The profile in (a) is representative for an ice virga that is present below a liquid-layer. Due to the ice below the liquid-layer (high depolarization) the first 30 min are classified as an ice-containing (ice producing) cloud profile. Without ice falling out of the cloud only the liquid-layer is present [low depolarization below and at the base of the liquid-layer as shown in panel (b)]. In the presence of ice [panel (a)] the liquid-layer base height is characterized by a strong decrease in depolarization as the signal is now dominated by the return of the liquid-water droplets. Within the liquid-layer the depolarization increases again due to multiple scattering. In panels (c) and (d) two profiles of the potential temperature θ are depicted, with (c) illustrating a coupled cloud and (d) a decoupled cloud with respect to the surface. Additionally, in (d) the decoupling height is marked.

where the gradient for the first time reached 25 % of the maximum gradient within these 250 m. This approach is similar to the one used within Cloudnet [Illingworth et al., 2007]. But the applied approach omitted a distinct threshold of the attenuated backscatter coefficient, as overlap effects in the near-range prevented a thorough calibration of the latter at heights below 120 m [Engelmann et al., 2016]. The lowest liquid-layer base in the 30 min period was then assigned as the liquid-layer base height of the respective interval.

If applicable the cloud top height was determined using the cloud radar observations. The highest, consecutive cloud radar pixel connected temporally (within the 30 min interval) and spatially to the liquid-layer base was set as the cloud top (the minimum signal detection threshold level of the radar to detect a cloud pixel is 5 times the signal-to-noise ratio detected in the co-channel of the cloud radar). In the case of clouds below the lowest detection limit of the cloud radar, the cloud top was determined using lidar observations. Finally, the 30 min interval was screened for the presence of ice virga below the liquid-layer base utilizing the Polly^{XT} 532 nm volume depolarization ratio. Based on theoretical considerations (see

Appendix A), a general quantification of the lidar 532 nm volume depolarization ratio for ice detection was made with the conclusion that a volume depolarization ratio of > 0.03 can be interpreted as ice occurrence [note that the molecular depolarization for the Polly^{XT} 532 nm channel is < 0.01 , Engelmann et al., 2016]. Depolarization by aerosol particles was neglected as only signals from clouds or virgae were considered here. The respective cloud signals are generally orders of magnitudes larger than aerosol signatures in the Arctic.

In Figure 5.1 (a) a simplified profile of the depolarization ratio is shown in the case of a cloud above the lidar. Ice particles cause enhanced volume depolarization ratio due to their non-spherical crystal shape which is demonstrated in the first profile in the ice virga below the liquid-layer. The signal from the liquid-layer is dominated by the backscatter from the cloud droplets (even though a few ice crystals would be present), as the lidar is more sensitive to the larger total surface area of the more numerous cloud droplets. The liquid droplets produce a depolarization ratio of zero due to their spherical shape. Within the liquid-layer, however, the depolarization ratio increases monotonically with increasing penetration depth due to multiple scattering [Jimenez et al., 2020]. The following classification was applied in the framework of the inspection of each 30 min period: A depolarization ratio close to 0 accompanied by a strong lidar backscatter indicates the presence of spherical liquid-water droplets. If the depolarization ratio below the liquid-layer is high (because of ice crystals falling out of the cloud), the cloud is classified as an 'ice-containing' cloud (15 – 16 UTC and 17 – 18 UTC in Figure 5.2). Otherwise, it is classified as a 'liquid cloud' only (16 – 17 UTC and 18 – 21 UTC in Figure 5.2).

The minimum cloud temperature is an important parameter in the sense of this study, as INP efficiency increases by about an order of magnitude every 5 K [DeMott et al., 2015]. Hence, the probability of ice production is highest in the cloud where the temperature is lowest. Especially in the Arctic, where temperature inversions at the cloud top are frequent, special care must be taken in determining the actual cloud minimum temperature. Using the temperature at the identified cloud top height might produce a bias toward positive temperatures because the likelihood of selecting a temperature from within or above the temperature inversion is high when using the highest detected cloud pixel. The approach was thus to assign the minimum temperature between cloud base and top as the minimum cloud temperature.

Cloud layers, that might have been affected by hydrometeors falling from above (cloud seeding) were filtered from the data set. Precipitation from the upper layer may have acted as ice nuclei in the lower one [Vassel et al., 2019]. The analyzed data set was corrected for these possible seeding effects based on cloud radar observations which can detect clouds up to the tropopause depending on their size and the concurrent atmospheric attenuation. Since the targeted clouds contained rather low amounts of liquid-water, the attributed attenuation effects on the cloud radar can likely be neglected. Cloud layers that were vertically closer

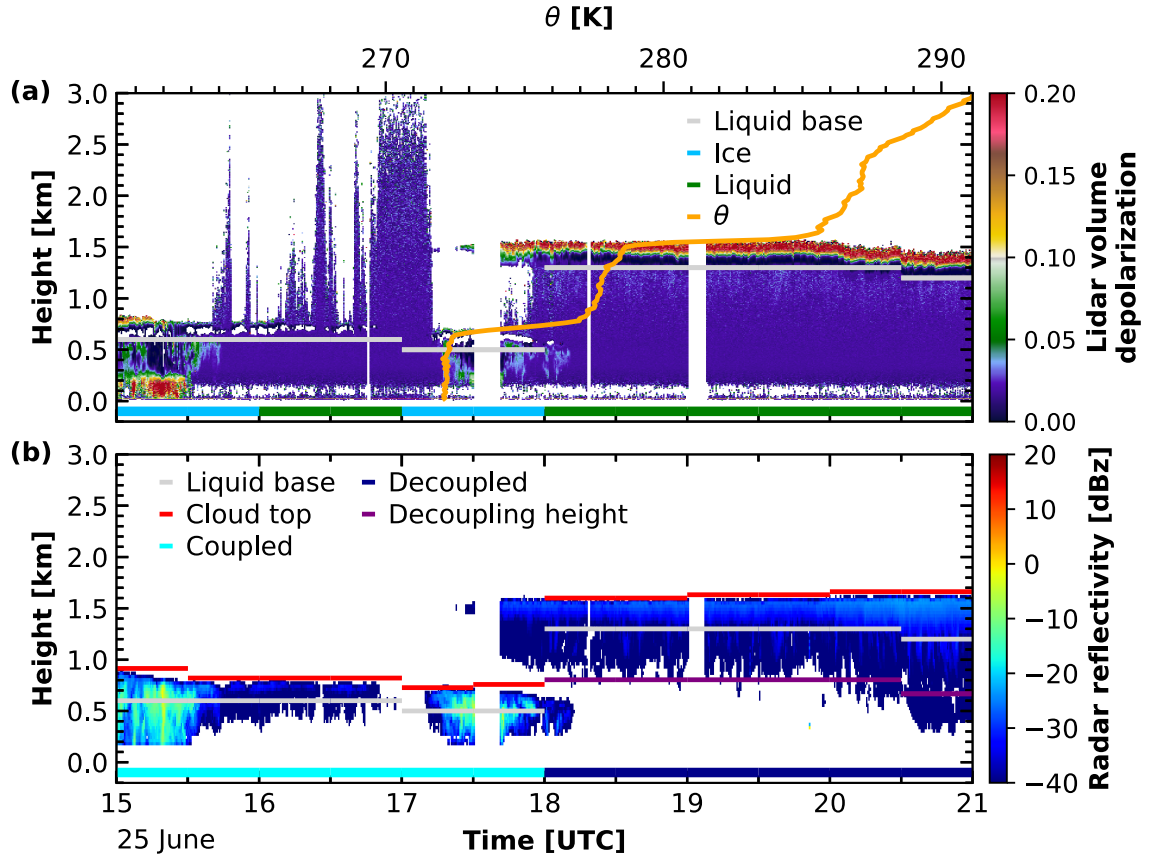


Figure 5.2: An example of the applied method on 25 June 2017 between 15 – 21 UTC. In (a) the lidar volume depolarization (not backscatter) is shown. Marked are also flags for liquid-layer base height (gray) and cloud phase (ice: blue; liquid: green). Additionally, the θ profile for the sounding launched at 17:15 UTC (orange) is plotted. In (b) the cloud radar reflectivity is depicted together with information on the liquid-layer base height (gray), cloud top height (red), the coupling state (cyan: coupled; dark blue: decoupled), and (if applicable) the decoupling height (purple).

than 1000 m to the subjacent cloud might have influenced the lower one and thus these periods have been excluded from the analysis.

5.1.2 Surface-coupling state

The surface-coupling state of the cloud was derived from the thermodynamic profiles of the radiosondes. Following Gierens et al. [2020], who introduced a simplified version of the coupling algorithm from Sotiropoulou et al. [2014], the profile of the potential temperature θ was examined starting at the liquid-layer base down to the surface. If the difference between the cumulative mean of θ and θ exceeded 0.5 K, the cloud was considered to be decoupled from the surface [Fig 5.1 (d)]. The according height was defined as the

decoupling height [marked in purple in Figure 5.1 (d) and Figure 5.2 (b)]. A quasi-constant θ profile on the other hand identified surface-coupled clouds [Fig 5.1 (c)]. In Figure 5.2 (a) the base of the clouds between 15 – 17 UTC was too low to be considered as 'decoupled' (500 – 600 m). The θ profile was nearly constant until the cloud base. From 17 UTC on, however, the liquid-layer base height was significantly higher (1200 – 1300 m) and due to the increase in θ at roughly 700 m these clouds were defined as 'decoupled'. Further details of the method to analyze coupled and decoupled clouds were published in Griesche et al. [2021].

5.2 Results: influence of surface coupling on heterogeneous ice formation temperature

The investigated period covers 1520 analyzed intervals of 30 min each. In 88 % of these periods, a cloud was identified and roughly 57 % of the investigated clouds were identified as ice-containing clouds. Approximately 62 % of the analyzed clouds were coupled to the surface whereas 38 % were decoupled from it; 64 % of the surface-coupled clouds but only 47 % of the decoupled clouds were defined as ice-containing clouds. No limit for the lowest decoupled liquid-layer base was set. The lowest decoupled liquid-layer was found at 100 m altitude. In the following, a more differentiated analysis of the derived cloud statistic is presented and thereafter discussed.

Following Kanitz et al. [2011] the fraction of ice-containing clouds for all observed clouds in different intervals of minimum cloud temperature in the range of heterogeneous freezing, starting at -40°C up to 0°C was analyzed. Figure 5.3 (a) shows the fraction of ice-containing clouds as a function of minimum cloud temperature for the Arctic (green) in contrast to findings from Leipzig [orange; Kanitz et al., 2011]. Below a minimum cloud temperature of -25°C most clouds from both data sets contained ice. At higher temperatures (minimum cloud temperature $> -10^{\circ}\text{C}$) above Leipzig on the other hand, usually, few to no ice-containing clouds were found. For the Arctic, a different pattern in this temperature regime was observed. Temperatures slightly below freezing are already sufficient for significant ice production: 35 % to 70 % of the investigated clouds with minimum cloud temperatures above -15°C showed signals of ice. As higher minimum cloud temperatures are usually associated with lower cloud heights, in the next step the data set was analyzed in terms of liquid-layer base height. In all analyzed temperature and liquid-layer base height intervals, liquid-water-containing clouds were identified.

Figure 5.3 (b) represents the fraction of ice-containing clouds as a function of liquid-layer base heights between 50 m and 4000 m. In general, there is a tendency for an increasing fraction of ice-containing clouds with increasing base height. An increase in liquid-layer base height may be associated with an increase in cloud top height, depending on the cloud vertical extent. A higher cloud top height in turn typically goes along with a decrease in minimum

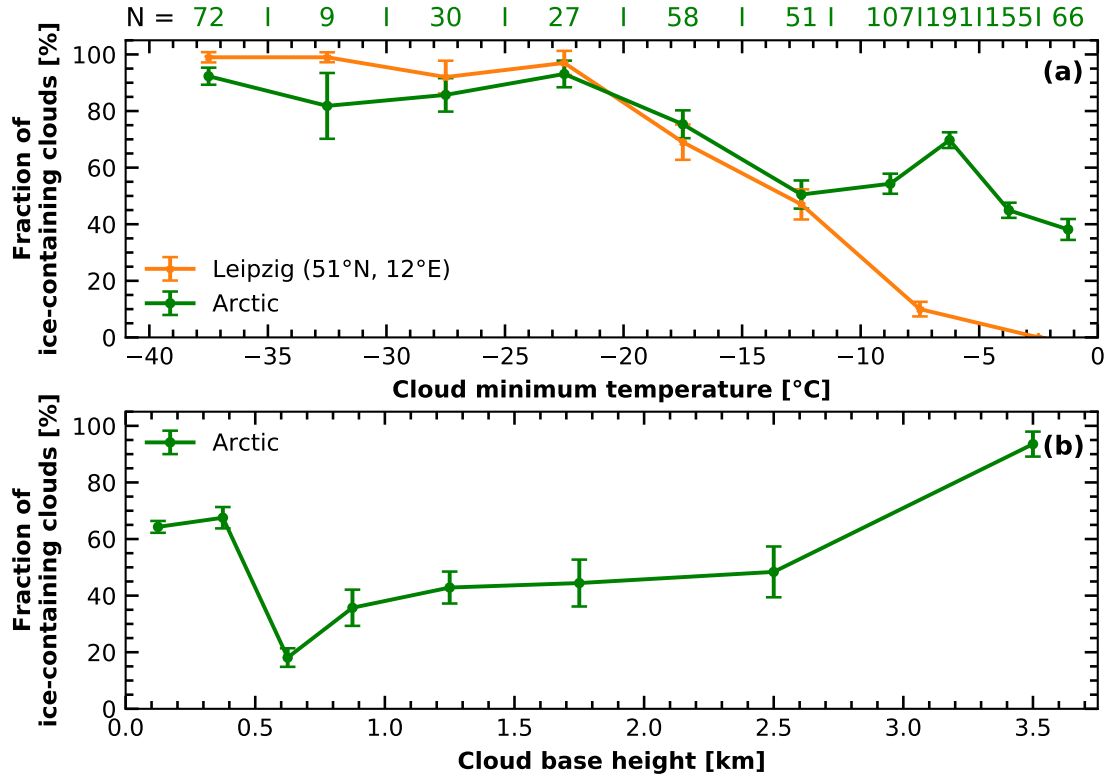


Figure 5.3: (a) Fraction of ice-containing clouds as a function of minimum cloud temperature within the heterogeneous ice nucleation regime. Data of all clouds of the Arctic 2017 field campaign are plotted in green. In orange, the results for Leipzig from Figure 3 in Kanitz et al. [2011] are shown. The error bars indicate the statistical uncertainty as in Seifert et al. [2010]. Temperature intervals increase with decreasing minimum cloud temperature due to decreased number of data ($\Delta T = 2.5^\circ\text{C}$ above -10°C and $\Delta T = 5^\circ\text{C}$ below -10°C). The numbers on top of the plot show the number of data for each temperature interval and the data points have been placed in the middle of the respective investigated interval. (b) Fraction of ice-containing clouds for different liquid-layer base height intervals. Base height intervals increase with increasing liquid-layer base height due to decreased number of data ($\Delta h = 0.25\text{ km}$ below 1 km , $\Delta h = 0.5\text{ km}$ between 1 km and 2 km , and $\Delta h = 1\text{ km}$ above 2 km).

cloud temperature. This leads to a higher probability of ice formation as more aerosol particles can act as possible INPs. The fraction of ice-containing clouds for liquid-layer base heights below 500 m , however, is also up to 70% . To further investigate if this effect may be linked to a possible INP source at the surface the data set was separated by the surface-coupling state of the clouds, as described in Section 5.1.2. The resulting distribution for both surface-coupled (cyan) and surface-decoupled clouds (dark blue) is shown in Figure 5.4. Between -15°C and 0°C , strong coupling effects can be seen. Surface-coupled ice-containing cloud intervals compared to decoupled ones occurred more frequently by a factor of $2 - 6$ (e.g., 164 vs. 27 in number of observed clouds and 83% vs 36% in frequency

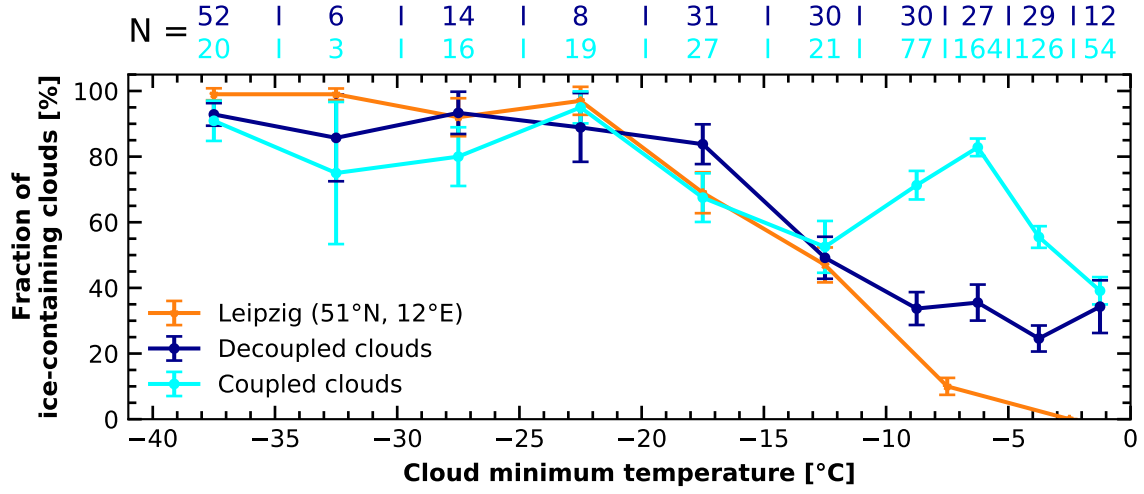


Figure 5.4: Same as Figure 5.3 (a) with the Arctic clouds separated by their coupling state (cyan: surface-coupled clouds; dark blue: surface-decoupled clouds).

of occurrence between -7.5°C and -5°C minimum cloud temperature). Below -15°C this effect vanished, and both curves show a similar distribution as found over Leipzig. Investigating lower minimum cloud temperature, the number of cases of surface-coupled clouds reduces.

5.3 Discussion of the observed surface-coupling effects

This study found an influence of a linkage between the surface and the cloud with respect to heterogeneous ice formation. As this study is one of the first to provide insights on the presented matter, a general discussion of the methodology and possible instrument effects on the ice detection and the determination of the coupling state is given here first. Afterwards possible causes for the observed linkage are discussed.

5.3.1 Methodological and instrumental effects

The presented analysis is based on well-established methods developed and applied in previous studies such as Ansmann et al. [2009] and Seifert et al. [2011, 2010, 2015] and Kanitz et al. [2011] and the data were carefully screened for ice occurrence solely using lidar data. Despite having a much more ice-sensitive Mira-35 cloud radar available, it was not utilized for ice detection. The reason was the frequent occurrence of low-level clouds below the lowest radar range gate of 155 m above the instrument. Such clouds were frequently observed during PS106 [50 % of the observational time; Griesche et al., 2020a] and hence cloud-radar-based statistics would be biased towards higher-level clouds. The phase separation approach to

derive the statistics for Leipzig presented in Figure 5.3 (a) and in Figure 5.4 was likewise based on lidar measurements [Kanitz et al., 2011]. To ensure a comparable sensitivity the statistics in this study were also based on the lidar observations. Nevertheless, statistics based on the available cloud radar observations have been additionally derived and are presented below.

Cloud radar for ice detection

To detect ice occurrence with the cloud radar, periods where the cloud radar showed enhanced reflectivity [as can be seen in Figure 5.2 (b)] and enhanced LDR were manually classified as ice-containing. The results are presented in Figure 5.5. As expected due to the higher ice sensitivity of the cloud radar, the detected ice cloud fraction overall increased. Yet, the observed effect remains the same: the surface-coupled clouds showed a stronger ice cloud occurrence compared to the decoupled clouds. The effect is smaller than in Figure 5.4. A reason could be that the lowest clouds, which were most likely affected by surface sources of INPs, are not well represented in these statistics. Quantitative differences are obvious compared to Figure 5.4 but the effect of a larger fraction of ice-containing clouds in the case of surface coupling is still visible. It should be mentioned, that the effect of increased ice cloud detection in statistics based on radar measurements compared to those from lidar data were also observed before in Leipzig, Germany, and in Punta Arenas, Chile, and are detailed explained by Bühl et al. [2013] and Radenz et al. [2021]. It should also be mentioned that cloud-relevant (in terms of cloud altering and precipitation) processes of ice formation can be

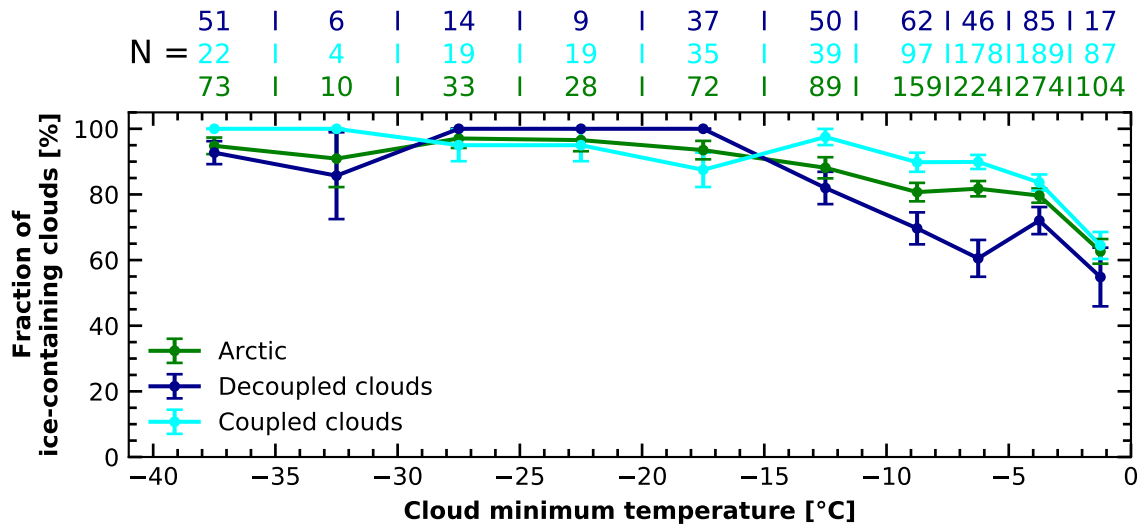


Figure 5.5: Same as Figure 5.4 but using the cloud radar for ice detection. In green the results of the complete data set are shown, in cyan for the coupled clouds and in dark blue for the decoupled clouds.

well observed with a lidar. The radar, in contrast, already detects individual ice particles, which may be — in terms of their low number concentration — not always a good measure for the classification of heterogeneous ice formation [Bühl et al., 2013].

Specular reflection

Oriented ice crystals can have a strong effect on the observed lidar signal. In the case of large, horizontally oriented plate crystals and a zenith-looking lidar the measured backscatter strongly increases while the depolarization ratio is close to zero [e.g., Noel and Sassen, 2005; Westbrook et al., 2010], which is called the effect of specular reflection. Hence, most ground-based lidars are tilted off-zenith by a few degrees, in the case of Polly^{XT} by 5°. This setting avoids most of the specular reflection effects, which otherwise may mask the presence of ice [Noel et al., 2002]. Yet, Silber et al. [2018] showed that the effects can still be visible up to an off-zenith angle of 10° in the case of planar ice crystals. Sassen and Takano [2000] found strong depolarization effects in the case of the rare event of oriented columns for an off-zenith angle 1 – 2°. However, to date, it has not been shown how randomly oriented columnar ice crystals influence the lidar signal at varying zenith angles as they form above –10 °C in the temperature regime where the strongest effect of surface coupling was found. According to Noel et al. [2004], columnar crystals with a high axis ratio can be expected to have high particle depolarization ratios on the order of 0.5. To summarize, misclassification of an ice-containing cloud for a liquid-water cloud can be excluded for the PS106 data set.

Sensitivity test with respect to the coupling retrieval

The approach to derive the coupling state is established in the literature and worked also well for the investigated clouds in this thesis. However, some limitations were found, as no height dimension was considered. That means a small increase in θ could still result in a situation that is classified as coupled if the distance was short enough. A cloud with its liquid-layer base, for example, at 200 m and a linear increase in θ from 260 K at the surface to just below 261 K at the liquid-layer base height would be identified as surface-coupled, even though the gradient is almost 5 K km⁻¹. This effect might have resulted in a larger fraction of lower clouds to be classified as surface-coupled. To check for the influence of possible misclassification in such a situation, a sensitivity test of the applied coupling retrieval was done. To perform the sensitivity test, a maximum gradient of the potential temperature between the surface and the liquid-layer base for surface-coupled situations was defined. The new requirement (in addition to the original one) for a surface-coupled classification was that the gradient between surface and liquid-layer base $\Delta\theta/\Delta z < (\Delta\theta/\Delta z)_{\text{lim}}$. This gradient threshold was chosen as $(\Delta\theta/\Delta z)_{\text{lim}} = 2 \text{ K/km}$, which was the lowest gradient found in the case of decoupled clouds using the presented approach to determine the surface-coupling state. In this case, the number of surface-decoupled cloud intervals increased at the expense of the surface-coupled ones (Figure 5.6). Also the fraction of ice-containing surface-decoupled clouds

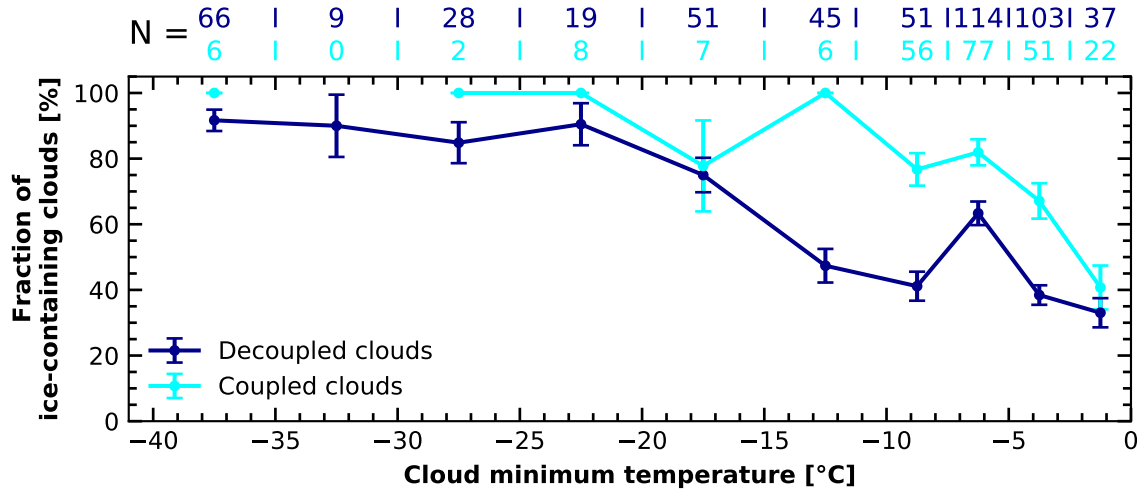


Figure 5.6: Same as Figure 5.4 but also using a threshold in the potential temperature gradient to identify surface coupling.

increased, although, not as much as the fraction of ice-containing surface-coupled clouds. By this further classification approach, the surface-coupling effect is even more obvious and even extends towards lower temperatures. However, the number of surface-coupled cloud intervals below -15°C is rather small and the findings here should be considered with care.

Also, possible biases introduced by the measurement uncertainty of the radiosonde were investigated. The measurement uncertainty in temperature and pressure of the radiosonde RS-92 is given by Vaisala to be $\Delta T = 0.5\text{ K}$ and $\Delta p = 1\text{ hPa}$ [Jensen et al., 2016]. As only observations within one profile are compared, systematic errors can be neglected and only the standard deviation of differences in pairs of soundings is of interest. This was given by Jensen et al. [2016] as $\sigma_T = 0.2\text{ K}$ ($< 100\text{ hPa}$) and $\sigma_p = 0.3\text{ hPa}$ ($> 100\text{ hPa}$). Using error propagation the error in the potential temperature $\Delta\theta$ can be estimated. The resulting uncertainty was used to calculate the surface-coupling state by varying the threshold for the coupling state ($0.5\text{ K} \pm \Delta\theta$). The results are shown in Figure 5.7. The variation in the threshold resulted in a change in the number of coupled cloud intervals. In the case of $0.5\text{ K} + \Delta\theta$, 31 % of the originally surface-coupled analyzed cloud intervals were classified as decoupled, while for $0.5\text{ K} - \Delta\theta$, 7.5 % of the originally surface-decoupled intervals were classified as coupled. Yet, the observed effect on the fraction of ice-containing clouds was within the statistical uncertainty of the original approach and thus the measurement uncertainty from the radiosondes was not further considered in the presented analysis.

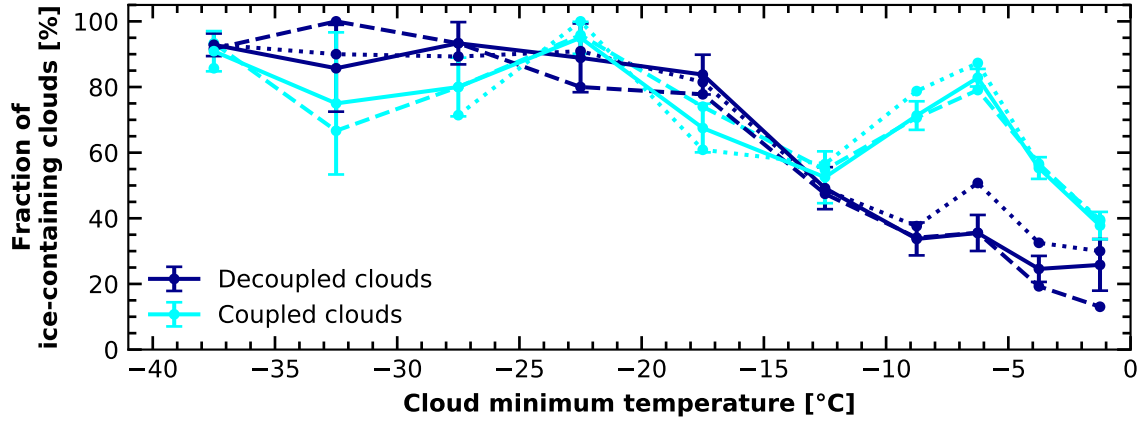


Figure 5.7: Continuous lines are the same as Figure 5.4. The dashed lines represent the respective results for the upper end of the error margin (i.e. profiles were classified as decoupled using a threshold for the coupling state of 0.5 plus the error in θ) and the dotted lines represent the lower end of the error margin (i.e. profiles were classified as decoupled using a threshold for the coupling state of 0.5 K minus the error in θ).

5.3.2 Possible causes for increased ice occurrence in surface-coupled clouds

The separation of the Arctic cloud data set into surface-coupled and -decoupled clouds revealed the presence of surface effects on the enhancement of the occurrence of ice formation. However, for clouds decoupled from the surface, or at greater heights and lower temperature, the ice-frequency statistics are similar to what is observed over Northern Hemisphere mid-latitude sites. This finding is consistent with previous findings that the free-tropospheric aerosol conditions in the Arctic are dominated by aged aerosol pollution mixed with dust and wildfire smoke from lower latitudes [e.g., Abbatt et al., 2019; Law et al., 2014; Willis et al., 2018, and references therein].

The reasons for the increase in ice-forming efficiency for low and surface-coupled clouds in the Arctic are caused by effects resulting from the linkage to the surface [Solomon et al., 2014]. A surface coupling of the cloud is accompanied by a well-mixed layer from the surface up to the liquid-layer base. Multiple processes of enhanced ice observation in low-level clouds were discussed in previous studies as potential candidates for explaining the presented observations. Yet, none of these studies considered also the coupling state of the cloud. However, they are listed and examined below.

In Shupe [2011] one reason for the high amount of low-level ice clouds was related to the occurrence of near-surface diamond dust. As this effect is stronger in winter and close to land [Intrieri and Shupe, 2004], it can be neglected as a dominating reason for the Arctic clouds during the investigated Polarstern cruise. Also by eye, periods of diamond dust were not observed during PS106.

An enhanced fraction of ice-containing clouds could be attributed to blowing snow as on the one hand, the lifted snow can be interpreted by the lidar as an ice cloud. On the other hand, blowing snow particles can act as seeds for ice crystals via the ice multiplication processes [Rogers and Vali, 1987]. Yet, the influence of blowing snow on the results can be ruled out. As Serreze and Barry [2014] pointed out, a minimum wind speed of 15 ms^{-1} is needed to lift the snow even a few meters above the ground. Since the wind speed during the PS106 campaign did not even reach this threshold (see Figure 5.8), it is very unlikely that blowing snow did affect the findings. In addition, the near-surface air temperature was frequently close to the freezing point and hence the snow was often too sticky to be mobilized. To also consider possible seeding effects from precipitating clouds above as found, e.g., in Vassel et al. [2019], the data set has been filtered for those situations with few to no effects on the results.

Sotiropoulou et al. [2020] highlighted the importance of secondary ice processes in Arctic stratocumulus clouds based on a large-eddy simulations (LES) study. The authors reported that weak updraft at warm subzero temperatures can increase the importance of ice production due to secondary ice formation, like rime splintering and collisional break-up. To assess a possible influence of these mechanisms, the Doppler velocities of the surface-coupled and -decoupled clouds were compared. Yet, no significant differences were found, neither in the relative distribution of the Doppler velocities nor in their respective mean values. Hence, no difference in the in-cloud updraft was derived. Also, the role of turbulence on the observed effect was examined using EDR. The EDR in the surface-coupled situations showed no difference, compared to the decoupled periods. However, the Doppler velocity, and accordingly the EDR estimation, is derived by the cloud radar data, which is not available at altitudes below 165 m above the surface.

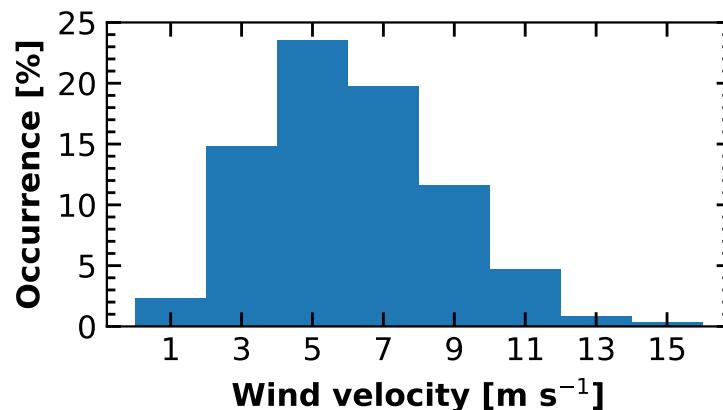


Figure 5.8: Histogram of the mean surface wind for the analyzed 30 min intervals. Data are from the wind sensor aboard Polarstern during PS106.

Another potential explanation is the presence of an increased number of INPs that are already active at -5°C in the surface-coupled clouds. The aerosol distribution in the summertime Arctic marine boundary layer is influenced by local sources and downward mixing from the free troposphere of long-range-transported aerosol [Willis et al., 2018]. Typically only material of biogenic sources is active as INPs at such high temperatures [Kanji et al., 2017]. Biological aerosol particles from areas of open water within the marginal sea ice zone or open leads or polynyas may be mixed into the coupled cloud layers where they can act as ice nuclei [Burrows et al., 2013] and increase the probability of ice production. The origin of such highly active INPs needed for such an effect is still under discussion in the literature. Wex et al. [2019] found the largest INPC in the Arctic in summer with INPs being active for temperatures up to -5°C . Hartmann et al. [2020] suggested these INPs may be of biogenic origin from local marine sources such as open leads or polynyas. Zeppenfeld et al. [2019] analyzed the ice-nucleating activity of sea surface microlayer (SML) samples from melt ponds and the marginal sea ice zone taken during PS106. The authors identified the SML as a possible source for Arctic INP. In addition, free glucose was found a potential tracer for the ice-nucleating activity of the water sampler. In an attempt to narrow down possible contributors to the ice-nucleating activity in the SML, Ickes et al. [2020] compared the ice nucleation ability of Arctic SML samples and two different predominant Arctic phytoplankton species. Even though, these samples showed ice nucleating activity already under moderate supercooling conditions, no clear evidence was found that the investigated phytoplankton species may serve as a local marine INP source. Hartmann et al. [2021] analyzed the ice-nucleating ability of bulk seawater (BSW), SML, fog water, and filter samples during the PS106 expedition. In addition, airborne INP measurements performed with a continuous-flow diffusion chamber from the ACLOUD campaign were investigated. The filter samples showed a significantly reduced ice-nucleating activity after been treated by a heating process, a clear evidence for the presence of biogenic INPs. However, the derived INPC from the BSW and SML samples were lower by a factor of 10^5 than the airborne INPC measurements. The INPC from the fog water and the ambient INPC showed a good agreement. This observed closure indicates that during fog events, all INP were activated as fog droplets. Thus, it is very likely, that the INP responsible for the high fraction of ice-containing surface-coupled clouds are of biogenic origin. However, besides strong indications that these INP also originate from local marine sources, a clear proof of this hypothesis is still missing.

Decoupling indicates a separation of the cloud from the surface due to a stable layer below the liquid-layer base. Decoupled clouds, however, also show a slightly enhanced fraction of ice-containing clouds, when compared to clouds observed above Leipzig. The life cycle of the cloud and its thermodynamic state before the observation is unknown. Hence, any explanation for the reasons behind this observation would be speculative. It could, for example, also be the case that turbulent boundary layer processes or frontal passages caused potential mixing from biological surface INP into the free troposphere, eventually.

To examine potential enhancement of aerosol effects on the surface-coupled clouds, a lidar-based aerosol analysis for PS106 was performed. Figure 5.9 shows profiles of the particle backscatter coefficient at 532 nm wavelength for nine different periods adjacent to cloud observations when Polly^{XT} was able to probe cloud-free air masses. These profiles were derived using the procedures described in Chapter 3.1.1 and by Baars et al. [2016]. In situations of persistent cloud cover when no clear-sky lidar calibration was possible, calibration of the particle backscatter coefficient profiles was performed as described in Jimenez et al. [2020]. The y-axis in Figure 5.9 was normalized to the respective decoupling height of each profile. A general tendency of reduction of the particle backscatter coefficient β above the decoupling height can be seen. The sharp increase visible in some of the profiles were caused by the liquid-layer base, where the backscattered signal strongly increases. From the particle backscatter coefficient, the lidar-particle extinction coefficient can be estimated by using a lidar ratio of 50 sr for non-marine aerosol [Groß et al., 2011; Müller et al., 2007; Tesche et al., 2009]. The particle extinction coefficients resulting from the profiles presented in Figure 5.9 are much smaller compared to typical values for marine aerosol [$40 - 100 \text{ Mm}^{-1}$; Bohlmann et al., 2018; Kanitz et al., 2013a], except for the two profiles on 27 June 2017 (note that a typical lidar ratio for marine aerosol is $< 50 \text{ sr}$ [Bohlmann et al., 2018; Groß et al., 2011] and would result in even smaller particle extinction coefficient

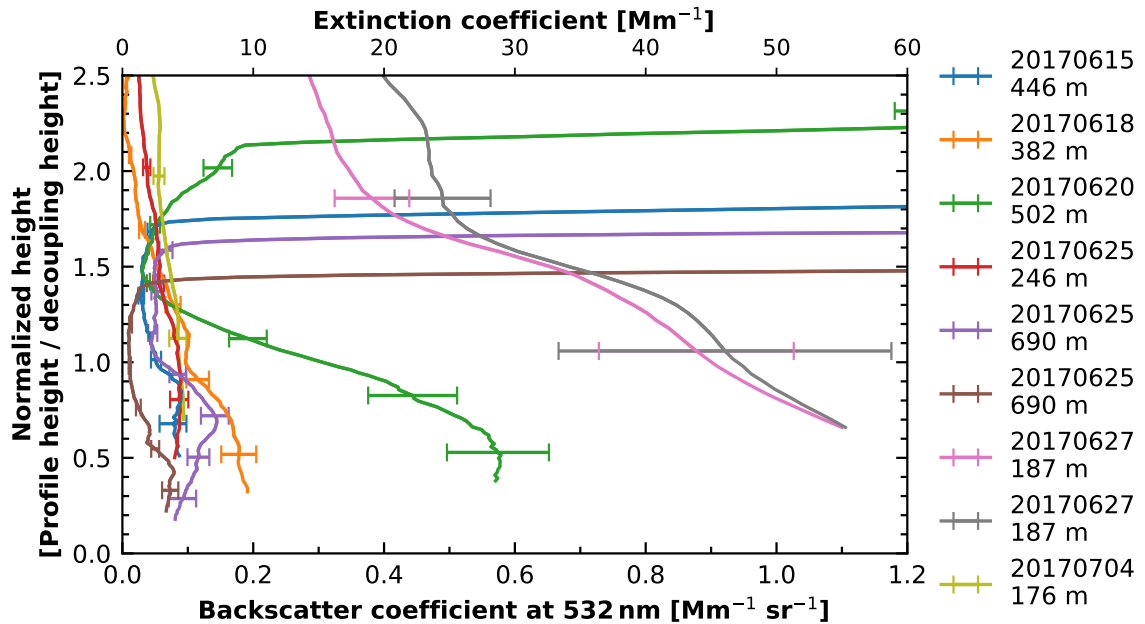


Figure 5.9: (a) Profiles of particle backscatter coefficient at 532 nm from Polly^{XT}. The date of the corresponding profiles together with the respective decoupling height is annotated on the right side. The height axis was normalized by the decoupling height. The particle extinction coefficient is derived by scaling the particle backscatter coefficient with an assumed lidar ratio of 50 sr.

values). AERONET photometer measurements at Arctic sites show typical values for the Ångström exponent (440 – 870 nm) around 1.5 (not shown) indicating a fine-mode-dominated aerosol distribution. The Ångström exponent for typically coarse-mode-dominated marine aerosol centers around 0.5 [Smirnov et al., 2009; Yin et al., 2019]. Both, the small values of particle extinction coefficient and the high Ångström exponents are clear indications that the observed aerosol was not of typical marine origin. Yet, an estimation of the INPC from the lidar measurements, as presented by Mamouri and Ansmann [2016] for different aerosol types, was not possible because the respective parameterizations for such biogenic aerosol particles in the Arctic are still missing.

For both coupling states at a minimum cloud temperature below -15°C , the occurrence of ice-containing clouds increased strongly and reached values close to 100 % at temperatures below -25°C . A rather similar pattern was found over Leipzig [Kanitz et al., 2011]. To provide further insights on this matter an air mass source attribution analysis was performed based on the Lagrangian particle dispersion model FLEXible PARTicle dispersion model (FLEXPART) [Pisso et al., 2019], as introduced by Radenz et al. [2021]. Throughout the analyzed period (1 June – 16 July 2017) particles were traced for 10 days, starting every 3 hours with height steps of 500 m. Based on the Moderate Resolution Imaging Spectroradiometer (MODIS) land cover classification from Broxton et al. [2014], seven categories, namely 'water' (sea-ice included), 'forest', 'savanna/shrubland', 'grass/cropland', 'urban', 'snow/ice' and 'barren' were defined as a possible source regions [Radenz et al., 2021]. The relative residence time of the particles below a reception height of 2 km above different possible aerosol source areas has been calculated and is shown in Figure 5.10. A strong decrease of 'water' as possible aerosol source region for particles arriving above 2 km is obvious, while the fraction of 'snow/ice' (note these are land-based ice sheets and glaciers, not the frozen Arctic ocean), 'savanna/shrubland', 'grass/cropland', and 'forest' increased. This distribution agrees with what has been found for the continental site Krauthausen in Germany [Radenz et al., 2021, Figure 15 therein], which confirms the common view that the aerosol in the free troposphere of the Arctic is brought there by long-range transport.

After ruling out the possibility of blowing snow, seeding effects, secondary ice formation, and diamond dust as reasons for the observations, the only plausible explanation is the presence of highly active INPs which are more abundant in surface-coupled than in -decoupled clouds. Given the mixture of the summertime marine boundary layer aerosol in the Arctic and the high temperatures where the effect was observed, the most likely source for these INPs is biogenic material from local marine sources. When transported from the Arctic Ocean into the cloud, these INP likely initiate ice crystal formation via immersion freezing processes.

The presented results are based on a 2-month campaign. And even though strong evidence was found that the effect is a consequence of aerosol of marine origin acting as INPs

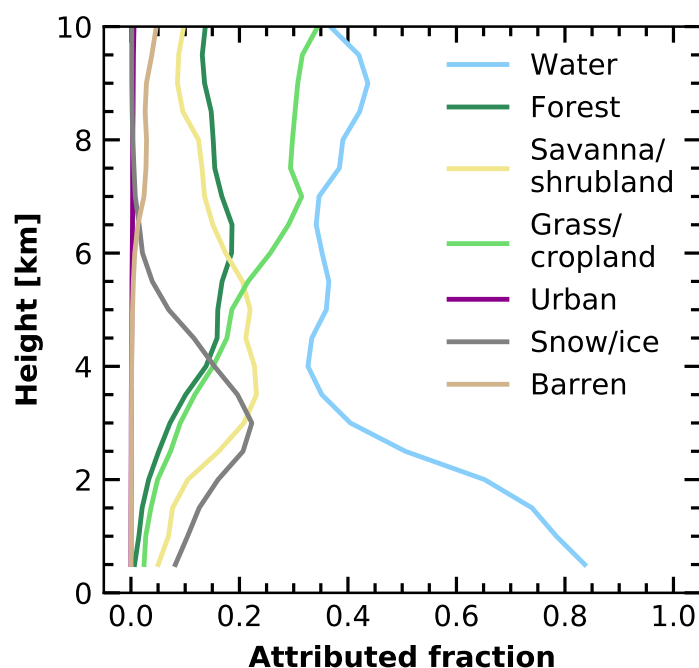


Figure 5.10: Fraction of residence time of air parcels below the reception height (2 km) above different possible aerosol source regions based on a FLEXPART analysis for the location of Polarstern during PS106.

in the cloud this rather short time coverage obviously cannot cover all situations which are of interest in this matter. The influence of the distance to open-water surfaces such as the open sea or leads and polynyas as well as a possible seasonal effect could not be studied from the PS106 data set. Based on the MOSAiC data set, which covers a full annual cycle in the Arctic Ocean with a variety of sea ice conditions, an investigation of effects from sea ice concentration and seasons is planned.

Chapter 6

Application of the data set in collaborative studies and radiative transfer simulations within (AC)³

Based on the OCEANET-Atmosphere observations and the Cloudnet processing, a valuable data set was derived. The standard Cloudnet output was improved to address the challenges of Arctic clouds and the requirements for collaborative studies together with other teams of the (AC)³ project. Additionally to the observations, the processed and quality-checked retrieved parameters are published in the long-term data archive Pangaea. The Cloudnet target classification [Griesche et al., 2020f], the ice water content and ice crystal effective radius [Griesche et al., 2020b,c], the liquid-water content and liquid droplet effective radius [Griesche et al., 2020d,e], and the low-level stratus mask [Griesche et al., 2020h] were made publicly available. To date, the unique data set was already widely used in different studies, e.g., as presented in Griesche et al. [2020a] and Griesche et al. [2021]. Additionally, the data set served as a reference for the cloud situation during tethered balloon studies of the Arctic boundary layer in Egerer et al. [2019] and was used for the evaluation of large-eddy simulations in Neggers et al. [2019]. In Barrientos Velasco et al. [2020] the Cloudnet data set was used as input for radiative closure studies and in Radenz et al. [2019] the cloud radar measurements were used for the demonstration of a novel radar spectrum multi-peak separation approach. In Egerer et al. [2021] the Cloudnet data set was used to determine cloud macrophysical and microphysical properties for a study on shallow humidity inversion above low-level clouds with tethered balloon measurements made during PASCAL. In Richter et al. [2021] the Cloudnet products were applied as a representative basis for the retrieval of microphysical cloud parameters from a mobile Fourier-transform infrared spectrometer. Furthermore, in Barrientos Velasco et al. [2021] it was used as input for radiative closure studies. The data set was additionally applied to assess the integrated water vapor derived by satellites and from land-based observations at Ny-Ålesund by Crewell et al. [2021].

The Transregional Collaborative Research Center (AC)³ was structured in different projects, to best cover the variety of feedbacks behind Arctic amplification. A focus of the (AC)³ project A01, in which this thesis is embedded, was the investigation of the performance and evaluation of radiative transfer simulations. In this chapter first radiative transfer simulations are briefly introduced and the calculation of the cloud radiative effect is explained. Subsequently, a case study is presented, which examines the potential improvements of radiative transfer simulations based on the detailed cloud observations introduced in Chapter 3.4.3. Simulated shortwave and longwave surface fluxes based on the standard Cloudnet products were considerably different compared to the observed irradiances. However, radiative closure was achieved by incorporating also the LLS which were observed below the lowest cloud radar range gate into the simulations. Finally, a statistical overview of similar cases during the PS106 campaign is given.

6.1 Radiative transfer simulations and cloud radiative effect

One of the goals of the (AC)³ project A01 in its first phase was to study cloud radiative effects in the Arctic utilizing radiative transfer simulations. Such simulations provide vertically resolved radiative fluxes for cloud and cloud-free conditions. In this way, the radiative effect of clouds can be investigated. The Cloudnet products during PS106 served as realistic input parameters for the radiative transfer simulations and the radiation measurements of OCEANET-Atmosphere as true validation data.

The radiative transfer simulations discussed in here were performed with the TROPOS Cloud and Aerosol Radiative Simulator (T-CARS) [Barlakas et al., 2020; Barrientos Velasco et al., 2021; Witthuhn et al., 2021]. T-CARS is a Python-based environment for simulating vertically resolved broadband radiative fluxes and heating rates for cloudy and cloud-free conditions. Its radiative transfer simulations were done using RRTMG which has been implemented into T-CARS. T-CARS uses the input of atmospheric properties (e.g., atmospheric profiles of trace gases, pressure, temperature and humidity), which are provided by atmospheric reanalysis data [i.e., ECMWF Reanalysis v5, Hersbach et al., 2020] or climatological profiles [i.e., Anderson et al., 1986]. Also surface properties such as temperature, pressure, and albedo are necessary. These values are provided either by satellites or surface sensors. Additionally, cloud properties like the liquid and ice water content and the liquid droplet and ice crystal effective radius are necessary to perform the simulations. Typically, these quantities are delivered by numerical weather prediction models but also satellite observations can be applied. In the case of PS106 the respective Cloudnet products introduced in Section 3.4 were utilized, which provide the respective properties in a much higher resolution as satellite observations do. To address the challenges of Arctic clouds, especially the frequent occurrence of optically-thick, low-level clouds, the standard Cloudnet output had to be adjusted. Therefore the previously introduced new approaches for the ice

crystal effective radius and the LLS cloud detection were added to the Cloudnet processing chain. Before the implementation and effects of these adjustments are demonstrated and discussed, a brief introduction into the assessment of the cloud radiative forcing is presented here.

Calculation of the cloud radiative effect

The cloud radiative effect (CRE) is an important measure to assess the impact of clouds on the radiative budget. The CRE can be determined using radiative transfer models like RRTMG. Based on the atmospheric, surface, and cloud input, the downward (\downarrow) and upward (\uparrow) broadband longwave (LW) and shortwave (SW) irradiances can be simulated. Using a model, this can be done for the same period for cloudy as well as for cloudless conditions. The LW and SW cloud radiative effect Γ at the surface (SFC) and the TOA can be derived by comparing the results for the cloudy and the cloudless situation [Ramanathan et al., 1989]

$$\Gamma_{X_{\text{SFC}}} = (X_{\text{SFC},\downarrow} - X_{\text{SFC},\uparrow})_{\text{cloudy}} - (X_{\text{SFC},\downarrow} - X_{\text{SFC},\uparrow})_{\text{cloudless}}, \quad (6.1)$$

and

$$\Gamma_{X_{\text{TOA}}} = (X_{\text{TOA},\uparrow})_{\text{cloudless}} - (X_{\text{TOA},\downarrow})_{\text{cloudy}}, \quad (6.2)$$

where X represents the respective longwave or shortwave irradiances.

The SFC and TOA net CRE are the sum of both, the short- and longwave CRE

$$\Gamma_{\text{netSFC}} = \Gamma_{\text{LWSFC}} + \Gamma_{\text{SWSFC}} \quad (6.3)$$

and

$$\Gamma_{\text{netTOA}} = \Gamma_{\text{LWTOA}} + \Gamma_{\text{SWTOA}}. \quad (6.4)$$

Finally, the net atmospheric (ATM) CRE (also referred to as divergence of the atmosphere) can be derived

$$\Gamma_{\text{netATM}} = \Gamma_{\text{netTOA}} - \Gamma_{\text{netSFC}}. \quad (6.5)$$

6.2 LLS treatment for improved radiative transfer simulations

For the realization of radiative transfer simulations, an accurate representation of the atmospheric state is necessary. The nature of Arctic clouds, especially the optically thick, low-altitude clouds, pose challenges on the task to derive the cloud microphysical properties for the entire tropospheric column. Strong lidar signal attenuation inside the LLS made the

continuous application of existing ice crystal effective radius retrievals based on a lidar-radar instrument synergy, as used, e.g., for the DARDAR-CLOUD algorithm [Cazenave et al., 2019], impossible. Hence, existing approaches to derive the ice water content and the extinction coefficient based on radar measurements alone were improved within this thesis to derive the ice crystal effective radius (see Section 3.4.3). This new method ensures the continuous identification of microphysical properties up to cloud top, which is a prerequisite to perform the radiative transfer simulations. The low altitude of the clouds, which was frequently below the lowest range gate of the cloud radar, was addressed using the near-range capabilities of the lidar Polly^{XT} (see Section 3.4.3). The near-range channel allowed a cloud detection down to a height of 50 m above the instrument and to adjust the cloud base height accordingly.

While the detection of the liquid phase inside clouds in Cloudnet is based on the lidar signal, the retrieval for the LWC and the liquid droplet effective radius ($r_{\text{eff,liq}}$) relies on the cloud radar reflectivity. However, the cloud radar measurements were not available at such low altitudes. In addition, in the case of complete lidar signal attenuation below the lowest cloud radar range gate, as shown for example in Figure 6.1 around 05:00 UTC and often between 07:50 – 09:30 UTC, no liquid phase was classified by Cloudnet. Thus, no liquid-water cloud microphysical properties were derived [see Figure 6.3 (a) and (b)]. To address this issue, first, the LLS cloud mask was used to identify the presence of a liquid-water cloud. In the case of a detected LLS, the column-integrated LWC (LWP_{int}) was compared to the LWP derived by the MWR HATPRO. Both quantities should be the same, when Cloudnet had identified a liquid-water cloud in the first place, i.e., the LLS did not cause a complete lidar signal attenuation. But if no liquid-water cloud was identified because the lidar signal was already completely attenuated below the first cloud radar range gate, then no LWC was derived by Cloudnet. Hence, the values for LWP and LWP_{int} should differ. The strong lidar signal attenuation, however, can only be caused by the presence of a liquid-water cloud layer. The respective liquid-water cloud microphysical properties were estimated using the difference $\Delta\text{LWP} = \text{LWP} - \text{LWP}_{\text{int}}$. In the case of $\Delta\text{LWP} > 10 \text{ g m}^{-2}$ ($\geq 150 \text{ g m}^{-2}$) a fixed value of $r_{\text{eff,liq}} = 8 \mu\text{m}$ ($30 \mu\text{m}$) was applied. The applied values were derived based on the distribution of the liquid droplet effective radius during PS106. The majority of $r_{\text{eff,liq}}$ was found below $10 \mu\text{m}$ and radii as large as $30 \mu\text{m}$ have been observed only in combination with increased values for LWP.

Signal attenuation by low-level clouds: 13 July 2017 01:00 – 11:00 UTC

To illustrate the procedure and highlight the benefits of applying the more sophisticated cloud classification scheme based on the LLS detection and the estimated values for $r_{\text{eff,liq}}$, its application is presented here for 13 July 2017. In Figure 6.1 an overview of the cloud observations between 01:00 UTC and 11:00 UTC are presented. The corresponding radiosonde profiles up to 4 km height are given in Figure 6.2. Figure 6.3 shows the derived Cloudnet liquid and ice products.

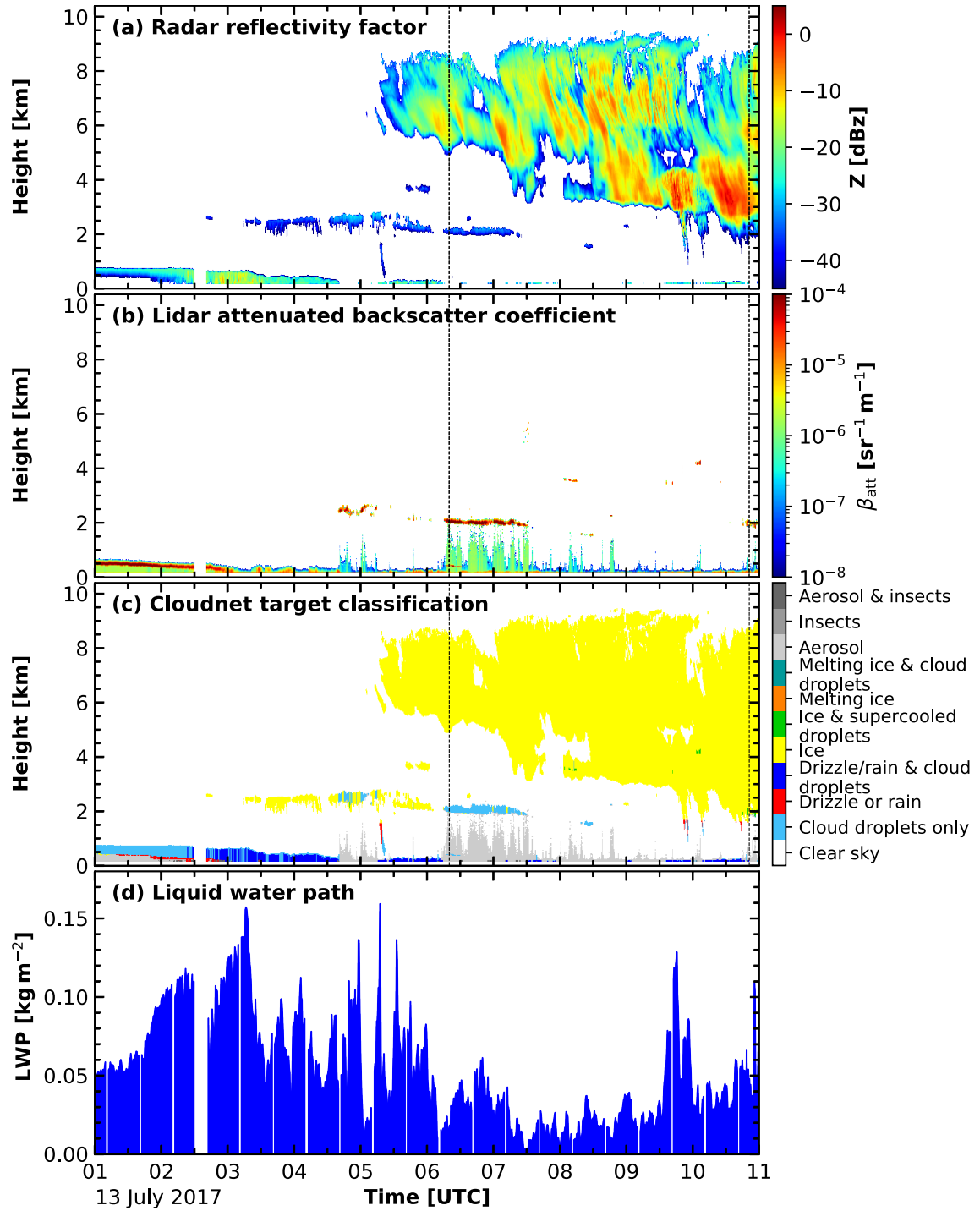


Figure 6.1: Cloud radar reflectivity (a), lidar attenuated backscatter (b), Cloudnet target classification (c), and LWP (d) between 0 and 10 km height for 13 July 2017 01:00 UTC to 11:00 UTC. The dashed lines mark the time of the radiosonde launches for the profiles shown in Figure 6.2 (b) and (c).

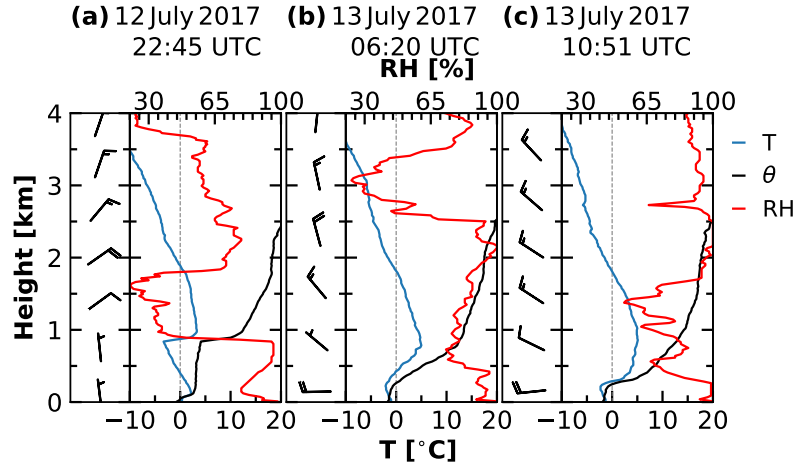


Figure 6.2: Thermodynamic profiles of temperature (blue), potential temperature (black), and relative humidity (red) up to 4 km height for three radiosonde launches relevant for the analyzed period. The start time and date are given above the respective profiles. The left part of each plot shows the wind barbs.

The period started with a liquid-water-dominated stratus cloud deck, which was located between 0.5 km and 1 km height and slowly descended towards lower altitudes. At the beginning of this period, the layer was thermodynamically decoupled from the surface, as can be seen by the θ profile in 6.2 (a). With decreasing cloud base height, this layer became coupled to the surface [6.2 (b)] and precipitation formed after 02:00 UTC. Between 04:30 UTC and 05:30 UTC and after 06:30 UTC this cloud was lower than the lowest detection limit of Cloudnet and therefore occasionally not identified by the original classification. Above this layer, at around 2.5 km height and between 03:00 UTC and 08:00 UTC an altocumulus cloud was observed. This cloud was only classified as 'mixed-phase' (green) or 'liquid' (blue) when the lidar was able to penetrate this layer. In the case of complete lidar signal attenuation in the LLS layer, the altocumulus layer was classified as 'ice' cloud (yellow). The missing liquid-water identification is reflected in the Cloudnet products as presented in Figure 6.3. After 04:30 UTC the liquid-water content [Figure 6.3 (a)] and liquid droplet effective radius [Figure 6.3 (b)] of the altocumulus layer as well as of the LLS cloud deck was only occasionally determined.

In Figure 6.4 (a) the simplified Cloudnet classification mask (above 165 m) combined with the LLS cloud classification mask (below 165 m) is shown. This mask revealed the presence of an LLS cloud almost continuously during the entire period after 02:00 UTC. Only during a short situation of very few or no low clouds from 06:30 UTC to 07:30 UTC no LLS was identified. Figure 6.4 (b) depicts the LWP derived by HATPRO in blue and the difference ΔLWP which is shown in orange. Two periods with $\Delta\text{LWP} > 10 \text{ g m}^{-2}$ were identified. The first period was observed between 04:30 UTC and 05:30 UTC with LWP

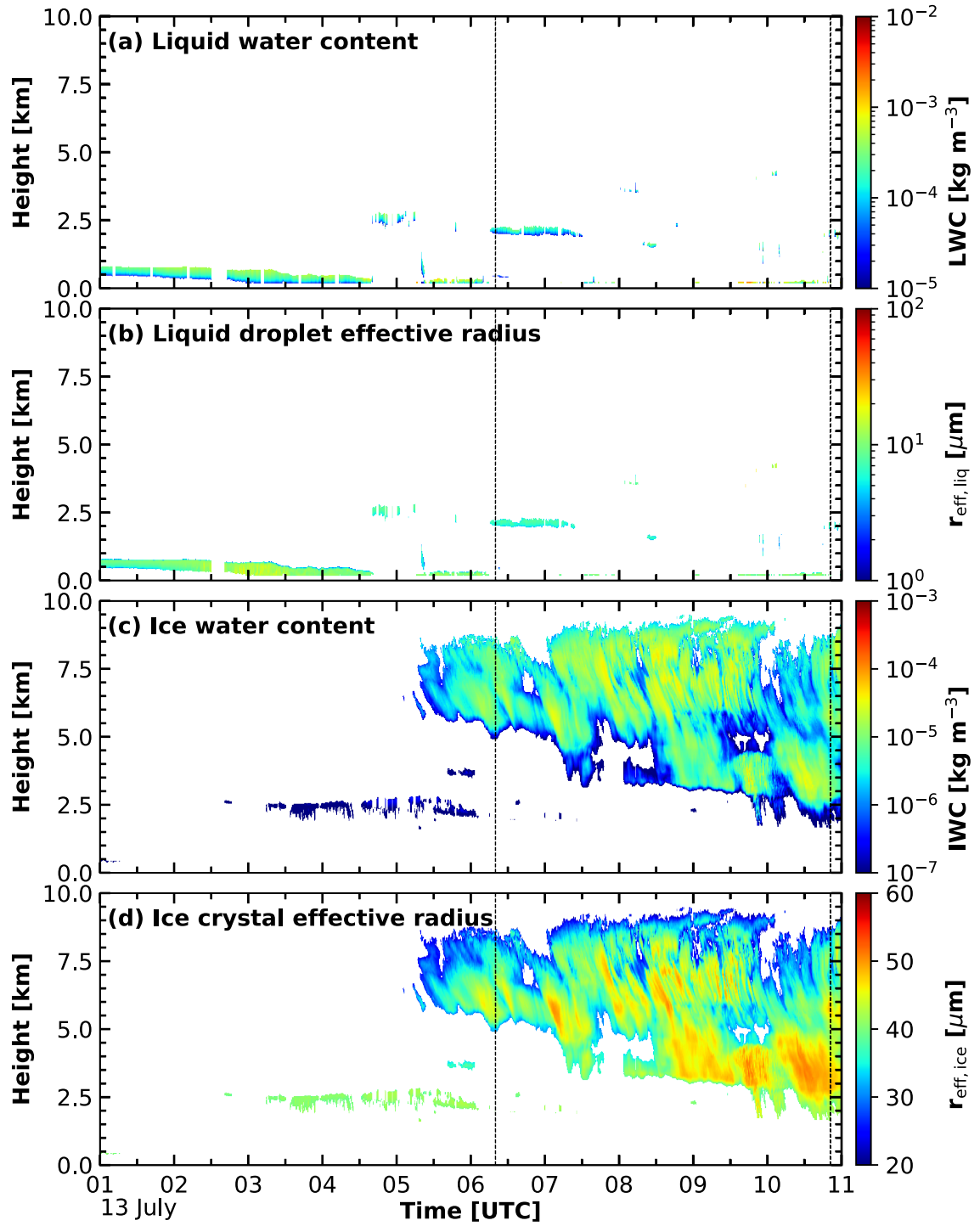


Figure 6.3: Microphysical cloud products for the same period as shown in Figure 6.1 derived by Cloudnet. Panel (a) shows the liquid-water content (LWC), (b) the liquid droplet effective radius $r_{\text{eff,liq}}$, (c) the ice water content (IWC), and (d) the ice crystal effective radius $r_{\text{eff,ice}}$. The dashed lines mark the radiosonde launches for the profiles shown in Figure 6.1 (b) and (c).

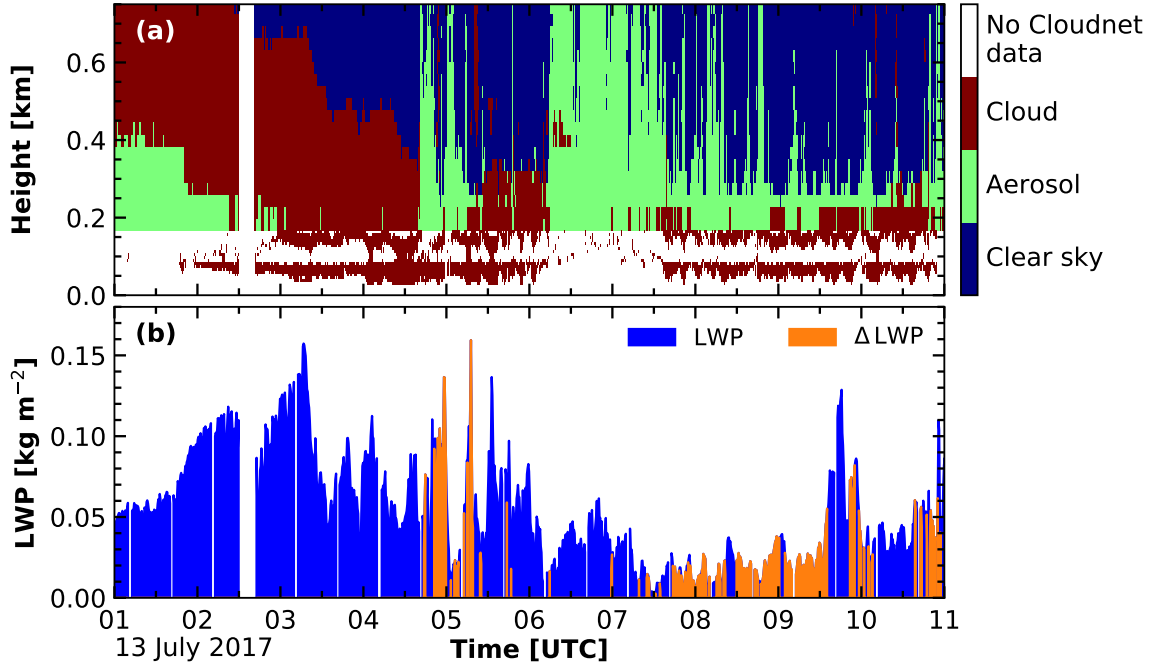


Figure 6.4: Panel (a) shows the low-level cloud mask for the same period as shown in Figure 6.1 derived from the Polly^{XT} near range signal (below 165 m) combined with a simplified Cloudnet classification mask (above 165 m). All clouds are shown in brown, aerosol in green and clear sky in blue. White areas denote situations where no Cloudnet data is available. In panel (b) the liquid-water path determined by the MWR HATPRO is depicted in blue. Additionally, the deviation between the LWP derived by HATPRO and by the integration of the liquid-water content, ΔLWP , is shown in orange.

values up to 150 g m^{-2} . During this period the altocumulus layer was present above the LLS in 2.5 km height. The second period with $\Delta\text{LWP} > 10 \text{ g m}^{-2}$ was between 07:30 UTC and 11:00 UTC. During this period, the LWP was lower, between 30 g m^{-2} and 80 g m^{-2} .

The increased values of ΔLWP verified the presence of liquid-water clouds as already indicated by the LLS mask. These clouds were not identified by the standard Cloudnet classification. Thus, using the standard Cloudnet classification the radiative effect of these clouds would be calculated solely based on their ice microphysical properties. However, liquid-water clouds have a much larger effect on the radiative budget than ice clouds. In the following, the effect of incorporating the identified liquid-water clouds into the radiative transfer simulations of T-CARS is evaluated.

Radiative transfer calculations: 13 July 2017 01:00 – 11:00 UTC

Based on the approach to first identify missed liquid-water clouds and then derive their cloud droplet effective radius radiative transfer simulations using T-CARS were performed. The results are shown in Figure 6.5 (a) for SW_{\downarrow} and in Figure 6.5 (c) for LW_{\downarrow} at the surface (for clarity reasons a running mean of 5 minutes was applied). In green, the results using the adjusted approach are depicted. Also, the results using the default Cloudnet classification scheme (blue, dashed) and measured irradiances (orange) are presented. In light blue, additionally, the results from the T-CARS simulations assuming a clear sky situation are shown. The measured SW_{\downarrow} irradiances are mainly driven by the solar zenith angle and thus follow a diurnal circle. One cause of the variations from this distribution, however, is the presence of clouds, especially liquid-water-containing clouds. Under these cloudy conditions, the SW_{\downarrow} irradiance fluctuated from about 90 W m^{-2} at 01:00 UTC to a maximum of 400 W m^{-2} at around 10:00 UTC [see Figure 6.5 (a)]. Around 05:00 UTC the T-CARS results based on the default classification yielded similar values for the irradiances as for the clear sky run (SW_{\downarrow} : 350 W m^{-2} ; LW_{\downarrow} : 250 W m^{-2}). The observed SW_{\downarrow} , however, was around 150 W m^{-2} (LW_{\downarrow} : 315 W m^{-2}). The derived irradiances based on the adjusted classification show a much better agreement with the observations.

The measured LW_{\downarrow} flux density is mainly driven by the presence of clouds. Yet, also the temperature of the cloud deck and hence the respective LW emission are of importance. The stratus cloud deck which was present below 1 km height almost during the entire period with rather high temperatures of above -5°C caused LW_{\downarrow} of about 315 W m^{-2} . Smaller deviations were observed when the LLS cloud deck was broken, at around 05:00 UTC and after 06:00 UTC [see Figure 6.5 (c)]. The presence of the stratocumulus at 2.5 km height with roughly the same temperature produced comparable LW_{\downarrow} irradiances. With the disappearance of the stratocumulus and still a broken cloud situation of the LLS deck at around 08:00 UTC [see Figure 6.1 (e)], the longwave downwelling irradiances reduced notably to around 280 W m^{-2} .

In Figure 6.5 (b) and (d) the histogram of the differences in the shortwave and longwave flux differences (simulations minus measurements) for the original cloud classification scheme (blue) and for the adjusted cloud detection scheme (green) are shown. Good performances of T-CARS based on the default Cloudnet classification mask were derived during situations when liquid-water was identified inside the clouds, e.g., until 04:00 UTC. However, differences between the measurements and simulations were up to $+200 \text{ W m}^{-2}$ for SW_{\downarrow} and -65 W m^{-2} for LW_{\downarrow} during periods when Cloudnet classified the clouds as pure ice, e.g., around 05:00 UTC and after 08:00 UTC. The mean downward flux difference and the respective standard deviation for the default approach during the complete period analyzed was $(45 \pm 91) \text{ W m}^{-2}$ for SW_{\downarrow} and $(-12 \pm 18) \text{ W m}^{-2}$ for LW_{\downarrow} (blue dotted and dashed lines in Fig 6.5 (b) and (d), respectively). Applying the more sophisticated adjusted approach for the LLS the differences were significantly smaller. In this case, the mean

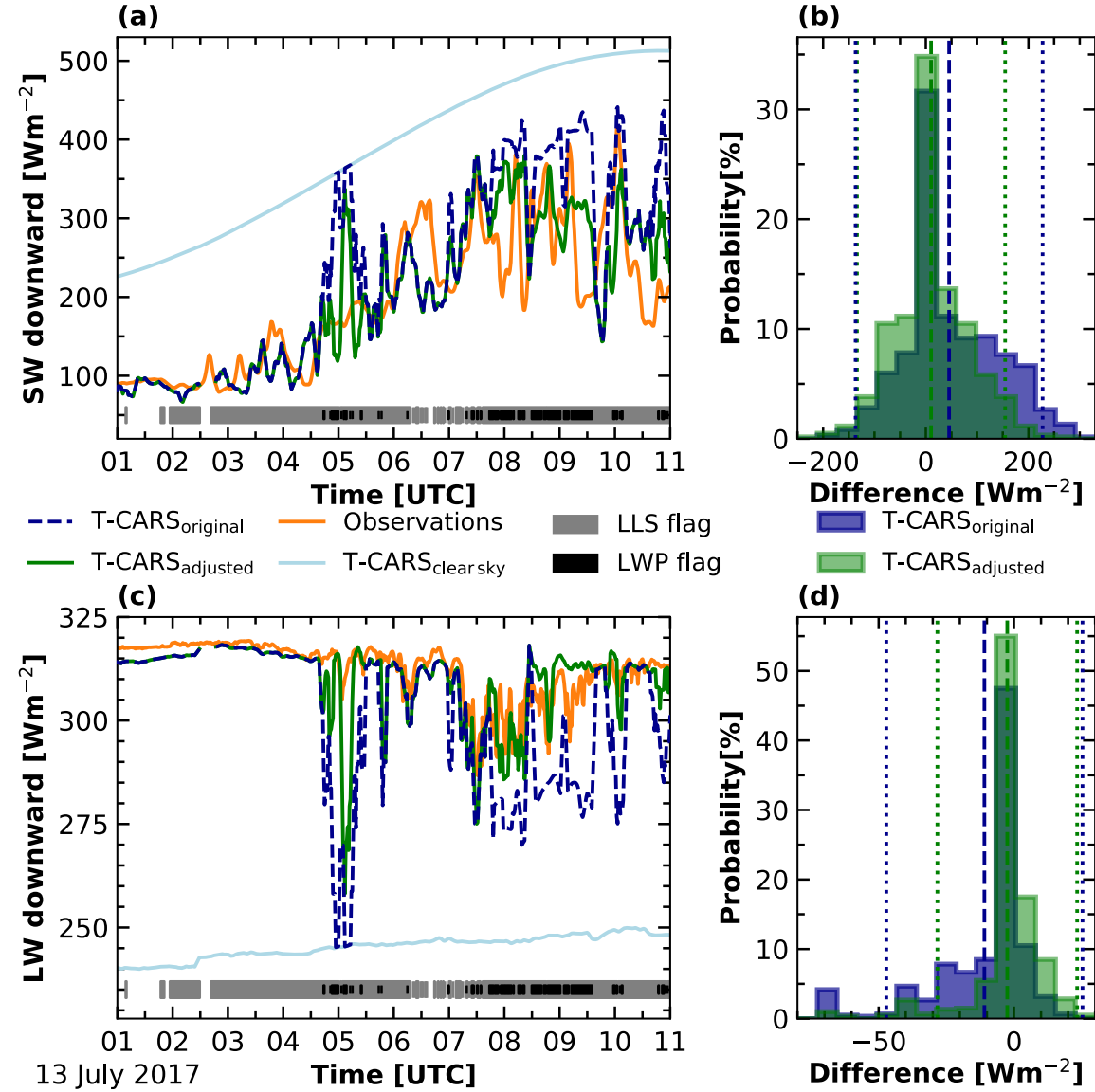


Figure 6.5: Results of the T-CARS simulations for the shortwave downwelling flux (a) and the longwave downwelling flux (c) at the surface for the same period as shown in Figure 6.1. In blue, the irradiances derived for the original Cloudnet classification and in green for the adjusted classification are shown together with the respective measured values from the OCEANET-Atmosphere pyranometer or pyrgeometer in orange. In light blue, the clear sky results from the T-CARS simulations are depicted. Additionally, the occurrence of LLS cloud is indicated by the gray LLS flag at the bottom of panels (a) and (c). The black LWP flag indicate periods with $\Delta\text{LWP} > 10 \text{ g m}^{-2}$. A histogram of the respective differences (simulated minus observed) is given in panels (b) and (d). The dashed lines in (b) and (d) depict the corresponding mean values and the dotted lines show the two- σ standard deviation. The gap in the T-CARS irradiances around 02:40 UTC is due to missing Cloudnet data.

downward flux difference and the standard deviation for SW_{\downarrow} was $(10 \pm 72) \text{ W m}^{-2}$, and for LW_{\downarrow} $(-2.5 \pm 12) \text{ W m}^{-2}$ (green dashed and dotted lines in Fig 6.5 (b) and (d), respectively).

The resulting cloud radiative effect can be derived based on the upwelling and downwelling irradiances from the T-CARS simulations and following Eq. (6.1) – (6.5). During the investigated period the net surface CRE decreased on average by 38 W m^{-2} , when applying the adjusted classification scheme compared to the default one. This decrease in CRE is because the cooling effect induced by the clouds in the shortwave dominated over the cloud longwave warming in this situation.

Figure 6.6 (a) shows the net atmospheric CRE for the original Cloudnet classification in dashed-blue and the adjusted approach in green. Diurnal variations are one of the main drivers of the atmospheric cloud radiative effect during this period. At the beginning of the period, a positive CRE was found due to the low solar elevation angle, which turned negative at around 05:00 UTC. However, the deviations based on the adjustments in the cloud classification as already apparent in Figure 6.5 (a) and (c) propagate and arise also in the net atmospheric cloud radiative effect as can be seen in the resulting differences shown in Figure 6.6 (b). Differences of up to 100 W m^{-2} were calculated, e.g., around 10:00 UTC. On average the T-CARS_{original} approach yielded a net atmospheric CRE of -46 W m^{-2} , while

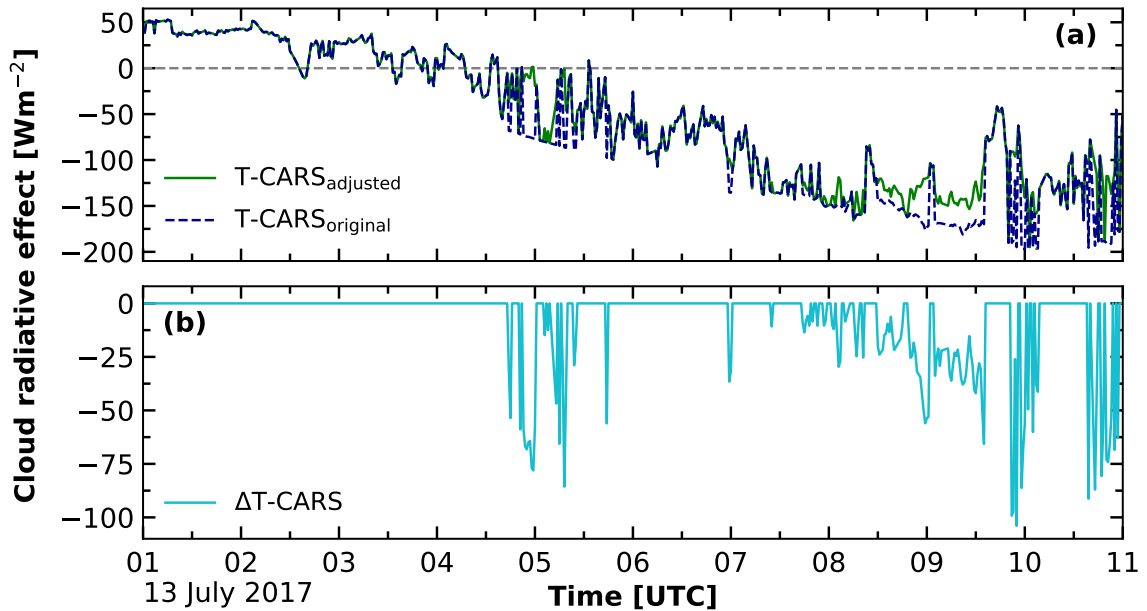


Figure 6.6: Net atmospheric CRE derived by T-CARS for the same period as shown in Figure 6.1. In panel (a) the CRE derived based on the original Cloudnet classification (blue, dashed) and the CRE using the adjusted approach presented in this thesis (green) are depicted. In panel (b) the respective difference ($\Delta\text{T-CARS} = \text{T-CARS}_{\text{original}} - \text{T-CARS}_{\text{adjusted}}$) is shown.

the net atmospheric CRE based on the T-CARS_{adjusted} simulation was -8 W m^{-2} during the presented period.

Statistical analysis

The presented case study shows the potential of a more sophisticated Arctic cloud classification approach on the performance of radiative transfer simulations. The discussed situation is to some extent representative for the whole PS106 campaign. During 8.5 % of the observational time an $\Delta\text{LWP} > 10 \text{ g m}^{-2}$ was observed. In 96.5 % of these cases LLS clouds were observed. As can be seen in Figure 6.7, the daily occurrence of $\Delta\text{LWP} > 10 \text{ g m}^{-2}$ (orange) is correlated with a high occurrence of LLS (purple). However, an increased appearance of horizontal visibility below 1 km (gray in Figure 6.7) seems not to be sufficient to explain the enhanced ΔLWP values altogether, for example on 5 and 6 July there was almost no fog detected but during 40 % of the day $\Delta\text{LWP} > 10 \text{ g m}^{-2}$.

Figure 6.7 (b) and (c) shows the daily distribution of the difference between simulated and observed downward irradiances (simulations minus observations), based on the standard Cloudnet products. The default T-CARS simulations overestimated the SW_{\downarrow} on most days during PS106, on average by more than 100 W m^{-2} . The LW_{\downarrow} deviations are more centered around 0 W m^{-2} , however, with values ranging between $\pm 300 \text{ W m}^{-2}$. On average LW_{\downarrow} was overestimated by more than 60 W m^{-2} during PS106. Days with a large daily mean difference (orange bar in each box) are partly correlated with a high frequency of occurrence of LLS during the day (for example during the end of June, beginning of July).

6.3 Discussion

The presented case study shows the potential of obtaining better radiative closure results by improving the liquid-water cloud detection scheme. In the case of failed liquid-water detection, large discrepancies between the simulated and observed downwelling SW and LW irradiances were observed. The reason the liquid-water occurrence was missed is due to complete attenuation of the lidar signal at height levels below the lowest detected range gate of the cloud radar. A way to detect liquid-water beyond lidar signal attenuation would be the application of a cloud radar multipeak analysis as proposed, e.g., by Radenz et al. [2019], or the application of an artificial neural network as introduced by Kalesse-Los et al. [2021]. However, these techniques make use of cloud radar measurements and thus they are only applicable in the case of higher-reaching clouds. For low-level clouds with a cloud top below the lowest range gate of the cloud radar, these approaches are of limited use. Single-layer LLS, i.e., LLS without another cloud layer above 165 m, have been observed during PS106 for about 5 % of the entire observational time and with a daily occurrence of up to 40 % [e.g., 1 June 2017, see Figure 4.13 (c)]. In combination with overlaying clouds, LLS have been observed during 50 % of the observational time. Also, the horizontal visibility sensor aboard

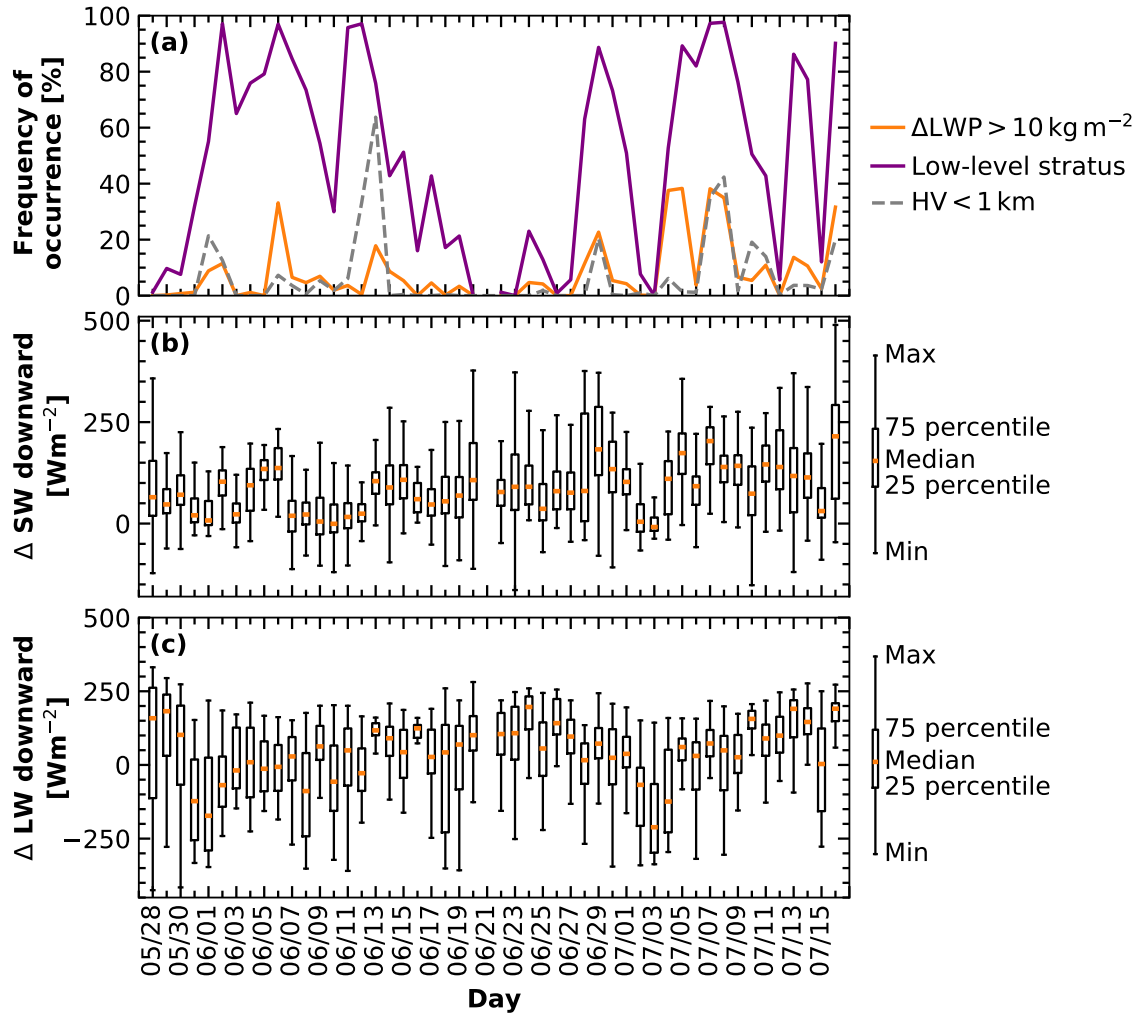


Figure 6.7: Daily occurrence of low-level stratus (purple) and horizontal visibility (HV) below 1 km (gray) during PS106 as in Figure 4.13 (b). The daily occurrence of $\Delta\text{LWP} > 10 \text{ g m}^{-2}$ is highlighted in orange. In panel (b) and (c) the daily distribution of the deviation of the simulated irradiance by T-CARS based simulation on the original classification scheme and the measurements are shown (simulation minus observation) for SW_{\downarrow} and LW_{\downarrow} .

Polarstern was not able to detect these clouds, because the LLS base was frequently too high. Hence, the application of the Polly^{XT} near-field capabilities is crucial to detect these clouds.

Besides the detection of these clouds, also the determination of the cloud microphysics for the LLS clouds poses a challenge. Approaches for liquid-water content and liquid droplet effective radius, as they are for example implemented in Cloudnet, often rely on cloud radar reflectivity [e.g., Frisch et al., 2002; O’Connor et al., 2005]. Additional approaches using lidar Raman dual-field-of-view capabilities exist meanwhile [Jimenez et al., 2020] (this technique did not yet exist for PS106). However, to apply these techniques a complete overlap between

the laser pulse footprint and the receiving field-of-view is mandatory and thus these methods are not applicable for the low-level clouds.

The liquid-water cloud microphysical properties were thus derived by a simple but effective analysis of the LWP. The combination of the LLS detection and the liquid-water cloud microphysic estimation proved to work well for the presented case study. The values calculated suggest that by applying the adjusted method radiative closure is achieved since the mean flux differences were below the instrumental uncertainties [i.e., $\pm 20 \text{ W m}^{-2}$ pyranometer (SW_{\downarrow}) and $\pm 10 \text{ W m}^{-2}$ for pyrgeometer (LW_{\downarrow}), Lanconelli et al., 2011].

The evaluation of the performance of radiative transfer simulations and throughout analysis of the simulations for the entire PS106 cruise were not in the scope of this study. Such studies were conducted in cooperation, e.g., by Barrientos Velasco et al. [2021] based on the introduced Cloudnet data set. The referred studies in the introduction of this chapter, the presented case study, and the performance of radiative transfer simulations are great examples of the strong collaborations within (AC)³.

Chapter 7

Summary and outlook

A synergistic data set from an extensive suite of ground-based remote-sensing instruments was presented. This data set was collected utilizing the OCEANET-Atmosphere platform during the 2-month Polarstern campaign PS106. PS106 was conducted in the rough environment of the High Arctic, north and northeast of Svalbard in the Arctic summer of 2017. The Cloudnet algorithm was used to derive the cloud micro- and macrophysical properties continuously. At the same time, different Cloudnet products were improved. Namely, approaches to derive eddy dissipation rates, ice crystal effective radius, and low-level stratus cloud occurrence. The observations conducted during PS106 and the retrieved Cloudnet products were published in the long-term data archive Pangaea [Griesche et al., 2019, 2020b,c,d,e,f,g,h,i]. This thesis describes and evaluates in detail the deployed instrumentation, data corrections, and applied processing schemes. A study on the influence of thermodynamic surface coupling on heterogeneous ice formation in Arctic clouds was presented. Also, the application of the data set to study the cloud occurrence and aerosol-cloud interactions during the PS106 cruise with a focus on low-level clouds was demonstrated. Finally, contributions of the data set towards improved radiative transfer simulations were highlighted.

Only a few campaigns with comparable equipment have been performed in recent years at these northern latitudes. A new feature of PS106 was the deployment of a motion-stabilized, vertically pointing 35-GHz cloud radar [Griesche et al., 2020a]. After the cruise, the cloud radar Doppler velocity was corrected for the movement of the ship. The reached leveling precision by the applied stabilization platform was better than 1° . The heave correction reduced the fraction of the ship's movement in the power spectral density of the cloud radar Doppler velocity by a factor of 15. It was shown that EDR could be derived from the Doppler velocities after the motion correction.

Cloudnet products were derived from the measurements and improved to address the challenges posed by Arctic clouds [Griesche et al., 2020a]. New approaches for the retrieval of eddy dissipation rates and ice crystal effective radius were presented. Additionally, the importance of the lowest detection range for remote-sensing instruments was highlighted.

This discussion resulted in the development of a new detection approach for low-level stratus cloud layers based on the Polly^{XT}_OCEANET measurements. These low clouds (between 50 m and 165 m height) are missed by most of the common remote-sensing techniques and were observed during 50 % of the observational time. The implementation of a new ice effective radii retrieval was one step towards continuous, high resolved radiative transfer simulations and eventually a better understanding of the radiative effects of clouds and aerosol on the Arctic climate.

The highlight of this thesis was the first presentation of heterogeneous ice-formation temperatures for Arctic mixed-phase clouds in dependence on their surface-coupling state. This study was published in Griesche et al. [2021]. Based on the analysis of lidar, cloud radar, and radiosonde observations differences in the occurrence of ice-containing clouds for surface-coupled and -decoupled clouds were investigated. Besides minimum cloud temperature, the data show a significant dependence of the liquid-water-dominated cloud layer base height and coupling state of the cloud on the probability of ice formation. Figure 5.4 compares the fraction of ice-containing clouds for different minimum cloud temperatures for coupled and decoupled situations. The strongest differences were found at minimum cloud temperatures slightly below freezing. Above -15°C , surface-coupled ice-containing clouds occur more frequently by a factor of 5 in numbers of observed clouds and by a factor of 2 in frequency of occurrence. Furthermore, the number of analyzed data is largest in this range, which underlines the significance of this finding. A similar ice cloud occurrence below -15°C as found over Leipzig together with a land-based aerosol source attribution suggests the presence of continental aerosol in the free troposphere. Potential reasons for the surface-coupling effects at the high subzero temperatures on cloud ice occurrence were examined through a literature survey. However, seeding from higher ice clouds, blown snow, and ice fog could be ruled out for the analyzed observation period. The most likely explanation was found to be a larger reservoir of biological ice-nucleating particles of marine origin in the surface-coupled marine boundary layer. The larger abundance of INP leads to higher freezing efficiency in those clouds which have at least their base in the boundary layer. This conclusion is corroborated by recent in-situ-based studies of the INPC which took place in close vicinity to open-water surfaces in the marine Arctic boundary layer.

Furthermore, the presented data set is of great value for radiative closure studies. In this thesis, it has been shown that a detailed characterization of the low-level clouds can significantly improve the quality of radiative transfer simulations. In the standard configuration of processing schemes for cloud microphysical products, such as Cloudnet, the low-level clouds are often underrepresented, which eventually leads to large differences in short- and longwave irradiances. A difference in the derived CRE of up to 100 W m^{-2} was calculated in the presented case study, when these low-level clouds were considered in T-CARS input compared to the application of the standard Cloudnet products. Since it has been shown by previous radiative studies, that low-level clouds are of great importance for

the Arctic energy budget, an accurate representation of these clouds in radiative studies is a prerequisite for the understanding of Arctic amplification.

Future work should confront the observed cloud macro- and microphysical properties as well as the EDR with high-resolution model simulations along the PS106 track that have been carried out in the framework of (AC)³. The herein introduced remote-sensing techniques are to be applied to the data set of the recently conducted one-year polar ice drift of RV Polarstern during the MOSAiC project [Shupe et al., 2020]. This data will provide an unprecedented view on Arctic aerosol and mixed-phase clouds. A Cloudnet data set derived from the MOSAiC observations is currently under development. This data set will substantially contribute to our understanding of the role of clouds in the current warming of the Arctic climate system. Improvement of the cloud microphysical and radiative properties may be achieved with an optimal estimation technique based on the synergistic combination of remote sensing, LES experiments, and radiative transfer model simulations. Such a method already introduced in Fielding et al. [2014, 2015] can give the opportunity to derive synthetic Cloudnet products for radiative transfer applications. Implementing this method is outside the scope of Project A01 phase 1 of (AC)³. However, its appliance can be relevant for, e.g., the MOSAiC data set.

Future studies should also focus on the linkage between types of aerosol raised to cloud level and the fraction of ice-containing clouds to confirm the hypothesis that INPs of biogenic origin play a significant role in heterogeneous ice formation in the Arctic at temperatures above -15°C . The observed effect is to be investigated using, e.g., LES and it should be checked if a variation in the INP abundance under different surface coupling situations can reproduce the findings. Additional Arctic and also Antarctic cloud data sets should be investigated with respect to their distance from the marginal ice zone, open leads, and polynyas. The MOSAiC observations provide already a valuable data set for a continuative study of Arctic mixed-phase clouds. Furthermore, TROPOS has planned to perform ground-based remote sensing at the Antarctic station Neumayer III starting in 2023. In the framework of the recently funded COALA project, the OCEANET-Atmosphere suite will be brought to the Neumayer III station for one year to deliver a Cloudnet data set. If indeed INPs from marine origin control heterogeneous ice formation that strongly, a decrease in this effect with increasing distance from open water should be detectable. For a better understanding of the phenomenon, measurements in different seasons and regions of the Earth should be made to determine if this effect is only characteristic for the Arctic summer. Also, a possible impact of the different ice occurrence under surface-coupled and -decoupled situations on the radiation balance are to be investigated. If in a changing Arctic low-level clouds are subject to different conditions that impact the cloud microphysics, this will feed back on the drivers of Arctic amplification.

Appendix A

Determination of a volume depolarization threshold for lidar-based ice detection

A lidar volume depolarization ratio threshold for the ice detection during aerosol free periods was used in Chapter 5. This threshold was determined by theoretical considerations of lidar scattering functions and their effect on the depolarization of the emitted light, as described, e.g., in Freudenthaler et al. [2009], and the relationships between temperature (T) and reflectivity (Z), and ice water content (IWC) and extinction coefficient (α) from Hogan et al. [2006].

The extinction coefficient was calculated for IWC between $10^{-7} \text{ kg m}^{-3}$ and 10 kg m^{-3} . From the extinction coefficient and a lidar ratio of 30 sr for ice clouds [Ansmann et al., 1992b] the theoretical particle backscatter coefficient was calculated as function of IWC and T. Following Elterman [1968] and Teillet [1990], the molecular extinction coefficient can be obtained. Using the constant molecular lidar ratio $S^{\text{mol}} = \frac{8\pi}{3}$ one can determine the molecular backscatter coefficient. The molecular volume depolarization ratio for Rayleigh scattering at 532 nm was approximated with 0.01 [Biele et al., 2000]. Following Freudenthaler et al. [2009], the theoretical volume depolarization ratio can then be calculated from the particle backscatter coefficient, the molecular backscatter coefficient, and the molecular volume depolarization ratio as a function of the particle volume depolarization ratio. The resulting relationship between IWC and volume depolarization ratio for -5°C (blue) and -30°C (orange) at 532 nm are shown in Figure A.1.

Additionally, the depolarization caused by scattering at molecules in the atmosphere is marked with the dashed green line. From this relationship, it follows that a distinct identification of ice using the volume depolarization ratio of the 532 nm wavelength is only possible above a volume depolarization ratio of 0.03, which corresponds to an IWC of

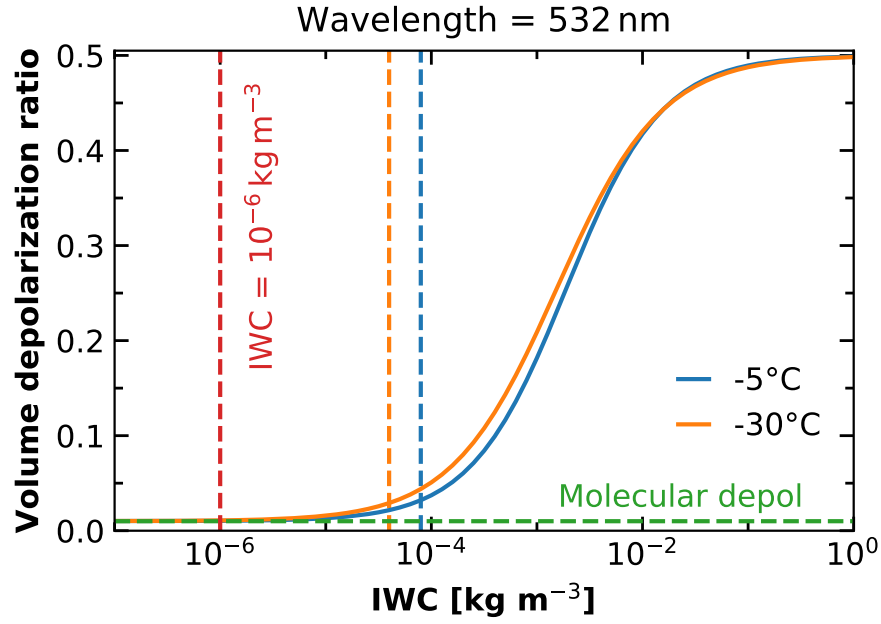


Figure A.1: Theoretically derived relationship between IWC and lidar volume depolarization ratio at 532 nm for -5°C (blue) and -30°C (orange). The respective vertical dashed lines mark the IWC at volume depolarization threshold of 0.03. The green dashed line marks the molecular depolarization and the red dashed line the IWC threshold for lidar based ice detection of $10^{-6} \text{ kg m}^{-3}$ from Bühl et al. [2013].

$8 \cdot 10^{-5} \text{ kg m}^{-3}$ for -5°C (dashed blue line; $4 \cdot 10^{-5} \text{ kg m}^{-3}$ at -30°C , dashed orange line). For comparison, also the threshold from Bühl et al. [2013] of $\text{IWC} = 10^{-6} \text{ kg m}^{-3}$ for ice detection using the 532 nm lidar volume depolarization ratio is shown in Figure A.1 by the dashed red line.

Bibliography

- Abbatt, J. P. D. et al. (2019). “Overview paper: New insights into aerosol and climate in the Arctic”. *Atmospheric Chemistry and Physics* 19.4, pp. 2527–2560. DOI: 10.5194/acp-19-2527-2019.
- Achtert, P., I. M. Brooks, B. J. Brooks, B. I. Moat, J. Prytherch, P. O. G. Persson, and M. Tjernström (2015). “Measurement of wind profiles by motion-stabilised ship-borne Doppler lidar”. *Atmospheric Measurement Techniques* 8.11, pp. 4993–5007. DOI: 10.5194/amt-8-4993-2015.
- Albrecht, B. A. (1989). “Aerosols, Cloud Microphysics, and Fractional Cloudiness”. *Science* 245.4923, pp. 1227–1230. ISSN: 0036-8075. DOI: 10.1126/science.245.4923.1227.
- Anderson, G., S. Clough, F. Kneizys, J. Chetwynd, and E. Shettle (1986). “AFGL Atmospheric Constituent Profiles (0.120km)”, p. 46.
- Anderson, T. L., R. J. Charlson, N. Bellouin, O. Boucher, M. Chin, S. A. Christopher, J. Haywood, Y. J. Kaufman, S. Kinne, J. A. Ogren, et al. (2005). “An “A-Train” strategy for quantifying direct climate forcing by anthropogenic aerosols”. *Bulletin of the American Meteorological Society* 86.12, pp. 1795–1810. DOI: 10.1175/BAMS-86-12-1795.
- Ansmann, A. (2019). “personal communication”.
- Ansmann, A., M. Riebesell, U. Wandinger, C. Weitkamp, E. Voss, W. Lahmann, and W. Michaelis (1992a). “Combined raman elastic-backscatter LIDAR for vertical profiling of moisture, aerosol extinction, backscatter, and LIDAR ratio”. *Applied Physics B* 55.1, pp. 18–28. ISSN: 1432-0649. DOI: 10.1007/BF00348608.
- Ansmann, A., M. Riebesell, and C. Weitkamp (1990). “Measurement of atmospheric aerosol extinction profiles with a Raman lidar”. *Opt. Lett.* 15.13, pp. 746–748. DOI: 10.1364/OL.15.000746.
- Ansmann, A., M. Tesche, D. Althausen, D. Müller, P. Seifert, V. Freudenthaler, B. Heese, M. Wiegner, G. Pisani, P. Knippertz, and O. Dubovik (2008). “Influence of Saharan dust on cloud glaciation in southern Morocco during the Saharan Mineral Dust Experiment”. *Journal of Geophysical Research: Atmospheres* 113.D4, p. D04210. DOI: 10.1029/2007JD008785.
- Ansmann, A., M. Tesche, P. Seifert, D. Althausen, R. Engelmann, J. Fruntke, U. Wandinger, I. Mattis, and D. Müller (2009). “Evolution of the ice phase in tropical altocumulus: SAMUM lidar observations over Cape Verde”. *Journal of Geophysical Research: Atmospheres* 114.D17, p. D17208. DOI: 10.1029/2008JD011659.
- Ansmann, A., U. Wandinger, M. Riebesell, C. Weitkamp, and W. Michaelis (1992b). “Independent measurement of extinction and backscatter profiles in cirrus clouds by using a combined Raman elastic-backscatter lidar”. *Appl. Opt.* 31.33, pp. 7113–7131. DOI: 10.1364/AO.31.007113.
- Arrhenius, S. (1897). “On the Influence of Carbonic Acid in the Air upon the Temperature of the Earth”. *Publications of the Astronomical Society of the Pacific* 9, p. 14. DOI: 10.1086/121158.

- Baars, H., A. Ansmann, D. Althausen, R. Engelmann, P. Artaxo, T. Pauliquevis, and R. Souza (2011). “Further evidence for significant smoke transport from Africa to Amazonia”. *Geophysical Research Letters* 38.20, p. L20802. DOI: 10.1029/2011GL049200.
- Baars, H., A. Ansmann, D. Althausen, R. Engelmann, B. Heese, D. Müller, P. Artaxo, M. Paixao, T. Pauliquevis, and R. Souza (2012). “Aerosol profiling with lidar in the Amazon Basin during the wet and dry season”. *Journal of Geophysical Research: Atmospheres* 117.D21, p. D21201. DOI: 10.1029/2012JD018338.
- Baars, H., T. Kanitz, R. Engelmann, D. Althausen, B. Heese, M. Komppula, J. Preißler, M. Tesche, A. Ansmann, U. Wandinger, J.-H. Lim, J. Y. Ahn, I. S. Stachlewska, V. Amiridis, E. Marinou, P. Seifert, J. Hofer, A. Skupin, F. Schneider, S. Bohlmann, A. Foth, S. Bley, A. Pfüller, E. Giannakaki, H. Lihavainen, Y. Viisanen, R. K. Hooda, S. N. Pereira, D. Bortoli, F. Wagner, I. Mattis, L. Janicka, K. M. Markowicz, P. Achtert, P. Artaxo, T. Pauliquevis, R. A. F. Souza, V. P. Sharma, P. G. van Zyl, J. P. Beukes, J. Sun, E. G. Rohwer, R. Deng, R.-E. Mamouri, and F. Zamorano (2016). “An overview of the first decade of Polly^{NET}: an emerging network of automated Raman-polarization lidars for continuous aerosol profiling”. *Atmospheric Chemistry and Physics* 16.8, pp. 5111–5137. DOI: 10.5194/acp-16-5111-2016.
- Baars, H., P. Seifert, R. Engelmann, and U. Wandinger (2017). “Target categorization of aerosol and clouds by continuous multiwavelength-polarization lidar measurements”. *Atmospheric Measurement Techniques* 10.9, pp. 3175–3201. DOI: 10.5194/amt-10-3175-2017.
- Barker, H. W., G. L. Stephens, P. T. Partain, J. W. Bergman, B. Bonnel, K. Campana, E. E. Clothiaux, S. Clough, S. Cusack, J. Delamere, J. Edwards, K. F. Evans, Y. Fouquart, S. Freidenreich, V. Galin, Y. Hou, S. Kato, J. Li, E. Mlawer, J.-J. Morcrette, W. O’Hirok, P. Räisänen, V. Ramaswamy, B. Ritter, E. Rozanov, M. Schlesinger, K. Shibata, P. Sporyshev, Z. Sun, M. Wendisch, N. Wood, and F. Yang (2003). “Assessing 1D Atmospheric Solar Radiative Transfer Models: Interpretation and Handling of Unresolved Clouds”. *Journal of Climate* 16.16, pp. 2676–2699. DOI: 10.1175/1520-0442(2003)016<2676:ADASRT>2.0.CO;2.
- Barlakas, V., H. Deneke, and A. Macke (2020). “The sub-adiabatic model as a concept for evaluating the representation and radiative effects of low-level clouds in a high-resolution atmospheric model”. *Atmospheric Chemistry and Physics* 20.1, pp. 303–322. DOI: 10.5194/acp-20-303-2020.
- Barrientos Velasco, C., H. Deneke, H. Griesche, P. Seifert, R. Engelmann, and A. Macke (2020). “Spatiotemporal variability of solar radiation introduced by clouds over Arctic sea ice”. *Atmospheric Measurement Techniques* 13.4, pp. 1757–1775. DOI: 10.5194/amt-13-1757-2020.
- Barrientos Velasco, C., H. Deneke, A. Hünerbein, H. J. Griesche, P. Seifert, and A. Macke (2021). “Radiative closure and cloud effects on the radiation budget based on satellite and ship-borne observations during the Arctic summer research cruise PS106”. (*in prep.*)
- Battan, L. J. (1973). *Radar observation of the atmosphere*. The University of Chicago Press, Chicago.
- Bellouin, N., J. Quaas, E. Gryspeerdt, S. Kinne, P. Stier, D. Watson-Parris, O. Boucher, K. S. Carslaw, M. Christensen, A.-L. Daniau, J.-L. Dufresne, G. Feingold, S. Fiedler, P. Forster, A. Gettelman, J. M. Haywood, U. Lohmann, F. Malavelle, T. Mauritsen, D. T. McCoy, G. Myhre, J. Mülmenstädt, D. Neubauer, A. Possner, M. Rugenstein, Y. Sato, M. Schulz, S. E. Schwartz, O. Sourdeval, T. Storelvmo, V. Toll, D. Winker, and B. Stevens (2020). “Bounding Global Aerosol Radiative Forcing of Climate Change”. *Reviews of Geophysics* 58.1. e2019RG000660 10.1029/2019RG000660, e2019RG000660. DOI: <https://doi.org/10.1029/2019RG000660>.
- Bergeron, T. (1935). “On the physics of clouds and precipitation”. *Proc. 5th Assembly U.G.G.I., Lisbon, Portugal, 1935*, pp. 156–180.

-
- Biele, J., G. Beyerle, and G. Baumgarten (2000). “Polarization lidar: Corrections of instrumental effects”. *Opt. Express* 7.12, pp. 427–435. DOI: 10.1364/OE.7.000427.
- Bigg, E. K. (1996). “Ice forming nuclei in the high Arctic”. *Tellus B* 48.2, pp. 223–233. DOI: 10.1034/j.1600-0889.1996.t01-1-00007.x.
- Blanchard, Y., A. Royer, N. T. O’Neill, D. D. Turner, and E. W. Eloranta (2017). “Thin ice clouds in the Arctic: cloud optical depth and particle size retrieved from ground-based thermal infrared radiometry”. *Atmospheric Measurement Techniques* 10.6, pp. 2129–2147. DOI: 10.5194/amt-10-2129-2017.
- Block, K., F. A. Schneider, J. Mülmenstädt, M. Salzmann, and J. Quaas (2020). “Climate models disagree on the sign of total radiative feedback in the Arctic”. *Tellus A: Dynamic Meteorology and Oceanography* 72.1, pp. 1–14. DOI: 10.1080/16000870.2019.1696139.
- Böhlmann, S., H. Baars, M. Radenz, R. Engelmann, and A. Macke (2018). “Ship-borne aerosol profiling with lidar over the Atlantic Ocean: from pure marine conditions to complex dust–smoke mixtures”. *Atmospheric Chemistry and Physics* 18.13, pp. 9661–9679. DOI: 10.5194/acp-18-9661-2018.
- Borquez, P., E. Luke, and P. Kollias (2016). “On the unified estimation of turbulence eddy dissipation rate using Doppler cloud radars and lidars”. *Journal of Geophysical Research: Atmospheres* 121.10, pp. 5972–5989. DOI: 10.1002/2015JD024543.
- Brooks, I. M., M. Tjernström, P. O. G. Persson, M. D. Shupe, R. A. Atkinson, G. Canut, C. E. Birch, T. Mauritsen, J. Sedlar, and B. J. Brooks (2017). “The Turbulent Structure of the Arctic Summer Boundary Layer During The Arctic Summer Cloud-Ocean Study”. *Journal of Geophysical Research: Atmospheres* 122.18, pp. 9685–9704. DOI: 10.1002/2017JD027234.
- Broxton, P. D., X. Zeng, D. Sulla-Menashe, and P. A. Troch (2014). “A Global Land Cover Climatology Using MODIS Data”. *Journal of Applied Meteorology and Climatology* 53.6, pp. 1593–1605. DOI: 10.1175/JAMC-D-13-0270.1.
- Bühl, J., A. Ansmann, P. Seifert, H. Baars, and R. Engelmann (2013). “Toward a quantitative characterization of heterogeneous ice formation with lidar/radar: Comparison of CALIPSO/CloudSat with ground-based observations”. *Geophys. Res. Lett.* 40.16, pp. 4404–4408. ISSN: 0094-8276. DOI: 10.1002/grl.50792.
- Bühl, J., P. Seifert, A. Myagkov, and A. Ansmann (2016). “Measuring ice- and liquid-water properties in mixed-phase cloud layers at the Leipzig Cloudnet station”. *Atmospheric Chemistry and Physics* 16.16, pp. 10609–10620. DOI: 10.5194/acp-16-10609-2016.
- Bühl, J., P. Seifert, M. Radenz, H. Baars, and A. Ansmann (2019). “Ice crystal number concentration from lidar, cloud radar and radar wind profiler measurements”. *Atmospheric Measurement Techniques* 12.12, pp. 6601–6617. DOI: 10.5194/amt-12-6601-2019.
- Burrows, S. M., C. Hoose, U. Pöschl, and M. G. Lawrence (2013). “Ice nuclei in marine air: biogenic particles or dust?” *Atmospheric Chemistry and Physics* 13.1, pp. 245–267. DOI: 10.5194/acp-13-245-2013.
- Caughey, S. J., J. C. Wyngaard, and J. C. Kaimal (1979). “Turbulence in the Evolving Stable Boundary Layer”. *Journal of the Atmospheric Sciences* 36.6, pp. 1041–1052. DOI: 10.1175/1520-0469(1979)036<1041:TITESB>2.0.CO;2.
- Cazenave, Q., M. Ceccaldi, J. Delanoë, J. Pelon, S. Groß, and A. Heymsfield (2019). “Evolution of DARDAR-CLOUD ice cloud retrievals: new parameters and impacts on the retrieved microphysical properties”. *Atmospheric Measurement Techniques* 12.5, pp. 2819–2835. DOI: 10.5194/amt-12-2819-2019.
-

- Cesana, G., J. E. Kay, H. Chepfer, J. M. English, and G. de Boer (2012). “Ubiquitous low-level liquid-containing Arctic clouds: New observations and climate model constraints from CALIPSO-GOCCP”. *Geophysical Research Letters* 39.20. DOI: 10.1029/2012GL053385.
- Choi, Y.-S., C.-H. Ho, C.-E. Park, T. Storelvmo, and I. Tan (2014). “Influence of cloud phase composition on climate feedbacks”. *Journal of Geophysical Research: Atmospheres* 119.7, pp. 3687–3700. DOI: 10.1002/2013JD020582.
- Chung, E.-S., K.-J. Ha, A. Timmermann, M. F. Stuecker, T. Bodai, and S.-K. Lee (2021). “Cold-Season Arctic Amplification Driven by Arctic Ocean-Mediated Seasonal Energy Transfer”. *Earth’s Future* 9.2, e2020EF001898. DOI: 10.1029/2020EF001898.
- Clough, S., M. Shephard, E. Mlawer, J. Delamere, M. Iacono, K. Cady-Pereira, S. Boukabara, and P. Brown (2005). “Atmospheric radiative transfer modeling: a summary of the AER codes”. *Journal of Quantitative Spectroscopy and Radiative Transfer* 91.2, pp. 233–244. ISSN: 0022-4073. DOI: 10.1016/j.jqsrt.2004.05.058.
- Creamean, J. M., G. de Boer, H. Telg, F. Mei, D. Dexheimer, M. D. Shupe, A. Solomon, and A. McComiskey (2021). “Assessing the vertical structure of Arctic aerosols using balloon-borne measurements”. *Atmospheric Chemistry and Physics* 21.3, pp. 1737–1757. DOI: 10.5194/acp-21-1737-2021.
- Creamean, J. M., R. M. Kirpes, K. A. Pratt, N. J. Spada, M. Maahn, G. de Boer, R. C. Schnell, and S. China (2018a). “Marine and terrestrial influences on ice nucleating particles during continuous springtime measurements in an Arctic oilfield location”. *Atmospheric Chemistry and Physics* 18.24, pp. 18023–18042. DOI: 10.5194/acp-18-18023-2018.
- Creamean, J. M., M. Maahn, G. de Boer, A. McComiskey, A. J. Sedlacek, and Y. Feng (2018b). “The influence of local oil exploration and regional wildfires on summer 2015 aerosol over the North Slope of Alaska”. *Atmospheric Chemistry and Physics* 18.2, pp. 555–570. DOI: 10.5194/acp-18-555-2018.
- Crewell, S., K. Ebell, P. Konjari, M. Mech, T. Nomokonova, A. Radovan, D. Strack, A. M. Triana-Gómez, S. Noël, R. Scarlat, G. Spreen, M. Maturilli, A. Rinke, I. Gorodetskaya, C. Viceto, T. August, and M. Schröder (2021). “A systematic assessment of water vapor products in the Arctic: from instantaneous measurements to monthly means”. *Atmospheric Measurement Techniques* 14.7, pp. 4829–4856. DOI: 10.5194/amt-14-4829-2021.
- Curry, J. A., P. V. Hobbs, M. D. King, D. A. Randall, P. Minnis, G. A. Isaac, J. O. Pinto, T. Uttal, A. Bucholtz, D. G. Cripe, H. Gerber, C. W. Fairall, T. J. Garrett, J. Hudson, J. M. Intrieri, C. Jakob, T. Jensen, P. Lawson, D. Marcotte, L. Nguyen, P. Pilewskie, A. Rangno, D. C. Rogers, K. B. Strawbridge, F. P. J. Valero, A. G. Williams, and D. Wylie (2000). “FIRE Arctic Clouds Experiment”. *Bulletin of the American Meteorological Society* 81.1, pp. 5–30. DOI: 10.1175/1520-0477(2000)081<0005:FACE>2.3.CO;2.
- Curry, J. A., J. L. Schramm, and E. E. Ebert (1995). “Sea Ice-Albedo Climate Feedback Mechanism”. *Journal of Climate* 8.2, pp. 240–247. DOI: 10.1175/1520-0442(1995)008<0240:SIACFM>2.0.CO;2.
- Curry, J. A., J. L. Schramm, W. B. Rossow, and D. Randall (1996). “Overview of Arctic Cloud and Radiation Characteristics”. *Journal of Climate* 9.8, pp. 1731–1764. ISSN: 0894-8755. DOI: 10.1175/1520-0442(1996)009<1731:00ACAR>2.0.CO;2.
- Dai, G., D. Althausen, J. Hofer, R. Engelmann, P. Seifert, J. Bühl, R.-E. Mamouri, S. Wu, and A. Ansmann (2018). “Calibration of Raman lidar water vapor profiles by means of AERONET

-
- photometer observations and GDAS meteorological data”. *Atmospheric Measurement Techniques* 11.5, pp. 2735–2748. DOI: 10.5194/amt-11-2735-2018.
- de Boer, G., E. W. Eloranta, and M. D. Shupe (2009). “Arctic Mixed-Phase Stratiform Cloud Properties from Multiple Years of Surface-Based Measurements at Two High-Latitude Locations”. *Journal of the Atmospheric Sciences* 66.9, pp. 2874–2887. DOI: 10.1175/2009JAS3029.1.
- de Boer, G., H. Morrison, M. D. Shupe, and R. Hildner (2011). “Evidence of liquid dependent ice nucleation in high-latitude stratiform clouds from surface remote sensors”. *Geophysical Research Letters* 38.1, p. L01803. DOI: 10.1029/2010GL046016.
- Delanoë, J., A. Protat, D. Bouniol, A. Heymsfield, A. Bansemer, and P. Brown (2007). “The Characterization of Ice Cloud Properties from Doppler Radar Measurements”. *Journal of Applied Meteorology and Climatology* 46.10, pp. 1682–1698. DOI: 10.1175/JAM2543.1.
- DeMott, P. J., T. C. J. Hill, C. S. McCluskey, K. A. Prather, D. B. Collins, R. C. Sullivan, M. J. Ruppel, R. H. Mason, V. E. Irish, T. Lee, C. Y. Hwang, T. S. Rhee, J. R. Snider, G. R. McMeeking, S. Dhaniyala, E. R. Lewis, J. J. B. Wentzell, J. Abbatt, C. Lee, C. M. Sultana, A. P. Ault, J. L. Axson, M. Diaz Martinez, I. Venero, G. Santos-Figueroa, M. D. Stokes, G. B. Deane, O. L. Mayol-Bracero, V. H. Grassian, T. H. Bertram, A. K. Bertram, B. F. Moffett, and G. D. Franc (2016). “Sea spray aerosol as a unique source of ice nucleating particles”. *Proceedings of the National Academy of Sciences* 113.21, pp. 5797–5803. ISSN: 0027-8424. DOI: 10.1073/pnas.1514034112.
- DeMott, P. J., A. J. Prenni, X. Liu, S. M. Kreidenweis, M. D. Petters, C. H. Twohy, M. S. Richardson, T. Eidhammer, and D. C. Rogers (2010). “Predicting global atmospheric ice nuclei distributions and their impacts on climate”. *Proceedings of the National Academy of Sciences* 107.25, pp. 11217–11222. ISSN: 0027-8424. DOI: 10.1073/pnas.0910818107.
- DeMott, P. J., A. J. Prenni, G. R. McMeeking, R. C. Sullivan, M. D. Petters, Y. Tobo, M. Niemand, O. Möhler, J. R. Snider, Z. Wang, and S. M. Kreidenweis (2015). “Integrating laboratory and field data to quantify the immersion freezing ice nucleation activity of mineral dust particles”. *Atmospheric Chemistry and Physics* 15.1, pp. 393–409. DOI: 10.5194/acp-15-393-2015.
- Diedenhoven, B. van, A. M. Fridlind, A. S. Ackerman, E. W. Eloranta, and G. M. McFarquhar (2009). “An evaluation of ice formation in large-eddy simulations of supercooled Arctic stratocumulus using ground-based lidar and cloud radar”. *Journal of Geophysical Research: Atmospheres* 114.D10, p. D10203. DOI: 10.1029/2008JD011198.
- Donohoe, A., K. C. Armour, A. G. Pendergrass, and D. S. Battisti (2014). “Shortwave and longwave radiative contributions to global warming under increasing CO₂”. *Proceedings of the National Academy of Sciences* 111.47, pp. 16700–16705. ISSN: 0027-8424. DOI: 10.1073/pnas.1412190111.
- Ebell, K., T. Nomokonova, M. Maturilli, and C. Ritter (2019). “Radiative Effect of Clouds at Ny-Ålesund, Svalbard, as Inferred from Ground-Based Remote Sensing Observations”. *Journal of Applied Meteorology and Climatology* 59.1, pp. 3–22. ISSN: 1558-8424. DOI: 10.1175/JAMC-D-19-0080.1.
- Egerer, U., A. Ehrlich, M. Gottschalk, H. Griesche, R. A. J. Neggers, H. Siebert, and M. Wendisch (2021). “Case study of a humidity layer above Arctic stratocumulus and potential turbulent coupling with the cloud top”. *Atmospheric Chemistry and Physics* 21.8, pp. 6347–6364. DOI: 10.5194/acp-21-6347-2021.
- Egerer, U., M. Gottschalk, H. Siebert, A. Ehrlich, and M. Wendisch (2019). “The new BELUGA setup for collocated turbulence and radiation measurements using a tethered balloon: first applications in the cloudy Arctic boundary layer”. *Atmospheric Measurement Techniques* 12.7, pp. 4019–4038. DOI: 10.5194/amt-12-4019-2019.
-

- Elterman, L. (1968). *UV, Visible, and IR Attenuation for Altitudes to 50 Km, 1968*. Environmental research papers. Air Force Cambridge Research Laboratories, Office of Aerospace Research, United States Air Force.
- Engelmann, R., A. Ansmann, K. Ohneiser, H. Griesche, M. Radenz, J. Hofer, D. Althausen, S. Dahlke, M. Maturilli, I. Veselovskii, C. Jimenez, R. Wiesen, H. Baars, J. Bühl, H. Gebauer, M. Haarig, P. Seifert, U. Wandinger, and A. Macke (2021). “Wildfire smoke, Arctic haze, and aerosol effects on mixed-phase and cirrus clouds over the North Pole region during MOSAiC: an introduction”. *Atmospheric Chemistry and Physics* 21.17, pp. 13397–13423. DOI: 10.5194/acp-21-13397-2021.
- Engelmann, R., T. Kanitz, H. Baars, B. Heese, D. Althausen, A. Skupin, U. Wandinger, M. Komppula, I. S. Stachlewska, V. Amiridis, E. Marinou, I. Mattis, H. Linné, and A. Ansmann (2016). “The automated multiwavelength Raman polarization and water-vapor lidar Polly^{XT}: the neXT generation”. *Atmospheric Measurement Techniques* 9.4, pp. 1767–1784. DOI: 10.5194/amt-9-1767-2016.
- Engström, A., J. Karlsson, and G. Svensson (2014). “The Importance of Representing Mixed-Phase Clouds for Simulating Distinctive Atmospheric States in the Arctic*[†]”. *Journal of Climate* 27.1, pp. 265–272. ISSN: 0894-8755. DOI: 10.1175/JCLI-D-13-00271.1.
- Fan, J., S. Ghan, M. Ovchinnikov, X. Liu, P. J. Rasch, and A. Korolev (2011). “Representation of Arctic mixed-phase clouds and the Wegener-Bergeron-Findeisen process in climate models: Perspectives from a cloud-resolving study”. *Journal of Geophysical Research: Atmospheres* 116.D1. DOI: <https://doi.org/10.1029/2010JD015375>.
- Feldl, N., S. Bordoni, and T. M. Merlis (2017). “Coupled High-Latitude Climate Feedbacks and Their Impact on Atmospheric Heat Transport”. *Journal of Climate* 30.1, pp. 189–201. DOI: 10.1175/JCLI-D-16-0324.1.
- Feldl, N., S. Po-Chedley, H. K. A. Singh, S. Hay, and P. J. Kushner (2020). “Sea ice and atmospheric circulation shape the high-latitude lapse rate feedback”. *npj Climate and Atmospheric Science* 3.1, p. 41. ISSN: 2397-3722. DOI: 10.1038/s41612-020-00146-7.
- Fernald, F. G. (1984). “Analysis of atmospheric lidar observations: some comments”. *Appl. Opt.* 23.5, pp. 652–653. DOI: 10.1364/AO.23.000652.
- Fielding, M. D., J. C. Chiu, R. J. Hogan, and G. Feingold (2014). “A novel ensemble method for retrieving properties of warm cloud in 3-D using ground-based scanning radar and zenith radiances”. *Journal of Geophysical Research: Atmospheres* 119.18, pp. 10, 912–10, 930. DOI: <https://doi.org/10.1002/2014JD021742>.
- Fielding, M. D., J. C. Chiu, R. J. Hogan, G. Feingold, E. Eloranta, E. J. O’Connor, and M. P. Cadetdu (2015). “Joint retrievals of cloud and drizzle in marine boundary layer clouds using ground-based radar, lidar and zenith radiances”. *Atmospheric Measurement Techniques* 8.7, pp. 2663–2683. DOI: 10.5194/amt-8-2663-2015.
- Findeisen, W. (1938). “Die kolloidmeteorologischen Vorgänge bei der Niederschlagsbildung”. *Meteorologische Zeitschrift* 55, pp. 121–133.
- Flanner, M., K. Shell, M. Barlage, D. Perovich, and M. Tschudi (2011). “Radiative forcing and albedo feedback from the Northern Hemisphere cryosphere between 1979 and 2008”. *Nature geoscience* 4, pp. 151–155. DOI: 10.1038/NGE01062.
- Francis, J. and N. Skific (2015). “Evidence linking rapid Arctic warming to mid-latitude weather patterns”. *Philosophical Transactions of the Royal Society A: Mathematical, Physical and Engineering Sciences* 373.2045, p. 20140170. DOI: 10.1098/rsta.2014.0170.

-
- Frehlich, R. and L. Cornman (2002). “Estimating Spatial Velocity Statistics with Coherent Doppler Lidar”. *Journal of Atmospheric and Oceanic Technology* 19.3, pp. 355–366. DOI: 10.1175/1520-0426-19.3.355.
- Freudenthaler, V., M. Esselborn, M. Wiegner, B. Heese, M. Tesche, A. Ansmann, D. MÜLLER, D. Althausen, M. Wirth, A. Fix, G. Ehret, P. Knippertz, C. Toledano, J. Gasteiger, M. Garhammer, and M. Seefeldner (2009). “Depolarization ratio profiling at several wavelengths in pure Saharan dust during SAMUM 2006”. *Tellus B: Chemical and Physical Meteorology* 61.1, pp. 165–179. DOI: 10.1111/j.1600-0889.2008.00396.x.
- Fridlind, A. M., A. S. Ackerman, G. McFarquhar, G. Zhang, M. R. Poellot, P. J. DeMott, A. J. Prenni, and A. J. Heymsfield (2007). “Ice properties of single-layer stratocumulus during the Mixed-Phase Arctic Cloud Experiment: 2. Model results”. *Journal of Geophysical Research: Atmospheres* 112.D24, p. D24202. DOI: 10.1029/2007JD008646.
- Frisch, A. S., G. Feingold, C. W. Fairall, T. Uttal, and J. B. Snider (1998). “On cloud radar and microwave radiometer measurements of stratus cloud liquid water profiles”. *Journal of Geophysical Research: Atmospheres* 103.D18, pp. 23195–23197. DOI: 10.1029/98JD01827.
- Frisch, A. S., M. Shupe, I. Djalalova, G. Feingold, and M. Poellot (2002). “The Retrieval of Stratus Cloud Droplet Effective Radius with Cloud Radars”. *Journal of Atmospheric and Oceanic Technology* 19.6, pp. 835–842. DOI: 10.1175/1520-0426(2002)019<0835:TR0SCD>2.0.CO;2.
- Fu, S. and H. Xue (2017). “The Effect of Ice Nuclei Efficiency on Arctic Mixed-Phase Clouds from Large-Eddy Simulations”. *Journal of the Atmospheric Sciences* 74.12, pp. 3901–3913. DOI: 10.1175/JAS-D-17-0112.1.
- Gierens, R., S. Kneifel, M. D. Shupe, K. Ebell, M. Maturilli, and U. Löhnert (2020). “Low-level mixed-phase clouds in a complex Arctic environment”. *Atmospheric Chemistry and Physics* 20.6, pp. 3459–3481. DOI: 10.5194/acp-20-3459-2020.
- GISTEMP-Team (2021). *GISS Surface Temperature Analysis (GISTEMP), version 4*. Tech. rep. last access: 01 June 2021. URL: data.giss.nasa.gov/gistemp/.
- Goosse, H., J. E. Kay, K. C. Armour, A. Bodas-Salcedo, H. Chepfer, D. Docquier, A. Jonko, P. J. Kushner, O. Lecomte, F. Massonnet, H.-S. Park, F. Pithan, G. Svensson, and M. Vancoppenolle (2018). “Quantifying climate feedbacks in polar regions”. *Nature Communications* 9.1, p. 1919. ISSN: 2041-1723. DOI: 10.1038/s41467-018-04173-0.
- Görsdorf, U., V. Lehmann, M. Bauer-Pfundstein, G. Peters, D. Vavriv, V. Vinogradov, and V. Volkov (2015). “A 35-GHz Polarimetric Doppler Radar for Long-Term Observations of Cloud Parameters—Description of System and Data Processing”. *Journal of Atmospheric and Oceanic Technology* 32.4, pp. 675–690. DOI: 10.1175/JTECH-D-14-00066.1.
- Granskog, M. A., I. Fer, A. Rinke, and H. Steen (2018). “Atmosphere-Ice-Ocean-Ecosystem Processes in a Thinner Arctic Sea Ice Regime: The Norwegian Young Sea ICE (N-ICE2015) Expedition”. *J. Geophys. Res. Oceans* 123.3, pp. 1586–1594. ISSN: 2169-9275. DOI: 10.1002/2017jc013328.
- Graversen, R. G., P. L. Langen, and T. Mauritsen (2014). “Polar Amplification in CCSM4: Contributions from the Lapse Rate and Surface Albedo Feedbacks”. *Journal of Climate* 27.12, pp. 4433–4450. ISSN: 0894-8755. DOI: 10.1175/JCLI-D-13-00551.1.
- Griesche, H. J., K. Ohneiser, P. Seifert, M. Radenz, R. Engelmann, and A. Ansmann (2021). “Contrasting ice formation in Arctic clouds: surface-coupled vs. surface-decoupled clouds”. *Atmospheric Chemistry and Physics* 21.13, pp. 10357–10374. DOI: 10.5194/acp-21-10357-2021.
-

- Griesche, H. J., P. Seifert, A. Ansmann, H. Baars, C. Barrientos Velasco, J. Bühl, R. Engelmann, M. Radenz, Y. Zhenping, and A. Macke (2020a). “Application of the shipborne remote sensing supersite OCEANET for profiling of Arctic aerosols and clouds during *Polarstern* cruise PS106”. *Atmospheric Measurement Techniques* 13.10, pp. 5335–5358. DOI: 10.5194/amt-13-5335-2020.
- Griesche, H. J., P. Seifert, R. Engelmann, R. Radenz, and J. Bühl (2019). *OCEANET-ATMOSPHERE PollyXT measurements during POLARSTERN cruise PS106*. data set. Leibniz-Institut für Troposphärenforschung e.V., Leipzig. DOI: 10.1594/PANGAEA.899458.
- (2020b). *Cloudnet ice particles effective radius during PS106*. data set. Leibniz-Institut für Troposphärenforschung e.V., Leipzig. DOI: 10.1594/PANGAEA.919386.
- (2020c). *Cloudnet IWC during PS106*. data set. Leibniz-Institut für Troposphärenforschung e.V., Leipzig. DOI: 10.1594/PANGAEA.919452.
- (2020d). *Cloudnet liquid droplet effective radius during PS106*. data set. Leibniz-Institut für Troposphärenforschung e.V., Leipzig. DOI: 10.1594/PANGAEA.919399.
- (2020e). *Cloudnet LWC during PS106*. data set. Leibniz-Institut für Troposphärenforschung e.V., Leipzig. DOI: 10.1594/PANGAEA.919383.
- (2020f). *Cloudnet target classification during POLARSTERN cruise PS106 classification*. data set. Leibniz-Institut für Troposphärenforschung e.V., Leipzig. DOI: 10.1594/PANGAEA.919463.
- (2020g). *OCEANET-ATMOSPHERE Cloud radar Mira-35 during PS106*. data set. Leibniz-Institut für Troposphärenforschung e.V., Leipzig. DOI: 10.1594/PANGAEA.919556.
- (2020h). *OCEANET-ATMOSPHERE low level stratus clouds during PS106*. data set. Leibniz-Institut für Troposphärenforschung e.V., Leipzig. DOI: 10.1594/PANGAEA.920246.
- (2020i). *OCEANET-ATMOSPHERE Microwave Radiometer Hatpro during POLARSTERN cruise PS106*. data set. Leibniz-Institut für Troposphärenforschung e.V., Leipzig. DOI: 10.1594/PANGAEA.919359.
- Groß, S., M. Tesche, V. Freudenthaler, C. Toledano, M. Wiegner, A. Ansmann, D. Althausen, and M. Seefeldner (2011). “Characterization of Saharan dust, marine aerosols and mixtures of biomass-burning aerosols and dust by means of multi-wavelength depolarization and Raman lidar measurements during SAMUM 2”. *Tellus B: Chemical and Physical Meteorology* 63.4, pp. 706–724. DOI: 10.1111/j.1600-0889.2011.00556.x.
- Hansen, J. and L. Nazarenko (2004). “Soot climate forcing via snow and ice albedos”. *Proceedings of the National Academy of Sciences* 101.2, pp. 423–428. ISSN: 0027-8424. DOI: 10.1073/pnas.2237157100.
- Harrington, J. Y. and P. Q. Olsson (2001). “On the potential influence of ice nuclei on surface-forced marine stratocumulus cloud dynamics”. *Journal of Geophysical Research: Atmospheres* 106.D21, pp. 27473–27484. DOI: 10.1029/2000JD000236.
- Hartmann, M., K. Adachi, O. Eppers, C. Haas, A. Herber, R. Holzinger, A. Hünnerbein, E. Jäkel, C. Jentsch, M. van Pinxteren, H. Wex, S. Willmes, and F. Stratmann (2020). “Wintertime Airborne Measurements of Ice Nucleating Particles in the High Arctic: A Hint to a Marine, Biogenic Source for Ice Nucleating Particles”. *Geophysical Research Letters* 47.13. e2020GL087770 10.1029/2020GL087770, e2020GL087770. DOI: 10.1029/2020GL087770.
- Hartmann, M., X. Gong, S. Kecorius, M. van Pinxteren, T. Vogl, A. Welti, H. Wex, S. Zeppenfeld, H. Herrmann, A. Wiedensohler, and F. Stratmann (2021). “Terrestrial or marine – indications towards the origin of ice-nucleating particles during melt season in the European Arctic up to 83.7° N”. *Atmospheric Chemistry and Physics* 21.15, pp. 11613–11636. DOI: 10.5194/acp-21-11613-2021.

-
- Hashino, T., M. Satoh, Y. Hagihara, S. Kato, T. Kubota, T. Matsui, T. Nasuno, H. Okamoto, and M. Sekiguchi (2016). “Evaluating Arctic cloud radiative effects simulated by NICAM with A-train”. *Journal of Geophysical Research: Atmospheres* 121.12, pp. 7041–7063. DOI: <https://doi.org/10.1002/2016JD024775>.
- Heese, B., H. Flentje, D. Althausen, A. Ansmann, and S. Frey (2010). “Ceilometer lidar comparison: backscatter coefficient retrieval and signal-to-noise ratio determination”. *Atmospheric Measurement Techniques* 3.6, pp. 1763–1770. DOI: 10.5194/amt-3-1763-2010.
- Herenz, P., H. Wex, S. Henning, T. B. Kristensen, F. Rubach, A. Roth, S. Borrmann, H. Bozem, H. Schulz, and F. Stratmann (2018). “Measurements of aerosol and CCN properties in the Mackenzie River delta (Canadian Arctic) during spring–summer transition in May 2014”. *Atmospheric Chemistry and Physics* 18.7, pp. 4477–4496. DOI: 10.5194/acp-18-4477-2018.
- Hersbach, H., B. Bell, P. Berrisford, S. Hirahara, A. Horányi, J. Muñoz-Sabater, J. Nicolas, C. Peubey, R. Radu, D. Schepers, A. Simmons, C. Soci, S. Abdalla, X. Abellan, G. Balsamo, P. Bechtold, G. Biavati, J. Bidlot, M. Bonavita, G. De Chiara, P. Dahlgren, D. Dee, M. Diamantakis, R. Dragani, J. Flemming, R. Forbes, M. Fuentes, A. Geer, L. Haimberger, S. Healy, R. J. Hogan, E. Hólm, M. Janisková, S. Keeley, P. Laloyaux, P. Lopez, C. Lupu, G. Radnoti, P. de Rosnay, I. Rozum, F. Vamborg, S. Villaume, and J.-N. Thépaut (2020). “The ERA5 global reanalysis”. *Quarterly Journal of the Royal Meteorological Society* 146.730, pp. 1999–2049. ISSN: 0035-9009. DOI: <https://doi.org/10.1002/qj.3803>.
- Hogan, R. J., M. P. Mittermaier, and A. J. Illingworth (2006). “The Retrieval of Ice Water Content from Radar Reflectivity Factor and Temperature and Its Use in Evaluating a Mesoscale Model”. *Journal of Applied Meteorology and Climatology* 45.2, pp. 301–317. DOI: 10.1175/JAM2340.1.
- Hogan, R. J. and E. O’Connor (2004). *Facilitating cloud radar and lidar algorithms: the Cloudnet Instrument Synergy / Target Categorization product*. Tech. rep. last access: 24 September 2020. URL: <http://www.met.rdg.ac.uk/~swrhgnrj/publications/categorization.pdf>.
- Hoose, C. and O. Möhler (2012). “Heterogeneous ice nucleation on atmospheric aerosols: a review of results from laboratory experiments”. *Atmospheric Chemistry and Physics* 12.20, pp. 9817–9854. DOI: 10.5194/acp-12-9817-2012.
- Ickes, L., G. C. E. Porter, R. Wagner, M. P. Adams, S. Bierbauer, A. K. Bertram, M. Bilde, S. Christiansen, A. M. L. Ekman, E. Gorokhova, K. Höhler, A. A. Kiselev, C. Leck, O. Möhler, B. J. Murray, T. Schiebel, R. Ullrich, and M. E. Salter (2020). “The ice-nucleating activity of Arctic sea surface microlayer samples and marine algal cultures”. *Atmospheric Chemistry and Physics* 20.18, pp. 11089–11117. DOI: 10.5194/acp-20-11089-2020.
- Illingworth, A. J., R. J. Hogan, E. O’Connor, D. Bouniol, M. E. Brooks, J. Delanoé, D. P. Donovan, J. D. Eastment, N. Gaussiat, J. W. F. Goddard, M. Haeffelin, H. K. Baltink, O. A. Krasnov, J. Pelon, J.-M. Piriou, A. Protat, H. W. J. Russchenberg, A. Seifert, A. M. Tompkins, G.-J. van Zadelhoff, F. Vinit, U. Willén, D. R. Wilson, and C. L. Wrench (2007). “Cloudnet”. *Bulletin of the American Meteorological Society* 88.6, pp. 883–898. DOI: 10.1175/BAMS-88-6-883.
- Intrieri, J. M., C. W. Fairall, M. D. Shupe, P. O. G. Persson, E. L. Andreas, P. S. Guest, and R. E. Moritz (2002). “An annual cycle of Arctic surface cloud forcing at SHEBA”. *Journal of Geophysical Research: Oceans* 107.C10, SHE 13-1-SHE 13-14. DOI: <https://doi.org/10.1029/2000JC000439>.
- Intrieri, J. M. and M. D. Shupe (2004). “Characteristics and Radiative Effects of Diamond Dust over the Western Arctic Ocean Region”. *Journal of Climate* 17.15, pp. 2953–2960. ISSN: 0894-8755. DOI: 10.1175/1520-0442(2004)017<2953:CAREOD>2.0.CO;2.
-

- IPCC (2013). “Technical Summary.” *Climate Change 2013: The Physical Science Basis. Contribution of Working Group I to the Fifth Assessment Report of the Intergovernmental Panel on Climate Change*. Ed. by Stocker, T. F., Qin, D., Plattner, G.-K., Tignor, M., Allen, S. K., Doschung, J., Nauels, A., Xia, Y., Bex, V., and Midgley, P. M. Cambridge, UK: IPCC, pp. 33–115. DOI: 10.1017/CB09781107415324.005.
- (2014). “Summary for Policymakers”. *Climate Change 2014 – Impacts, Adaptation and Vulnerability: Part A: Global and Sectoral Aspects: Working Group II Contribution to the IPCC Fifth Assessment Report*. Ed. by Field, C. B., Barros, V., Dokken, D. J., Mach, K. J., Mastrandrea, M. D., Bilir, T. E., Chatterjee, M., Ebi, K. L., Estrada, Y. O., Genova, R. C., Girma, B., Kissel, E. S., Levy, A. N., MacCracken, S., Mastrandrea, P. R., and White, L. L. Vol. 1. Cambridge University Press, pp. xv–xvi.
- (2019). “Climate Change and Land: an IPCC special report on climate change, desertification, land degradation, sustainable land management, food security, and greenhouse gas fluxes in terrestrial ecosystems”. Ed. by Shukla, P., Skea, J., Slade, R., Diemen, R. van, Haughey, E., Malley, J., Pathak, M., and Pereir, J. P. Chap. Technical Summary. In press.
- Jacob, D. J., J. H. Crawford, H. Maring, A. D. Clarke, J. E. Dibb, L. K. Emmons, R. A. Ferrare, C. A. Hostetler, P. B. Russell, H. B. Singh, A. M. Thompson, G. E. Shaw, E. McCauley, J. R. Pederson, and J. A. Fisher (2010). “The Arctic Research of the Composition of the Troposphere from Aircraft and Satellites (ARCTAS) mission: design, execution, and first results”. *Atmospheric Chemistry and Physics* 10.11, pp. 5191–5212. DOI: 10.5194/acp-10-5191-2010.
- Jensen, M. P., D. J. Holdridge, P. Survo, R. Lehtinen, S. Baxter, T. Toto, and K. L. Johnson (2016). “Comparison of Vaisala radiosondes RS41 and RS92 at the ARM Southern Great Plains site”. *Atmospheric Measurement Techniques* 9.7, pp. 3115–3129. DOI: 10.5194/amt-9-3115-2016.
- Jimenez, C., A. Ansmann, R. Engelmann, D. Donovan, A. Malinka, J. Schmidt, P. Seifert, and U. Wandinger (2020). “The dual-field-of-view polarization lidar technique: a new concept in monitoring aerosol effects in liquid-water clouds – theoretical framework”. *Atmospheric Chemistry and Physics* 20.23, pp. 15247–15263. DOI: 10.5194/acp-20-15247-2020.
- Jouan, C., J. Pelon, E. Girard, G. Ancellet, J. P. Blanchet, and J. Delanoë (2014). “On the relationship between Arctic ice clouds and polluted air masses over the North Slope of Alaska in April 2008”. *Atmospheric Chemistry and Physics* 14.3, pp. 1205–1224. DOI: 10.5194/acp-14-1205-2014.
- Kaimal, J. C., J. C. Wyngaard, D. A. Haugen, O. R. Coté, Y. Izumi, S. J. Caughey, and C. J. Readings (1976). “Turbulence Structure in the Convective Boundary Layer”. *Journal of the Atmospheric Sciences* 33.11, pp. 2152–2169. DOI: 10.1175/1520-0469(1976)033<2152:TSITCB>2.0.CO;2.
- Kalesse, H., G. de Boer, A. Solomon, M. Oue, M. Ahlgrimm, D. Zhang, M. D. Shupe, E. Luke, and A. Protat (2016a). “Understanding Rapid Changes in Phase Partitioning between Cloud Liquid and Ice in Stratiform Mixed-Phase Clouds: An Arctic Case Study”. *Monthly Weather Review* 144.12, pp. 4805–4826. DOI: 10.1175/MWR-D-16-0155.1.
- Kalesse, H. and P. Kollias (2013). “Climatology of High Cloud Dynamics Using Profiling ARM Doppler Radar Observations”. *Journal of Climate* 26.17, pp. 6340–6359. DOI: 10.1175/JCLI-D-12-00695.1.
- Kalesse, H., W. Szyrmer, S. Kneifel, P. Kollias, and E. Luke (2016b). “Fingerprints of a riming event on cloud radar Doppler spectra: observations and modeling”. *Atmospheric Chemistry and Physics* 16.5, pp. 2997–3012. DOI: 10.5194/acp-16-2997-2016.
- Kalesse-Los, H., W. Schimmel, E. Luke, and P. Seifert (2021). “Evaluating cloud liquid detection using cloud radar Doppler spectra in a pre-trained artificial neural network against Cloudnet liquid

-
- detection”. *Atmospheric Measurement Techniques Discussions* 2021, pp. 1–19. DOI: 10.5194/amt-2021-60.
- Kanamitsu, M. (1989). “Description of the NMC Global Data Assimilation and Forecast System”. *Weather and Forecasting* 4.3, pp. 335–342. DOI: 10.1175/1520-0434(1989)004<0335:DOTNGD>2.0.CO;2.
- Kanitz, T., A. Ansmann, R. Engelmann, and D. Althausen (2013a). “North-south cross sections of the vertical aerosol distribution over the Atlantic Ocean from multiwavelength Raman/polarization lidar during Polarstern cruises”. *Journal of Geophysical Research: Atmospheres* 118.6, pp. 2643–2655. DOI: 10.1002/jgrd.50273.
- Kanitz, T., A. Ansmann, P. Seifert, R. Engelmann, J. Kalisch, and D. Althausen (2013b). “Radiative effect of aerosols above the northern and southern Atlantic Ocean as determined from shipborne lidar observations”. *Journal of Geophysical Research: Atmospheres* 118.22, pp. 12, 556–12, 565. DOI: 10.1002/2013JD019750.
- Kanitz, T., P. Seifert, A. Ansmann, R. Engelmann, D. Althausen, C. Casiccia, and E. G. Rohwer (2011). “Contrasting the impact of aerosols at northern and southern midlatitudes on heterogeneous ice formation”. *Geophysical Research Letters* 38.17, p. L17802. DOI: 10.1029/2011GL048532.
- Kanji, Z. A., L. A. Ladino, H. Wex, Y. Boose, M. Burkert-Kohn, D. J. Cziczo, and M. Krämer (2017). “Overview of Ice Nucleating Particles”. *Meteorological Monographs* 58, pp. 1.1–1.33. DOI: 10.1175/AMSMONOGRAPHS-D-16-0006.1.
- Kay, J. E. and T. L’Ecuyer (2013). “Observational constraints on Arctic Ocean clouds and radiative fluxes during the early 21st century”. *Journal of Geophysical Research: Atmospheres* 118.13, pp. 7219–7236. DOI: 10.1002/jgrd.50489.
- Kecorius, S., T. Vogl, P. Paasonen, J. Lampilahti, D. Rothenberg, H. Wex, S. Zeppenfeld, M. van Pinxteren, M. Hartmann, S. Henning, X. Gong, A. Welti, M. Kulmala, F. Stratmann, H. Herrmann, and A. Wiedensohler (2019). “New particle formation and its effect on cloud condensation nuclei abundance in the summer Arctic: a case study in the Fram Strait and Barents Sea”. *Atmospheric Chemistry and Physics* 19.22, pp. 14339–14364. DOI: 10.5194/acp-19-14339-2019.
- Kipp and Zonen (2021a). *CGR 4 Pyrgeometer Instruction Manual*. Tech. rep. Last access: 11 September 2021. URL: <https://www.kippzonen.com/Download/38/Manual-CGR4-Pyrgeometer>.
- (2021b). *CMP series Pyranometer Instruction Manual*. Tech. rep. Last access: 11 September 2021. URL: <https://www.kippzonen.com/Download/72/Manual-Pyranometers-CMP-series-English>.
- Klein, S. A., R. B. McCoy, H. Morrison, A. S. Ackerman, A. Avramov, G. de Boer, M. Chen, J. N. S. Cole, A. D. Del Genio, M. Falk, M. J. Foster, A. Fridlind, J.-C. Golaz, T. Hashino, J. Y. Harrington, C. Hoose, M. F. Khairoutdinov, V. E. Larson, X. Liu, Y. Luo, G. M. McFarquhar, S. Menon, R. A. J. Neggers, S. Park, M. R. Poellot, J. M. Schmidt, I. Sednev, B. J. Shipway, M. D. Shupe, D. A. Spangenberg, Y. C. Sud, D. D. Turner, D. E. Veron, K. v. Salzen, G. K. Walker, Z. Wang, A. B. Wolf, S. Xie, K.-M. Xu, F. Yang, and G. Zhang (2009). “Intercomparison of model simulations of mixed-phase clouds observed during the ARM Mixed-Phase Arctic Cloud Experiment. I: single-layer cloud”. *Quarterly Journal of the Royal Meteorological Society* 135.641, pp. 979–1002. DOI: 10.1002/qj.416.
- Klepp, C., S. Michel, A. Protat, J. Burdanowitz, N. Albern, M. Kahnert, A. Dahl, V. Louf, S. Bakan, and S. A. Buehler (2018). “OceanRAIN, a new in-situ shipboard global ocean surface-reference dataset of all water cycle components”. *Sci Data* 5, p. 180122. ISSN: 2052-4463. DOI: 10.1038/sdata.2018.122.
-

- Klett, J. D. (1985). "Lidar inversion with variable backscatter/extinction ratios". *Appl. Opt.* 24.11, pp. 1638–1643. DOI: 10.1364/AO.24.001638.
- Knudsen, E. M., B. Heinold, S. Dahlke, H. Bozem, S. Crewell, I. V. Gorodetskaya, G. Heygster, D. Kunkel, M. Maturilli, M. Mech, C. Viceto, A. Rinke, H. Schmithüsen, A. Ehrlich, A. Macke, C. Lüpkes, and M. Wendisch (2018). "Meteorological conditions during the ACLOUD/PASCAL field campaign near Svalbard in early summer 2017". *Atmospheric Chemistry and Physics* 18.24, pp. 17995–18022. DOI: 10.5194/acp-18-17995-2018.
- Komurcu, M., T. Storelvmo, I. Tan, U. Lohmann, Y. Yun, J. E. Penner, Y. Wang, X. Liu, and T. Takemura (2014). "Intercomparison of the cloud water phase among global climate models". *Journal of Geophysical Research: Atmospheres* 119.6, pp. 3372–3400. DOI: <https://doi.org/10.1002/2013JD021119>.
- Korolev, A. and P. Field (2008). "The effect of dynamics on mixed-phase clouds: Theoretical considerations". *Journal of the Atmospheric Sciences* 65, pp. 66–86. DOI: <https://doi.org/10.1175/2007JAS2355.1>.
- Lanconelli, C., M. Busetto, E. G. Dutton, G. König-Langlo, M. Maturilli, R. Sieger, V. Vitale, and T. Yamanouchi (2011). "Polar baseline surface radiation measurements during the International Polar Year 2007–2009". *Earth System Science Data* 3.1, pp. 1–8. DOI: 10.5194/essd-3-1-2011.
- Law, K. S., A. Stohl, P. K. Quinn, C. A. Brock, J. F. Burkhardt, J.-D. Paris, G. Ancellet, H. B. Singh, A. Roiger, H. Schlager, J. Dibb, D. J. Jacob, S. R. Arnold, J. Pelon, and J. L. Thomas (2014). "Arctic Air Pollution: New Insights from POLARCAT-IPY". *Bulletin of the American Meteorological Society* 95.12, pp. 1873–1895. DOI: 10.1175/BAMS-D-13-00017.1.
- Lenssen, N., G. Schmidt, J. Hansen, M. Menne, A. Persin, R. Ruedy, and D. Zyss (2019). "Improvements in the GISTEMP uncertainty model". *J. Geophys. Res. Atmos.* 124.12, pp. 6307–6326. DOI: 10.1029/2018JD029522.
- Liu, Y., J. R. Key, S. A. Ackerman, G. G. Mace, and Q. Zhang (2012). "Arctic cloud macrophysical characteristics from CloudSat and CALIPSO". *Remote Sensing of Environment* 124, pp. 159–173. ISSN: 0034-4257. DOI: <https://doi.org/10.1016/j.rse.2012.05.006>.
- Liu, Y., M. D. Shupe, Z. Wang, and G. Mace (2017). "Cloud vertical distribution from combined surface and space radar–lidar observations at two Arctic atmospheric observatories". *Atmospheric Chemistry and Physics* 17.9, pp. 5973–5989. DOI: 10.5194/acp-17-5973-2017.
- Lohmann, U. (2017). "Anthropogenic Aerosol Influences on Mixed-Phase Clouds". *Current Climate Change Reports* 3.1, pp. 32–44. ISSN: 2198-6061. DOI: 10.1007/s40641-017-0059-9.
- Löhnert, U. and S. Crewell (2003). "Accuracy of cloud liquid water path from ground-based microwave radiometry 1. Dependency on cloud model statistics". *Radio Science* 38.3, p. 8041. DOI: 10.1029/2002RS002654.
- Lothon, M., D. H. Lenschow, D. Leon, and G. Vali (2005). "Turbulence measurements in marine stratocumulus with airborne Doppler radar". *Quarterly Journal of the Royal Meteorological Society* 131.609, pp. 2063–2080. DOI: 10.1256/qj.04.131.
- Macke, A. and H. Flores (2018). *The Expeditions PS106/1 and 2 of the Research Vessel POLARSTERN to the Arctic Ocean in 2017*. Alfred Wegener Institute for Polar and Marine Research. Bremerhaven. DOI: 10.2312/BzPM_0719_2018.
- Mamouri, R. E. and A. Ansmann (2016). "Potential of polarization lidar to provide profiles of CCN- and INP-relevant aerosol parameters". *Atmospheric Chemistry and Physics* 16.9, pp. 5905–5931. DOI: 10.5194/acp-16-5905-2016.
-

-
- Manabe, S. and R. T. Wetherald (1967). “Thermal Equilibrium of the Atmosphere with a Given Distribution of Relative Humidity.” *Journal of the Atmospheric Sciences* 24.3, pp. 241–259. DOI: 10.1175/1520-0469(1967)024<0241:TEOTAW>2.0.CO;2.
- (1975). “The Effects of Doubling the CO₂ Concentration on the climate of a General Circulation Model”. *Journal of the Atmospheric Sciences* 32.1, pp. 3–15. ISSN: 0022-4928. DOI: 10.1175/1520-0469(1975)032<0003:TEODTC>2.0.CO;2.
- Mariage, V., J. Pelon, F. Blouzon, S. Victori, N. Geyskens, N. Amarouche, C. Drezen, A. Guillot, M. Calzas, M. Garracio, N. Wegmuller, N. Sennéchaël, and C. Provost (2017). “IAOOS microlidar-on-buoy development and first atmospheric observations obtained during 2014 and 2015 arctic drifts”. *Opt. Express* 25.4, A73–A84. DOI: 10.1364/OE.25.000A73.
- Maturilli, M. (2017). *High resolution radiosonde measurements from station Ny-Ålesund (2017-06)*. data set. Alfred Wegener Institute - Research Unit Potsdam. DOI: 10.1594/PANGAEA.879822.
- Mauritsen, T., R. Graversen, D. Klocke, P. Langen, B. Stevens, and L. Tomassini (2013). “Climate feedback efficiency and synergy”. *Climate Dynamics*, pp. 2539–2554. DOI: 10.1007/s00382-013-1808-7.
- Mauritsen, T., J. Sedlar, M. Tjernström, C. Leck, M. Martin, M. Shupe, S. Sjogren, B. Sierau, P. O. G. Persson, I. M. Brooks, and E. Swietlicki (2011). “An Arctic CCN-limited cloud-aerosol regime”. *Atmospheric Chemistry and Physics* 11.1, pp. 165–173. DOI: 10.5194/acp-11-165-2011.
- McFarquhar, G. M., S. Ghan, J. Verlinde, A. Korolev, J. W. Strapp, B. Schmid, J. M. Tomlinson, M. Wolde, S. D. Brooks, D. Cziczo, M. K. Dubey, J. Fan, C. Flynn, I. Gultepe, J. Hubbe, M. K. Gilles, A. Laskin, P. Lawson, W. R. Leitch, P. Liu, X. Liu, D. Lubin, C. Mazzoleni, A.-M. Macdonald, R. C. Moffet, H. Morrison, M. Ovchinnikov, M. D. Shupe, D. D. Turner, S. Xie, A. Zelenyuk, K. Bae, M. Freer, and A. Glen (2011). “Indirect and Semi-direct Aerosol Campaign”. *Bulletin of the American Meteorological Society* 92.2, pp. 183–201. DOI: 10.1175/2010BAMS2935.1.
- Mech, M., L.-L. Kliensch, A. Anhäuser, T. Rose, P. Kollias, and S. Crewell (2019). “Microwave Radar/radiometer for Arctic Clouds (MiRAC): first insights from the ACLOUD campaign”. *Atmospheric Measurement Techniques* 12.9, pp. 5019–5037. DOI: 10.5194/amt-12-5019-2019.
- Meier, W. N., G. K. Hovelsrud, B. E. H. van Oort, J. R. Key, K. M. Kovacs, C. Michel, C. Haas, M. A. Granskog, S. Gerland, D. K. Perovich, A. Makshtas, and J. D. Reist (2014). “Arctic sea ice in transformation: A review of recent observed changes and impacts on biology and human activity”. *Rev. Geophys.* 52.3, pp. 185–217. ISSN: 8755-1209. DOI: 10.1002/2013rg000431.
- Meischner, P., R. Baumann, H. Höller, and T. Jank (2001). “Eddy Dissipation Rates in Thunderstorms Estimated by Doppler Radar in Relation to Aircraft In Situ Measurements”. *Journal of Atmospheric and Oceanic Technology* 18.10, pp. 1609–1627. DOI: 10.1175/1520-0426(2001)018<1609:EDRITE>2.0.CO;2.
- Merk, D., H. Deneke, B. Pospichal, and P. Seifert (2016). “Investigation of the adiabatic assumption for estimating cloud micro- and macrophysical properties from satellite and ground observations”. *Atmospheric Chemistry and Physics* 16.2, pp. 933–952. DOI: 10.5194/acp-16-933-2016.
- Miles, N. L., J. Verlinde, and E. E. Clothiaux (2000). “Cloud Droplet Size Distributions in Low-Level Stratiform Clouds.” *Journal of the Atmospheric Sciences* 57.2, pp. 295–311. DOI: 10.1175/1520-0469(2000)057<0295:CDSDIL>2.0.CO;2.
- Mioche, G., O. Jourdan, M. Ceccaldi, and J. Delanoë (2015). “Variability of mixed-phase clouds in the Arctic with a focus on the Svalbard region: a study based on spaceborne active remote sensing”. *Atmospheric Chemistry and Physics* 15.5, pp. 2445–2461. DOI: 10.5194/acp-15-2445-2015.
-

- Mishchenko, M. I. and K. Sassen (1998). “Depolarization of lidar returns by small ice crystals: An application to contrails”. *Geophysical Research Letters* 25.3, pp. 309–312. DOI: doi.org/10.1029/97GL03764.
- Mlawer, E. J., S. J. Taubman, P. D. Brown, M. J. Iacono, and S. A. Clough (1997). “Radiative transfer for inhomogeneous atmospheres: RRTM, a validated correlated-k model for the longwave”. *Journal of Geophysical Research: Atmospheres* 102.D14, pp. 16663–16682. DOI: <https://doi.org/10.1029/97JD00237>.
- Morrison, A. L., J. E. Kay, W. R. Frey, H. Chepfer, and R. Guzman (2019). “Cloud Response to Arctic Sea Ice Loss and Implications for Future Feedback in the CESM1 Climate Model”. *Journal of Geophysical Research: Atmospheres* 124.2, pp. 1003–1020. DOI: [10.1029/2018JD029142](https://doi.org/10.1029/2018JD029142).
- Morrison, H., G. de Boer, G. Feingold, J. Harrington, M. D. Shupe, and K. Sulia (2012). “Resilience of persistent Arctic mixed-phase clouds”. *Nature Geoscience* 5.1, pp. 11–17. DOI: [10.1038/ngeo1332](https://doi.org/10.1038/ngeo1332).
- Morrison, H., P. Zuidema, A. S. Ackerman, A. Avramov, G. de Boer, J. Fan, A. M. Fridlind, T. Hashino, J. Y. Harrington, Y. Luo, M. Ovchinnikov, and B. Shipway (2011). “Intercomparison of cloud model simulations of Arctic mixed-phase boundary layer clouds observed during SHEBA/FIRE-ACE”. *Journal of Advances in Modeling Earth Systems* 3.2, p. M05001. DOI: [10.1029/2011MS000066](https://doi.org/10.1029/2011MS000066).
- Müller, D., A. Ansmann, I. Mattis, M. Tesche, U. Wandinger, D. Althausen, and G. Pisani (2007). “Aerosol-type-dependent lidar ratios observed with Raman lidar”. *Journal of Geophysical Research: Atmospheres* 112.D16, p. D16202. DOI: [10.1029/2006JD008292](https://doi.org/10.1029/2006JD008292).
- Müller, D., U. Wandinger, and A. Ansmann (1999). “Microphysical particle parameters from extinction and backscatter lidar data by inversion with regularization: theory”. *Appl. Opt.* 38.12, pp. 2346–2357. DOI: [10.1364/AO.38.002346](https://doi.org/10.1364/AO.38.002346).
- Murray, B. J., D. O’Sullivan, J. D. Atkinson, and M. E. Webb (2012). “Ice nucleation by particles immersed in supercooled cloud droplets”. *Chem. Soc. Rev.* 41 (19), pp. 6519–6554. DOI: [10.1039/C2CS35200A](https://doi.org/10.1039/C2CS35200A).
- Myagkov, A., P. Seifert, U. Wandinger, J. Bühl, and R. Engelmann (2016). “Relationship between temperature and apparent shape of pristine ice crystals derived from polarimetric cloud radar observations during the ACCEPT campaign”. *Atmospheric Measurement Techniques* 9.8, pp. 3739–3754. DOI: [10.5194/amt-9-3739-2016](https://doi.org/10.5194/amt-9-3739-2016).
- Neale, R. B., A. Gettelman, S. Park, A. J. Conley, D. Kinnison, D. Marsh, A. K. Smith, F. Vitt, H. Morrison, P. Cameron-smith, W. D. Collins, M. J. Iacono, R. C. Easter, X. Liu, M. A. Taylor, C.-c. Chen, P. H. Lauritzen, D. L. Williamson, R. Garcia, J.-f. Lamarque, M. Mills, S. Tilmes, S. J. Ghan, P. J. Rasch, and M. Meteorology (2012). “Description of the NCAR Community Atmosphere Model (CAM 5.0)”. *NCAR TECHNICAL NOTE*.
- Neggers, R. A. J., J. Chylik, U. Egerer, H. Griesche, V. Schemann, P. Seifert, H. Siebert, and A. Macke (2019). “Local and Remote Controls on Arctic Mixed-Layer Evolution”. *Journal of Advances in Modeling Earth Systems* 11.7, pp. 2214–2237. DOI: [10.1029/2019MS001671](https://doi.org/10.1029/2019MS001671).
- Nicholls, S. (1978). “Measurements of turbulence by an instrumented aircraft in a convective atmospheric boundary layer over the sea”. *Quarterly Journal of the Royal Meteorological Society* 104.441, pp. 653–676. DOI: [10.1002/qj.49710444109](https://doi.org/10.1002/qj.49710444109).
- Noel, V., G. Roy, L. Bissonnette, H. Chepfer, and P. Flamant (2002). “Analysis of lidar measurements of ice clouds at multiple incidence angles”. *Geophysical Research Letters* 29.9, pp. 52-1-52-4. DOI: <https://doi.org/10.1029/2002GL014828>.

-
- Noel, V. and K. Sassen (2005). “Study of Planar Ice Crystal Orientations in Ice Clouds from Scanning Polarization Lidar Observations”. *Journal of Applied Meteorology* 44.5, pp. 653–664. DOI: 10.1175/JAM2223.1.
- Noel, V., D. M. Winker, M. McGill, and P. Lawson (2004). “Classification of particle shapes from lidar depolarization ratio in convective ice clouds compared to in situ observations during CRYSTAL-FACE”. *Journal of Geophysical Research: Atmospheres* 109.D24, p. D24213. DOI: <https://doi.org/10.1029/2004JD004883>.
- Nomokonova, T., K. Ebell, U. Löhnert, M. Maturilli, C. Ritter, and E. O’Connor (2019). “Statistics on clouds and their relation to thermodynamic conditions at Ny-Ålesund using ground-based sensor synergy”. *Atmospheric Chemistry and Physics* 19.6, pp. 4105–4126. DOI: 10.5194/acp-19-4105-2019.
- Norgren, M. S., G. de Boer, and M. D. Shupe (2018). “Observed aerosol suppression of cloud ice in low-level Arctic mixed-phase clouds”. *Atmospheric Chemistry and Physics* 18.18, pp. 13345–13361. DOI: 10.5194/acp-18-13345-2018.
- Nucciarone, J. J. and G. S. Young (1991). “Aircraft Measurements of Turbulence Spectra in the Marine Stratocumulus-topped Boundary Layer”. *Journal of the Atmospheric Sciences* 48.22, pp. 2382–2392. DOI: 10.1175/1520-0469(1991)048<2382:AMOTSI>2.0.CO;2.
- O’Connor, E. J., R. J. Hogan, and A. J. Illingworth (2005). “Retrieving Stratocumulus Drizzle Parameters Using Doppler Radar and Lidar”. *Journal of Applied Meteorology* 44.1, pp. 14–27. DOI: 10.1175/jam-2181.1.
- O’Connor, E. J., A. J. Illingworth, I. M. Brooks, C. D. Westbrook, R. J. Hogan, F. Davies, and B. J. Brooks (2010). “A Method for Estimating the Turbulent Kinetic Energy Dissipation Rate from a Vertically Pointing Doppler Lidar, and Independent Evaluation from Balloon-Borne In Situ Measurements”. *Journal of Atmospheric and Oceanic Technology* 27.10, pp. 1652–1664. DOI: 10.1175/2010JTECHA1455.1.
- O’Sullivan, D., M. P. Adams, M. D. Tarn, A. D. Harrison, J. Vergara-Temprado, G. C. E. Porter, M. A. Holden, A. Sanchez-Marroquin, F. Carotenuto, T. F. Whale, J. B. McQuaid, R. Walshaw, D. H. P. Hedges, I. T. Burke, Z. Cui, and B. J. Murray (2018). “Contributions of biogenic material to the atmospheric ice-nucleating particle population in North Western Europe”. *Scientific Reports* 8.1, p. 13821. ISSN: 2045-2322. DOI: 10.1038/s41598-018-31981-7.
- Pisso, I., E. Sollum, H. Grythe, N. I. Kristiansen, M. Cassiani, S. Eckhardt, D. Arnold, D. Morton, R. L. Thompson, C. D. Groot Zwaaftink, N. Evangeliou, H. Sodemann, L. Haimberger, S. Henne, D. Brunner, J. F. Burkhardt, A. Fouilloux, J. Brioude, A. Philipp, P. Seibert, and A. Stohl (2019). “The Lagrangian particle dispersion model FLEXPART version 10.4”. *Geoscientific Model Development* 12.12, pp. 4955–4997. DOI: 10.5194/gmd-12-4955-2019.
- Pithan, F. and T. Mauritsen (2014). “Arctic amplification dominated by temperature feedbacks in contemporary climate models”. *Nature Geoscience* 7, p. 181. DOI: 10.1038/ngeo2071.
- Porter, J. N., M. Miller, C. Pietras, and C. Motell (2001). “Ship-Based Sun Photometer Measurements Using Microtops Sun Photometers”. *Journal of Atmospheric and Oceanic Technology* 18.5, pp. 765–774. DOI: 10.1175/1520-0426(2001)018<0765:SBSPMU>2.0.CO;2.
- Pruppacher, H. R. and J. D. Klett (1997). “Microphysics of clouds and precipitation”, vol 18 Kluwer Academic Publishers”. *Atmospheric and Oceanographic Sciences Library*.
- Qiu, S., X. Dong, B. xi, and J.-L. Li (2015). “Characterizing Arctic mixed-phase cloud structure and its relationship with humidity and temperature inversion using ARM NSA Observations”. *Journal of Geophysical Research: Atmospheres* 120, pp. 7737–7746. DOI: 10.1002/2014JD023022.
-

- Qiu, S., B. Xi, and X. Dong (2018). “Influence of Wind Direction on Thermodynamic Properties and Arctic Mixed-Phase Clouds in Autumn at Utqiagvik, Alaska”. *Journal of Geophysical Research: Atmospheres* 123.17, pp. 9589–9603. DOI: 10.1029/2018JD028631.
- Radenz, M., J. Bühl, P. Seifert, H. Griesche, and R. Engelmann (2019). “peakTree: a framework for structure-preserving radar Doppler spectra analysis”. *Atmospheric Measurement Techniques* 12.9, pp. 4813–4828. DOI: 10.5194/amt-12-4813-2019.
- Radenz, M., P. Seifert, H. Baars, A. A. Floutsi, Z. Yin, and J. Bühl (2021). “Automated time-height-resolved air mass source attribution for profiling remote sensing applications”. *Atmospheric Chemistry and Physics* 21.4, pp. 3015–3033. DOI: 10.5194/acp-21-3015-2021.
- Rader, F., R. Traversi, M. Severi, S. Becagli, K.-J. Müller, K. Nakoudi, and C. Ritter (2021). “Overview of Aerosol Properties in the European Arctic in Spring 2019 Based on In Situ Measurements and Lidar Data”. *Atmosphere* 12.2. DOI: 10.3390/atmos12020271.
- Radke, L. F., J. A. Coakley, and M. D. King (1989). “Direct and Remote Sensing Observations of the Effects of Ships on Clouds”. *Science* 246.4934, pp. 1146–1149. ISSN: 0036-8075. DOI: 10.1126/science.246.4934.1146.
- Ramanathan, V., R. D. Cess, E. F. Harrison, P. Minnis, B. R. Barkstrom, E. Ahmad, and D. Hartmann (1989). “Cloud-Radiative Forcing and Climate: Results from the Earth Radiation Budget Experiment”. *Science* 243.4887, pp. 57–63. ISSN: 0036-8075. DOI: 10.1126/science.243.4887.57.
- Richter, P., M. Palm, C. Weinzierl, H. Griesche, P. M. Rowe, and J. Notholt (2021). “A dataset of microphysical cloud parameters, retrieved from Emission-FTIR spectra measured in Arctic summer 2017”. *Earth System Science Data Discussions* 2021, pp. 1–30. DOI: 10.5194/essd-2021-284.
- Rogers, D. C. and G. Vali (1987). “Ice Crystal Production by Mountain Surfaces”. *Journal of Applied Meteorology and Climatology* 26.9, pp. 1152–1168. DOI: 10.1175/1520-0450(1987)026<1152:ICPBMS>2.0.CO;2.
- Rose, T., S. Crewell, U. Löhnert, and C. Simmer (2005). “A network suitable microwave radiometer for operational monitoring of the cloudy atmosphere”. *Atmospheric Research* 75.3. CLIWA-NET: Observation and Modelling of Liquid Water Clouds, pp. 183–200. ISSN: 0169-8095. DOI: 10.1016/j.atmosres.2004.12.005.
- Rouse, W. R. (1987). “Examples of Enhanced Global Solar Radiation Through Multiple Reflection from an Ice-Covered Arctic Sea”. *Journal of Applied Meteorology and Climatology* 26.6, pp. 670–674. DOI: 10.1175/1520-0450(1987)026<0670:EOEGSR>2.0.CO;2.
- Sandvik, A., M. Biryulina, N. G. Kvamstø, J. J. Stamnes, and K. Stamnes (2007). “Observed and simulated microphysical composition of arctic clouds: Data properties and model validation”. *Journal of Geophysical Research: Atmospheres* 112.D5, p. D05205. DOI: 10.1029/2006JD007351.
- Sasano, Y., E. V. Browell, and S. Ismail (1985). “Error caused by using a constant extinction/backscattering ratio in the lidar solution”. *Appl. Opt.* 24.22, pp. 3929–3932. DOI: 10.1364/AO.24.003929.
- Sassen, K. (2005). “Polarization in Lidar”. *Lidar: Range-Resolved Optical Remote Sensing of the Atmosphere*. New York, NY: Springer New York, pp. 19–42. ISBN: 978-0-387-25101-1. DOI: 10.1007/0-387-25101-4_2.
- Sassen, K. and Y. Takano (2000). “Parry arc: a polarization lidar, ray-tracing, and aircraft case study”. *Appl. Opt.* 39.36, pp. 6738–6745. DOI: 10.1364/AO.39.006738.
- Sathe, A. and J. Mann (2013). “A review of turbulence measurements using ground-based wind lidars”. *Atmospheric Measurement Techniques* 6.11, pp. 3147–3167. DOI: 10.5194/amt-6-3147-2013.

-
- Satheesh, S. and K. Krishna Moorthy (2005). “Radiative effects of natural aerosols: A review”. *Atmospheric Environment* 39.11, pp. 2089–2110. ISSN: 1352-2310. DOI: 10.1016/j.atmosenv.2004.12.029.
- Sato, K., J. Inoue, Y.-M. Kodama, and J. E. Overland (2012). “Impact of Arctic sea-ice retreat on the recent change in cloud-base height during autumn”. *Geophysical Research Letters* 39.10. DOI: 10.1029/2012GL051850.
- Schneider, E. K., B. P. Kirtman, and R. S. Lindzen (1999). “Tropospheric Water Vapor and Climate Sensitivity.” *Journal of Atmospheric Sciences* 56.11, pp. 1649–1658. DOI: 10.1175/1520-0469(1999)056<1649:TWVACS>2.0.CO;2.
- Schnell, R. C. and G. Vali (1976). “Biogenic Ice Nuclei: Part I. Terrestrial and Marine Sources”. *Journal of the Atmospheric Sciences* 33.8, pp. 1554–1564. ISSN: 0022-4928. DOI: 10.1175/1520-0469(1976)033<1554:BINPIT>2.0.CO;2.
- Schotland, R. M., K. Sassen, and R. Stone (1971). “Observations by Lidar of Linear Depolarization Ratios for Hydrometeors”. *Journal of Applied Meteorology (1962-1982)* 10.5, pp. 1011–1017. ISSN: 00218952, 2163534X. DOI: 10.1175/1520-0450(1971)010<1011:OBLOLD>2.0.CO;2.
- Schweiger, A. J. and J. R. Key (1994). “Arctic Ocean Radiative Fluxes and Cloud Forcing Estimated from the ISCCP C2 Cloud Dataset, 1983–1990”. *Journal of Applied Meteorology (1988-2005)* 33.8, pp. 948–963. ISSN: 08948763, 15200450. DOI: 10.1175/1520-0450(1994)033<0948:AORFAC>2.0.CO;2.
- Seifert, P., A. Ansmann, S. Groß, V. Freudenthaler, B. Heinold, A. Hiebsch, I. Mattis, J. Schmidt, F. Schnell, M. Tesche, U. Wandinger, and M. Wiegner (2011). “Ice formation in ash-influenced clouds after the eruption of the Eyjafjallajökull volcano in April 2010”. *Journal of Geophysical Research: Atmospheres* 116.D20, D00U04. DOI: 10.1029/2011JD015702.
- Seifert, P., A. Ansmann, I. Mattis, U. Wandinger, M. Tesche, R. Engelmann, D. Müller, C. Pérez, and K. Haustein (2010). “Saharan dust and heterogeneous ice formation: Eleven years of cloud observations at a central European EARLINET site”. *J. Geophys. Res.* 115.D20, p. D20201. ISSN: 0148-0227. DOI: 10.1029/2009jd013222.
- Seifert, P., C. Kunz, H. Baars, A. Ansmann, J. Bühl, F. Senf, R. Engelmann, D. Althausen, and P. Artaxo (2015). “Seasonal variability of heterogeneous ice formation in stratiform clouds over the Amazon Basin”. *Geophysical Research Letters* 42.13, pp. 5587–5593. DOI: 10.1002/2015GL064068.
- Serreze, M. C. and R. G. Barry (2011). “Processes and impacts of Arctic amplification: A research synthesis”. *Global and Planetary Change* 77.1, pp. 85–96. ISSN: 0921-8181. DOI: 10.1016/j.gloplacha.2011.03.004.
- (2014). *The Arctic Climate System*. 2nd ed. Cambridge Atmospheric and Space Science Series. Cambridge University Press. DOI: 10.1017/CB09781139583817.
- Shaw, G. E. (1995). “The Arctic Haze Phenomenon”. *Bulletin of the American Meteorological Society* 76.12, pp. 2403–2414. DOI: 10.1175/1520-0477(1995)076<2403:TAHP>2.0.CO;2.
- Shibata, T., K. Shiraishi, M. Shiobara, S. Iwasaki, and T. Takano (2018). “Seasonal Variations in High Arctic Free Tropospheric Aerosols Over Ny-Ålesund, Svalbard, Observed by Ground-Based Lidar”. *Journal of Geophysical Research: Atmospheres* 123.21, pp. 12, 353–12, 367. DOI: <https://doi.org/10.1029/2018JD028973>.
- Shine, K. P. (1984). “Parametrization of the shortwave flux over high albedo surfaces as a function of cloud thickness and surface albedo”. *Quarterly Journal of the Royal Meteorological Society* 110.465, pp. 747–764. DOI: <https://doi.org/10.1002/qj.49711046511>.
-

- Shupe, M. D. (2007). "A ground-based multisensor cloud phase classifier". *Geophysical Research Letters* 34.22, p. L22809. DOI: 10.1029/2007GL031008.
- (2011). "Clouds at Arctic Atmospheric Observatories. Part II: Thermodynamic Phase Characteristics". *Journal of Applied Meteorology and Climatology* 50.3, pp. 645–661. ISSN: 1558-8424. DOI: 10.1175/2010JAMC2468.1.
- Shupe, M. D., I. M. Brooks, and G. Canut (2012). "Evaluation of turbulent dissipation rate retrievals from Doppler Cloud Radar". *Atmospheric Measurement Techniques* 5.6, pp. 1375–1385. DOI: 10.5194/amt-5-1375-2012.
- Shupe, M. D., G. de Boer, K. Dethloff, E. Hunke, W. Maslowski, A. McComiskey, O. Perrson, D. Randall, M. Tjernstrom, D. Turner, and J. Verlinde (2018). "The Multidisciplinary Drifting Observatory for the Study of Arctic Climate (MOSAIC) Atmosphere Science Plan". *DOE Office of Science Atmospheric Radiation Measurement (ARM) Program (United States)*. last access: 20 September 2020. URL: <https://www.osti.gov/biblio/1421919>.
- Shupe, M. D. and J. M. Intrieri (2004). "Cloud Radiative Forcing of the Arctic Surface: The Influence of Cloud Properties, Surface Albedo, and Solar Zenith Angle". *Journal of Climate* 17.3, pp. 616–628. ISSN: 0894-8755. DOI: 10.1175/1520-0442(2004)017<0616:CRFOTA>2.0.CO;2.
- Shupe, M. D., P. Kollias, S. Y. Matrosov, and T. L. Schneider (2004). "Deriving Mixed-Phase Cloud Properties from Doppler Radar Spectra". *Journal of Atmospheric and Oceanic Technology* 21.4, pp. 660–670. DOI: 10.1175/1520-0426(2004)021<0660:DMCPFD>2.0.CO;2.
- Shupe, M. D., S. Y. Matrosov, and T. Uttal (2006). "Arctic Mixed-Phase Cloud Properties Derived from Surface-Based Sensors at SHEBA". *Journal of the Atmospheric Sciences* 63.2, pp. 697–711. ISSN: 0022-4928. DOI: 10.1175/JAS3659.1.
- Shupe, M. D., P. O. G. Persson, I. M. Brooks, M. Tjernstrom, J. Sedlar, T. Mauritsen, S. Sjogren, and C. Leck (2013). "Cloud and boundary layer interactions over the Arctic sea ice in late summer". *Atmospheric Chemistry and Physics* 13.18, pp. 9379–9399. ISSN: 1680-7316. DOI: 10.5194/acp-13-9379-2013.
- Shupe, M. D., M. Rex, K. Dethloff, E. Damm, A. A. Fong, R. Gradinger, C. Heuzé, B. Loose, A. Makarov, W. Maslowski, M. Nicolaus, D. Perovich, B. Rabe, A. Rinke, V. Sokolov, and A. Sommerfeld (2020). "Arctic Report Card 2020: The MOSAiC Expedition: A Year Drifting with the Arctic Sea Ice". DOI: <https://doi.org/10.25923/9g3v-xh92>.
- Shupe, M. D., T. Uttal, and S. Y. Matrosov (2005). "Arctic Cloud Microphysics Retrievals from Surface-Based Remote Sensors at SHEBA". *Journal of Applied Meteorology* 44.10, pp. 1544–1562. DOI: 10.1175/JAM2297.1.
- Shupe, M. D., V. P. Walden, E. Eloranta, T. Uttal, J. R. Campbell, S. M. Starkweather, and M. Shiobara (2011). "Clouds at Arctic Atmospheric Observatories. Part I: Occurrence and Macrophysical Properties". *Journal of Applied Meteorology and Climatology* 50.3, pp. 626–644. DOI: 10.1175/2010JAMC2467.1.
- Siebert, H., H. Franke, K. Lehmann, R. Maser, E. W. Saw, D. Schell, R. A. Shaw, and M. Wendisch (2006a). "Probing Finescale Dynamics and Microphysics of Clouds with Helicopter-Borne Measurements". *Bulletin of the American Meteorological Society* 87.12, pp. 1727–1738. DOI: 10.1175/BAMS-87-12-1727.
- Siebert, H., K. Lehmann, and M. Wendisch (2006b). "Observations of Small-Scale Turbulence and Energy Dissipation Rates in the Cloudy Boundary Layer". *Journal of the Atmospheric Sciences* 63.5, pp. 1451–1466. DOI: 10.1175/JAS3687.1.
-

-
- Silber, I., J. Verlinde, E. W. Eloranta, C. J. Flynn, and D. M. Flynn (2018). “Polar Liquid Cloud Base Detection Algorithms for High Spectral Resolution or Micropulse Lidar Data”. *Journal of Geophysical Research: Atmospheres* 123.8, pp. 4310–4322. DOI: 10.1029/2017JD027840.
- Smirnov, A., B. N. Holben, I. Slutsker, D. M. Giles, C. R. McClain, T. F. Eck, S. M. Sakerin, A. Macke, P. Croot, G. Zibordi, P. K. Quinn, J. Sciare, S. Kinne, M. Harvey, T. J. Smyth, S. Piketh, T. Zielinski, A. Proshutinsky, J. I. Goes, N. B. Nelson, P. Larouche, V. F. Radionov, P. Goloub, K. Krishna Moorthy, R. Matarrese, E. J. Robertson, and F. Jourdin (2009). “Maritime Aerosol Network as a component of Aerosol Robotic Network”. *Journal of Geophysical Research: Atmospheres* 114.D6, p. D06204. DOI: 10.1029/2008JD011257.
- Solomon, A., G. Feingold, and M. D. Shupe (2015). “The role of ice nuclei recycling in the maintenance of cloud ice in Arctic mixed-phase stratocumulus”. *Atmospheric Chemistry and Physics* 15.18, pp. 10631–10643. DOI: 10.5194/acp-15-10631-2015.
- Solomon, A., M. D. Shupe, P. O. G. Persson, and H. Morrison (2011). “Moisture and dynamical interactions maintaining decoupled Arctic mixed-phase stratocumulus in the presence of a humidity inversion”. *Atmospheric Chemistry and Physics* 11.19, pp. 10127–10148. DOI: 10.5194/acp-11-10127-2011.
- Solomon, A., M. D. Shupe, O. Persson, H. Morrison, T. Yamaguchi, P. M. Caldwell, and G. de Boer (2014). “The Sensitivity of Springtime Arctic Mixed-Phase Stratocumulus Clouds to Surface-Layer and Cloud-Top Inversion-Layer Moisture Sources”. *Journal of the Atmospheric Sciences* 71.2, pp. 574–595. ISSN: 0022-4928. DOI: 10.1175/JAS-D-13-0179.1.
- SOMAG (2017). *GSM 4000 – Specifications*. Last access: 20 September 2020. SOMAG AG Jena. URL: <https://www.somag-ag.de/gsm-4000/>.
- Sotiropoulou, G., J. Sedlar, M. Tjernström, M. D. Shupe, I. M. Brooks, and P. O. G. Persson (2014). “The thermodynamic structure of summer Arctic stratocumulus and the dynamic coupling to the surface”. *Atmospheric Chemistry and Physics* 14.22, pp. 12573–12592. DOI: 10.5194/acp-14-12573-2014.
- Sotiropoulou, G., S. Sullivan, J. Savre, G. Lloyd, T. Lachlan-Cope, A. M. L. Ekman, and A. Nenes (2020). “The impact of secondary ice production on Arctic stratocumulus”. *Atmospheric Chemistry and Physics* 20.3, pp. 1301–1316. DOI: 10.5194/acp-20-1301-2020. URL: <https://acp.copernicus.org/articles/20/1301/2020/>.
- Sotiropoulou, G., M. Tjernström, J. Sedlar, P. Achtert, B. J. Brooks, I. M. Brooks, P. O. G. Persson, J. Prytherch, D. J. Salisbury, M. D. Shupe, P. E. Johnston, and D. Wolfe (2016). “Atmospheric Conditions during the Arctic Clouds in Summer Experiment (ACSE): Contrasting Open Water and Sea Ice Surfaces during Melt and Freeze-Up Seasons”. *Journal of Climate* 29.24, pp. 8721–8744. DOI: 10.1175/JCLI-D-16-0211.1.
- Sreenivasan, K. R. (1995). “On the universality of the Kolmogorov constant”. *Physics of Fluids* 7.11, pp. 2778–2784. DOI: 10.1063/1.868656.
- Stein, A. F., R. R. Draxler, G. D. Rolph, B. J. B. Stunder, M. D. Cohen, and F. Ngan (2015). “NOAA’s HYSPLIT Atmospheric Transport and Dispersion Modeling System”. *Bulletin of the American Meteorological Society* 96.12, pp. 2059–2077. DOI: 10.1175/BAMS-D-14-00110.1.
- Stephens, G. L. (2005). “Cloud Feedbacks in the Climate System: A Critical Review”. *Journal of Climate* 18.2, pp. 237–273. DOI: 10.1175/JCLI-3243.1.
- Stephens, G. L., D. G. Vane, S. Tanelli, E. Im, S. Durden, M. Rokey, D. Reinke, P. Partain, G. G. Mace, R. Austin, T. L’Ecuyer, J. Haynes, M. Lebsock, K. Suzuki, D. Waliser, D. Wu, J. Kay, A. Gettelman, Z. Wang, and R. Marchand (2008). “CloudSat mission: Performance and early
-

- science after the first year of operation”. *Journal of Geophysical Research: Atmospheres* 113.D8, D00A18. DOI: 10.1029/2008JD009982.
- Stuecker, M. F., C. M. Bitz, K. C. Armour, C. Proistosescu, S. M. Kang, S.-P. Xie, D. Kim, S. McGregor, W. Zhang, S. Zhao, W. Cai, Y. Dong, and F.-F. Jin (2018). “Polar amplification dominated by local forcing and feedbacks”. *Nature Climate Change* 8.12, pp. 1076–1081. ISSN: 1758-6798. DOI: 10.1038/s41558-018-0339-y.
- Sun, Z. and K. P. Shine (1995). “Parameterization of Ice Cloud Radiative Properties and Its Application to the Potential Climatic Importance of Mixed-Phase Clouds”. *Journal of Climate* 8.7, pp. 1874–1888. ISSN: 0894-8755. DOI: 10.1175/1520-0442(1995)008<1874:POICRP>2.0.CO;2.
- Szyrmer, W. and I. Zawadzki (1997). “Biogenic and Anthropogenic Sources of Ice-Forming Nuclei: A Review”. *Bulletin of the American Meteorological Society* 78.2, pp. 209–228. ISSN: 0003-0007. DOI: 10.1175/1520-0477(1997)078<0209:BAASOI>2.0.CO;2.
- Tan, I. and T. Storelvmo (2019). “Evidence of Strong Contributions From Mixed-Phase Clouds to Arctic Climate Change”. *Geophysical Research Letters* 46.5, pp. 2894–2902. DOI: 10.1029/2018GL081871.
- Tan, I., T. Storelvmo, and M. D. Zelinka (2016). “Observational constraints on mixed-phase clouds imply higher climate sensitivity”. *Science* 352.6282, pp. 224–227. ISSN: 0036-8075. DOI: 10.1126/science.aad5300.
- Teillet, P. M. (1990). “Rayleigh optical depth comparisons from various sources”. *Appl. Opt.* 29.13, pp. 1897–1900. DOI: 10.1364/AO.29.001897.
- Tesche, M., A. Ansmann, D. MÜLLER, D. Althausen, I. Mattis, B. Heese, V. Freudenthaler, M. Wiegner, M. Esselborn, G. Pisani, and P. Knippertz (2009). “Vertical profiling of Saharan dust with Raman lidars and airborne HSRL in southern Morocco during SAMUM”. *Tellus B: Chemical and Physical Meteorology* 61.1, pp. 144–164. DOI: 10.1111/j.1600-0889.2008.00390.x.
- Thomson, E. S., D. Weber, H. G. Bingemer, J. Tuomi, M. Ebert, and J. B. C. Pettersson (2018). “Intensification of ice nucleation observed in ocean ship emissions”. *Scientific Reports* 8.1, p. 1111. ISSN: 2045-2322. DOI: 10.1038/s41598-018-19297-y.
- Tjernström, M., C. Leck, C. E. Birch, J. W. Bottenheim, B. J. Brooks, I. M. Brooks, L. Bäcklin, R. Y.-W. Chang, G. de Leeuw, L. Di Liberto, S. de la Rosa, E. Granath, M. Graus, A. Hansel, J. Heintzenberg, A. Held, A. Hind, P. Johnston, J. Knulst, M. Martin, P. A. Matrai, T. Mauritsen, M. Müller, S. J. Norris, M. V. Orellana, D. A. Orsini, J. Paatero, P. O. G. Persson, Q. Gao, C. Rauschenberg, Z. Ristovski, J. Sedlar, M. D. Shupe, B. Sierau, A. Sirevaag, S. Sjogren, O. Stetzer, E. Swietlicki, M. Szczodrak, P. Vaattovaara, N. Wahlberg, M. Westberg, and C. R. Wheeler (2014). “The Arctic Summer Cloud Ocean Study (ASCOS): overview and experimental design”. *Atmospheric Chemistry and Physics* 14.6, pp. 2823–2869. DOI: 10.5194/acp-14-2823-2014.
- Tjernström, M., C. Leck, P. O. G. Persson, M. L. Jensen, S. P. Oncley, and A. Targino (2004). “The Summertime Arctic Atmosphere: Meteorological Measurements during the Arctic Ocean Experiment 2001”. *Bulletin of the American Meteorological Society* 85.9, pp. 1305–1322. DOI: 10.1175/BAMS-85-9-1305.
- Tukiainen, S., E. O’Connor, and A. Korpinen (2020). “CloudnetPy: A Python package for processing cloud remote sensing data”. *Journal of Open Source Software* 5.53, p. 2123. DOI: 10.21105/joss.02123.
- Twomey, S. (1974). “Pollution and the planetary albedo”. *Atmospheric Environment (1967)* 8.12, pp. 1251–1256. ISSN: 0004-6981. DOI: 10.1016/0004-6981(74)90004-3.

-
- (1977). “The Influence of Pollution on the Shortwave Albedo of Clouds.” *Journal of Atmospheric Sciences* 34.7, pp. 1149–1154. DOI: 10.1175/1520-0469(1977)034<1149:TIOPOT>2.0.CO;2.
- Uttal, T., J. A. Curry, M. G. McPhee, D. K. Perovich, R. E. Moritz, J. A. Maslanik, P. S. Guest, H. L. Stern, J. A. Moore, R. Turenne, A. Heiberg, M. C. Serreze, D. P. Wylie, O. G. Persson, C. A. Paulson, C. Halle, J. H. Morison, P. A. Wheeler, A. Makshtas, H. Welch, M. D. Shupe, J. M. Intrieri, K. Stamnes, R. W. Lindsey, R. Pinkel, W. S. Pegau, T. P. Stanton, and T. C. Grenfeld (2002). “Surface Heat Budget of the Arctic Ocean”. *Bulletin of the American Meteorological Society* 83.2, pp. 255–276. DOI: 10.1175/1520-0477(2002)083<0255:SHBOTA>2.3.CO;2.
- Uttal, T. et al. (2016). “International Arctic Systems for Observing the Atmosphere: An International Polar Year Legacy Consortium”. *Bulletin of the American Meteorological Society* 97.6, pp. 1033–1056. DOI: 10.1175/BAMS-D-14-00145.1.
- Vassel, M., L. Ickes, M. Maturilli, and C. Hoose (2019). “Classification of Arctic multilayer clouds using radiosonde and radar data in Svalbard”. *Atmospheric Chemistry and Physics* 19.7, pp. 5111–5126. DOI: 10.5194/acp-19-5111-2019.
- Vavrus, S. (2004). “The Impact of Cloud Feedbacks on Arctic Climate under Greenhouse Forcing*.”. *Journal of Climate* 17.3, pp. 603–615. ISSN: 0894-8755. DOI: 10.1175/1520-0442(2004)017<0603:TIOCFO>2.0.CO;2.
- Verlinde, J., M. Rambukkange, E. Clothiaux, G. Mcfarquhar, and E. Eloranta (2013). “Arctic multilayered, mixed-phase cloud processes revealed in millimeter-wave cloud radar Doppler spectra”. *Journal of Geophysical Research* 118.23, pp. 13, 199–13, 213. DOI: 10.1002/2013JD020183.
- Vüllers, J., P. Achtert, I. M. Brooks, M. Tjernström, J. Prytherch, A. Burzik, and R. Neely III (2021). “Meteorological and cloud conditions during the Arctic Ocean 2018 expedition”. *Atmospheric Chemistry and Physics* 21.1, pp. 289–314. DOI: 10.5194/acp-21-289-2021.
- Wegener, A. (1912). “Thermodynamik der Atmosphäre”. *Nature* 90.2237, pp. 31–31. ISSN: 1476-4687. DOI: 10.1038/090031a0.
- Weitkamp, C., ed. (2005). *Lidar*. Springer-Verlag New York. ISBN: 978-0-387-40075-4. DOI: 10.1007/b106786.
- Wendisch, M., M. Brückner, J. P. Burrows, S. Crewell, K. Dethloff, K. Ebell, C. Lüpkes, A. Macke, J. Notholt, J. Quaas, A. Rinke, and I. Tegen (2017). “Understanding causes and effects of rapid warming in the Arctic”. *Eos* 98, pp. 22–26. DOI: 10.1029/2017E0064803.
- Wendisch, M. et al. (2019). “The Arctic Cloud Puzzle: Using ACLOUD/PASCAL Multiplatform Observations to Unravel the Role of Clouds and Aerosol Particles in Arctic Amplification”. *Bulletin of the American Meteorological Society* 100.5, pp. 841–871. DOI: 10.1175/BAMS-D-18-0072.1.
- Wessel, P., J. F. Luis, L. Uieda, R. Scharroo, F. Wobbe, W. H. F. Smith, and D. Tian (2019). “The Generic Mapping Tools Version 6”. *Geochemistry, Geophysics, Geosystems* 20.11, pp. 5556–5564. DOI: 10.1029/2019GC008515.
- Westbrook, C. D. and A. J. Illingworth (2011). “Evidence that ice forms primarily in supercooled liquid clouds at temperatures $> -27^{\circ}\text{C}$ ”. *Geophysical Research Letters* 38.14. DOI: 10.1029/2011GL048021.
- (2013). “The formation of ice in a long-lived supercooled layer cloud”. *Quarterly Journal of the Royal Meteorological Society* 139.677, pp. 2209–2221. DOI: 10.1002/qj.2096.
- Westbrook, C. D., A. J. Illingworth, E. J. O’Connor, and R. J. Hogan (2010). “Doppler lidar measurements of oriented planar ice crystals falling from supercooled and glaciated layer clouds”. *Quarterly Journal of the Royal Meteorological Society* 136.646, pp. 260–276. DOI: <https://doi.org/10.1002/qj.528>.
-

- Wex, H., L. Huang, W. Zhang, H. Hung, R. Traversi, S. Becagli, R. J. Sheesley, C. E. Moffett, T. E. Barrett, R. Bossi, H. Skov, A. H  nerbein, J. Lubitz, M. L  ffler, O. Linke, M. Hartmann, P. Herenz, and F. Stratmann (2019). “Annual variability of ice-nucleating particle concentrations at different Arctic locations”. *Atmospheric Chemistry and Physics* 19.7, pp. 5293–5311. DOI: 10.5194/acp-19-5293-2019.
- Willis, M. D., W. R. Leaitch, and J. P. Abbatt (2018). “Processes Controlling the Composition and Abundance of Arctic Aerosol”. *Reviews of Geophysics* 56.4, pp. 621–671. DOI: <https://doi.org/10.1029/2018RG000602>.
- Winker, D. M., J. Pelon, J. A. Coakley, S. A. Ackerman, R. J. Charlson, P. R. Colarco, P. Flamant, Q. Fu, R. M. Hoff, C. Kittaka, T. L. Kubar, H. Le Treut, M. P. McCormick, G. M  gie, L. Poole, K. Powell, C. Trepte, M. A. Vaughan, and B. A. Wielicki (2010). “The CALIPSO Mission”. *Bulletin of the American Meteorological Society* 91.9, pp. 1211–1230. DOI: 10.1175/2010BAMS3009.1.
- Wittuhnn, J., A. H  nerbein, F. Filipitsch, S. Wacker, S. Meilinger, and H. Deneke (2021). “Aerosol properties and aerosol–radiation interactions in clear-sky conditions over Germany”. *Atmospheric Chemistry and Physics* 21.19, pp. 14591–14630. DOI: 10.5194/acp-21-14591-2021.
- Wulfmeyer, V. and T. Janji   (2005). “Twenty-Four-Hour Observations of the Marine Boundary Layer Using Shipborne NOAA High-Resolution Doppler Lidar”. *Journal of Applied Meteorology* 44.11, pp. 1723–1744. DOI: 10.1175/JAM2296.1.
- Yin, Z., A. Ansmann, H. Baars, P. Seifert, R. Engelmann, M. Radenz, C. Jimenez, A. Herzog, K. Ohneiser, K. Hanbuch, L. Blarel, P. Goloub, G. Dubois, S. Victori, and F. Maupin (2019). “Aerosol measurements with a shipborne Sun–sky–lunar photometer and collocated multiwavelength Raman polarization lidar over the Atlantic Ocean”. *Atmospheric Measurement Techniques* 12.10, pp. 5685–5698. DOI: 10.5194/amt-12-5685-2019.
- Yoshida, Y. and S. Asano (2005). “Effects of the Vertical Profiles of Cloud Droplets and Ice Particles on the Visible and Near-Infrared Radiative Properties of Mixed-Phase Stratocumulus Clouds”. *Journal of the Meteorological Society of Japan. Ser. II* 83.4, pp. 471–480. DOI: 10.2151/jmsj.83.471.
- Young, G., H. M. Jones, T. W. Choularton, J. Crosier, K. N. Bower, M. W. Gallagher, R. S. Davies, I. A. Renfrew, A. D. Elvidge, E. Darbyshire, F. Marengo, P. R. A. Brown, H. M. A. Ricketts, P. J. Connolly, G. Lloyd, P. I. Williams, J. D. Allan, J. W. Taylor, D. Liu, and M. J. Flynn (2016). “Observed microphysical changes in Arctic mixed-phase clouds when transitioning from sea ice to open ocean”. *Atmospheric Chemistry and Physics* 16.21, pp. 13945–13967. DOI: 10.5194/acp-16-13945-2016.
- Zeppenfeld, S., M. van Pinxteren, M. Hartmann, A. Bracher, F. Stratmann, and H. Herrmann (2019). “Glucose as a Potential Chemical Marker for Ice Nucleating Activity in Arctic Seawater and Melt Pond Samples”. *Environmental Science & Technology* 15, pp. 8747–8756. ISSN: 0013-936X. DOI: 10.1021/acs.est.9b01469.
- Zhang, D., Z. Wang, P. Kollias, A. M. Vogelmann, K. Yang, and T. Luo (2018). “Ice particle production in mid-level stratiform mixed-phase clouds observed with collocated A-Train measurements”. *Atmospheric Chemistry and Physics* 18.6, pp. 4317–4327. DOI: 10.5194/acp-18-4317-2018.
- Zhang, D., Z. Wang, A. Heymsfield, J. Fan, and T. Luo (2014). “Ice Concentration Retrieval in Stratiform Mixed-Phase Clouds Using Cloud Radar Reflectivity Measurements and 1D Ice Growth Model Simulations”. *Journal of the Atmospheric Sciences* 71.10, pp. 3613–3635. DOI: 10.1175/JAS-D-13-0354.1.
- Zhang, D., Z. Wang, T. Luo, Y. Yin, and C. Flynn (2017). “The occurrence of ice production in slightly supercooled Arctic stratiform clouds as observed by ground-based remote sensors at
-

the ARM NSA site”. *Journal of Geophysical Research: Atmospheres* 122.5, pp. 2867–2877. DOI: 10.1002/2016JD026226.

Zhang, Y., A. Macke, and F. Albers (1999). “Effect of crystal size spectrum and crystal shape on stratiform cirrus radiative forcing”. *Atmospheric Research* 52.1, pp. 59–75. ISSN: 0169-8095. DOI: [https://doi.org/10.1016/S0169-8095\(99\)00026-5](https://doi.org/10.1016/S0169-8095(99)00026-5). URL: <https://www.sciencedirect.com/science/article/pii/S0169809599000265>.

Zhou, M. Y., D. H. Lenschow, B. B. Stankov, J. C. Kaimal, and J. E. Gaynor (1985). “Wave and Turbulence Structure in a Shallow Baroclinic Convective Boundary Layer and Overlying Inversion”. *Journal of the Atmospheric Sciences* 42.1, pp. 47–57. DOI: 10.1175/1520-0469(1985)042<0047:WATSIA>2.0.CO;2.

List of abbreviations and acronyms

(AC) ³	Arctic Amplification: Climate Relevant Atmospheric and Surface Processes and Feedback Mechanisms
ACI	aerosol-cloud-interaction
ACLOUD	Arctic Cloud Observations Using Airborne Measurements during Polar Day
ACSE	Arctic Clouds in Summer
AERONET	Aerosol Robotic Network
AOE	Arctic Ocean Experiment
ARI	aerosol-radiation-interaction
ARM	Atmospheric Radiation Measurement
ARSCL	Active Remote Sensing of Clouds
ASCOS	Arctic Summer Cloud Ocean Study
ATM	atmospheric
CALIPSO	Cloud-Aerosol Lidar and Infrared Pathfinder Satellite Observation
CAM5.1	Community Atmosphere Model version 5.1
CCN	cloud condensation nuclei
CCNC	CCN number concentration
CO ₂	carbon dioxide
CRE	cloud radiative effect
DOE	Department of Energy
EDR	eddy dissipation rate
FFT	Fast Fourier Transformation
FLEXPART	FLEXible PARTicle dispersion model
GDAS	Global Data Assimilation System
HATPRO	Humidity And Temperature Profiler
HV	horizontal visibility
HYSPLIT	Hybrid Single-Particle Lagrangian IntegratedTrajectory model
IAOOS	Ice Atmosphere Arctic Ocean Observing System
IMU	inertial measurement unit

INP	ice-nucleating particle
INPC	INP number concentration
IWC	ice-water content
IWP	ice-water path
IWV	integrated water vapor
KAZR	Ka-band ARM zenith radar
LDR	linear depolarization ratio
LES	large-eddy simulations
lidar	light detection and ranging
LLS	low-level stratus
LW	longwave
LW _↓	global terrestrial downward directed irradiance
LWC	liquid-water content
LWP	liquid-water path
LWP _{int}	column-integrated LWC
MEMS	micro-electro-mechanical systems
MODIS	Moderate Resolution Imaging Spectroradiometer
MOSAiC	Multidisciplinary Drifting Observatory for the Study of Arctic Climate
MWR	microwave radiometer
NSA	North Slope of Alaska
PAMARCMiP 2018	Polar Airborne Measurements and Arctic Regional Climate Model Simulation Project 2018
PASCAL	Physical Feedbacks of Arctic Boundary Layer, Sea Ice, Cloud and Aerosol
PEARL	Polar Environment Atmospheric Research Laboratory
PSD	particle size distribution
radar	radio detection and ranging
RRTMG	Rapid Radiative Transfer Model for General Circulation Models
RV	research vessel
SFC	surface
SHEBA	Surface Heat Budget of the Arctic
SiPCA	Survival of Polar Cod in the Arctic Ocean
SNR	signal-to-noise-ratio
SO ₂	sulfur dioxide
SW	shortwave
SW _↓	global solar downward directed irradiance
T-CARS	TROPOS Cloud and Aerosol Radiative Simulator
TKE	turbulence kinetic energy
TOA	top of the atmosphere

TROPOS

Leibniz Institute for Tropospheric Research
